University of Alberta

Internal Dynamics of Weakly Bound Complexes with CH_4, C_2H_2, and C_2H_4 Studied by Fourier Transform Microwave Spectroscopy and *ab initio* Calculations

by

©

Yaqian Liu

A thesis submitted to the Faculty of Graduate Studies and Research in partial fulfillment
of the requirements for the degree of Doctor of Philosophy

Department of Chemistry

Edmonton, Alberta

Fall, 2002

National Library of Canada
Acquisitions and Bibliographic Services
395 Wellington Street
Ottawa ON K1A 0N4
Canada

Bibliothèque nationale du Canada
Acquisitions et services bibliographiques
395, rue Wellington
Ottawa ON K1A 0N4
Canada

Your file Votre référence

Our file Notre référence

The author has granted a non-exclusive licence allowing the National Library of Canada to reproduce, loan, distribute or sell copies of this thesis in microform, paper or electronic formats.

L'auteur a accordé une licence non exclusive permettant à la Bibliothèque nationale du Canada de reproduire, prêter, distribuer ou vendre des copies de cette thèse sous la forme de microfiche/film, de reproduction sur papier ou sur format électronique.

The author retains ownership of the copyright in this thesis. Neither the thesis nor substantial extracts from it may be printed or otherwise reproduced without the author's permission.

L'auteur conserve la propriété du droit d'auteur qui protège cette thèse. Ni la thèse ni des extraits substantiels de celle-ci ne doivent être imprimés ou autrement reproduits sans son autorisation.

0-612-81226-X

Canada

University of Alberta

Library Release Form

Name of Author: Yaqian Liu

Title of Thesis: Internal Dynamics of Weakly Bound Complexes with CH_4, C_2H_2, and C_2H_4 Studied by Fourier Transform Microwave Spectroscopy and *ab initio* Calculations

Degree: Doctor of Philosophy

Year this Degree Granted: 2002

Permission is hereby granted to the University of Alberta Library to reproduce single copies of the thesis and to lend or sell such copies for private, scholarly or scientific research purpose only.

The author reserves all other publication and other rights in association with the copyright in the thesis, and except as herein before provided, neither the thesis nor any substantial portion thereof may be printed or otherwise reproduced in any material form whatever without the author's prior written permission.

Liu, Yaqian

#205, 10735-81 Avenue
Edmonton, Alberta, Canada
T6E 1Y2

Date: May 9, 2002

University of Alberta

Faculty of Graduate Studies and Research

The undersigned certify that they have read, and recommend to the Faculty of Graduate Studies and Research for acceptance, a thesis entitled "Internal Dynamics of Weakly Bound Complexes with CH_4, C_2H_2, and C_2H_4 Studied by Fourier Transform Microwave Spectroscopy and *ab initio* Calculations" submitted by Yaqian Liu in partial fulfillment of the requirement for the degree of Doctor of Philosophy.

W. J
Supervisor Dr. W. Jäger

Serge Kotovych
Dr. G. Kotovych

Mark McDermott
Dr. M. T. McDermott

P-N. Roy
Dr. P-N. Roy

Helmy S. Sherif
Dr. H. S. Sherif

N.P.C. Westwood
External Examiner Dr. N. Westwood

Date: May 8, 2002

ABSTRACT

Rotational spectra of various isotopomers of six hydrocarbon-containing van der Waals complexes, namely Ar-ethylene, Ne-ethylene, Ar-acetylene, Ne-acetylene, Kr-methane, and CO-methane, were recorded using a pulsed molecular beam Fourier transform microwave spectrometer. *Ab initio* interaction potential energy surfaces of Ne-ethylene, Ne-acetylene, Kr-methane, and Ar-methane were constructed. The resulting spectroscopic and theoretical data were utilized to derive information about structure and internal dynamics of these complexes.

Transition doubling was observed in the spectra of Ar-ethylene and Ne-ethylene, which is attributed to a tunneling motion of the ethylene subunit. The spectra of the Ar-trans-D_2-ethylene and Ne-trans-D_2-ethylene isotopomers suggest that the internal rotation of ethylene about the C=C bond is responsible for the observed transition doubling. This conclusion is further supported by the results from *ab initio* calculations. It is evident from the *ab initio* minimum energy paths that the internal rotation about the C=C bond is preferred mainly because the radial movement involved with this motion is not as pronounced as in the internal rotation about the *c*-principal axis of the ethylene monomer.

The presence of a strong coupling between large amplitude radial and angular internal motions was inferred from the analyses of the obtained spectroscopic data of rare gas-acetylene complexes. This strong radial-angular coupling is also evident from the *ab initio* potential energy surface of Ne-acetylene. Information about the energy level ordering of the excited van der Waals bending states was also derived from the observed spectra. Different states were observed for Ar-acetylene and Ne-acetylene. This suggests

that an energy level reordering occurs when the binding partner of acetylene changes from Ar to Ne.

Rotational transitions within various internal rotor states were measured for the Kr-methane and CO-methane dimers. This is evidence for a nearly free internal rotation of methane within these weakly bound complexes. The recorded spectrum of CO-methane closely resembles that of Kr-methane, indicating that CO also undergoes nearly free internal rotation within the dimer. *Ab initio* calculations of Kr-methane and Ar-methane predict that the angular dynamics does not change significantly when the binding partner of methane changes from Kr to Ar.

ACKNOWLEDGMENTS

I wish to thank Dr. W. Jäger, my supervisor, for his invaluable guidance, assistance, and patience, which make this thesis possible.

I am grateful to all the members of Dr. Jäger's research group for their support and encouragement. In particular, I would like to thank Dr. Y. Xu for many useful suggestions and fruitful discussions regarding my research projects.

Special thanks to Dr. A. Jordan, my teaching assistant coordinator, for her moral support and advice on many difficult occasions.

Finally, I wish to acknowledge my family, H. Liu, C. Meng, J. Liu, and M. Chen, for their endless support and for believing in me.

Table of Contents

Chapter Page

1 INTRODUCTION 1

2 BASIC THEORY OF FOURIER TRANSFORM MICROWAVE SPECTROSCOPY AND SPECTROMETER 9
- 2.1 Theoretical Background 10
- 2.2 Molecular Beam 16
- 2.3 Spectrometer 18
  - 2.3.1 Mechanical Details 19
  - 2.3.2 Electrical Details 20
  - 2.3.3 Timing Sequence 23

3 *AB INITIO* CALCULATIONS AND MOLECULAR SYMMETRY GROUP ANALYSES 33
- 3.1 *Ab initio* Calculations 33
  - 3.1.1 Methods and Basis Sets 33
  - 3.1.2 Basis Set Superposition Error 36
  - 3.1.3 Computational Details 37
- 3.2 Molecular Symmetry Group Analyses 39
  - 3.2.1 Molecular Symmetry Group and Elements 39
  - 3.2.2 Nuclear Spin Statistical Weights 41
  - 3.2.3 Examples of Molecular Symmetry Group Analyses 42

4 INTERNAL ROTATION MOTION OF ETHYLENE IN Rg-ETHYLENE 57
- 4.1 Previous Work and Motivation for this Study 57
- 4.2 Spectral Search and Assignments 60
  - 4.2.1 Ar-C_2H_4 61
  - 4.2.2 Ne-C_2H_4 65
- 4.3 Discussion of Experimental Results 68
  - 4.3.1 Spectroscopic Constants and Structure 68
  - 4.3.2 Relative Intensity and Tunneling Motion 70
  - 4.3.3 Coriolis Interaction and Barrier to Internal Rotation Motion 76
- 4.4 Potential Energy Surfaces of Ne-C_2H_4 80
- 4.5 Summary 84

5 MICROWAVE AND *AB INITIO* STUDIES OF Ar-, Ne-ACETYLENE 106
  5.1 Isotopic Study of the Internal Dynamics of Ar-C_2H_2 107
    5.1.1 Previous Work 107
    5.1.2 Spectral Assignments and Analyses 109
    5.1.3 Results and Discussion 113
  5.2 Rotational Spectrum and Potential Energy Surface of Ne-C_2H_2 117
    5.2.1 Motivation 117
    5.2.2 Observed Spectra and Assignments 119
    5.2.3 Discussion of Spectroscopic Results 123
    5.2.4 Potential Energy Surfaces of Ne-C_2H_2 134
  5.3 Summary 136

6 SPECTROSCOPIC AND THEORETICAL STUDIES OF METHANE-CONTAINING VAN DER WAALS SYSTEMS 153
  6.1 Previous Studies on CH_4-containing van der Waals Dimers 153
  6.2 Observed Spectra and Analyses 157
    6.2.1 Kr-CH_4 157
    6.2.2 CO-CH_4 163
  6.3 Discussion of Spectroscopic Results of Kr-CH_4 165
    6.3.1 Spectroscopic Constants and Structure 165
    6.3.2 Coriolis Interaction in the j=1 State 170
    6.3.3 Tentative Assignments of the j=2 State 172
  6.4 Potential Energy Surface of Kr-CH_4 176
  6.5 Discussion of CO-CH_4 177
  6.6 Discussion of Ar-CH_4 178
  6.7 Summary 180

7 CONCLUSIONS 206

BIBLIOGRAPHY 210

List of Tables

Table Page

3-1 Character table for Ne-C_2H_4. 50

3-2 Symmetry labels and spin statistical weights of energy levels of Ne-ethylene isotopomers from molecular symmetry group analyses. 50

3-3 Character table of the T_d(M) molecular symmetry group for Kr-CH_4. 51

3-4 Direct product table for the T_d group. 51

3-5 Symmetry labels and spin statistical weights of energy levels of Kr-CH_4 isotopomers. 51

4-1 Measured transition frequencies of Ar-ethylene isotopomers (m=0). 86

4-2 Measured transition frequencies of Ar-ethylene isotopomers (m=1). 87

4-3 Derived spectroscopic constants for Ar-ethylene isotopomers. 88

4-4 Measured transition frequencies of Ne-ethylene isotopomers (m=0). 89

4-5 Measured transition frequencies of Ne-ethylene isotopomers (m=1). 90

4-6 Derived spectroscopic constants of Ne-ethylene isotopomers (m=0). 91

4-7 Derived spectroscopic constants of Ne-ethylene isotopomers (m=1). 92

4-8 *Ab initio* interaction energies of Ne-ethylene with basis set 1. 93

4-9 *Ab initio* interaction energies of Ne-ethylene with basis set 2. 94

5-1 Rotational transition frequencies of Ar-acetylene isotopomers. 138

5-2 Spectroscopic constants of Ar-acetylene isotopomers. 139

5-3 Spectroscopic constants of Ar-acetylene isotopomers from fits of individual K-stacks. 140

5-4 Measured transition frequencies of Ne-acetylene isotopomers. 141

5-5 Frequencies of the deuterium nuclear quadrupole hyperfine components of the J=1-0, Σ_0 transitions. 141

5-6 Spectroscopic constants of Ne-acetylene isotopomers (Σ_0 state). 142

5-7 Comparison of the experimental and calculated transition frequencies of Ne-acetylene. 142

5-8 *Ab initio* MP4 interaction energies of Ne-HCCH. 143

5-9 *Ab initio* CCSD(T) interaction energies of Ne-HCCH. 144

6-1 Measured transition frequencies of Kr-CH_4 isotopomers. 182

6-2 Measured transition frequencies of ^{83}Kr-CH_4 and ^{83}Kr-$^{13}CH_4$. 183

6-3 Measured transition frequencies of Kr-$^{13}CH_4$ isotopomers. 184

6-4 Measured transition frequencies of Kr-CD_4 isotopomers. 185

6-5 Measured transition frequencies of deuterated ^{83}Kr-CH_4. 186

6-6 Measured transition frequencies of Kr-CH_3D and Kr-CHD_3. 187

6-7 Measured transition frequencies of $^{12}C^{16}O$-CH_4 isotopomers. 188

6-8 Measured transition frequencies of ^{13}CO-CH_4 isotopomers. 189

6-9 Bond length, stretching frequency, and force constant of Kr-methane isotopomers. 190

6-10 Computed dipole moment values for Kr-CH_4 (ϕ=0°). 191

6-11 Interaction energies of Kr-CH_4. 192

6-12 Interaction energies of Ar-CH_4 (ϕ=0°). 194

6-13 Bond length, stretching frequency, and force constant of CO-methane isotopomers. 195

6-14 Comparison of CO-CH_4 with CO-rare gas complexes. 195

6-15 Computed dipole moment values of Ar-CH_4 (ϕ=0°). 196

List of Figures

Figure Page

2-1 Block vector diagram to visualize the π/2-condition. 25

2-2 The mechanical setup of the spectrometer. 26

2-3 A representative spectrum showing the Doppler splitting. 27

2-4 Detailed electronic setup of the spectrometer. 28

2-5 Schematic diagram of the circuit for excitation pulse generation. 30

2-6 Schematic diagram of the superheterodyne detection system. 31

2-7 Experimental timing diagram. 32

3-1 The effects of the four elements of the molecular symmetry group of H_2O. 52

3-2 Numbering of the identical nuclei used for the molecular symmetry group analysis for Ne-C_2H_4. 53

3-3 Illustration of the equivalence of the nuclear permutation-inversion operation (14)(23)(56)* and its corresponding equivalent rotation $R_{\text{int}}R_b^{\pi}$ (out-of-plane motion). 54

3-4 The two isomers of Ne-cis-D_2-ethylene. 55

3-5 Numbering of the four equivalent hydrogen nuclei in Kr-CH_4 for molecular symmetry group analysis. 56

4-1 $(R\ \theta\ \phi)$ coordinates used to describe the geometry of Rg-C_2H_4. 95

4-2 Observed transition doubling of the $J_{K_aK_c}=2_{02}-1_{01}$ transition of the Ar-C_2H_4 isotopomer. 96

4-3 A representative spectrum of the $J_{K_aK_c}=1_{01}-0_{00}$, $m=1$ transition of ^{20}Ne-C_2H_4. 97

4-4 A representative spectrum of the $J_{K_aK_c}=1_{01}-0_{00}$, $m=0$ transition of ^{20}Ne-trans-D_2-ethylene. 98

4-5 Schematic energy level diagram for Rg-C_2H_4. 99

4-6 Schematic energy level diagram for Rg-trans-D$_2$-ethylene for the case of in-plane motion. 100

4-7 Schematic energy level diagram of Rg-trans-D$_2$-ethylene for the case of out-of-plane motion. 101

4-8 One dimensional *ab initio* potential energy curves for Ne-ethylene. 102

4-9 Minimum energy paths for Ne-ethylene. 104

5-1 Structural parameters used to describe the Rg-acetylene van der Waals dimers. 145

5-2 Observed transition intensities of the K_a=0 and K_a=1 transitions of Ar-C$_2$H$_2$. 146

5-3 A spectrum of the $J_{K_aK_c}=1_{01}-0_{00}$ transition of Ar-DCCH. 147

5-4 The correlation between the free rotor and rigid rotor energy levels for the Ar-HCCH van der Waals dimer. 148

5-5 Representative spectra of the J=1-0, Σ_0 transitions of ^{20}Ne-DCCD and ^{20}Ne-DCCH. 149

5-6 Schematic energy level diagram for ^{20}Ne-DCCH. 151

5-7 The angular dependence of the minimum interaction energy of Ne-HCCH. 152

6-1 Energy level correlation diagram for Kr-CH$_4$ 197

6-2 Structural parameters used to describe the Rg-methane van der Waals complexes. 198

6-3 The Coriolis interaction between the j=1, K=0 and j=1, K=1 states. 199

6-4 Rotational spectrum of the J=1-0 transition of Kr-CH$_4$ (j=1, K=0). 200

6-5 Representative spectra of the J=1-0 and 2-1 transitions of ^{83}Kr-CH$_4$ (j=1, K=0). 201

6-6 Spectrum of the J=1-0 rotational transition of ^{83}Kr-CH$_3$D (j=0, K=0 state). 202

6-7 Representative spectrum of the J=1-0 transition of ^{13}C^{17}O-CH$_4$ (j=0, K=0). 203

6-8 The angular dependence of the dipole moments of Kr-CH_4 and Ar-CH_4 (ϕ fixed at 0°). 204

6-9 The angular dependence of the interaction energies of Kr-CH_4 and Ar-CH_4 (ϕ fixed at 0°). 205

1

INTRODUCTION

Weakly bound complexes, often called van der Waals complexes, are molecular clusters formed in the gas phase (or in a molecular beam) between two or more neutral monomers (*1*,*2*). The name 'van der Waals complex' indicates already that the nature of the bond between the constituent monomers is quite different from that in chemically bound species. The main attractive contribution comes from long-range dispersion forces (*3*). Typically, binding energies in these weakly bound systems are only of the order of 100 cm^{-1} (*4*), which is several orders of magnitude smaller than those of chemical bonds (*5*).

The primary goal of studying weakly bound molecular systems is to provide detailed understanding of interactions between molecules. Such interactions are involved in an extensive range of chemical, physical, and biological phenomena, including phase transitions (*6*,*7*,*8*), solvation processes (*9*,*10*), inelastic energy transfer (*11*,*12*,*13*), photofragmentation dynamics (*14*), protein folding (*15*,*16*), and enzyme reaction mechanisms (*15*,*17*). Generally, it is convenient to express intermolecular interactions in terms of intermolecular potential energy surfaces, which describe the dependence of the interaction energy on the separations and relative orientations of constituent molecules. The main task of the study of van der Waals complexes is therefore the characterization of the associated intermolecular potentials. However, intermolecular potential energy surfaces can not be measured directly. Instead, properties, any of which depend on the interaction potential, must be measured. A model potential can be proposed and then adjusted to bring the properties calculated from the model potential into agreement with experimental measurements. The measurements that provide the most detailed information about an intermolecular potential energy surface are often spectroscopic ones.

Since the pioneering work of Welsh and co-workers in 1964 (*18*), high resolution spectra of van der Waals complexes have been, and still are, a rich source of information about intermolecular potential energy surfaces. A range of techniques, including molecular beam electric resonance spectroscopy (*19,20,21*), pulsed nozzle Fourier transform microwave spectroscopy (*22,23,24*), millimeter wave spectroscopy (*25,26,27*), infrared spectroscopy (*28,29,30,31,32*), and laser induced fluorescence spectroscopy (*33,34,35*), have been applied to observe the spectra of numerous van der Waals complexes. A number of review papers on high resolution spectroscopic studies of weakly bound complexes have appeared in literature (for example see refs. *36,37,38,39,40,41,42,43*), and an extensive bibliography of references has been compiled (*44*).

The earliest high resolution studies of weakly bound molecular clusters focused on the determination of the structures of the complexes and the extent of large amplitude zero-point motions of the monomers within the complexes. For these purposes, the method of molecular beam Fourier transform microwave spectroscopy has been widely applied to provide accurate ground state rotational and centrifugal distortion constants, from which detailed insights into the features of the intermolecular potential energy surface near the potential minimum can be obtained. As a result of the extremely high resolving ability of this technique, nuclear quadrupole hyperfine structures of rotational transitions are resolved in many cases and nuclear quadrupole coupling constants are obtained, from which information about large amplitude zero-point motions of the constituents can be inferred. Often other small splittings, not observable with other spectroscopic techniques, can be resolved with the Fourier transform microwave technique. A good example is the detection of the small *l*/*K*-type doubling splitting of the j=1, K=1 transitions of F symmetry in Ar-SiH_4, which could not be obtained from the infrared spectra. The splitting is sensitive to the corresponding potential energy surface and was used as a test of existing potentials (*45*).

Contrary to any spectroscopic method, which probes only a certain region of the potential energy surface, *ab initio* calculations are capable of arbitrarily sampling any region of the interaction potential. In this sense, *ab initio* electronic structure calculations play an important role in the advancement of the knowledge about intermolecular forces (*43,46,47,48,49*). Earlier applications of *ab initio* methods focused on qualitatively comparing theoretical results with experimental measurements and understanding intermolecular forces. Due to rapid progresses in computational algorithms and advancements in computer hardware, *ab initio* techniques are now capable of providing potential energy surfaces of spectroscopic accuracy (less than 1 cm^{-1} error). This could be illustrated with the state-of-the-art *ab initio* study of the Ne-CO dimer (*50,51*). Two potentials were obtained, one using symmetry adapted perturbation theory (*50*), the other using the supermolecular coupled-cluster theory with single and double excitations and noniterative perturbational treatment of triple excitations (*51*). As shown in ref. *51*, a variety of properties calculated from the two potentials agrees very well with experimental measurements, including rotational-vibrational spectra, integral scattering cross sections, differential scattering cross sections, pressure broadening, and second virial coefficients. In particular, frequencies of rotational transitions obtained from Fourier transform microwave spectroscopy are reproduced to within 2%.

Very often in the study of intermolecular forces, one starts by studying small clusters, such as dimers and trimers, which are more approachable both experimentally and theoretically. Ultimately, the molecular level description of small clusters is expected to contribute to an understanding of bulk properties. In the same context, complexes of rare gas (Rg) atoms with various molecules become especially useful model systems. Rg atoms are spherically symmetric so that the dimensionalities of intermolecular potential energy surfaces of Rg-containing complexes are greatly reduced compared to systems where the Rg atom is substituted by a molecule. Highly resolved rotational and vibrational spectra for ground and excited states of these systems may be measured and assigned. In addition, the *ab initio* calculation is greatly simplified with the reduced number of degrees of freedom. Finally, the problem of quantum treatment of nuclear dynamics in these cases has been solved and theoretical spectra may be obtained from *ab initio* potentials. Comparison of *ab initio* and experimental spectra thus provides a very stringent test of the *ab initio* potential and guides further improvements of the potential energy surface. For example, in studying solvation processes of organic species, the simplest prototypical systems are van der Waals complexes of organic molecules with rare gas atoms. Earlier studies along this line mainly focused on systems of relatively large aromatic molecules (*52,53,54,55,56*). The large number of atoms involved in such cases makes accurate *ab initio* calculations less accessible (*57*). It is expected that studies on relatively smaller systems, such as CH_4-, C_2H_2-, and C_2H_4-Rg dimers, where accurate *ab initio* potential energy surfaces can be constructed, would give guidance as to which models will work and where approximations can be made.

Since Rg atoms have no permanent multipole moments, the electrostatic contribution, i.e., the interaction between permanent multipole moments, to the attraction is completely missing in Rg-molecule systems. The induction energy is normally small compared to the dispersion energy (*5*). Therefore, the dispersion interaction is the dominant contribution. As a result of the extremely weak binding, large amplitude internal motions can often occur. A few examples of different types of large amplitude internal motions are given below.

The intermolecular potential energy surfaces of weakly bound systems can be quite complex and many display multiple minima separated by small barriers. Tunneling between these minima can often occur. For example, both rotational spectroscopic and theoretical studies on the Ne-cyclopropane dimer revealed that the cyclopropane subunit undergoes tunneling motions within the dimer (*58,59*). Tunneling splittings were also observed in the rotational spectra of various ethylene-containing complexes (*60,61,62,63*). Such tunneling motions often result in complications in the observed rotational and vibrational spectra. However, with proper interpretation, valuable information about the tunneling mechanism and the tunneling barrier can be obtained.

In the case of Ne-cyclopropane, the three-dimensional intermolecular motion is comparatively rigid in the radial coordinate such that the van der Waals stretching and bending coordinates may be approximately separated (*58,59*). However, in some weakly bound complexes, such as Rg-HCN, there is strong coupling between the two coordinates. This strong radial-angular coupling causes unusual spectroscopic observations (*24,64,65,66,67,68,69,70*). Not surprisingly, spectroscopic studies of the isoelectronic analog of Ar-HCN, Ar-HCCH, also revealed some unusual features of the corresponding intermolecular potential energy surface (*71,72,73,74,75,76*). For these van der Waals systems, it is difficult to derive information about the potential energy surfaces from the spectroscopic data using conventional procedures, where an approximate separation between the van der Waals stretching and bending coordinates is normally applied (*58*).

Some tunneling motions can be modeled as a hindered rotation of the monomer about one of its principal inertial axes. In some cases, as the binding energy gets smaller and the potential gets more isotropic, internal rotations about all principal axes become feasible. This is often termed "nearly free internal rotation" of the monomer within the complex. In such cases, the rotational and vibrational spectra often show complicated, irregular structures, and conventional fitting procedures based on the semi-rigid rotor model often fail to adequately describe the spectra. Combined efforts of spectroscopists and theoreticians are necessary to fully understand the nature of the internal dynamics of such floppy systems. Examples for this case are Rg-H_2O (*77,78,79,80,81,82*) and Rg-NH_3 (*83,84,85,86,87,88,89,90*) systems. A large amount of spectroscopic as well as theoretical results has been collected for these systems so that the nature of the corresponding potential energy surfaces is relatively well understood, in particular for Ar-H_2O and Ar-NH_3. In contrast to the extensive work on the Rg-HF (*21,91,92,93,94*), Rg-H_2O, and Rg-NH_3 systems, the next system of this series, namely Rg-CH_4, is less studied. It is anticipated that CH_4 also undergoes nearly free internal rotation within the complexes, similar to its H_2O and NH_3 counterparts.

In the following chapters of this thesis, spectroscopic and theoretical results of seven weakly bound molecular systems, namely Ar-C_2H_4, Ne-C_2H_4, Ar-C_2H_2, Ne-C_2H_2, Kr-CH_4, Ar-CH_4, and CO-CH_4, are presented. Besides the fact that these systems are likely candidates for studying various interesting internal motions, the first six systems form a series of work on Rg-(simple hydrocarbon) dimers. In fact, CO-CH_4, as shown in chapter 6, closely resembles a Rg-CH_4 dimer. As mentioned earlier, these systems can be regarded as a starting point of a molecular level study of the microsolvation processes of organic species.

The remainder of this thesis consists of three major parts: theory and spectrometer setup, results, and conclusions. The first part includes chapter 2 and chapter 3. A theoretical description of the method, Fourier transform microwave spectroscopy, is given in chapter 2, followed by a detailed description of the spectrometer used for recording the rotational spectra. In chapter 3, after a brief description of the *ab initio* methods and basis sets, computational details of constructing the potential energy surfaces of the Ne-C_2H_4, Ne-C_2H_2, Kr-CH_4, and Ar-CH_4 systems are given. Molecular symmetry group analyses, which are used to facilitate spectral assignments and to interpret the resulting spectra, are also discussed in chapter 3. The Ne-C_2H_4 and Kr-CH_4 systems are used as examples to illustrate how molecular symmetry group analyses are performed. The results part is composed of three chapters, where spectroscopic and theoretical results of C_2H_4-, C_2H_2-, and CH_4-containing systems are presented in chapter 4, chapter 5, and chapter 6, respectively. Finally, general conclusions based on this thesis work are drawn in chapter 7.

2

BASIC THEORY OF FOURIER TRANSFORM MICROWAVE SPECTROSCOPY AND SPECTROMETER

Fourier transform microwave spectroscopy is unlike traditional absorption and emission spectroscopic techniques. It measures the spontaneous molecular emission signal of an ensemble of molecules as a function of time, after applying a microwave pulse at an appropriate frequency, with appropriate power and duration. A Fourier transform of the time-domain signal gives the power spectrum in the frequency-domain. This time-domain spectroscopic technique shows definite advantages in sensitivity and resolution over its frequency-domain counterpart (*95,96*). A molecular beam Fourier transform microwave spectrometer combines the features of molecular beams with the advantages of Fourier transform microwave spectroscopy, and is proven to be well suited for the studies of transient or short-lived species (*97*), for example, van der Waals complexes. After the pioneering work by Balle and Flygare in 1981 (*97,98*), many modifications have been made to further improve the sensitivity and resolution of molecular beam Fourier transform microwave spectrometers (*58,99,100,101,102,103,104,105*), and to incorporate special applications, such as double resonance (*106,107*), laser ablation (*108,109*), electric discharge (*110,111*), and Stark effect measurements (*112*). This chapter starts with a description of the theoretical basis of Fourier transform microwave spectroscopy, followed by a discussion about the advantages of the molecular beam technique. Finally, the details of the molecular beam Fourier transform microwave spectrometer used in this laboratory are discussed, including the mechanical setup of the spectrometer, electronic and microwave components, and timing sequence of an experiment.

2.1 THEORETICAL BACKGROUND

In Fourier transform microwave spectroscopy, one deals with a time-dependent phenomenon, so that the theory describing it has to be based on the time-dependent Schrödinger theory. Detailed theoretical derivations have been given in refs. *96*, *113*, *114*, *115*, *116*, and *117*. Here, only a brief outline is given. A model system consisting of an ensemble of N two-level particles (see figure 2-1) is considered. The molecular ensemble interacts with the electromagnetic field of the incident microwave pulse through an electric dipole interaction. It is further assumed that molecules do not interact with each other and that each molecule interacts with the external field in the same manner. The time-dependent wavefunction of the two-level system can be expanded as:

$$|\Psi(t)\rangle = c_a(t)|a\rangle + c_b(t)|b\rangle, \tag{2-1}$$

where $|a\rangle$ and $|b\rangle$ are the wavefunctions of the two involved stationary levels, corresponding to the time-independent Hamiltonian operator, H_0, with energies E_a and E_b, respectively. c_a and c_b are time-dependent complex coefficients. In the density matrix formalism (*118,119,120*), the density matrix $\rho(t)$ of the ensemble is given by:

$$\rho = \begin{pmatrix} \rho_{aa} & \rho_{ab} \\ \rho_{ba} & \rho_{bb} \end{pmatrix} = \begin{pmatrix} \frac{1}{N}\sum_{i}^{N} c_{ai}(t)c_{ai}(t)^{*} & \frac{1}{N}\sum_{i}^{N} c_{ai}(t)c_{bi}(t)^{*} \\ \frac{1}{N}\sum_{i}^{N} c_{bi}(t)c_{ai}(t)^{*} & \frac{1}{N}\sum_{i}^{N} c_{bi}(t)c_{bi}(t)^{*} \end{pmatrix}. \tag{2-2}$$

The star denotes the complex conjugate of the coefficient. The time evolution of the density matrix is described by:

$$i\hbar\frac{\partial\rho}{\partial t} = H\rho - \rho H = [H,\rho]. \tag{2-3}$$

H is the matrix representation of the time-dependent Hamiltonian, which can be expressed as the sum of the time-independent part, H_0, and the time-dependent part, H_t. H_t describes the electric dipole interaction between the molecule dipole moment and the microwave electromagnetic field, and is given as:

$$H_t = -\mu\varepsilon_0\cos(\omega t), \tag{2-4}$$

with μ being the transition dipole moment, ε_0 being the microwave field amplitude, and ω being the angular frequency of the external microwave radiation. The matrix elements of the Hamiltonian in the $|a\rangle$, $|b\rangle$ basis are:

$$\begin{aligned} H_{aa} &= E_a \\ H_{bb} &= E_b \\ H_{ab} &= H_{ba} = -\mu_{ab}\varepsilon_0\cos(\omega t). \end{aligned} \tag{2-5}$$

$\mu_{ab} = \mu_{ba}$ are matrix elements of the dipole moment operator:

$$\mu = \begin{pmatrix} 0 & \mu_{ab} \\ \mu_{ba} & 0 \end{pmatrix}. \tag{2-6}$$

Using equations 2-2 to 2-6, the time derivatives of density matrix elements can be evaluated, resulting in a set of coupled linear differential equations:

$$\begin{aligned}
\frac{\partial \rho_{aa}}{\partial t} &= i\chi \cos(\omega t)(\rho_{ba} - \rho_{ab}) \\
\frac{\partial \rho_{bb}}{\partial t} &= -i\chi \cos(\omega t)(\rho_{ba} - \rho_{ab}) \\
\frac{\partial \rho_{ab}}{\partial t} &= i\omega_0 \rho_{ab} + i\chi \cos(\omega t)(\rho_{bb} - \rho_{aa}) \\
\frac{\partial \rho_{ba}}{\partial t} &= \left(\frac{\partial \rho_{ab}}{\partial t}\right)^{*} = -i\omega_0 \rho_{ba} - i\chi \cos(\omega t)(\rho_{bb} - \rho_{aa}),
\end{aligned} \tag{2-7}$$

where $\omega_0 = {(E_b - E_a)}/{\hbar}$ is the transition frequency and $\chi = \left({\mu_{ab}\varepsilon_0}/{\hbar}\right)$ is the Rabi frequency. The Rabi frequency describes the strength of the interaction between the external electromagnetic radiation and the molecular ensemble. This set of equations can be simplified by transformation into the interaction representation (*96,115*), corresponding to a frame that rotates with angular frequency ω:

$$\begin{aligned}
\underline{\rho_{aa}} &= \rho_{aa} \\
\underline{\rho_{bb}} &= \rho_{bb} \\
\underline{\rho_{ab}} &= \rho_{ab} e^{-i\omega t} \\
\underline{\rho_{ba}} &= \rho_{ba} e^{i\omega t}.
\end{aligned} \tag{2-8}$$

By applying the 'rotation wave approximation' and neglecting the 2ω terms (*96,115*), and by introducing the following real variables:

$$\begin{aligned}
u &= \underline{\rho_{ba}} + \underline{\rho_{ab}} \\
v &= i\left(\underline{\rho_{ba}} - \underline{\rho_{ab}}\right) \\
w &= \underline{\rho_{aa}} - \underline{\rho_{bb}} \\
s &= \underline{\rho_{aa}} + \underline{\rho_{bb}},
\end{aligned} \tag{2-9}$$

equation 2-7 is simplified to:

$$\begin{aligned}
\frac{\partial u}{\partial t} &= -\Delta\omega v \\
\frac{\partial v}{\partial t} &= \Delta\omega u - \chi w \\
\frac{\partial w}{\partial t} &= \chi v \\
\frac{\partial s}{\partial t} &= 0,
\end{aligned} \tag{2-10}$$

where $\Delta\omega = \omega_0 - \omega$ is the off-resonance of the transition frequency from the external microwave radiation. The variable s corresponds to the population sum of levels $|a\rangle$ and $|b\rangle$, and w is the population difference. This set of equations is similar to the Bloch equations in NMR (*121,122,123*) and is commonly denoted as the electric field analogues of the Bloch equations. For clarity, relaxation effects have been neglected in the above consideration.

In the time-domain experiment, the polarization P (macroscopic dipole moment/volume), which is proportional to the detected emission signal, is of interest. It is evaluated as follows. The ensemble average of an observable O is given by:

$$\langle O\rangle = Tr\{O\rho\}, \tag{2-11}$$

where Tr denotes the trace of the matrix product. Using equation 2-2 and 2-6, the ensemble average of the dipole moment is obtained as:

$$\langle\mu\rangle = \mu_{ab}\{\rho_{ab}(t) + \rho_{ba}(t)\}. \tag{2-12}$$

The polarization in the laboratory frame is then given by:

$$
\begin{aligned}
P(t) &= {}^1N\langle\mu\rangle = {}^1N\mu_{ab}\{\rho_{ab}(t) + \rho_{ba}(t)\} \\
&= {}^1N\mu_{ab}\left\{\underline{\rho_{ab}}(t)e^{i\omega t} + \underline{\rho_{ba}}(t)e^{-i\omega t}\right\} \\
&= {}^1N\mu_{ab}\{u\cos(\omega t) - v\sin(\omega t)\},
\end{aligned}
\tag{2-13}
$$

where ${}^1N$ is the number density of the molecule ensemble.

During the initial phase of the experiment, the coherence terms $u(0) = v(0) = 0$, corresponding to zero polarization, and the population difference $w(0) = w_0 = \Delta N_0$. The condition of "hard" pulses, i.e., $\chi >> \Delta\omega$, is assumed. Neglecting the $\Delta\omega$ terms, equation 2-10 simplifies to:

$$
\begin{aligned}
\frac{\partial u}{\partial t} &= 0 \\
\frac{\partial v}{\partial t} &= -\chi w \\
\frac{\partial w}{\partial t} &= \chi v,
\end{aligned}
\tag{2-14}
$$

with the solutions:

$$
\begin{aligned}
u(t) &= 0 \\
v(t) &= -w_0\sin(\chi t) \\
w(t) &= w_0\cos(\chi t).
\end{aligned}
\tag{2-15}
$$

In an actual experiment, it is desirable to prepare, or to polarize, the molecule ensemble to obtain maximum polarization such that the emission signal is the strongest. From 2-15, the maximum polarization is achieved when $\sin(\chi t)=1$, which leads to an optimum microwave pulse length $t_p = (\pi/2\chi)$. This is usually referred to as a "$\pi/2$-pulse". After a $\pi/2$-pulse, the initial population difference ΔN_0 is completely converted to polarization with $w(\pi/2\chi)=0$. This situation is illustrated using the Bloch vector diagram in figure 2-1.

During the detection period, the microwave excitation pulse is switched off, so that $\chi = 0$. The off-resonance $\Delta\omega$ can no longer be neglected. The process of emission of the molecular ensemble is therefore described by:

$$\begin{aligned}\frac{\partial u}{\partial t} &= -\Delta\omega v\\ \frac{\partial v}{\partial t} &= \Delta\omega u\\ \frac{\partial w}{\partial t} &= 0.\end{aligned} \qquad (2\text{-}16)$$

Assuming initial conditions of $u(\pi/2\chi) = 0$, $v(\pi/2\chi) = -\Delta N_0$, and $w(\pi/2\chi) = 0$ (after a $\pi/2$-pulse), solutions to equation 2-16 are given by:

$$\begin{aligned}u(t') &= \Delta N_0 \sin(\Delta\omega t')\\ v(t') &= -\Delta N_0 \cos(\Delta\omega t')\\ w(t') &= 0.\end{aligned} \qquad (t' = t - t_p) \qquad (2\text{-}17)$$

Recalling equation 2-13, the polarization during the emission period is given by:

$$\begin{aligned}P(t') &= {}^1N\mu_{ab}\{u\cos(\omega t') - v\sin(\omega t')\}\\ &= {}^1N\mu_{ab}\Delta N_0 \sin(\omega_0 t'),\end{aligned} \qquad (2\text{-}18)$$

showing that P oscillates with the transition frequency ω_0. This is the source for the emission signal of the molecular ensemble.

From the above considerations, it is shown that the polarization P has a linear dependence on the initial population difference ΔN_0 (equation 2-18). This suggests that one way of improving the sensitivity of Fourier transform microwave spectroscopy is to increase the initial population difference. This relates to the following discussion of the advantages of the molecular beam technique.

2.2 MOLECULAR BEAM

The characteristics of molecular beams and their applications in spectroscopy have been discussed in detail (*124,125,126*). A pulsed molecular beam, or supersonic jet, is formed by expanding a pulse of gas phase molecules from a high pressure gas reservoir into a low pressure region through a pulsed nozzle. During such a rapid adiabatic expansion, random translational kinetic energy is converted into directed mass flow through binary collisions. As a result, the mass flow velocity increases while the velocity distribution narrows. The translational temperature, as a measure of the velocity distribution, decreases substantially. Translational temperatures as low as 0.03 K have been reported (*125,127*). Subsequently, the cold translational bath acts as a refrigerant to cool down the other degrees of freedom, including rotational and vibrational degrees of freedom, also through two-body collisions. It is believed that the rate of energy flow from rotational degrees of freedom to translational degrees of freedom is relatively fast, leading to extensive rotational cooling.

Assuming ideal gas behavior and an adiabatic expansion, it can be shown that:

$$\left(\frac{n}{n_0}\right) = \left(\frac{T}{T_0}\right)^{\frac{1}{\gamma-1}}, \tag{2-19}$$

where n and T are number density and temperature, respectively. Subscript 0 denotes gas reservoir quantities, and γ denotes the heat capacity ratio of the gas. As the temperature drops during the initial phase of the expansion, n also decreases. Eventually, the expansion proceeds to a state where the density is so low that no further collisions occur. From this point on, the system is said to be frozen and the distribution of the various degrees of freedom no longer changes.

The above short description shows that a molecular beam provides low temperatures and a collisionless environment. These features have significant impacts on the Fourier transform microwave spectroscopic investigations of weakly bound complexes.

First of all, the low temperatures and the collisionless environment stabilize the otherwise unstable van der Waals complexes. Van der Waals dimers are formed during the initial phase of the expansion, through three-body collisions:

$$A + B + C = A\cdots B + C^{*},$$

where the third body C is needed to carry away the excess kinetic energy (*125,128,129,130,131*). At room temperature, the binding energy of a van der Waals dimer is usually very much less than the thermal energy kT. It is therefore unstable with respect to collisions with surrounding molecules. However, the translational temperature is so low in a molecular beam that no further collisions occur, and van der Waals molecules, once formed, persist.

Secondly, the low rotational temperature achieved with application of the molecular beam technique increases the initial population difference ΔN_0. This effect can be easily illustrated by calculating the population differences between various rotational levels at T=0.5 K, a typical rotational temperature achieved in the experiment, and at T=300 K (*132*). Assuming a rigid linear molecule, the relative population of a certain rotational level is given by the Boltzmann distribution:

$$\frac{N_J}{N} = \frac{(2J+1)}{Z} e^{\frac{-\hbar BJ(J+1)}{kT}} , \qquad (2\text{-}20)$$

where N_J is the population of the rotational level with rotational quantum number J, N is the total population, k is the Boltzmann constant, B is the rotational constant, and Z is the partition function:

$$Z = \sum_J (2J+1) e^{\frac{-\hbar BJ(J+1)}{kT}} . \qquad (2\text{-}21)$$

Population differences were calculated assuming a rotational constant of 2.5 GHz, and are listed below:

	T=0.5 K	T=300 K
$\Delta N_{1\text{-}0}/N$	8.4×10^{-2}	3.2×10^{-7}
$\Delta N_{4\text{-}3}/N$	7.4×10^{-2}	8.9×10^{-6}
$\Delta N_{10\text{-}9}/N$	1.7×10^{-9}	5.8×10^{-5}.

The subscript 'f-i' denotes the energy levels involved in the rotational transition from the initial level with rotational quantum number 'i' to the final level with quantum number 'f'. For low J transitions, such as J=1-0 and 4-3, there are large gains in ΔN_0 at T=0.5 K compared with that at T=300 K.

The above calculations also indicate that the population decreases quickly with increasing J in a molecular beam, as a result of the low temperature. This effect again works to our advantage. It shifts the population distribution towards low J levels and greatly simplifies the spectra by depopulating higher J levels.

2.3 SPECTROMETER

In the remaining part of this chapter, I will discuss in detail the setup of the pulsed molecular beam Fourier transform microwave spectrometer used in this laboratory (*58*, *107*). The basic setup follows the original design of Balle and Flygare (*97*). The operating principle is based on pulsed coherent excitation of a molecular ensemble, followed by superheterodyne detection of the coherent molecular emission signal.

2.3.1 Mechanical Details

A schematic diagram of the mechanical setup of the molecular beam Fourier transform microwave spectrometer is given in figure 2-2. The sample cell is formed by two spherical aluminum mirrors with diameter of 260 mm and radius of curvature of 380 mm. The two mirrors form a microwave cavity of the Fabry-Perot type, where the molecules of interest interact with the microwave excitation pulse. The sample cell is situated inside a cylindrical stainless-steel vacuum chamber (50 cm in diameter and 70 cm in length). One of the mirrors is fixed and mounted into the flange cover of the vacuum chamber. At the center of this mirror is a wire hook antenna, which couples the microwave excitation pulse into the microwave cavity and transmits the subsequent molecular response out of the cavity. The other mirror of the sample cell is mounted onto two linear bearings such that it can be accurately positioned to fulfil the standing-wave requirement of the cavity. This is done by means of a computer controlled Motor Mike drive. A second antenna is placed at the center of the movable mirror and is connected to a microwave diode detector, which in turn is linked to an oscilloscope. This allows for monitoring the cavity resonance and enables automated spectral scans (*102*).

A pulsed nozzle is placed closely above the antenna, near the center of the fixed mirror. In this configuration, a molecular pulse expands through the nozzle and travels parallel to the microwave cavity axis (*101*). As a result, all transitions are detected as doublets, due to the Doppler effect. A representative spectrum showing the Doppler splitting is depicted in figure 2-3. Through copper tubing, the nozzle is connected to a stainless-steel gas cylinder, where the sample mixture is prepared. Ne is normally used as the carrier gas, seeded with a small amount of the substance to be investigated. In a typical experiment, stagnation pressures of 5-6 atm are used. Under these conditions, the recorded rotational transitions have typical line widths of 7 kHz (full-width at half-height). A measurement accuracy of about 1 kHz is achieved.

An efficient vacuum system is necessary to maintain a low pressure in the chamber. A 12 inch diffusion pump working at a pumping speed of 2000 *l*/min is used to evacuate the chamber. An 800 *l*/min mechanical pump is used to back the diffusion pump. A pressure of 10^{-6} Torr can be achieved with this arrangement.

It should be pointed out that Fourier transform microwave spectrometers can not provide accurate absolute intensity measurements. Intensity measurements depend on many factors such as the sample condition, the antenna configuration etc., which are difficult to reproduce. However, relative intensity comparisons between two transitions can be made fairly reliably, especially when the two transitions are close in frequency. These relative intensity comparisons are very useful for spectral assigning purposes, as will be shown in later chapters.

2.3.2 Electrical Details

The detailed electronic setup of the spectrometer is schematically given in figure

2-4. Before each experiment, the microwave cavity needs to be tuned into resonance with the excitation frequency. For this purpose, the microwave power inside the cavity is probed with a wire hook antenna **24** placed at the center of the moveable mirror. The signal is monitored by a microwave diode detector **25**, which is connected to an oscilloscope **26**.

Each measurement starts with the injection of a short pulse of the studied gas mixture into the sample cell by opening nozzle **1**. As a result of the rapid adiabatic expansion through the nozzle, a molecular beam with very low effective translational and rotational temperatures is formed. It travels collisionlessly through the cavity, parallel to the cavity axis. At this phase of the expansion, the dipole moments of the molecules are randomly oriented such that there is no macroscopic dipole moment or polarization.

After an adjustable delay, a microwave excitation pulse is fed into the cavity. The microwave pulse is formed in the following manner. The microwave radiation at frequency ν produced by a Hewlett Packard microwave synthesizer **2** (operating in the range 1-20 GHz) first passes through an isolator **3**, and is divided into two parts by a power divider **4**. One part is used to generate the excitation pulse, the other is used for heterodyne signal detection. The excitation part passes through another isolator **5**, a microwave PIN diode switch **6**, and is fed into a double balanced mixer **7**, where it mixes with a 20 MHz signal to generate sidebands at ν-20 MHz and ν+20 MHz. The radiation passes through optional attenuator **8** and/or an optional microwave power amplifier **9**[1]

---

[1] For the Fourier transform microwave studies of the dimers described in this thesis, the microwave power amplifier is needed to achieve the $\pi/2$ condition. This is a consequence

(71), and a second microwave PIN diode switch **10**. Switches **6** and **10** are opened and closed synchronously to produce the microwave excitation pulse. The resulting microwave pulse is coupled into the microwave cavity **13** through a circulator **11** and a wire hook antenna **12** to excite the gas molecules. If one or more rotational transitions of the studied molecule is contained within the bandwidths of the excitation pulse and the microwave cavity, the individual molecular dipole moments align with the electromagnetic field of the microwave excitation pulse. It is then said that a macroscopic dipole moment is induced in the molecular ensemble. It oscillates phase-coherently, resulting in spontaneous emission of electromagnetic radiation at frequency ν_m. A schematic diagram of the circuit for generating the excitation pulse is also given in figure 2-5.

The molecular emission signal, at frequency ν-20+$\Delta\nu$, where $\Delta\nu = \nu_m - \nu + 20$ is the difference of the molecular transition frequency from the frequency of the external microwave radiation, is coupled out of the cavity through antenna **12** and is directed to the detection circuit by circulator **11**. A superheterodyne detection scheme is applied for the detection of the emission signal. A third microwave PIN diode switch **14** is placed after the circulator. It is closed during the excitation period, in order to protect the detection circuit. When the switch opens, the molecular emission signal passes through. It is preamplified by a low noise microwave amplifier **15** before it reaches an image rejection mixer **16.** The second half of the microwave radiation at frequency ν produced by the

---

of the small dipole moments, on the order of 10^{-2} D or even smaller, of the Rg-(nonpolar molecule) systems.

microwave synthesizer serves as the local frequency ν_{loc} to downconvert the molecular signal to 20-$\Delta\nu$ MHz, i.e., into the radio frequency range. This signal is amplified and downconverted a second time to 15+$\Delta\nu$ MHz by mixing with a 35 MHz signal. The superheterodyne detection system is also schematically shown in figure 2-6. The final signal around 15 MHz is A/D converted and sampled by a transient recorder **22**. The data is then stored in a personal computer **23** for averaging. For transitions with no hyperfine structure, 4 k data points are recorded at 20 nsec intervals. For spectra containing narrow hyperfine splittings, 4 k data points at up to 120 nsec intervals are recorded to achieve higher resolution. After sufficient signal averaging, a Fourier transformation of the time-domain data is performed and the frequency spectrum with rotational transition frequencies results. 4 k zero data can be added to the end of the recorded time-domain data before the Fourier transformation in order to increase the resolution in the frequency-domain spectrum.

2.3.3 Timing Sequence

To ensure proper signal averaging, it is essential to start data acquisition at the same time and phase for each experiment. The synchronization is realized by phase correlating all events to the internal 10 MHz standard of the microwave synthesizer. It is used to generate the 20 MHz signal for generating the sidebands of the source frequency, the 35 MHz signal for the second downconversion of the molecular signal, and the 50 MHz clock for data acquisition used by the transient recorder. It is also used as a clock for a pulse generator that produces the various TTL pulses needed. A schematic representation of the pulse sequence is plotted in figure 2-7. For each experiment, a molecular pulse, typically with a pulse width of 1 msec, is generated for the nozzle **1**. After an appropriate delay, a microwave pulse (on the order of μsec) is used to open microwave PIN diode switches **6** and **10**. The durations of the molecular pulse and the microwave pulse can be adjusted to achieve optimal experimental conditions. The delay between the molecular pulse and the microwave pulse is also adjustable, typically between 0.05 and 0.1 msec. A TTL pulse of appropriate duration is generated for the protective switch **14**, in order to keep it closed during the excitation period. At the end of a protective delay, a trigger is sent to the transient recorder **22** to start data acquisition. The timing of the trigger pulse is such that the main part of the excitation radiation has dissipated, while the molecular signal is still strong for detection. The entire sequence is preceded by the same sequence without the molecular pulse to obtain a background signal that is subtracted from the background+molecular signal.

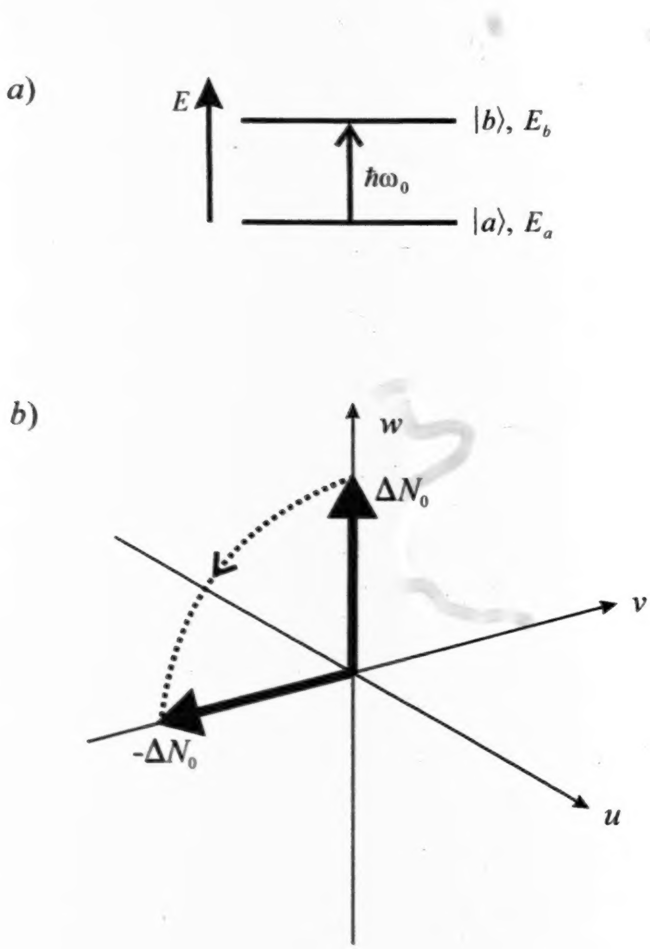
a)
E
$|b\rangle, E_b$
$\hbar\omega_0$
$|a\rangle, E_a$
b)
w
ΔN_0
v
$-\Delta N_0$
u

Figure 2-1: Block vector diagram to visualize the π/2-condition (*b*). The two-level model system used is depicted above the diagram (*a*). ΔN_0 is the initial population difference between the two involved rotational levels. The optimum polarization is obtained by applying a $t_p = (\pi/2\chi)$ pulse. The initial Bloch vector $(u, v, w)=(0, 0, \Delta N_0)$ rotates 90° to $(0, -\Delta N_0, 0)$. It is said that the initial population difference is completely converted into polarization.

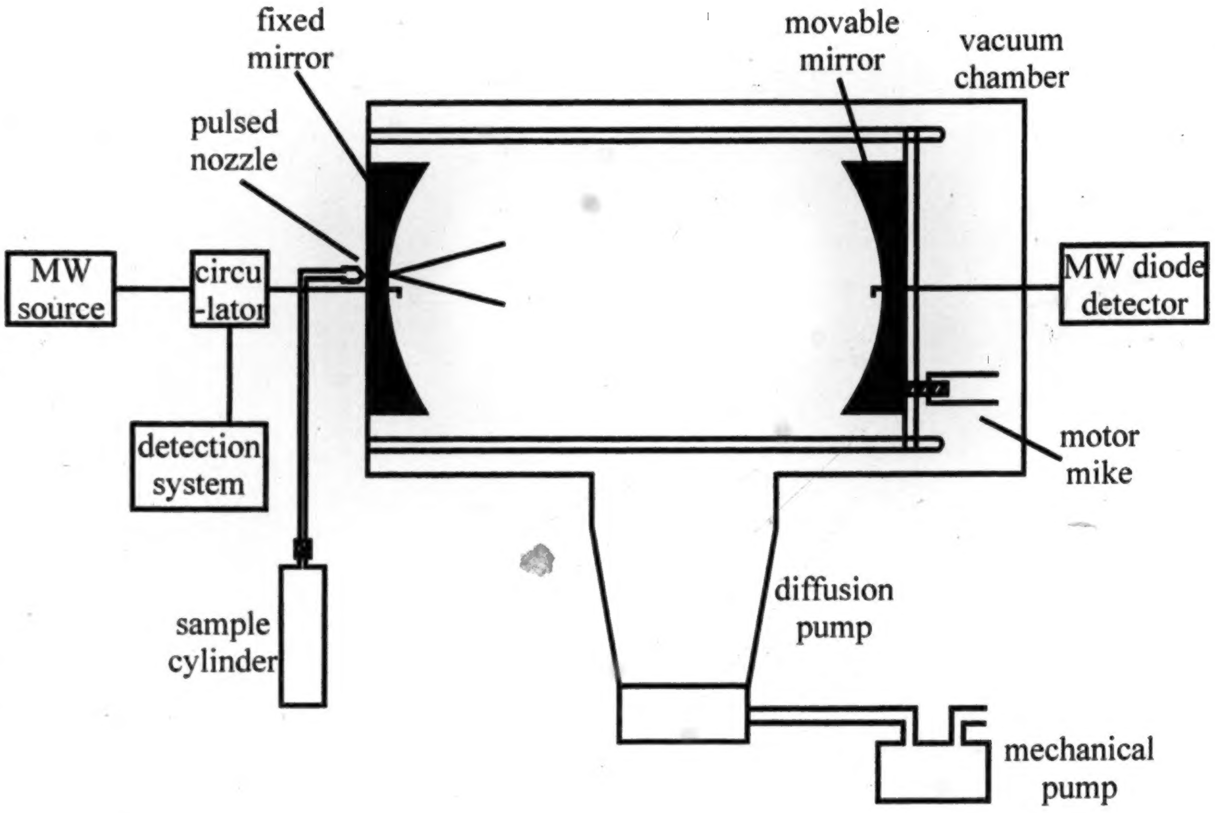
fixed
mirror
pulsed
nozzle
movable
mirror
vacuum
chamber
MW
source
circu
-lator
MW diode
detector
detection
system
motor
mike
sample
cylinder
diffusion
pump
mechanical
pump

Figure 2-2: The mechanical setup of the spectrometer.

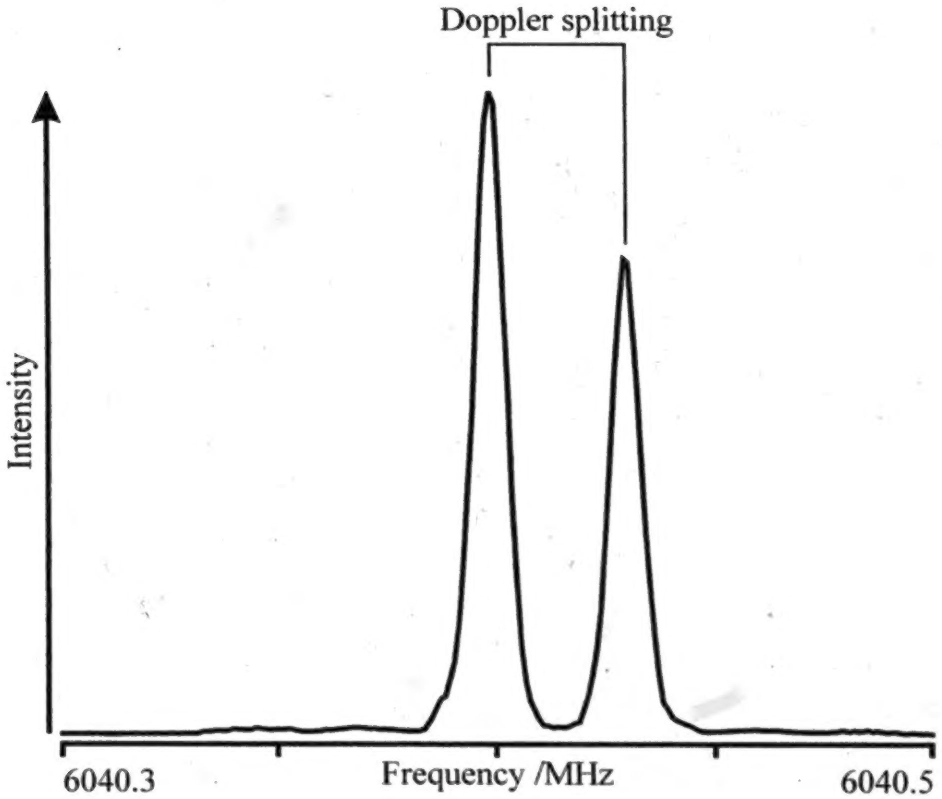

Figure 2-3: A representative spectrum showing the Doppler splitting. Shown is the J=1-0, j=0, K=0 transition of CO-CH_3D. The transition is split into two Doppler components, as a result of the parallel injection of the molecular pulse with respect to the microwave cavity axis. The average of the frequencies of the two components is recorded as the transition frequency.

7

Figure 2-4: Detailed electronic setup of the spectrometer. **1**: nozzle, **2**: microwave synthesizer, **3**: isolator, **4**: microwave power divider, **5**: isolator, **6**: microwave PIN diode switch, **7**: double balanced mixer, **8**: attenuator (optional), **9**: microwave amplifier (optional), **10**: microwave PIN diode switch, **11**: circulator, **12**: microwave antenna, **13**: microwave cavity and sample cell, **14**: protective microwave PIN diode switch, **15**: microwave amplifier, **16**: image rejection mixer, **17**: isolator, **18**: RF amplifier, **19**: radio-frequency mixer, **20**: 15 MHz bandpass filter, **21**: RF amplifier, **22**: transient recorder, **23**: personal computer, **24**: antenna used to monitor the microwave power inside the cavity, **25**: microwave diode detector, **26**: oscilloscope.

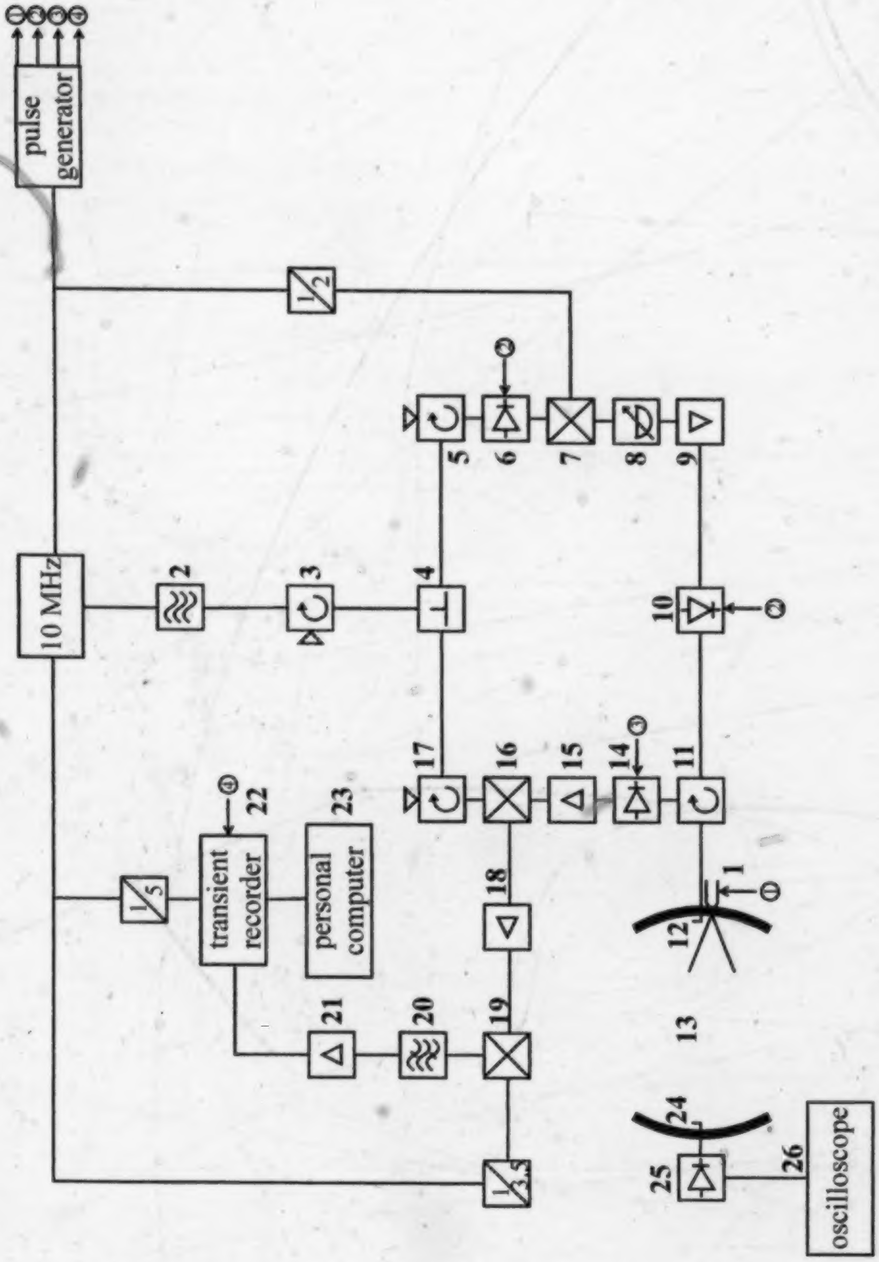
pulse generator
①
②
③
④
10 MHz
1/2
1/5
1/3.5
transient recorder
personal computer
oscilloscope

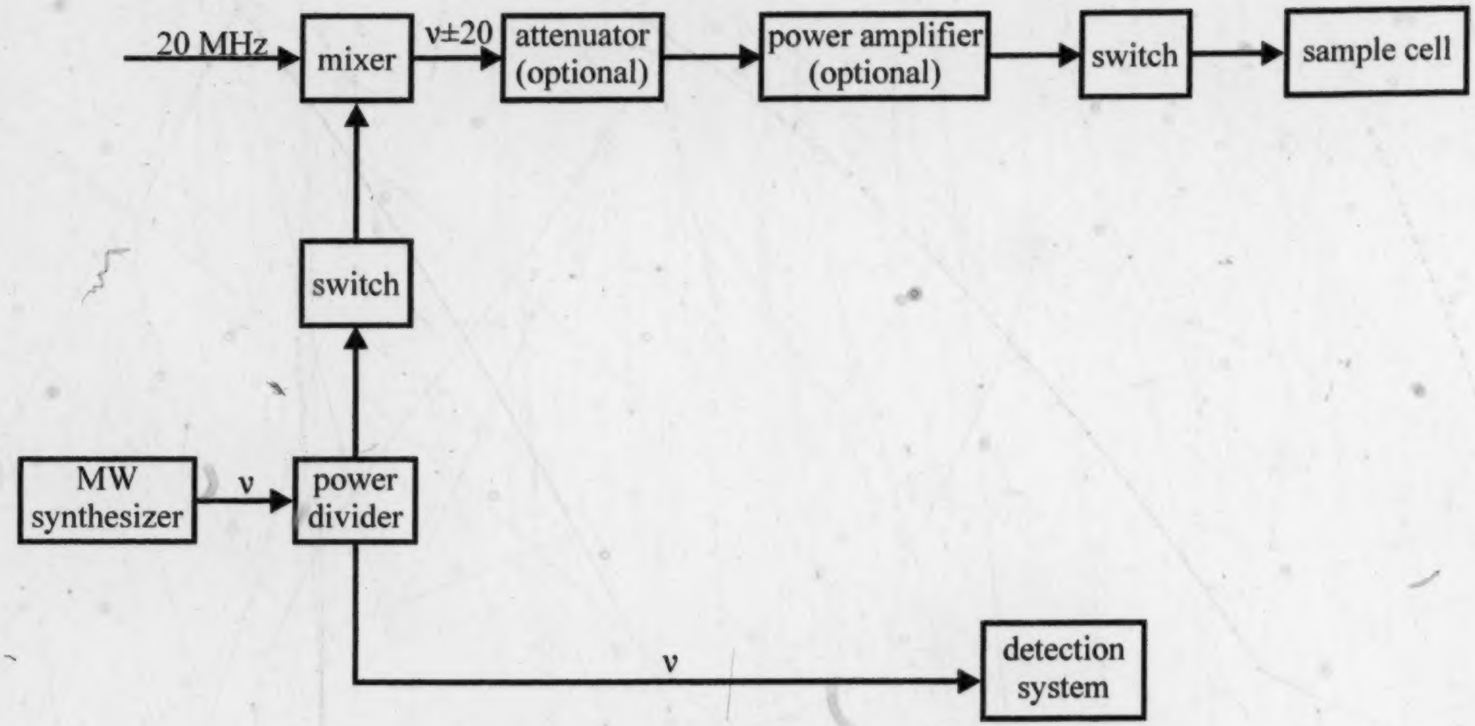
20 MHz
mixer
v±20
attenuator (optional)
power amplifier (optional)
switch
sample cell
switch
MW synthesizer
v
power divider
v
detection system

Figure 2-5: Schematic diagram of the circuit for excitation pulse generation.

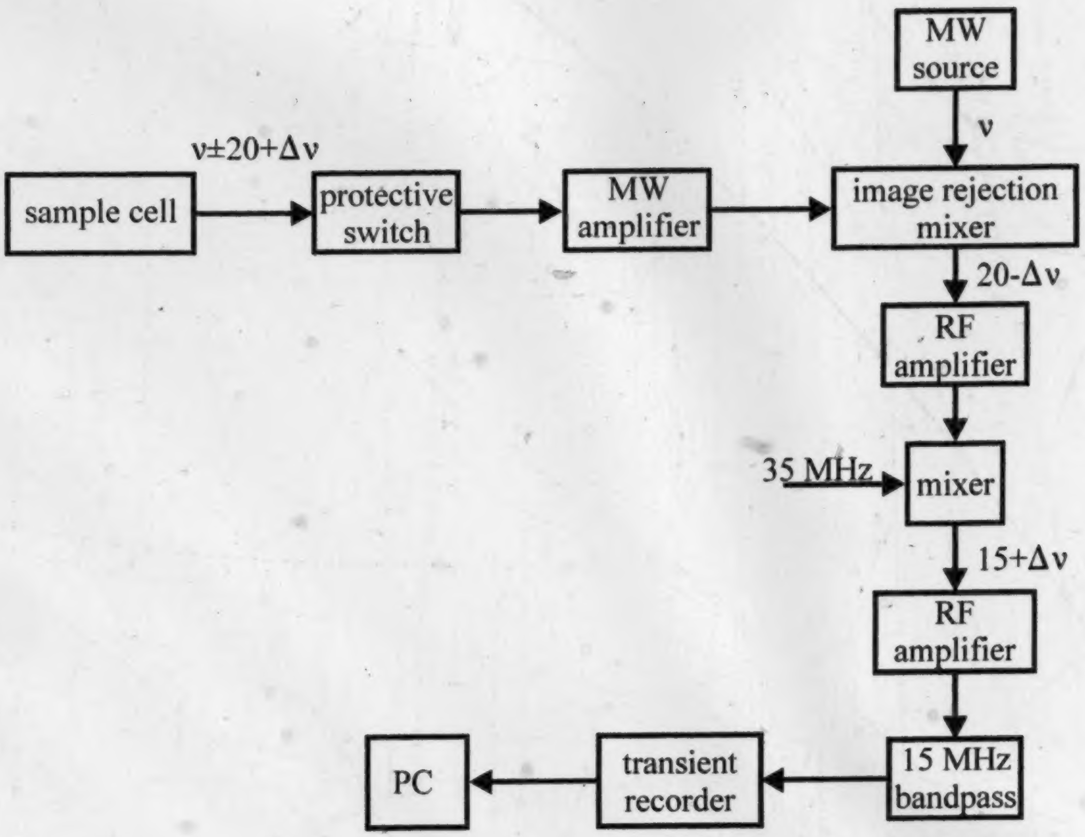
MW source
ν
ν±20+Δν
sample cell
protective switch
MW amplifier
image rejection mixer
20-Δν
RF amplifier
35 MHz
mixer
15+Δν
RF amplifier
15 MHz bandpass
transient recorder
PC

Figure 2-6: Schematic diagram of the superheterodyne detection system.

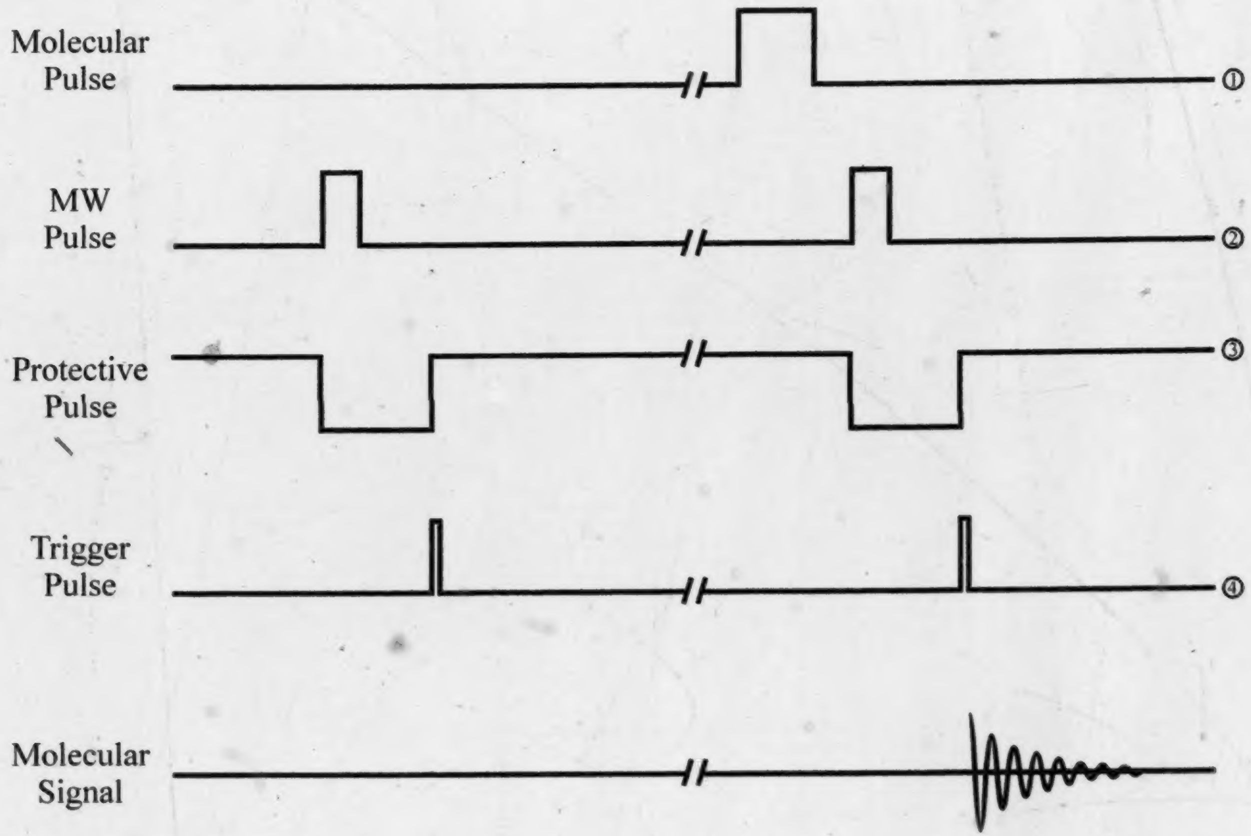
Molecular Pulse
MW Pulse
Protective Pulse
Trigger Pulse
Molecular Signal
①
②
③
④

Figure 2-7: Experimental timing diagram.

3

AB INITIO CALCULATIONS AND MOLECULAR SYMMETRY GROUP ANALYSES

3.1 *AB INITIO* CALCULATIONS

Accurate *ab initio* calculations can be used to enrich and to refine our understanding of the nature of intermolecular interactions. *Ab initio* single-point energy calculations are the basis for an accurate characterization and an analytical representation of the multidimensional potential energy surface. Together with subsequent quantum treatments of nuclear dynamics, it can provide quantitative comparisons with spectroscopic data. Many reviews and books on this subject have appeared in the literature (*46*,*47*,*48*,*49*,*133*,*134*,*135*). In this section, a brief outline of the *ab initio* methods and the basis sets used to construct the potential energy surfaces of the Ne-C_2H_4, Ne-C_2H_2, Kr-CH_4, and Ar-CH_4 systems is given, followed by a discussion on basis set superposition error. Finally, the details of the theoretical calculations of the individual systems are given.

3.1.1 Methods and Basis Sets

In most weakly bound molecular systems, particularly in the four systems studied here, namely Ne-C_2H_4, Ne-C_2H_2, Kr-CH_4, and Ar-CH_4, the dispersion interaction is the dominant contribution to the attractive force. This fact imposes much difficulty in constructing *ab initio* intermolecular potentials for these systems. Firstly, post-Hartree-Fock level of theories must be used to account for electron correlations, since dispersion is an intermolecular correlation effect. Secondly, dispersion energy has a very high demand on basis set sizes (*46*). Therefore, high correlation level of theories and large basis sets are required to adequately describe the intermolecular interactions present in weakly bound complexes.

For all the *ab initio* calculations described in this thesis, a supermolecular approach is applied, where the interaction energy ΔE_{AB} between a pair of molecules, A and B, is obtained as the difference between the dimer energy E^{AB} and the sum of the monomer energies (E^A+E^B) (*46,136*):

$$\Delta E_{AB} = E^{AB} - \left(E^A + E^B\right). \tag{3-1}$$

For example, in the case of Ne-C_2H_4, the interaction energy between Ne and C_2H_4 is obtained from a series of three calculations, i.e., the calculations of the total energies of Ne-C_2H_4, Ne, and C_2H_4, respectively. It is clear from 3-1 that methods suitable for studies of van der Waals interactions must have the property of being size-consistent (*137*), meaning that the energy of the dimer AB at infinite separation should be the sum of the energies of the two constituent monomers.

Two methods were applied to construct the potential energy surfaces for the four dimers mentioned above: Møller-Plesset perturbation theory to the fourth order (MP4) (*138,139,140*) and coupled-cluster theory with single, double, and perturbatively linked triple excitations (CCSD(T)) (*140,141,142*).

The MP4 method is easy to apply due to the widespread availability of the quantum chemistry code. It has been widely applied to obtain valuable insights into potential energy surfaces for weakly bound molecular systems. However, a major drawback of this method is that the Møller-Plesset perturbation theory is considered to be divergent so that its performance at critical points, for example, minima and transition points, needs to be carefully monitored (*49,143*).

It has been shown that the CCSD(T) method is more advanced than the MP4 level of theory and should be regarded as "the method of first choice" for *ab initio* calculations of weakly bound complexes (*46*) whenever the computational capability allows so. Compared to MP4, the CCSD(T) method is more computationally demanding. Its application for van der Waals complexes has only recently become feasible.

For most of the calculations, Dunning's aug-cc-pVTZ basis functions are used for the nucleus-centered basis sets (*144,145,146,147*)). They were chosen because they contain polarization functions with high angular quantum numbers, d, f, and even higher, that are required to properly account for the dispersion energy (*47*). Additional sets of functions, called bond functions, were supplemented to the nucleus-centered basis sets (*148,149,150,151,152*). These functions are specially designed to recover the dispersion term and were placed at the center of the van der Waals bond, the region particularly difficult to describe using nucleus-centered basis sets. It has been found that bond functions substantially improve the recovery of the dispersion energy and the improvement does not depend much on the location of the bond functions (*149,152*).

For the construction of the abovementioned four potential energy surfaces, the molecular subunits, namely C_2H_4, C_2H_2, and CH_4, were treated as rigid bodies in their vibrationally averaged geometries, in order to reduce the dimensionality of the intermolecular potential energy surfaces. This has been proven to be a reasonable approximation which allows to predict intermolecular vibration-rotation-tunneling dynamics and other properties (*49*).

3.1.2 Basis Set Superposition Error

In addition to using a size-consistent method, E^{AB}, E^{A}, and E^{B} should all be evaluated in a numerically consistent manner. The evaluation of ΔE_{AB} requires the subtraction of two large values, E^{AB} and $(E^{A}+E^{B})$, which are several orders of magnitude larger than the interaction energy. Very often, it is not possible to obtain E^{AB}, E^{A}, and E^{B} values accurate to within an error smaller than ΔE_{AB}. In order to make the difference, ΔE_{AB}, still meaningful, it is necessary to keep the evaluation of all three values numerically consistent. This requirement implies that the same basis set must be used for the energy calculations of all three relevant systems.

Using χ_{AB}, χ_{A}, and χ_{B} to denote the basis sets for the dimer *AB*, monomer *A*, and monomer *B*, respectively, the effect on the interaction energy ΔE_{AB} can be examined using:

$$\Delta E_{AB} = E^{AB}(\chi_{AB}) - \left(E^{A}(\chi_{A}) + E^{B}(\chi_{B})\right).$$

$E^{AB}(\chi_{AB})$, the sum of the interaction energy ΔE_{AB} and the monomer energies $(E^{A}+E^{B})$, is calculated with the dimer basis set, such that each individual monomer takes advantage of the basis set for the other monomer. This leads to a lowering in the monomer energies, compared to the values obtained with the individual monomer basis sets, $E^A(\chi_A)$ and $E^B(\chi_B)$. Consequently, such obtained ΔE_{AB} is underestimated. This effect is termed 'basis set superposition error'. In order to eliminate basis set superposition error, all energies, E^{AB}, E^A, and E^B, must be evaluated within the same basis set, the complete dimer basis set χ_{AB}. This method was developed by Boys and Bernardi (*153*), and is called 'counterpoise correction'. Proofs of the validity of this method can be found in references such as ref. *154*.

3.1.3 Computational Details

In the following paragraphs, the computational details for the determinations of potential energy surfaces for the Ne-C_2H_4, Ne-C_2H_2, Kr-CH_4, and Ar-CH_4 systems are given.

a. Ne-C_2H_4

Two basis sets were used in the *ab initio* calculations of the pointwise intermolecular potential energy surfaces of Ne-C_2H_4. Basis set 1 is comparable to the one previously used for the analogous Ar-ethylene dimer (*155*). The 6-31+G(2d, 2p) basis functions were used for C and H, and the Huzinaga type of basis functions were used for Ne, contracted to [7s,5p,2d] (*155,156,157*). A total of 110 basis functions resulted. Basis set 2 contained Sadlej's pVTZ basis functions for C and H (*158*) obtained from the Extensible Computational Chemistry Environment Basis Set Database (*159*), and Dunning's aug-cc-pVTZ basis functions for Ne (*144,145*). In addition, at the midpoint of the van der Waals bond, Tao's (3s3p2d) bond functions were added (*149,152*). The total number of basis functions in this basis set is 166. Intermolecular energies were computed using the MP4 level of theory with frozen-core approximation (*160*). The full counterpoise method was applied for the correction of the basis set superposition error (*153*). All calculations were carried out using the GAUSSIAN 94 package (*161*). In constructing the potential energy surface, the structure of the ethylene monomer was fixed at the known effective zero-point structure (*162*).

b. Ne-C_2H_2

The aug-cc-pVTZ basis functions were used for all atoms (*144,145*), with Tao's (3s3p2d) bond functions added (*149,152*) at the midpoint of the van der Waals bond. The resulting total number of basis functions is 206. Two potential energy surfaces were constructed, one at the MP4 level of theory with frozen-core approximation, the other with the CCSD(T) method. The basis set superposition error was corrected by carrying out the full counterpoise procedure (*153*). The MOLPRO package developed by Werner and Knowles was utilized (*163*) for the single point calculations, with the C_2H_2 structure fixed at *r*(C-H)=2.0042 bohr and *r*(C-C)=2.2737 bohr (*164*).

c. Kr-CH_4 and Ar-CH_4

The *ab initio* calculations of the Kr-CH_4 and Ar-CH_4 systems followed closely that of Ne-C_2H_2. The MOLPRO package was also used to construct the potential energy surfaces (*163*). The CCSD(T) method (*165*) was used combined with aug-cc-pVTZ basis set for all atoms (*144,145,146,147*). Again, Tao's bond functions were used and placed at the mid point between the Rg atom and C (*149,152*). The CH_4 molecule was kept rigid with the C-H bond fixed at the experimentally determined value, *r*(C-H)=2.052 bohr (*166*). In addition to the single point energy calculations, dipole moment calculations were also performed at selected configurations (*167*,*168*,*169*). It was calculated as the first derivative of energy by the finite difference approximation (*170*). At each configuration, two energy calculations were performed, one with a finite electric field added along the direction from the C atom to the Rg atom, the other with the same field strength but along the opposite direction. The dipole moment value was then obtained as the ratio of the energy difference to the electric field difference.

3.2 MOLECULAR SYMMETRY GROUP ANALYSES

The potential energy surfaces of weakly bound molecular complexes are characterized by relatively low dissociation energies and large intermolecular separations. Consequently, these complexes can very often not be well described with an equilibrium structure about which only small amplitude vibrational replacements occur. Instead, large amplitude internal motions involving one or more monomers are often observed. As a result, the point symmetry groups widely used to label the energy levels of rigid molecules become insufficient for these nonrigid molecular systems. Molecular symmetry groups, on the other hand, provide the means of identifying and symmetry labeling the energy levels. In many cases, the observed rotational and vibrational spectra are interpreted with the aid of proper molecular symmetry group analyses. In this section, the definition of a molecular symmetry group is given. It is illustrated how the molecular symmetry group is used to label ro-vibrational energy levels and to obtain nuclear spin statistical weights, with Ne-C_2H_4 and Kr-CH_4 as examples.

3.2.1 Molecular Symmetry Group and Elements

A molecular symmetry group is the group of all feasible nuclear permutation and permutation-inversion operations of identical nuclei in a molecule (*1,171*). It is a subgroup of the complete nuclear permutation inversion group. It is termed a "symmetry group" because all elements in the group commute with the Hamiltonian of the molecule, meaning that the total energy of the system is invariant with respect to operations corresponding to each element. An element is said to be feasible if the motion corresponding to this element produces observable spectroscopic splittings. For example, each of the rotational transitions of NH_3 in the recorded far-infrared absorption spectrum appeared as a doublet, while those of PH_3 were observed as singlets (*172*). The doubling in the NH_3 spectrum was attributed to the inversion motion of the molecule. Consequently, the inversion operation is considered to be a feasible element of the molecular symmetry group of NH_3. On the other hand, it is not a feasible element for PH_3, since no inversion splitting was resolved.

The simple case of H_2O is considered below as an example to illustrate the elements of a molecular symmetry group. The molecular symmetry group of H_2O consists of the following four elements: E, (12), E^*, and (12)*. E is the identity operation, meaning "doing nothing" to the system considered. (12) is a nuclear permutation operation, referring to the interchange of the two hydrogen nuclei, numbered 1 and 2, respectively. E^* is the inversion operation, referring to the inversion of the spatial coordinates of all nuclei and electrons through the center-of-mass of the molecule (*1*). Finally, (12)* is a nuclear permutation-inversion operation, referring to the interchange of the two hydrogen nuclei followed by an inversion operation. The effects of the four operations on H_2O are shown in figure 3-1.

Each element of a molecular symmetry group corresponds to an equivalent rotation, which is a combination of rotations of the molecule about its principal inertial axes and sometimes of feasible internal motions, for example, the inversion motion in NH_3. For the H_2O molecule discussed above, the equivalent rotations of the four elements, E, (12), E^*, and (12)*, are R^0, R_b^π, R_c^π, and R_a^π, respectively, where R^0 is the identity, and R_i^π (i=a, b, and c) is a rotation of the molecule about the i-principal inertial axis by 180 degrees. The principal inertial axes frame of H_2O is also shown in figure 3-1.

3.2.2 Nuclear Spin Statistical Weights

Similar to a point symmetry group, a molecular symmetry group has a set of irreducible representations with which we can label a state of the molecule of interest. This is done by determining the effect of each element in the group on the wavefunction of the particular state. The total wavefunction of a system is usually approximated by a direct product (*173*):

$$\Psi_{tot} = \psi_{el}\psi_{vib}\psi_{rot}\psi_{tun}\psi_{ns}, \tag{3-2}$$

where the individual terms correspond to the electronic, vibrational, rotational, tunneling or internal rotation, and nuclear spin wavefunction, respectively. Each component can be classified with an irreducible representation of the molecular symmetry group. The resulting total wavefunction must be either symmetric or anti-symmetric with respect to the interchange of identical nuclei, depending on the spins of the identical nuclei. Nuclei with half-integer spins must obey Fermi-Dirac statistics, while nuclei with integer spins follow Bose-Einstein statistics. For example, the interchange of the two protons in H_2O

must change the sign of the total wavefunction, since protons are fermions with nuclear spins I_H=1/2. On the other hand, the interchange of the two deuterons in D_2O must leave the total wavefunction unchanged, since deuterons are bosons with nuclear spins I_D=1. For our interest, ψ_{el} and ψ_{vib} in the above expression are considered to be totally symmetric, since most often only the rotational transitions within the ground electronic and ground vibrational state are measured. Equation 3-2 thus simplifies to:

$$\Psi_{tot} = \psi_{rot}\psi_{tun}\psi_{ns}. \tag{3-3}$$

The rotational-tunneling part of the wavefunction must combine with nuclear spin wavefunctions of a particular symmetry in order to fulfil the symmetry requirement of the total wavefunction. In general, the number of nuclear spin states depends on the symmetry of the nuclear spin wavefunction. This is how nuclear spin statistical weights arise. By performing a molecular symmetry group analysis and obtaining nuclear spin statistical weights, one can interpret the relative intensity pattern and assign an observed spectrum. In many cases, such analyses are very helpful in determining which internal motion produces the observed splittings.

3.2.3 Examples of Molecular Symmetry Group Analyses

In the following paragraphs, I will use the Ne-C_2H_4 and Kr-CH_4 systems as examples to illustrate how molecular symmetry group analyses are performed and how nuclear spin statistical weights are obtained.

a. Ne-C_2H_4

The effective structure of Ar-C_2H_4 was previously determined from high resolution infrared spectra to be a planar, T-shaped geometry with Ar sitting on the *b* principal inertial axis (see figure 3-2) of the ethylene monomer (*155*). Tunneling splitting was observed in the rotationally resolved infrared spectrum. It was concluded from the observed relative intensity pattern that the out-of-plane motion, the internal rotation of ethylene about the C-C bond, is the motion responsible for the observed splitting. The conclusion was based on the statement that the spin statistics are different for the two possible tunneling motions, i.e., the out-of-plane motion and the in-plane-motion where ethylene rotates about its *c*'-axis (see figure 3-2) (*155*). However, when I carried out the molecular symmetry group analysis for the normal isotopomer, Ar-$^{12}C_2H_4$, the same nuclear spin statistics were obtained for the two motions. Here, I present the results from the molecular symmetry group analyses for various isotopomers of the Ne-C_2H_4 van der Waals complex, assuming first an out-of-plane motion and then an in-plane motion. The planar, T-shaped configuration was assumed, similar to that of Ar-C_2H_4. In the next chapter, these results will be used to interpret the observed spectra and to determine which motion is the feasible motion.

The proper molecular symmetry group for the normal isotopomer, Ne-$^{12}C_2H_4$, assuming either an out-of-plane motion or an in-plane motion is D_{2h}(M), which is isomorphic with the D_{2h} point group. The character table for a D_{2h}(M) group (*1*) is given in table 3-1, with the equivalent rotations of each element separately given for the two motions. The numbering of the identical nuclei is given in figure 3-2. The feasible elements include the identity, the interchange of equivalent hydrogen nuclei and carbon nuclei, the inversion operation, and the products of these. The equivalent rotations include the rotation of the dimer about the *a*-, *b*-, or *c*-principal inertial axes (see figure

3-2) of the complex, and the internal rotation of the ethylene monomer about its a'-axis (out-of-plane motion, R_{tun}) or its c'-axis (in-plane motion, R'_{tun}). The equivalence of the nuclear permutation-inversion operation (14)(23)(56)* and its corresponding equivalent rotation $R_{tun}R_b^\pi$ is illustrated in figure 3-3 as an example.

The symmetry classification of each term in equation 3-3 can be determined individually using the character table. The case of the out-of-plane motion is first considered. Starting with the first term, ψ_{rot}, the symmetry classification depends on the asymmetric rotor quantum numbers, K_a and K_c. It can be determined by examining the symmetry behavior of the wavefunction under operations that contain rotations about *a*-, *b*-, and *c*-axes, i.e., R_a^π, R_b^π, and R_c^π. For example, for even K_a/K_c, the rotational wavefunction stays the same under an R_a^π/R_c^π operation, and for odd K_a/K_c, the rotational wavefunction changes sign under an R_a^π/R_c^π operation. A_g, A_u, B_{1u}, and B_{1g} symmetries are obtained for the K_aK_c=*ee*, *eo*, *oe*, and *oo* rotational energy levels, respectively. I have used the conventional *ee*, *eo*, *oe*, and *oo* notations of rotational levels (*174*), where *e* stands for even and *o* stands for odd.

The symmetries of the tunneling wavefunctions can be determined in a similar manner. In this case, it is the R_{tun} operation that needs to be considered. In the ground tunneling state, the tunneling wavefunction does not change sign under any operation that contains R_{tun} so that it belongs to the totally symmetric A_g symmetry. For the first excited tunneling state, the tunneling wavefunction has to change sign under any operation that contains R_{tun} such that it belongs to the B_{2u} symmetry. For our purpose, these are the only two tunneling states that need to be considered, since the higher ones are not sufficiently populated in the cold molecular beam.

Lastly, the symmetries of the nuclear spin wavefunctions are considered. For the normal isotopomer with ^{12}C, only the hydrogen nuclear spins need to be considered, since ^{12}C has a nuclear spin of I=0 such that the nuclear spin wavefunctions remain unaffected under a permutation operation. With four equivalent hydrogens, the total number of nuclear spin wavefunctions is $(2I_H+1)^4=16$. Among the 16 nuclear spin wavefunctions, the numbers of wavefunctions that remain unchanged after permutation operations (12)(34), (13)(24)(56), and (14)(23)(56) are 4, 4, and 4, respectively. For example, using the conventional α and β symbols to denote spin-up and spin-down, the only spin combinations that remain unchanged under a (12)(34) operation are $\alpha\alpha\alpha\alpha$, $\alpha\alpha\beta\beta$, $\beta\beta\alpha\alpha$, and $\beta\beta\beta\beta$. Since an inversion operation does not affect the spin coordinates, the total representation of the 16 nuclear spin wavefunctions is thus:

$$\Gamma_{ns} = 16, 4, 4, 4, 16, 4, 4, 4,$$

with respect to E, (12)(34), (13)(24)(56), (14)(23)(56), E^*, (12)(34)*, (13)(24)(56)*, and (14)(23)(56)*. It decomposes into:

$$\Gamma_{ns} = 7A_g \oplus 3B_{1u} \oplus 3B_{2u} \oplus 3B_{3g}.$$

Here, $\oplus$ denotes direct sum.

The symmetry of the total wavefunction can then be determined by directly multiplying the individual components:

$$\Gamma_{total} = \Gamma_{rot} \otimes \Gamma_{tun} \otimes \Gamma_{ns}.$$

$\otimes$ is used to denote direct product. The resulting symmetry can only be A_g and A_u for

Ne-$^{12}C_2H_4$, governed by the fact that hydrogen nuclei are fermions and the exchange of an even number of pairs of hydrogen nuclei, such as (12)(34), must leave the total wavefunction invariant. The last thing to do then is to combine the individual components with the proper symmetry to form total wavefunctions of the right symmetry, using the following expression:

$$\begin{pmatrix} A_g \\ A_u \end{pmatrix} = \begin{pmatrix} A_g \\ A_u \\ B_{1u} \\ B_{1g} \end{pmatrix} \otimes \begin{pmatrix} A_g \\ B_{2u} \end{pmatrix} \otimes \begin{pmatrix} 7A_g \\ 3B_{1u} \\ 3B_{2u} \\ 3B_{3g} \end{pmatrix}.$$

The resulting allowed combinations are given in table 3-2. m is used to denote the tunneling states, with m=0 being the ground tunneling state and m=1 being the first excited tunneling state. The rotational levels are symmetry labeled with the symmetry of the corresponding nuclear spin wavefunctions, and the spin statistical weights are given in parentheses. For example, in the m=0 state where the tunneling wavefunction is of A_g symmetry, an *oo* rotational level with the rotational wavefunction of B_{1g} symmetry, must combine with nuclear spin wavefunctions of B_{1u} symmetry to give a total wavefunction of A_u symmetry. Therefore, the *oo* rotational levels in the ground tunneling state are symmetry-labeled with B_{1u} and have a nuclear spin statistical weight of 3.

The same procedure was carried out for the in-plane motion, and also for three rare isotopomers, namely Ne-C_2D_4, Ne-$^{13}C_2H_4$, and Ne-trans-1,2-$C_2D_2H_2$. The results are listed in table 3-2. For the Ne-cis-1,2-$C_2D_2H_2$ isotopomer, no tunneling motion that exchanges between two equivalent configurations exists. Instead, two different isomers are formed, one is the D-atom-bonded isomer in which the two deuterium atoms are between carbon and Ne (see figure 3-4), and the other is the H-atom-bonded one in which the two hydrogen atoms are between carbon and Ne instead (see figure 3-4). Only the spectrum of the lower energy D-atom-bonded isomer was observed (see chapter 4). For comparison purpose, a molecular symmetry group analysis was performed for this isomer of Ne-cis-1,2-$C_2D_2H_2$. In chapter 4, the results listed in table 3-2 are used to interpret the observed spectra and to deduce information about the nature of the tunneling motion.

b. Kr-CH_4

It was established from the observed infrared spectra of Kr-CH_4 that the methane subunit is nearly freely rotating within the dimer (*32,175*). The molecular symmetry group of Kr-CH_4 is therefore the same as that of free CH_4 and is designated as T_d(M), isomorphic to the T_d point group. The character table of the T_d(M) group for Kr-CH_4 is given in table 3-3 (*1*) and the numbering of the equivalent hydrogen nuclei is depicted in figure 3-5. In table 3-3, the nuclear permutation operation (123) refers to an operation of simultaneously replacing nucleus 1 with nucleus 2, nucleus 2 with nucleus 3, and nucleus 3 with nucleus 1. A C_{3v} equilibrium geometry was assumed, similar to that of Ar-CH_4, where the rare gas atom sits above a face of the CH_4 tetrahedron (*176,177*). Based on the character table, the symmetries of the rotational wavefunctions are A_1 for l=even levels and A_2 for l=odd levels, determined by the effects of the R_c^π operation. Here, the ($J\ j\ l$) notation is applied (*178*), where j is the quantum number for the internal rotation of the CH_4 subunit, l is the quantum number for the end-over-end rotation of the complex, and J is the total quantum number, i.e., the vector sum of j and l. The symmetries of the internal rotation wavefunction have been previously determined to be A_1, F_1, and F_2+E for

j=0, 1, and 2, respectively (*1,179,180*). Among the total $(2I_H+1)^4$=16 nuclear spin wavefunctions, the numbers of wavefunctions that remain unchanged under E, (123), (14)(23), (1423)*, and (23)* operations are 16, 4, 4, 2, and 8, respectively. Therefore, the 16 nuclear spin wavefunctions have a total representation of:

$$\Gamma_{ns} = 16, 4, 4, 2, 8,$$

which can be decomposed to:

$$\Gamma_{ns} = 5A_1 \oplus E \oplus 3F_2. \tag{3-4}$$

The total wavefunction must be of A_1 or A_2 symmetry. This is because protons are fermions and must obey Fermi-Dirac statistics. Nuclear permutation operations that involve the exchange of an even number of pairs of protons, such as (123) and (14)(23), must leave the total wavefunction unchanged, while other operations that involve the exchange of an odd number of pairs of protons, such as (1423) and (23), must change the sign of the total wavefunction. Using the direct product table (*181*) (table 3-4) and the expression:

$$\begin{pmatrix} A_1 \\ A_2 \end{pmatrix} = \begin{pmatrix} A_1 \\ A_2 \end{pmatrix} \otimes \begin{pmatrix} A_1 \\ F_2 \\ F_2 \oplus E \end{pmatrix} \otimes \begin{pmatrix} 5A_1 \\ E \\ 3F_2 \end{pmatrix},$$

nuclear spin statistical weights for each of the internal rotor states were obtained, as listed in table 3-5. Only the lowest internal rotor state of each nuclear spin symmetry is listed. The higher ones are not expected to be appreciably populated in the molecular beam. Again, the energy levels are symmetry labeled with the symmetry of the corresponding nuclear spin wavefunctions, and the spin statistical weights are given in parentheses. Note that the spin statistical weights for the j=2 levels of E symmetry are 2, twice the number of E symmetry nuclear spin wavefunctions from equation 3-4. The j=2 levels, with rotational wavefunctions of A_1 or A_2 symmetry and internal rotation wavefunction of E symmetry, must combine with nuclear spin wavefunctions of E symmetry. Using table 3-4, the direct products of $A_1 \otimes E \otimes E$ and $A_2 \otimes E \otimes E$ decompose into A_1+A_2+E. From one E symmetry nuclear spin wavefunction, two allowed total wavefunctions, A_1+A_2, result. This explains the doubling of the corresponding nuclear spin statistical weights.

The same procedure was also performed for the two rare isotopomers, namely Kr-^{13}CH$_4$ and Kr-CD$_4$. The obtained results are also given in table 3-5. The partial substitution of a proton with a deuteron in the Kr-CH$_3$D and Kr-CHD$_3$ isotopomers breaks the T_d(M) symmetry. Instead, the character table of the C_{3v}(M) molecular symmetry group is used (*1*). Using the tabulated symmetries of internal rotational levels (*1*), nuclear spin statistical weights were obtained in a similar manner and are also listed in table 3-5. The j=0 and 1 states of Kr-CH$_3$D/Kr-CHD$_3$ are of A_1/(A_1+A_2) and E/E symmetries, respectively. Unlike the T_d symmetry isotopomers, the j=2 state is no longer metastable in these C_{3v} symmetry isotopomers (see table 3-5).

Table 3-1: Character table for Ne-C_2H_4. A=(12)(34), B=(13)(24)(56), C=(14)(23)(56).

D_{2h}(M)	E	A	B	C	E^*	A^*	B^*	C^*
Equiv. Rot. (out-of-plane)	R^0	R_{tun}	R_a^π	$R_{tun}R_a^\pi$	R_c^π	$R_{tun}R_c^\pi$	R_b^π	$R_{tun}R_b^\pi$
Equiv. Rot. (in-plane)	R^0	$R'_{tun}R_a^\pi$	R_a^π	R'_{tun}	R_c^π	$R'_{tun}R_b^\pi$	R_b^π	$R'_{tun}R_c^\pi$
A_g:	1	1	1	1	1	1	1	1
A_u:	1	1	1	1	-1	-1	-1	-1
B_{1g}:	1	1	-1	-1	-1	-1	1	1
B_{1u}:	1	1	-1	-1	1	1	-1	-1
B_{2g}:	1	-1	1	-1	-1	1	-1	1
B_{2u}:	1	-1	1	-1	1	-1	1	-1
B_{3g}:	1	-1	-1	1	1	-1	-1	1
B_{3u}:	1	-1	-1	1	-1	1	1	-1

Table 3-2: Symmetry labels and spin statistical weights of energy levels of Ne-ethylene isotopomers from molecular symmetry group analyses.

		ee & *eo*, m=0	*oe* & *oo*, m=0	*ee* & *eo*, m=1	*oe* & *oo*, m=1
		Out-of-Plane Motion			
Ne-C_2H_4	D_{2h}(M)	A_g (7)	B_{1u} (3)	B_{2u} (3)	B_{3g} (3)
Ne-C_2D_4	D_{2h}(M)	A_g (27)	B_{1u} (18)	B_{2u} (18)	B_{3g} (18)
Ne-$^{13}C_2H_4$	D_{2h}(M)	B_{1u} (16)	A_g (24)	B_{3g} (12)	B_{2u} (12)
Ne-trans-1,2-$C_2D_2H_2$	C_{2h}(M)	B_u (15)	A_g (21)	A_g (21)	B_u (15)
Ne-cis-1,2-$C_2D_2H_2$[a]	C_{2v}(M)	B_2 (15)	A_1 (21)	-	-
		In-Plane Motion			
Ne-C_2H_4	D_{2h}(M)	A_g (7)	B_{1u} (3)	B_{2u} (3)	B_{3g} (3)
Ne-C_2D_4	D_{2h}(M)	A_g (27)	B_{1u} (18)	B_{2u} (18)	B_{3g} (18)
Ne-$^{13}C_2H_4$	D_{2h}(M)	B_{1u} (16)	B_{2u} (12)	B_{3g} (12)	A_g (24)
Ne-trans-1,2-$C_2D_2H_2$	C_{2h}(M)	B_u (15)	B_u (15)	A_g (21)	A_g (21)

[a]The molecular symmetry analysis is only performed for the D-atom-bonded isomer.

Table 3-3: Character table of the T_d(M) molecular symmetry group for Kr-CH$_4$.

T_d(M)	E 1	(123) 8	(14)(23) 3	(1423)* 6	(23)* 6
Equivalent Rotation	R^0	C_3^{methane}	C_2^{methane}	R_c^{π}	R_c^{π}
A_1:	1	1	1	1	1
A_2:	1	1	1	-1	-1
E:	2	-1	2	0	0
F_1:	3	0	-1	1	-1
F_2:	3	0	-1	-1	1

Table 3-4: Direct product table for the T_d group.

	A_1	A_2	E	F_1	F_2
A_1	A_1	A_2	E	F_1	F_2
A_2	A_2	A_1	E	F_2	F_1
E	E	E	A_1+A_2+E	F_1+F_2	F_1+F_2
F_1	F_1	F_2	F_1+F_2	$A_1+E+F_1+F_2$	$A_2+E+F_1+F_2$
F_2	F_2	F_1	F_1+F_2	$A_2+E+F_1+F_2$	$A_1+E+F_1+F_2$

Table 3-5: Symmetry labels and spin statistical weights of energy levels of Kr-CH$_4$ isotopomers.

		j=0	j=1	j=2
Kr-^{12}CH$_4$	T_d(M)	A_1 (5)	F_2 (3)	E (2)
Kr-^{13}CH$_4$	T_d(M)	A_1 (5)	F_2 (3)	E (2)
Kr-^{12}CD$_4$	T_d(M)	A_1 (15)	F_1+F_2 (18)	E (6)
Kr-CH$_3$D	C_{3v}(M)	A_1 (4)	E (4)	-
Kr-CHD$_3$	C_{3v}(M)	A_1+A_2 (11)	E (16)	-

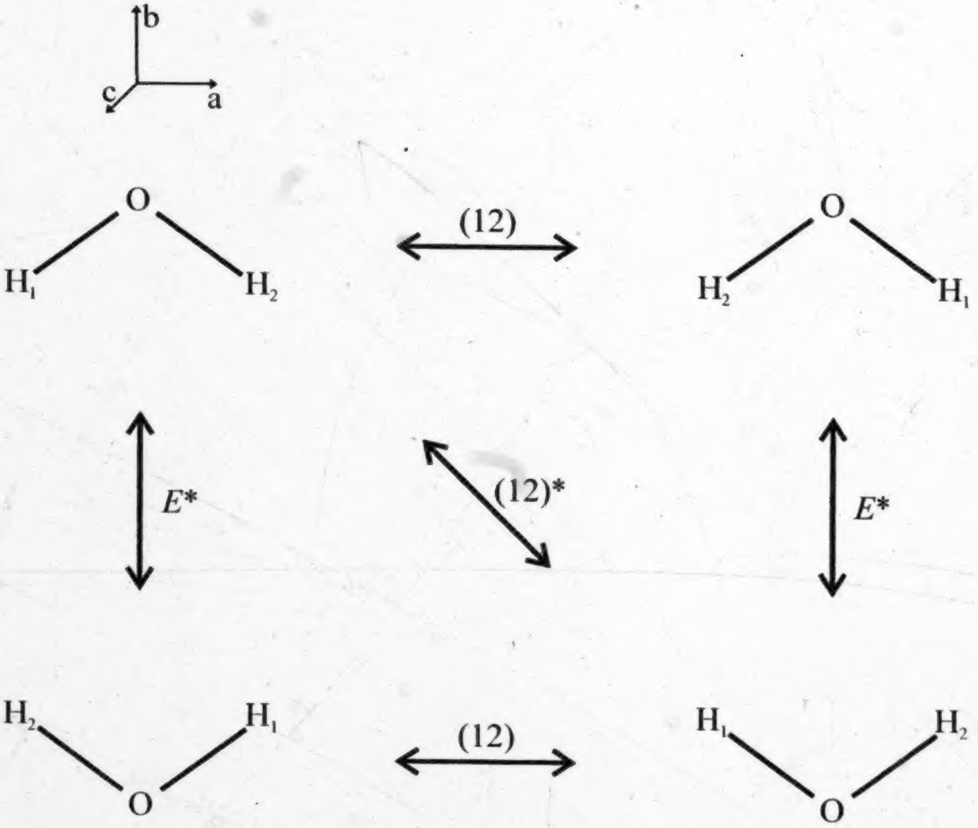

Figure 3-1: The effects of the four elements of the molecular symmetry group of H_2O. (12) refers to the interchange of H_1 and H_2. E^* refers to the inversion of the spatial coordinates of all nuclei and electrons. (12)* denotes the product of the above two operations. The *a*-, *b*-, and *c*-principal inertial axes of the molecule are also shown. (12), E^*, and (12)* correspond to rotations of the molecule about its *b*-, *c*-, and *a*-principal inertial axes, respectively.

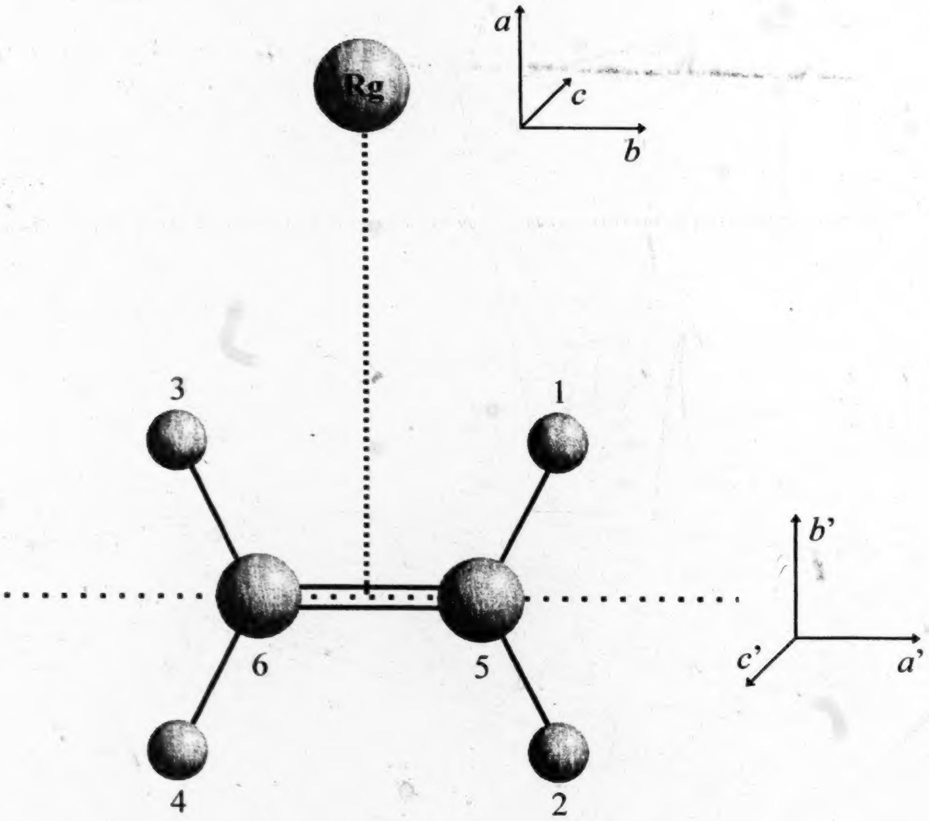

Figure 3-2: Numbering of the identical nuclei used for the molecular symmetry group analysis for Ne-C_2H_4. *a*, *b*, and *c* refer to the principal inertial axes of the complex, while *a*', *b*', and *c*' refer to those of the ethylene monomer. These principal inertial axes frames also apply to Ar-C_2H_4.

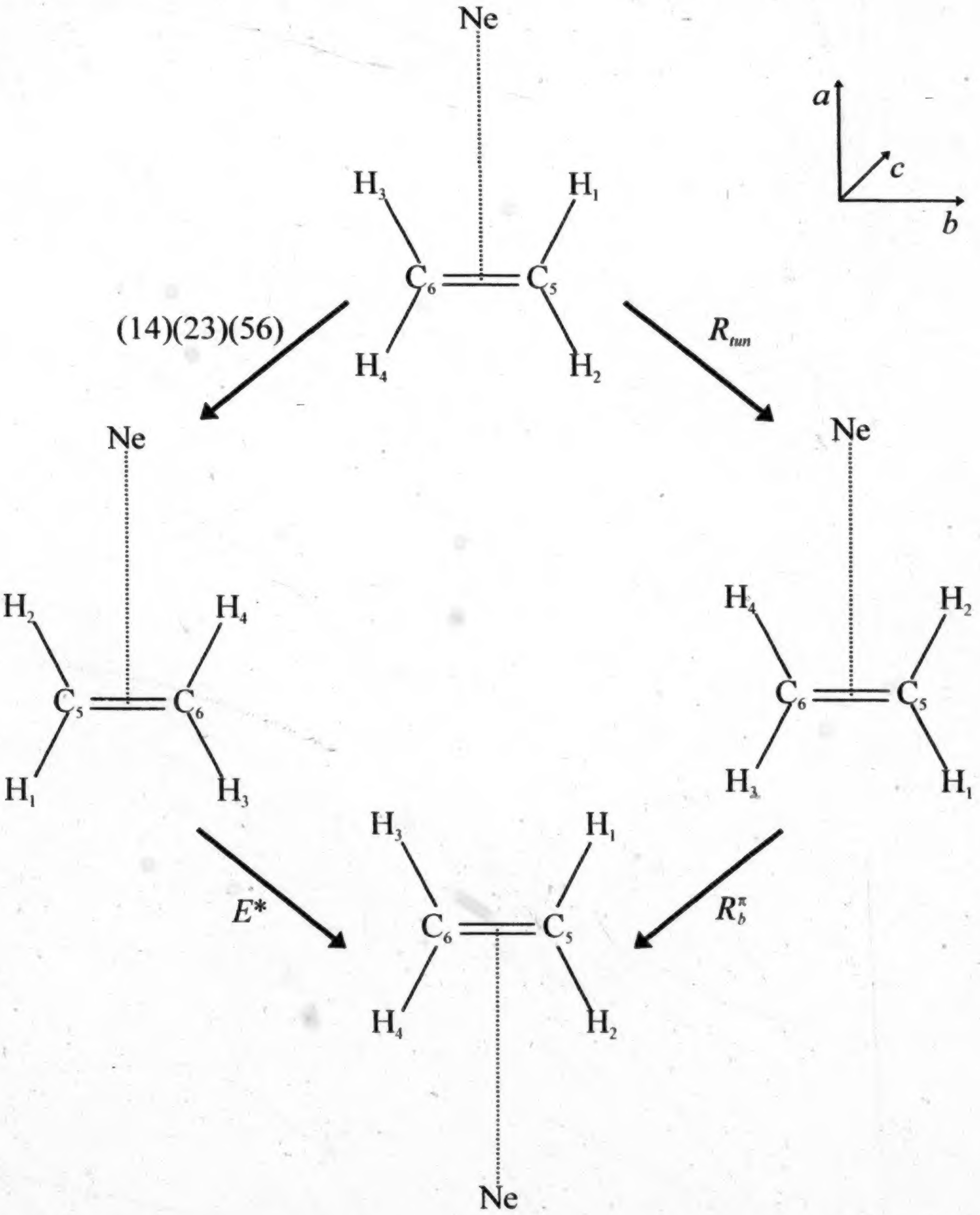
Ne
a
c
b
H3
H1
C6
C5
H4
H2
(14)(23)(56)
R_{tun}
Ne
H2
H4
C5
C6
H1
H3
Ne
H4
H2
C6
C5
H3
H1
E^*
R_b^π
H3
H1
C6
C5
H4
H2
Ne

Figure 3-3: Illustration of the equivalence of the nuclear permutation-inversion operation (14)(23)(56)* and its corresponding equivalent rotation $R_{tun}R_b^\pi$ (out-of-plane motion).

a) D-atom-bonded isomer:

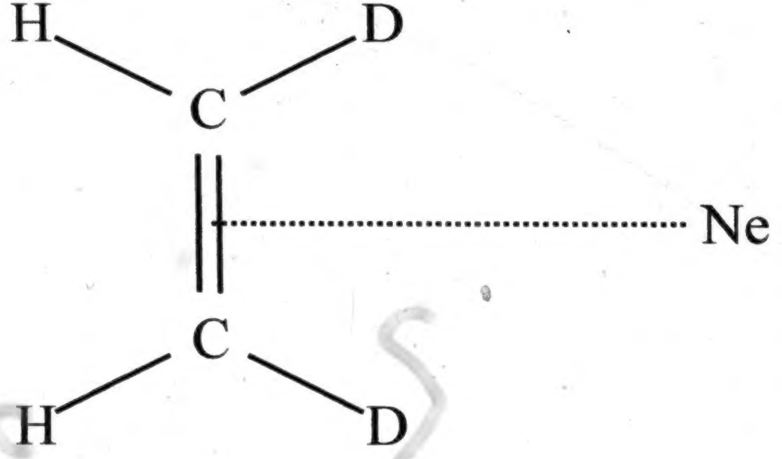

b) H-atom-bonded isomer:

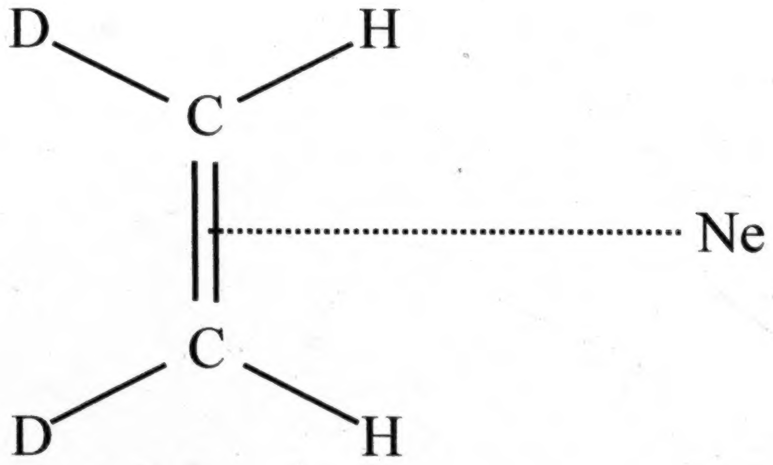

Figure 3-4: The two isomers of Ne-cis-D_2-ethylene. The two deuterium atoms are between carbon and Ne in the D-atom-bonded isomer (*a*), whereas the two hydrogen atoms are between carbon and Ne in the H-atom-bonded isomer (*b*).

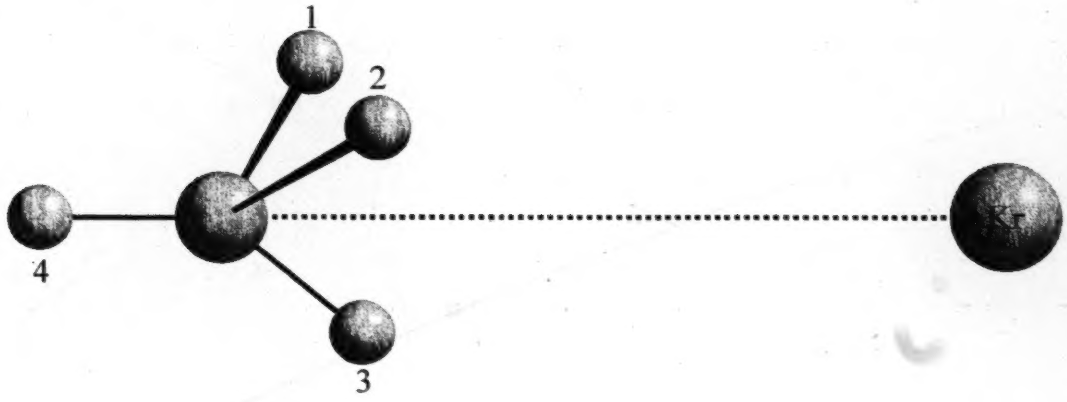

Figure 3-5: Numbering of the four equivalent hydrogen nuclei in Kr-CH_4 for molecular symmetry group analysis. A C_{3v} equilibrium configuration for Kr-CH_4, where Kr approaches the face center of the CH_4 tetrahedron, is assumed. Such an equilibrium geometry for Ar-CH_4 is obtained theoretically (*177*).

4

INTERNAL ROTATION OF ETHYLENE IN Rg-ETHYLENE

4.1 PREVIOUS WORK AND MOTIVATION FOR THIS STUDY

Previous spectroscopic and theoretical studies on several ethylene-containing van der Waals complexes have shown that the ethylene subunit can undergo large amplitude internal rotation motions within the complexes. The microwave spectrum of the C_2H_4-SO_2 dimer displayed tunneling doubling, arising from an internal rotation motion of the ethylene subunit in its molecular plane, that is an internal rotation about the *c*-principal inertial axis of the monomer (see figure 3-2) (*60*). In a following theoretical study of this dimer at the MP2 level of theory, various possible tunneling motions were considered (*182*). The most likely occurring tunneling motion was determined to be the rotation in the ethylene molecular plane, in agreement with the experiment. Transition doubling was also observed in the microwave spectrum of the C_2H_4-C_2H_2 van der Waals dimer. However, in this case it was determined that the doubling is a result of an internal rotation of ethylene about the C=C bond, i.e., its *a*-principal inertial axis (*61*). Another scenario of internal motions involving ethylene was discovered in the C_2H_4-CO_2 and

C_2H_4-N_2O dimers. Both the infrared spectra and *ab initio* calculations indicate that the two subunits of the dimers rotate with respect to one another about the axis connecting the centers-of-mass (*62,63*). Compared to these polyatomic-polyatomic systems, the Rg-ethylene dimers are less complex in the sense that the number of internal degrees of freedom is reduced. This reduction facilitates more detailed investigations of the nature of the internal motions of ethylene in complexes, both spectroscopically and theoretically.

Rg-ethylene dimers have been the subject of a number of experimental and theoretical studies. A few vibrational predissociation spectra of the Rg-ethylene complexes were reported, including the Ar-ethylene spectra near the ν_9 and ν_{11} modes of free ethylene (*183*), and the Ar-, Ne-, and Kr-ethylene spectra near the ν_7 mode of free ethylene (*184,185*). These spectra were interpreted in terms of a hindered internal rotation of the ethylene subunit. Estimates for the barrier to the internal rotation were made to be 12.5 and 30.0 cm^{-1} for Ne-C_2H_4 and Ar-C_2H_4, respectively (*185*). However, unique determinations of the structures of the complexes were not achieved. High resolution infrared spectra of Ar-ethylene, near the ν_9 and ν_{11} modes, were recorded by Miller and co-workers (*155*). These rotationally resolved spectra show transition doubling, which was attributed to a tunneling motion of the ethylene monomer. Spectral analyses established a T-shaped, planar structure with Ar sitting on the *b*-axis of ethylene. The two possible tunneling paths, namely the in-plane motion where ethylene rotates about its *c*-axis and the out-of-plane motion where ethylene rotates about its *a*-axis, i.e., the C=C bond, were considered. It was concluded that only the spin statistical weights obtained from a molecular symmetry group analysis assuming an out-of-plane motion were consistent with the observed intensity pattern. The barrier to this internal rotation motion was estimated to be 76 cm^{-1} from the observed tunneling splittings. To date, no such high resolution spectrum is available for Ne-ethylene.

On the theoretical side, Hutson *et al.* constructed empirical intermolecular potentials for Ne-ethylene and Ar-ethylene. The obtained potentials have global minima at C_{2v} geometries with the rare gas atoms located perpendicularly above the ethylene plane (*186*). Improved potentials for Ne-ethylene were later constructed by fitting to the barrier height reported by Western *et al.* (*185*). The global minimum was found to be at R=3.33 Å, θ=35°, and ϕ=90° (*187,188,189*). Here, R is the separation between Ne and the center-of-mass of the ethylene monomer, θ is the out-of-plane angle between the R vector and the molecular plane of ethylene, and ϕ is the angle between the R vector and the C=C bond axis (see figure 4-1). *Ab initio* potentials of Ar-ethylene were constructed at the SCF, MP2, and MP4 levels, with the 6-31+G[2*d*,2*p*] basis set for the ethylene subunit and the Vohralik basis set for Ar (*155*). The global potential minimum was determined to be at R=3.89 Å, θ=10°, and ϕ=90° at the MP4 level. The dissociation energy, D_e, was evaluated to be 174 cm^{-1}. The energy difference between the planar structure with θ=0° and the global minimum was only 0.08 cm^{-1}. A one dimensional potential energy curve describing the out-of-plane internal rotation motion was obtained by fixing R at the equilibrium distance of 3.89 Å. The barrier to this motion was determined to be 56 cm^{-1}. The potential energy curve for the in-plane internal rotation motion was also computed at the fixed equilibrium intermolecular distance. The potential becomes repulsive as ethylene rotates, indicating that this motion requires a fair amount of radial movement.

For this reason, the in-plane internal rotation motion is less likely to be the feasible tunneling motion that is responsible for the observed splittings. This conclusion agrees with the one drawn from the recorded infrared spectra. No *ab initio* potential has been reported for the Ne-ethylene van der Waals dimer so far.

By recording the rotational spectra of the Rg-ethylene complexes, it was hoped that further spectroscopic evidence for the occurring tunneling motion could be obtained. It was also expected that the nature of the internal rotation motions of ethylene in such dimers could be deduced by constructing an *ab initio* potential energy surface for Ne-C_2H_4. Furthermore, when the binding partner of ethylene changes from Ar to Ne, the intermolecular potential is expected to be more isotropic as a consequence of the weaker intermolecular interaction. This comparative study of Ar-C_2H_4 and Ne-C_2H_4 therefore provides an opportunity to investigate the effect of the size and polarizability of the Rg atom on the internal rotation motions of the ethylene monomer within the complex.

4.2 SPECTRAL SEARCH AND ASSIGNMENTS

For the Ar-ethylene isotopomers, the sample mixture contained 0.3% C_2H_4 and 1% Ar. Enough Ne was added to maintain a total pressure of 6 atm. For Ne-ethylene, a sample mixture of 0.5% C_2H_4 in Ne was used. Increasing the amount of C_2H_4 resulted in a decrease in transition intensity, possibly due to a greater yield of larger $(C_2H_4)_n$ complexes. ^{22}Ne-containing isotopomers were measured in their natural abundances (^{22}Ne: ~10%). Isotopomers containing $^{13}C_2H_4$, C_2D_4, trans-1,2-$C_2D_2H_2$ (trans-D_2-ethylene), and cis-1,2-$C_2D_2H_2$ (cis-D_2-ethylene) were measured using isotopically enriched samples (98% ^{13}C and 98% D, respectively, Merck Sharp & Dohme of Canada).

4.2.1 Ar-C_2H_4

For the normal isotopomer, Ar-C_2H_4, the spectrum was predicted using the rotational and centrifugal distortion constants determined from the recorded infrared spectra (*155*). The two $J_{K_aK_c}$=2_{02}-1_{01} transitions, one for each tunneling state, were predicted to be between 7.6 and 7.7 GHz, with a tunneling splitting of about 60 MHz. The first two transitions were located at 7655 MHz and 7633 MHz. The one at higher frequency was approximately twice as intense as the other, as shown in figure 4-2. From a molecular symmetry group analysis (see table 3-2), the K_a=0, m=0 and K_a=0, m=1 states were determined to have spin statistical weights of 7 and 3, respectively. Here, m is the internal rotation quantum number. Consequently, the higher frequency transition was assigned to the ground tunneling state, i.e., m=0, and the lower frequency transition was assigned to the first excited tunneling state, i.e., m=1. Further spectral searches revealed a pair of transitions with approximately the same intensity at 7523 MHz and 7515 MHz. These transitions were assigned to be the $J_{K_aK_c}$=2_{12}-1_{11} transitions. Another pair of equally intense transitions was easily located at frequencies almost symmetrically above the assigned $J_{K_aK_c}$=2_{02}-1_{01} transitions, and were assigned to be the $J_{K_aK_c}$=2_{11}-1_{10} transitions. With these assignments, the following spectral search for further transitions was relatively straightforward. Altogether, 13 transitions were measured for both the ground and the first excited tunneling state. The K_a=0, m=0 transitions were the most intense. No hyperfine structure from nuclear spin-spin and spin-rotation interactions associated with the four I=½ hydrogen nuclei was observed.

Assuming the same separation between the Ar atom and the center-of-mass of the ethylene monomer, frequencies of the $J_{K_aK_c}=2_{02}-1_{01}$ transitions for the Ar-C_2D_4 isotopomer were predicted to be around 6960 MHz. Considering the heavier mass and consequently a lower zero-point energy, a shorter effective separation was expected. This consideration led to a search at frequencies higher than the initial prediction. In addition, a relatively smaller tunneling splitting was expected, as a result of the larger mass of the rotating subunit. Two transitions were located at 7029 MHz and 7024 MHz, with a splitting of only 5 MHz. For comparison, the tunneling splitting of the same transition was 22 MHz for Ar-C_2H_4. Assuming an asymmetry splitting between the $K_a=0$ and $K_a=1$ transitions similar to that of Ar-C_2H_4, the $K_a=1$ transitions were easily located. Altogether, 12 transitions were measured for each tunneling state. The $J_{K_aK_c}=1_{01}-0_{00}$ transitions, predicted to be at ~3.5 GHz, are beyond the normal operating range of the spectrometer. Broadening of the transitions, and sometimes narrow splittings, were observed. This is attributed to the nuclear quadrupole interactions between the deuterium nuclei and the overall rotation of the complex. Due to the narrowness of the splittings and the complexity of the hyperfine structure of four quadrupolar nuclei, individual hyperfine components could not be assigned. Center frequencies were taken at the positions of maximum intensities.

The spectral search for Ar-$^{13}C_2H_4$ transitions followed a similar procedure. 13 transitions were recorded for each tunneling state. Unlike the case of the normal isotopomers, the $K_a=1$, $m=0$ transitions were the most intense in this case. This is in agreement with the expected spin statistical weights obtained from a molecular symmetry group analysis assuming an out-of-plane motion (see table 3-2).

There are two isomers of the Ar-cis-D_2-ethylene isotopomer: a D-atom-bonded one in which the two deuterons are closer to Ar and an H-atom-bonded one in which the two protons are closer to Ar (see figure 3-4). Between the two, the D-atom-bonded isomer is more stable due to a lower zero-point energy. Considering the low temperature achieved in the molecular beam, it was expected that transitions of the D-atom-bonded isomer would show intensities comparable to those of the ground state transitions of other isotopomers. Transitions of the H-atom-bonded isomer, on the other hand, were expected to be much weaker, or even not observable, because of low populations of the energy levels. 13 transitions, analogous to the m=0 ground tunneling state transitions of Ar-C_2H_4, were recorded and assigned to the D-atom-bonded isomer. The K_a=1 transitions were more intense than the K_a=0 transitions. This is in agreement with the spin statistical weights of 21 and 15 for the two states. Line broadening was also observed, but the hyperfine components could not be resolved. Spectral scans with a fair number of averaging cycles were carried out to locate transitions of the higher energy, less populated H-atom-bonded isomer. However, no additional transition could be assigned.

In the search for Ar-trans-D_2-ethylene transitions, the K_a=0 transitions were easily located. Four transitions, with J values ranging from 1 to 5, were recorded for both the m=0 and the m=1 state. Transitions within the m=1 state were noticeably stronger than those within the m=0 state, in agreement with the spin statistical weights of 21 and 15 for the two states. No transition corresponding to a K_a=1 transition could be assigned, despite intensive spectral searches.

All measured transition frequencies for the five isotopomers of Ar-ethylene are listed in tables 4-1 and 4-2, along with the quantum number assignments. Watson's A-reduction Hamiltonian in its I^r representation (*190*) was used to fit spectroscopic constants to the transition frequencies. Transitions within the two tunneling states were fitted separately. Since only a-type transitions, i.e., transitions with $\Delta K_a=0$, were measured, there was not enough information to determine the A rotational constant. For the normal isotopomer, the A rotational constant was first fixed at 29.75 GHz, the value determined from the infrared spectra (*155*). It was later varied until the best fit was obtained. The resulting value for A was 29.9 GHz, only 0.5% larger than the value determined from the infrared spectra. For the remaining minor isotopomers, the A rotational constant was fixed at a value scaled with the b rotational constant of the corresponding substituted ethylene monomer. Individual b values were calculated from the reported structure parameters of C_2H_4 (*162*), assuming they do not change significantly upon substitution. Two rotational constants, B and C, and three quartic centrifugal distortion constants, Δ_J, Δ_{JK}, and δ_J, were determined. Δ_K and δ_K could not be determined with only a-type transitions available, and were fixed at zero. In the analysis of the Ar-trans-D_2-ethylene spectrum, only two spectroscopic constants, namely $(B+C)/2$ and Δ_J, were determined from the fitting procedure, since only $K_a=0$ transitions were observed. All resulting spectroscopic constants are listed in table 4-3, along with the standard deviations of the fits. The standard deviations obtained for the C_2H_4- and $^{13}C_2H_4$-containing isotopomers are on the same order as the experimental uncertainties. Those for the deuterated species are much larger. This is mainly a result of the unresolved deuterium nuclear quadrupole hyperfine structures in the spectra of these isotopomers.

4.2.2 Ne-C_2H_4

The weaker interaction between Ne and ethylene compared to that between Ar and ethylene is expected to lower the barriers to internal motions. Consequently, larger tunneling splittings compared to those of Ar-ethylene, or even a different tunneling scenario, are possible. This makes it rather difficult to predict rotational transition frequencies of Ne-ethylene. In addition, the dipole moment of Ne-ethylene decreases from its Ar analog as a result of the reduced polarizability of Ne. Therefore, lower transition intensities are expected, adding further difficulty to spectral searches for transitions of Ne-ethylene.

Nevertheless, the initial prediction was made utilizing the structural information obtained from the rotational spectrum of Ar-ethylene. The intermolecular separation *R* was estimated from the *R* value of Ar-ethylene (see table 4-3) by comparing to the corresponding distances in the Ar-cyclopropane and Ne-cyclopropane complexes (*58*). It was used to calculate the rotational constants, *B* and *C*, of ^{20}Ne-C_2H_4, and then to predict rotational transition frequencies. Unexpectedly, this procedure predicted the K_a=0, m=0 transitions rather well. These transitions were located relatively easily. They are approximately an order of magnitude weaker than the corresponding Ar-C_2H_4 transitions. Three times longer microwave excitation pulses were needed to optimize the excitation, indicating a smaller dipole moment compared to that of Ar-C_2H_4 (see chapter 2). The assignment of the K_a=0, ^{20}Ne-C_2H_4 transitions was confirmed by finding the $J_{K_aK_c}=1_{01}-0_{00}$ transition, and by finding the analogous transitions of the ^{22}Ne-C_2H_4 isotopomer.

However, the search for $K_a=1$, $m=0$, and all $m=1$ transitions was non-trivial. Only after a number of transitions were recorded and carefully analyzed, was it possible to make the final assignments.

Ten transitions, with J ranging from 0 to 4, were recorded for both the $m=0$ and the $m=1$ state of ^{20}Ne-C_2H_4 and ^{22}Ne-C_2H_4. The observed relative intensity pattern was similar to that of Ar-C_2H_4. A tunneling splitting of 124 MHz of the $J_{K_aK_c}=1_{01}$-0_{00} transition was observed for ^{20}Ne-C_2H_4, more than an order of magnitude larger than the value of 11 MHz for Ar-C_2H_4. Partially resolved hyperfine structures associated with nuclear spin-spin and spin-rotation interactions of the four $I=\frac{1}{2}$ hydrogen nuclei were observed in low J, $m=1$ transitions. A representative spectrum of the $J_{K_aK_c}=1_{01}$-0_{00}, $m=1$ transition of ^{20}Ne-C_2H_4 is shown in figure 4-3. A tentative assignment of the individual hyperfine components was made, but the fitting result was unsatisfactory, giving standard deviations on the order of 10 kHz. The frequencies of the strongest components were reported as the center frequencies with estimated accuracies of 10 kHz.

After the measurements of the Ne-C_2H_4 isotopomers, the spectral searches for the minor isotopomers containing C_2D_4 and cis-D_2-ethylene were relatively straightforward. Transitions within both the ground and the excited tunneling state were measured for the C_2D_4-containing isotopomers. Only transitions for the D-atom-bonded isomers were measured for the cis-D_2-ethylene-containing isotopomers, similar to the case of Ar-cis-D_2-ethylene. Transition broadening was observed, resulting mainly from the nuclear quadrupole interactions of the deuterium nuclei with the overall rotation of the complex.

However, in the case of the Ne-trans-D_2-ethylene isotopomers, a very different spectral pattern was observed than for Ar-trans-D_2-ethylene. Not only the two K_a=0 progressions were recorded, i.e., the K_a=0, m=0 and K_a=0, m=1 progressions, but two additional K_a=1 progressions were also observed. They were assigned to be transitions within the lower K_a=1, m=0 and higher K_a=1, m=0 states, respectively. In addition, transitions within the K_a=0, m=1 and lower K_a=1, m=0 states displayed irregular energy level spacings, indicating that a Coriolis interaction may occur between these two states. Altogether, nine m=0 transitions and three m=1 transitions were measured. Hyperfine structure caused by the quadrupole interaction of the two deuterium nuclei was also observed. A sample transition is shown in figure 4-4.

All measured transition frequencies of the eight Ne-ethylene isotopomers are listed in tables 4-4 and 4-5, along with the quantum number assignments. Picketts's fitting program was used to fit for spectroscopic constants (*191*). For the normal isotopomer ^{20}Ne-C_2H_4, the A rotational constant was fixed at 28.2 GHz, the value that gave the best fit. For the remaining minor isotopomers, the A rotational constant was then fixed at a value scaled with the b rotational constant of the corresponding substituted ethylene monomer (*162*). Two rotational constants, B and C, three quartic centrifugal distortion constants, Δ_J, Δ_{JK}, and δ_J, and three sextic centrifugal distortion constants, Φ_J, Φ_{JK}, and ϕ_J, were determined. The inclusion of the three sextic centrifugal distortion constants reduced the standard deviation from 440 kHz to 2.1 kHz for ^{20}Ne-C_2H_4 in the m=0 state. For the ground tunneling state of Ne-trans-D_2-ethylene, all measured transitions could still be fitted to the same set of spectroscopic constants with a standard deviation of 2.1 kHz, although the lower K_a=1 state is probably perturbed. The perturbation is evident from the unusual centrifugal distortion constants compared to those of other isotopomers. For the three K_a=0, m=1 transitions, only $(B+C)/2$ and Δ_J were fitted. The perturbation was revealed by the huge standard deviation of the fit. All resulting spectroscopic constants are listed in tables 4-6 and 4-7. Also included are the standard deviations of the individual fits. A fit including a Coriolis interaction term between the lower K_a=1, m=0 and K_a=0, m=1 states was performed for the ^{20}Ne-trans-D_2-ethylene isotopomer, but the standard deviation of the fit was on the order of tens of MHz.

4.3 DISCUSSION OF EXPERIMENTAL RESULTS

4.3.1 Spectroscopic Constants and Structure

All measured transitions of Ar-ethylene and Ne-ethylene are *a*-type transitions. This is consistent with a T-shaped, planar structure. For such a structure, the dipole moment of the complex is along the *a*-principal inertial axis of the dimer. A non-planar structure other than the configuration where the Rg atom is located on the *c*-axis of ethylene, i.e., θ=90°, would have a non-zero dipole moment component along the *c*-principal inertial axis, resulting in an observation of *c*-type transitions. A search for *c*-type transitions was carried out, but no additional transition was recorded. On the other hand, for a planar, but not T-shaped structure, *b*-type transitions are also expected. The absence of *b*-type transitions confirms the T-shaped structure. Further structural information may be obtained from the *A* rotational constant. In this study, the *A* rotational constant of Rg-C_2H_4 was obtained by manually changing the value until the best fit was obtained. It may appear that such obtained *A* values can hardly provide any valid information about the structures of the complexes. However, the fact that the value of 29.9 GHz determined for Ar-C_2H_4 agrees well with the value of 29.75 GHz determined from the infrared spectra suggests that it is meaningful to some degree. For a rigid T-shaped, planar structure, the *A* rotational constant of a Rg-C_2H_4 dimer equals the *b* rotational constant of the ethylene monomer. The determined *A* values, 29.9 GHz for Ar-C_2H_4 and 28.2 GHz for Ne-C_2H_4, are close to the *b* rotational constant of C_2H_4, 30.3 GHz (*155*). The small variations from the *b* value are attributed to the large amplitude internal motions of the ethylene monomer within the complexes. Between the two possible tunneling motions, the in-plane motion would lead to an increase of the *A* rotational constant from its rigid rotor value, and the out-of-plane motion would decrease the value. The reduced *A* value thus suggests that the out-of-plane motion has a larger contribution to the vibrationally averaged rotational constant than the in-plane motion.

With the T-shaped, planar structure established, and assuming that the monomer structure does not change upon complex formation, only one structural parameter is needed to describe the system: the distance *R* between the Rg atom and the center-of-mass of the ethylene subunit. The rotational constant $(B+C)/2$, together with the known structure of ethylene (*162*), were used to determined the effective separation R_0. The obtained values are given in tables 4-3 and 4-6. A value of 3.916 Å was determined for the ground state of Ar-C_2H_4. All the R_0 values determined for the minor isotopomers are in line with this value, with small isotopic variations. For example, the separation in

Ar-C_2D_4 is shortened by ΔR_0=0.02 Å due to a lowered zero-point energy. A similar shortening was also observed in Ar-$^{13}C_2H_4$, but to a lesser degree, with ΔR_0=0.002 Å. The bond distance shortening ΔR_0 upon ^{22}Ne substitution of 0.002 Å is comparable to that in ^{22}Ne-cyclopropane, where ΔR_0=0.004 Å (*58*). The difference ΔR_0 between Ar-C_2H_4 and Ne-C_2H_4 of 0.124 Å is consistent with the corresponding bond length difference in other Rg-containing van der Waals complexes. For example, for the Ar- and Ne-cyclopropane pair, the bond length difference ΔR_0 is 0.130 Å (*58*).

It is often observed that the Rg atom locates closest to the site of most positive electrostatic potential in a Rg-molecule van der Waals complex (*58*). Examples can be found in the Rg-cyclopropane systems. It was determined that the Rg-cyclopropane complexes have structures of C_{3v} symmetry, where the Rg atoms are located above the ring plane of the cyclopropane unit, on its C_3 symmetry axis (*58*). The T-shaped, planar structures of the Rg-ethylene systems are equivalent to the C_{3v} structures of Rg-cyclopropane, in the sense that the Rg atoms are located at the sites of most positive electrostatic potential, avoiding the π system of ethylene, or the pseudo-π system of cyclopropane. Similarly, equivalent structures were also reported for water-ethylene and water-cyclopropane. However, water does bond to the π system of ethylene, or the pseudo-π system of cyclopropane in these hydrogen-bonded systems (*192,193,194*).

4.3.2 Relative Intensity and Tunneling Motion

Molecular symmetry group analyses were performed for the various isotopomers of Rg-ethylene as described in **3.2.3**. The out-of-plane motion was first assumed, and then the in-plane motion. Spin statistical weights were obtained and are listed in table 3-2. In the following paragraphs, the experimentally observed relative intensities are compared to the spin statistical weights, in order to determine which tunneling motion is responsible for the observed transition doubling.

a. Ar-, Ne-C_2H_4

For the Rg-C_2H_4 isotopomers, the same sets of spin statistical weights were obtained for the two possible tunneling motions, i.e., the out-of-plane motion and the in-plane motion of the ethylene subunit (see table 3-2). A schematic energy level diagram of the Rg-C_2H_4 isotopomers is depicted in figure 4-5, with arrows indicating the lowest rotational transitions measured in this study. Each of the four observed states, i.e., K_a=0, m=0; K_a=1, m=0; K_a=0, m=1; and K_a=1, m=1, has nuclear spin wavefunctions of a unique symmetry associated with it. The obtained spin statistical weights are 7, 3, 3, and 3 for the above four states, respectively. Since nuclear spin conversion is a forbidden process in the molecular beam, all four states are metastable, and transitions within all these states are expected to be observable. Relative transition intensities are expected to be proportional to the corresponding spin statistical weights. Experimentally, transitions occurring within all four states were observed. The K_a=0, m=0 transitions are the most intense. The transitions within the other three states have approximately half the intensity of the K_a=0, m=0 transitions. This observation is in good agreement with the prediction from the molecular symmetry group analyses. However, this comparison does not provide information about the nature of the tunneling motion.

b. Ar-, Ne-C_2D_4

The molecular symmetry group analyses for the Ar-, Ne-C_2D_4 isotopomers, assuming the out-of-plane motion of the ethylene monomer, suggest that the same four states, i.e., K_a=0, m=0; K_a=1, m=0; K_a=0, m=1; and K_a=1, m=1, are metastable and spin statistical weights of 27, 18, 18, and 18, respectively, are predicted (see table 3-2). The same results were obtained assuming the in-plane motion, similar to the case of Rg-C_2H_4. The observed relative transition intensity patterns agree with the obtained spin statistical weights.

c. *Ar-$^{13}C_2H_4$*

The molecular symmetry group analysis for the Ar-$^{13}C_2H_4$ isotopomer also suggests that all four states are metastable. This is in agreement with the observation of transitions within all four states. However, in this case, different spin statistical weights for the individual states were obtained when different tunneling motions were assumed. When the out-of-plane motion of the ethylene monomer is assumed, spin statistical weights are 16, 24, 12, and 12 for the K_a=0, m=0; K_a=1, m=0; K_a=0, m=1; and K_a=1, m=1 states, respectively. They are 16, 12, 12, and 24 when the in-plane motion is assumed (see table 3-2). The difference arises because the symmetries of the nuclear spin wavefunctions associated with the K_a=1, m=0 and K_a=1, m=1 states are reversed for the two motions. The out-of-plane motion would lead to an observation of more intense K_a=1, m=0 transitions compared to K_a=1, m=1 transitions, since the spin statistical weights are 24 and 12 for the two states. The opposite would occur in the case of in-plane motion. The statistical weights in this case are 12 and 24 for the two states. Therefore, the Ar-$^{13}C_2H_4$ isotopomer provides a possibility to distinguish between the two tunneling motions. The observed rotational spectrum of Ar-$^{13}C_2H_4$ supports the occurrence of the out-of-plane motion, since the recorded $K_a=1$, $m=0$ transitions are approximately 1.5-2 times stronger than the $K_a=1$, $m=1$ transitions.

d. Ar-, Ne-cis-D_2-ethylene

Between the two isomers, namely D- and H-atom-bonded, of the Rg-cis-D_2-ethylene isotopomers, the population of the D-atom-bonded isomer is greatly enriched as a consequence of a lower zero-point energy. This enrichment is achieved through the repeated dissociation and reassociation processes during the initial phase of the molecular expansion. For this reason, the measured transitions were assigned to the D-atom-bonded isomer. For comparison purpose, a molecular symmetry group analysis was also performed for the D-atom-bonded isomer of Rg-cis-D_2-ethylene. According to the analysis, the two observed states, namely $K_a=0$ and $K_a=1$, are metastable. Nuclear spin statistical weights for the two states are 15 and 21, respectively. Therefore, transitions within the $K_a=1$ state are expected to be stronger than those within the $K_a=0$ state. This agrees with the observation of more intense $K_a=1$ transitions compared to the $K_a=0$ transitions.

e. Ar-, Ne-trans-D_2-ethylene

The above considerations regarding the Ar-$^{13}C_2H_4$ isotopomer suggested that the out-of-plane motion is the occurring tunneling motion. This conclusion came from the relative intensities of the $K_a=1$, $m=0$ and $K_a=1$, $m=1$ transitions. In the following, it is shown that the rotational spectra of the isotopomers containing trans-D_2-ethylene provide an even more convincing proof of the occurrence of the out-of-plane motion.

For the trans-D_2-ethylene-containing isotopomers, molecular symmetry group analyses for the case of the in-plane motion and the case of the out-of-plane motion give significantly different results. This is illustrated in figures 4-6 and 4-7. Schematic energy level diagrams for the Rg-trans-D_2-ethylene isotopomers are plotted, one for the case of the in-plane motion (figure 4-6), the other for the case of the out-of-plane motion (figure 4-7).

The case of the in-plane motion is considered first. The results from the molecular symmetry group analysis suggest that the K_a=0, m=0 and K_a=1, m=0 states are associated with nuclear spin wavefunctions of the same symmetry. Consequently, the higher energy K_a=1, m=0 state is no longer metastable. Considering the low temperature achieved in the molecular beam, this state is not expected to be well populated. Complexes initially in this state would relax down to the lower energy K_a=0, m=0 state. The situation in the excited tunneling state is similar. The K_a=1, m=1state is not metastable. However, since the symmetry of nuclear spin wavefunctions associated with the K_a=0, m=1 state is different from that of the K_a=0, m=0 state, the K_a=0, m=1 state is still metastable. This implies that the in-plane motion would lead to an observation of two K_a=0 progressions, one from each tunneling state. Transitions within the ground tunneling state are expected to be weaker, since spin statistical weights are 15 and 21 for the K_a=0, m=0 and K_a=0, m=1 states.

When the case of the out-of-plane motion is considered, the situation gets more complicated. The molecular symmetry group analysis shows that the K_a=0, m=0 and K_a=1, m=1 states are associated with nuclear spin wavefunctions of the same symmetry. The K_a=1, m=0 and K_a=0, m=1 pair has also the same symmetry, but a different one other than that of the other pair. Consequently, the K_a=1, m=1 state is not metastable. On the other hand, it depends on the relative energy of the K_a=1, m=0 and K_a=0, m=1 states to determine which one is metastable. There are three possibilities. First of all, if the K_a=0, m=1 state is much higher in energy than the K_a=1, m=0 state, the latter is metastable. Rotational spectra similar to those of the D-atom-bonded isomers of Rg-cis-D_2-ethylene would be expected, with an observation of K_a=0 and K_a=1 transitions within the ground tunneling state. Spin statistical weights of 15 and 21 are obtained for these two states. Secondly, if the opposite is true, the K_a=0, m=1 state becomes metastable. Transitions within the K_a=0, m=0 and K_a=0, m=1 states are expected, similar to the case of the in-plane motion. Even the spin statistical weights are the same as for the case of the in-plane motion, i.e., 15 for the K_a=0, m=0 state and 21 for the K_a=0, m=1 state. Finally, there is a possibility that the two involved states have similar energies. As a result, the two states would have similar populations. Observation of transitions within both states can then be expected.

The results obtained from molecular symmetry group analyses can now be compared to the experimental observations. The recorded Ar-trans-D_2-ethylene rotational spectrum included two K_a=0 progressions. No K_a=1 transitions could be assigned. Between the two sets of K_a=0 transitions, the one within the m=1 state was more intense. For the Ne-trans-D_2-ethylene isotopomers, two K_a=1 progressions were also measured in addition to the two K_a=0 progressions. The observation of these K_a=1 transitions undoubtedly excludes the possibility of the in-plane motion being the tunneling motion responsible for the observed transition doubling and therefore confirms the occurrence of the out-of-plane motion. The K_a=0, m=0 transitions are slightly weaker than the K_a=0, m=1 transitions, in agreement with the spin statistical weights of 15 and 21 for the two states. The K_a=1, m=0 transitions have similar intensities as the K_a=0, m=0 transitions and are weaker than the K_a=0, m=1 transitions, suggesting that the K_a=1, m=0 state is slightly above the K_a=0, m=1 state. This is the situation depicted in figure 4-7. The arrows in the figure represent the lowest J transitions observed for the Ne-trans-D_2-ethylene isotopomers.

The difference in the observed rotational spectra of Ar-trans-D_2-ethylene and Ne-trans-D_2-ethylene is discussed in the following section.

4.3.3 Coriolis Interaction and Barrier to Internal Rotation Motion

The above relative transition intensity considerations established that the out-of-plane motion is responsible for the observed transition doubling in the spectra of the Rg-ethylene van der Waals systems. However, one question remains: why are the observed rotational spectra of Ar-trans-D_2-ethylene and Ne-trans-D_2-ethylene so different? In the case of Ar-trans-D_2-ethylene, only two sets of K_a=0 transitions were observed. In the case of Ne-trans-D_2-ethylene, besides the two K_a=0 progressions, K_a=1 transitions within the ground tunneling state were also observed. In addition, a Coriolis interaction was detected to occur between the lower K_a=1, m=0 state and the K_a=0, m=1 state. It is likely that the difference in the spectra is caused by different barriers to the internal rotation motion of ethylene within the Ar-trans-D_2-ethylene and Ne-trans-D_2-ethylene systems.

The energy difference between the K_a=0, m=0 and the K_a=0, m=1 state is very sensitive to the barrier height. If a high barrier is experienced during the tunneling motion, this energy difference is small. In the extreme case of an infinitely high barrier, these two states become degenerate. On the other hand, a low barrier results in a large energy difference. In the zero-barrier, i.e., free rotor, limit, the ground tunneling state correlates to the ground state of free ethylene, and the first excited tunneling state correlates to the first excited rotational state of free ethylene, which is approximately 2 cm^{-1} above the ground state (*162*).

For the Ar-trans-D_2-ethylene isotopomer, only two K_a=0 progressions were observed. From the molecular symmetry group analysis for the out-of-plane motion, it was determined that the K_a=1, m=0 state is associated with nuclear spin wavefunctions of the same symmetry as the K_a=0, m=1 state. The failure to observe K_a=1, m=0 transitions indicates that this state lies considerably above the K_a=0, m=1 state. When the binding partner of ethylene changes from Ar to Ne, the barrier to the tunneling motion is expected to decrease. The consequence of the lowered barrier is to move the K_a=0, m=1 state upwards relative to the K_a=0, m=0 state, increasing the energy difference between the two states. This is indirectly reflected in the observed spectra through a larger tunneling splitting for Ne-C_2H_4. The splitting between the two $J_{K_aK_c}=1_{01}-0_{00}$ transitions is 11 MHz for Ar-C_2H_4 and 125 MHz for ^{20}Ne-C_2H_4. At the same time, the K_a=1, m=0 state moves in the opposite direction, i.e., the separation between the K_a=1, m=0 and the K_a=0, m=0 state decreases. This separation is approximately *A-B*. The obtained spectroscopic constants give *A-B*=28 GHz for Ar-C_2H_4 and 25.2 GHz for ^{20}Ne-C_2H_4. The overall effect is that the K_a=1, m=0 and the K_a=0, m=1 state are moving closer to each other when going from Ar to Ne as the binding partner. This is confirmed by the observation of the K_a=1, m=0 transitions of Ne-trans-D_2-ethylene.

It is difficult to infer information about the barrier to the tunneling motion directly from the tunneling splittings in the rotational spectra. The observed splittings reflect the difference in rotational energy level spacings within each of the two tunneling states. However, by comparing the observed relative intensities and the degree of perturbation of the transition patterns, information about the energy level ordering between the K_a=1, m=0 and K_a=0, m=1 states can be obtained. Careful intensity comparisons between the same J, K_a=1, m=0 and K_a=0, m=1 transitions were performed for Ne-trans-D_2-ethylene. The K_a=0, m=1 transitions were slightly stronger than the K_a=1, m=0 transitions. This suggests that the K_a=0, m=1 state is slightly lower in energy. A more convincing indication came from the observed transition patterns. Irregular transition patterns were observed, arising from a Coriolis interaction occurring between the K_a=0, m=1 and the lower K_a=1, m=0 state. When fitted separately to $(B+C)/2$ and Δ_J constants, the K_a=0, m=1 transitions gave a large, positive value for the centrifugal distortion constant Δ_J, while the lower K_a=1, m=0 transitions gave a negative Δ_J value. This suggests that the K_a=0, m=1 state is lower in energy between the two perturbed states, such that the energy levels within this state are 'compressed' by the Coriolis interaction. On the other hand, the energy levels within the higher energy K_a=1, m=0 state are 'stretched out'.

A comparison of the difference between the $(B+C)/2$ values of the two tunneling states among the isotopomers further corroborates this finding. The difference of the rotational constants of the two tunneling states $(B+C)/2$, $\Delta(B+C)/2$, can be considered an indirect measure of the energy difference between the two states. It is expected to decrease with increasing mass of the rotating subunit. The values are 6 MHZ, 2 MHz, and 1 MHz for Ar-C_2H_4, Ar-trans-D_2-ethylene, and Ar-C_2D_4, respectively. The corresponding values are 62 MHz, -10 MHz, and 37 MHz for ^{20}Ne-C_2H_4, ^{20}Ne-trans-D_2-ethylene, and ^{20}Ne-C_2D_4, respectively. It is evident from this comparison that the values for ^{20}Ne-ethylene do not follow the expected trend. The reduced magnitude of $\Delta(B+C)/2$ for the Ne-trans-D_2-ethylene isotopomer suggests that the effect of the perturbation is to reduce the energy difference between the two K_a=0 states. This supports that the K_a=0, m=1 state is indeed lower in energy than the K_a=1, m=0 state as depicted in figure 4-7.

The above consideration of the ordering of the two perturbed states suggests that the maximum energy gap between the K_a=0, m=0 and K_a=0, m=1 states is approximately A-B=0.84 cm^{-1}, the difference between the K_a=0, m=0 and K_a=1, m=0 states. This information is used to obtain the minimum barrier height of the out-of-plane internal rotation motion.

The one dimensional flexible model for intramolecular motion developed by Meyer (*195*) was used to fit the energy difference between the m=0 and m=1 tunneling states to the barrier height. The case of Ar-C_2H_4 was first considered. From the infrared spectrum, the energy difference between the two tunneling states was determined to be 0.1033 cm^{-1} (*155*). A simple $V_2\cos(2\theta)$ potential is assumed as the potential for the out-of-plane internal rotation (*155*). θ is the out-of-plane angle between the R vector and the ethylene molecular plane. Complete separation of van der Waals stretching and bending modes is assumed. The intermolecular separation R is fixed at the determined effective bond distance of 3.916 Å. The barrier height $-2V_2$ was adjusted to fit the energy difference, yielding a value of 76 cm^{-1}. This value is the same as the one reported in ref. *155*. Encouraged by this, the case of Ne-C_2H_4 is considered next. To fit an energy difference of 0.84 cm^{-1}, a barrier height of $-2V_2$=30.7 cm^{-1} resulted. In general, the energy difference deceases with an increase in the barrier to the tunneling motion. The fitting result suggests that a barrier of at least 30.7 cm^{-1} is experienced when ethylene undergoes the out-of-plane internal rotation motion in the Ne-C_2H_4 van der Waals dimer.

4.4 POTENTIAL ENERGY SURFACES OF Ne-C_2H_4

From the recorded rotational spectra, it was determined that the out-of-plane motion is responsible for the tunneling splitting. Information about the barrier to the tunneling motion was also obtained. It is desirable to compare the experimental results to the features of the corresponding potential energy surfaces. For this purpose, *ab initio* potential energy surfaces for Ne-C_2H_4 were constructed. One dimensional potential energy curves of the two possible tunneling motions were subsequently mapped out, and the results were compared with the experimental results.

Computational details are given in **3.1.3** (*a*). The potential energy surface was first constructed with ϕ fixed at 90°, corresponding to configurations where the *R* vector is perpendicular to the C =C bond. The intermolecular separation *R* and the angle between *R* and the ethylene molecular plane θ were varied (see figure 4-1). θ=0° corresponds to a planar, T-shaped geometry, with the Ne atom sitting on the *b*-axis of the monomer; θ=90° corresponds to a geometry where the Ne atom is sitting above the ethylene molecular plane, on the *c*-axis of the monomer. 114 points were calculated using basis set 1, with R ranging from 3.5 Å to 4.0 Å in intervals of 0.1 Å, and angle θ from 0° to 90° in intervals of 5°. 110 points were calculated using basis set 2, with R ranging from 3.5 Å to 4.5 Å in intervals of 0.1 Å, and angle θ from 0° to 90° in intervals of 10°. Points with ϕ values other than 90° were later calculated with θ fixed at 0°.

The obtained intermolecular energies are given in tables 4-8 and 4-9. With basis set 1, the global minimum was located at $R = 3.7$ Å, $\theta = 0°$, and $\phi = 90°$. The resulting equilibrium separation R_e is in agreement with the experimentally determined effective separation R_0 of 3.791 Å. The difference is attributed to zero-point vibrational averaging. For comparison, the *ab initio* value of R_e is 3.89 Å for Ar-C_2H_4, only 0.02 Å shorter than the effective separation R_0 of 3.916 Å from the spectral analysis (*155*). This is an indication of a weaker anisotropy in the radial coordinate when the binding partner changes from Ar to Ne. The dissociation energy, D_e, is calculated to be 51.7 cm^{-1} for Ne-ethylene, less than 1/3 of the value of Ar-ethylene, 174 cm^{-1} (*155*). The obtained dissociation energy is comparable to similar systems such as Ne-acetylene (52.3 cm^{-1}) (*196*), Ne-HCN (57 cm^{-1}) (*197*) and Ne-N_2 (44 cm^{-1}) (*198*).

One dimensional potential energy curves describing the two possible tunneling motions were first constructed by fixing R at the equilibrium value of 3.7 Å, as described in ref. *155*. The resulting curves are plotted in figure 4-8. The two-fold barrier to the out-of-plane motion was determined to be 31 cm^{-1}. It was determined to be 56 cm^{-1} for Ar-C_2H_4 (*155*). At the equilibrium bond distance, the potential is mainly repulsive along the ϕ coordinator. A four-fold barrier of 369 cm^{-1} was determined for the in-plane-motion, more than an order of magnitude higher than the barrier to the out-of-plane motion. The repulsive energies are a clear indication that the in-plane rotation requires large radial movements in order to overcome the steric hindrance resulting from the hydrogens.

Minimum energy paths were then constructed to examine the movement along the radial coordinate involved with the two motions. They were constructed by allowing R to vary at each fixed θ, ϕ combination in order to locate the lowest energy (figure 4-9). The resulting barrier heights are similar for the two motions, about 25 cm^{-1}. When the radial coordinate is examined, it is apparent that the in-plane rotation requires a much larger amount of radial movement. To follow the minimum energy path, R changes from 3.7 to 4.5 Å in the in-plane motion, and from 3.7 to 4.0 Å in the out-of-plane motion. This confirms that the out-of-plane motion is the kinetically preferred motion.

It is doubtful that the small basis set 1 is sufficient to recover the dispersion energy of this weakly bound system accurately. The basis set effect was examined by using the larger basis set 2 to reconstruct the potential energy surface. The overall topology of the potential energy surface obtained with basis set 2 is very similar to the previous one. The global minimum was located at a shorter bond distance of 3.6 Å, and the depth of the well is lowered to 80.4 cm^{-1}. Potential energy paths were extracted from the potential energy surface. When fixing R at the equilibrium value of 3.6 Å, barrier heights of 37 cm^{-1} and 509 cm^{-1} were determined for the out-of-plane and in-plane motions, respectively. When the minimum energy paths were constructed, the resulting barrier heights and R ranges are 33.5 cm^{-1} and 3.6-3.8 Å for the out-of-plane motion, and

41.6 cm^{-1} and 3.6-4.4 Å for the in-plane motion. The barrier to the in-plane internal rotation is slightly higher than that of the out-of-plane motion. The R variation associated with the out-of-plane motion is again much smaller than that associated with the in-plane motion.

Clearly, the theoretical results also support that the out-of-plane motion is the tunneling motion occurring in the Ne-ethylene system, in good agreement with the experimental results. In addition, these results suggest that the out-of-plane motion is the preferred tunneling motion mainly because it involves a smaller amount of radial movement.

The *ab initio* barrier height for the out-of-plane internal rotation motion can be compared to the fitted values using the flexible model (see **4.3.3**). The case where the van der Waals stretching and bending modes are assumed to be separated is first considered. For Ar-C_2H_4, a barrier of 56 cm^{-1} was obtained from *ab initio* calculations using a relatively small basis set (*155*), which only accounts for 74% of the value of 76 cm^{-1} determined from the fitting procedure. This suggests that the small basis set tends to underestimate the barrier. In the case of Ne-C_2H_4, the basis set 1 is comparable to the one used for Ar-C_2H_4 (*155*). Therefore, the obtained *ab initio* barrier of 31 cm^{-1} is expected to be underestimated. This is consistent with the result from the fitting procedure, where a minimum barrier height of 30.7 cm^{-1} was determined. This is further supported by the increased barrier height of 37 cm^{-1} when the larger basis set 2 is used.

The *ab initio* points were fitted to a $\cos(n\theta)$ series, including even terms up to n=4 (*155*):

$$V = V_0 + V_2 \cos(2\theta) + V_4 \cos(4\theta).$$

The resulting parametrized potential was used to obtain the energy difference between the m=0 and m=1 states, again using the flexible model fitting procedure (*195*). The obtained energy difference ΔE is 0.82 cm^{-1} using basis set 1 and 0.61 cm^{-1} using basis set 2. These values are in agreement with the maximum energy difference $\Delta E_{\max}$ of 0.84 cm^{-1} obtained from the analysis of the rotational spectrum.

However, the *ab initio* calculations show that the variation in the radial coordinate may not be neglected, indicating that the van der Waals stretching and bending modes can not be treated as uncoupled. Even for the out-of-plane internal rotation, the intermolecular separation R has to change from 3.7 Å to 4.0 Å using basis set 1 and from 3.6 Å to 3.8 Å using basis set 2 to follow the minimum energy path. In order to examine the effect of the coupling between the van der Waals stretching and bending modes on the energy difference of the two lowest tunneling states, a fitting procedure was performed with the R constraint removed. The intermolecular separation R is allowed to vary as a function of θ. Using the *ab initio* minimum energy path, the energy difference ΔE was determined to be 0.47 cm^{-1} using basis set 1 and 0.50 cm^{-1} using basis set 2. These values are again in agreement with the conclusion from the experimental observations that the K_a=0, m=1 state is lower in energy compared to the K_a=1, m=0 state.

4.5 SUMMARY

Rotational spectra of various isotopomers of the Ar-C_2H_4 and Ne-C_2H_4 van der Waals complexes were recorded. The observed spectra are in accord with planer, T-shaped structures for the Rg-ethylene dimers, in agreement with the determination from the infrared spectrum of Ar-ethylene (*155*). Each transition was observed as a doublet as a result of an internal tunneling motion of the ethylene monomer. Relative intensity patterns agree with spin statistical weights from molecular symmetry group analyses assuming the out-of-plane internal rotation motion. The observation of K_a=1, m=0 transitions of Ne-trans-D_2-ethylene further supports that the out-of-plane motion is responsible for the tunneling splitting. A Coriolis interaction between the lower K_a=1, m=0 and K_a=0, m=1 states is evident in the spectra of Ne-trans-D_2-ethylene. It is inferred that the K_a=1, m=0 state lies slightly above the K_a=0, m=1 state. This provides an upper bound for the energy difference between the two tunneling states. This information was used to obtain the lower limit of the barrier height for the out-of-plane motion. *Ab initio* potential energy surfaces were obtained at the MP4 level of theory. The theoretical results also support that the out-of-plane motion is the tunneling motion that occurs in the Ne-C_2H_4 system. Furthermore, the *ab initio* calculations suggest that the out-of-plane rotation is the preferred tunneling motion mainly because the radial movement associated with this motion is much smaller than that associated with the in-plane internal rotation motion. The energy difference between the m=0 and m=1 states was obtained using the *ab initio* one dimensional potential energy curve for the out–of-plane motion. The resulting values show that the K_a=0, m=1 state is lower in energy compared to the K_a=1, m=0 state, in agreement with the observed rotational spectrum.

Table 4-1: Measured transition frequencies (in MHz) of Ar-ethylene isotopomers (m=0).

$J'_{K'_aK'_c}$-$J''_{K''_aK''_c}$	ν_{obs}	$\Delta\nu^a$	ν_{obs}	$\Delta\nu$	ν_{obs}	$\Delta\nu$
	Ar-C_2H_4		Ar-C_2D_4		Ar-$^{13}C_2H_4$	
1_{01}-0_{00}	3828.3480	1.6			3683.2439	-2.4
2_{02}-1_{01}	7655.6566	-0.4	7029.3339	-1.2	7365.5068	-1.2
2_{11}-1_{10}	7786.3736	0.7	7172.4351	-14.8	7492.5158	1.5
2_{12}-1_{11}	7523.1257	-1.6	6886.1755	11.5	7236.9232	-1.0
3_{03}-2_{02}	11480.8957	-1.4	10541.0230	0.8	11045.8001	-1.1
3_{12}-2_{11}	11677.7502	-0.5	10757.0550	7.3	11237.0914	-0.4
3_{13}-2_{12}	11283.0627	0.4	10327.7790	-6.1	10853.8734	0.9
4_{04}-3_{03}	15303.0352	0.8	14049.1350	-2.6	14723.1461	1.4
4_{13}-3_{12}	15566.9577	0.2	14339.7002	9.0	14979.6532	0.3
4_{14}-3_{13}	15041.0467	1.6	13767.6540	-3.8	14469.0080	1.5
5_{05}-4_{04}	19121.0406	0.1	17552.5041	2.1	18396.5612	0.5
5_{14}-4_{13}	19453.2684	-0.9	17919.7176	-5.6	18719.5238	-0.6
5_{15}-4_{14}	18796.4276	-0.1	17205.2090	2.1	18081.7236	-1.3
	Ar-cis-D_2-ethylene (D-atom-bonded)		Ar-trans-D_2-ethylene			
1_{01}-0_{00}	3772.9588	15.0				
2_{02}-1_{01}	7544.6961	-5.6	7324.5271	4.0		
2_{11}-1_{10}	7687.1434	9.5				
2_{12}-1_{11}	7401.4384	-4.5				
3_{03}-2_{02}	11314.0831	-6.5	10984.0672	-1.8		
3_{12}-2_{11}	11528.8737	-5.9				
3_{13}-2_{12}	11100.5206	1.4				
4_{04}-3_{03}	15079.9226	-3.6	14640.3544	-2.2		
4_{13}-3_{12}	15368.4391	1.1				
4_{14}-3_{13}	14797.6326	7.8				
5_{05}-4_{04}	18841.0422	6.0	18292.3009	1.3		
5_{14}-4_{13}	19205.0761	-1.1				
5_{15}-4_{14}	18492.1036	-5.4				

[a] $\Delta\nu = \nu_{obs} - \nu_{calc}$ in kHz.

Table 4-2: Measured transition frequencies (in MHz) of Ar-ethylene isotopomers (m=1).

$J'_{K'_aK'_c}$-$J''_{K''_aK''_c}$	Ar-C_2H_4		Ar-C_2D_4		Ar-$^{13}C_2H_4$		Ar-trans-D_2-ethylene	
	ν_{obs}	$\Delta\nu^a$	ν_{obs}	$\Delta\nu$	ν_{obs}	$\Delta\nu$	ν_{obs}	$\Delta\nu$
1_{01}-0_{00}	3817.2018	2.8			3673.3252	0.3		
2_{02}-1_{01}	7633.4734	-2.0	7024.9629	-0.6	7345.7658	-1.6	7309.4841	-1.0
2_{11}-1_{10}	7750.3453	-1.0	7165.6133	-3.4	7460.4158	2.2		
2_{12}-1_{11}	7515.0978	0.2	6884.1861	10.5	7229.8204	1.4		
3_{03}-2_{02}	11447.9061	-1.2	10534.5521	-2.2	11016.4441	-1.4	10961.6412	0.3
3_{12}-2_{11}	11623.8401	-0.1	10746.8483	-8.6	11189.0509	-1.4		
3_{13}-2_{12}	11271.0980	-0.3	10324.8215	-5.4	10843.2858	-1.1		
4_{04}-3_{03}	15259.5761	1.3	14040.6816	1.9	14684.4812	0.8	14610.6941	0.8
4_{13}-3_{12}	15495.3202	1.7	14326.2304	16.3	14915.8111	0.7		
4_{14}-3_{13}	15025.2431	0.5	13763.7522	-4.3	14455.0265	1.2		
5_{05}-4_{04}	19067.5593	-0.1	17542.1909	0.0	18348.9930	0.8	18255.6090	-0.4
5_{14}-4_{13}	18776.9131	-0.3	17903.0443	-6.5	18640.0567	-0.6		
5_{15}-4_{14}	19364.1089	-0.9	17200.4012	2.5	18064.4619	-0.9		

$^a\Delta\nu = \nu_{obs} - \nu_{calc}$ in kHz.

Table 4-3: Derived spectroscopic constants for Ar-ethylene isotopomers.[a]

m=0	Ar-C_2H_4	Ar-C_2D_4	Ar-$^{13}C_2H_4$	Ar-cis-D_2-ethylene[b]	Ar-trans-D_2-ethylene[c]
Rotational constants (in MHz):					
A (fixed)	29900	21800	28400	25200	
B	1980.0561(4)	1829.261(3)	1905.5863(4)	1957.962(2)	
C	1848.3856(4)	1686.074(3)	1777.7473(4)	1815.070(2)	
$(B+C)/2$	1914.2209(4)	1757.668(3)	1841.6668(4)	1886.516(2)	1831.4928(7)
Quartic centrifugal distortion constants (in kHz):					
Δ_J	23.809(3)	17.75(2)	21.809(4)	22.05(2)	45.26(2)
Δ_{JK}	342.8(1)	198.7(8)	312.5(1)	267.5(7)	
δ_J	1.491(4)	1.36(3)	1.374(5)	1.45(3)	
Standard deviation of the fit (in kHz):					
σ	1.2	9.2	1.6	8.6	3.6
Effective separation (in Å):					
R_0	3.916	3.896	3.913	3.907	3.905

m=1	Ar-C_2H_4	Ar-C_2D_4	Ar-$^{13}C_2H_4$		Ar-trans-D_2-ethylene[c]
Rotational constants (in MHz):					
A (fixed)	29900	21800	28400		
B	1967.4752(5)	1826.942(3)	1894.3701(4)		
C	1849.8160(5)	1686.187(3)	1779.0395(4)		
$(B+C)/2$	1908.6456(5)	1756.564(3)	1836.7048(4)		1827.7158(2)
Quartic centrifugal distortion constants (in kHz):					
Δ_J	23.048(4)	17.33(2)	21.183(4)		43.097(5)
Δ_{JK}	280.7(1)	202.1(8)	256.3(1)		
δ_J	1.085(5)	1.07(3)	1.043(5)		
Standard deviation of the fit (in kHz):					
σ	1.6	9.0	1.5		1.0
Effective separation (in Å):					
R_0	3.922	3.898	3.919		3.909

[a] Watson's *A*-reduction Hamiltonian in its I^r representation was used (*190*).

[b] For the D-atom-bonded isomer only.

[c] Only K_a=0 transitions fitted.

Table 4-4: Measured transition frequencies (in MHz) of Ne-ethylene isotopomers (*m*=0).

$J'_{K'_aK'_c}$- $J''_{K''_aK''_c}$	^{20}Ne-C_2H_4		^{20}Ne-C_2D_4		^{20}Ne-cis-D_2-ethylene (D-atom-bonded)		^{20}Ne-trans-D_2-ethylene	
	ν_{obs}	$\Delta\nu^a$	ν_{obs}	$\Delta\nu$	ν_{obs}	$\Delta\nu$	ν_{obs}	$\Delta\nu$
1_{01}-0_{00}	5637.3926	3.5	5321.3814	22.7	5583.5392	2.9	5486.7120	-4.2
2_{02}-1_{01}	11267.4144	0.8	10634.2483	-8.0	11157.7648	-2.9	10965.6413	4.2
2_{11}-1_{10}	11591.6624	-2.1	10994.5672	-7.5	11502.4071	-0.1	11302.3527	-0.1
2_{12}-1_{11}	10884.1223	-2.1	10254.3998	-7.2	10775.6159	0.0	10362.9639	0.0
3_{03}-2_{02}	16882.6984	-3.3	15930.2500	-7.1	16713.1987	1.2	16429.0188	-1.7
3_{12}-2_{11}	17373.1656	2.4	16479.2050	8.4	17237.4953	0.1	16940.3245	-0.1
3_{13}-2_{12}	16315.5555	2.4	15371.2340	8.5	16146.0731	0.0	15583.9825	0.0
4_{04}-3_{03}	22475.8704	1.3	21201.0018	3.7	22239.9748	-0.2	21869.0618	0.3
4_{13}-3_{12}	23137.3470	-0.7	21948.4992	-2.5	22952.4742	0.0	22562.4041	0.1
4_{14}-3_{13}	21734.1092	-0.8	20475.6618	-2.8	21495.6952	0.0		
	^{22}Ne-C_2H_4		^{22}Ne-C_2D_4		^{22}Ne-cis-D_2-ethylene (D-atom-bonded)		^{22}Ne-trans-D_2-ethylene	
1_{01}-0_{00}	5361.3046	1.0	5054.2296	-7.7	5309.0446	-2.8	5213.7817	-3.0
2_{02}-1_{01}	10716.1688	0.2	10101.3814	11.6	10610.0061	0.7	10420.8970	2.9
2_{11}-1_{10}	11010.7624	-0.6	10425.8876	-1.9	10921.2543	1.1	10725.1480	0.1
2_{12}-1_{11}	10377.1309	-0.6	9759.7941	-2.1	10267.1465	1.0	9859.6013	0.0
3_{03}-2_{02}	16058.1480	-0.9	15134.2881	-7.8	15894.6210	1.2	15614.7092	-1.2
3_{12}-2_{11}	16503.3982	0.6	15627.8414	2.1	16367.4608	-1.2	16076.1071	-0.1
3_{13}-2_{12}	15556.1330	0.7	14630.6093	2.4	15385.0584	-1.2	14832.5201	0.0
4_{04}-3_{03}	21380.7861	0.3	20145.9300	2.0	21154.3108	-0.5	20788.5482	0.2
4_{13}-3_{12}	21980.6297	-0.2	20816.5234	-0.6	21795.9468	0.4	21413.0992	0.0
4_{14}-3_{13}	20723.5544	-0.2	19490.4570	-0.8	20483.9026	0.4		

[a] $\Delta\nu = \nu_{obs} - \nu_{calc}$ in kHz.

Table 4-5: Measured transition frequencies (in MHz) of Ne-ethylene isotopomers (m=1).

$J'_{K'_aK'_c}$-$J''_{K''_aK''_c}$	^{20}Ne-C_2H_4		^{20}Ne-C_2D_4		^{20}Ne-trans-D_2-ethylene	
	ν_{obs}	$\Delta\nu^a$	ν_{obs}	$\Delta\nu$	ν_{obs}	$\Delta\nu$
1_{01}-0_{00}	5512.6646	27.0	5247.7323	-9.9	5503.3756	2186
2_{02}-1_{01}	11021.0529	10.2	10489.8380	2.8	10973.7104	-1749
2_{11}-1_{10}	11150.9530	-18.7	10763.6770	3.6		
2_{12}-1_{11}	10853.3770	-18.6	10211.7446	3.5		
3_{03}-2_{02}	16520.8182	-31.0	15720.6022	3.9	16396.3294	437
3_{12}-2_{11}	16717.3478	21.2	16136.7816	-4.1		
3_{13}-2_{12}	16264.3442	21.4	15308.7194	-4.1		
4_{04}-3_{03}	22007.4298	11.4	20934.2908	-1.8		
4_{13}-3_{12}	22272.4706	-6.5	21499.348	1.2		
4_{14}-3_{13}	21656.0776	-6.8	20394.9795	1.3		
	^{22}Ne-C_2H_4		^{22}Ne-C_2D_4		^{22}Ne-trans-D_2-ethylene	
1_{01}-0_{00}	5254.5125	24.6	4990.9100	-4.2	5245.0491	2528
2_{02}-1_{01}	10505.0768	8.0	9976.9056	4.0	10455.5780	-2022
2_{11}-1_{10}	10625.7340	-16.3	10225.7354	0.1		
2_{12}-1_{11}	10346.4691	-16.3	9723.6906	0.1		
3_{03}-2_{02}	15747.7031	-26.7	14953.0053	-1.6	15618.2990	506
3_{12}-2_{11}	15929.9409	18.5	15330.6473	-0.1		
3_{13}-2_{12}	15505.6959	18.7	14577.5985	-0.1		
4_{04}-3_{03}	20978.2517	9.9	19914.2234	0.2		
4_{13}-3_{12}	21223.4740	-5.7	20425.8856	0.0		
4_{14}-3_{13}	20647.7776	-5.9	19421.9610	0.0		

[a] $\Delta\nu = \nu_{obs} - \nu_{calc}$ in kHz.

Table 4-6: Derived spectroscopic constants of Ne-ethylene isotopomers (m=0).[a]

	^{20}Ne-C_2H_4	^{20}Ne-C_2D_4	^{20}Ne-cis-D_2-ethylene[b]	^{20}Ne-trans-D_2-ethylene	^{22}Ne-C_2H_4	^{22}Ne-C_2D_4	^{22}Ne-cis-D_2-ethylene[b]	^{22}Ne-trans-D_2-ethylene
Rotational constants (in MHz):								
A(fixed)	28200	20900	24000	24000	28200	20900	24000	24000
B	2996.377(1)	2846.250(1)	2973.645(1)	2985.504(1)	2839.773(1)	2694.110(1)	2818.237(1)	2830.849(1)
C	2641.620(1)	2475.578(1)	2610.659(1)	2501.135(1)	2522.109(1)	2360.555(1)	2491.528(1)	2382.879(1)
Quartic centrifugal distortion constants (in MHz):								
Δ_J	0.15170(4)	0.11728(4)	0.19156(4)	-0.02322(5)	0.14454(4)	0.10672(4)	0.17912(4)	-0.07800(5)
Δ_{JK}	8.1762(3)	3.7264(3)	5.5771(3)	37.7588(5)	6.2196(3)	3.1645(3)	4.6587(3)	36.6124(5)
δ_J	0.03095(5)	0.01830(5)	-0.01383(5)	0.46808(7)	0.02658(5)	0.01603(5)	-0.01088(5)	0.48422(7)
Sextic centrifugal distortion constants (in kHz):								
Φ_J	-0.069(1)	-0.019(1)	-0.170(1)	-1.913(2)	-0.064(1)	-0.039(1)	-0.154(1)	-1.880(2)
Φ_{JK}	-16.40(1)	-15.71(1)	-35.08(1)	314.71(3)	-9.41(1)	-12.65(1)	-29.15(1)	349.50(3)
ϕ_J	0.016(2)	-0.013(2)	-0.161(2)	1.462(3)	0.011(2)	0.023(2)	-0.16(2)	1.431(3)
Standard deviation of the fit (in kHz):								
σ	2.2	9.5	1.4	2.1	0.6	5.3	1.2	1.4
Effective separation (in Å):								
R_0	3.791	3.742	3.787	3.755	3.790	3.740	3.785	3.753

[a] Watson's A-reduction Hamiltonian in its I^r representation used.

[b] For the D-atom-bonded isomer only.

Table 4-7: Derived spectroscopic constants of Ne-ethylene isotopomers (m=1).[a]

	^{20}Ne-C_2H_4	^{20}Ne-C_2D_4	^{20}Ne-trans-D_2-ethylene[a]	^{22}Ne-C_2H_4	^{22}Ne-C_2D_4	^{22}Ne-trans-D_2-ethylene[b]
Rotational constants (in MHz):						
A(fixed)	28200	20900		28200	20900	
B	2830.125(1)	2762.042(1)		2696.627(1)	2621.161(1)	
C	2683.108(1)	2486.120(1)		2558.415(1)	2370.145(1)	
$(B+C)/2$	2756.616(1)	2624.081(1)	2752.8378(4)	2627.521(1)	2495.653(1)	2623.5476(4)
Quartic centrifugal distortion constants (in MHz):						
Δ_J	0.14850(4)	0.10488(4)	1.12162(2)	0.13841(4)	0.09797(4)	1.14345(2)
Δ_{JK}	4.4760(3)	1.2441(3)		4.5317(3)	1.1334(3)	
δ_J	-0.05535(5)	-0.00134(5)		-0.04429(5)	-0.00028(5)	
Sextic centrifugal distortion constants (in kHz):						
Φ_J	-0.099(1)	-0.031(1)		-0.081(1)	-0.035(1)	
Φ_{JK}	-50.14(1)	-8.68(1)		-43.55(1)	-7.00(1)	
ϕ_J	-0.02(15)	0.010(2)		0.014(2)	-0.015(2)	
Standard deviation of the fit (in kHz):						
σ	19.0	4.3	1636	16.7	1.9	1892
Effective separation (in Å):						
R_0	3.843	3.774	3.755	3.836	3.769	3.747

[a] Watson's A-reduction Hamiltonian in its I^r representation used.

[b] Only K_a=0 transitions fitted.

Table 4-8: *Ab initio* interaction energies of Ne-ethylene with basis set 1 (in cm^{-1}).

R /Å	ϕ=90°									
	θ=0°	10°	20°	30°	40°	50°	60°	70°	80°	90°
3.5	-42.9	-42.1	-39.4	-34.6	-27.9	-20.2	-12.6	-6.3	-2.2	-0.8
3.6	-49.9	-48.9	-46.0	-41.3	-35.2	-28.7	-22.6	-17.7	-14.5	-13.4
3.7	-51.7	-50.7	-47.9	-43.5	-38.2	-32.8	-27.8	-24.1	-21.6	-20.8
3.8	-50.5	-49.5	-46.9	-43.0	-38.4	-34.0	-30.1	-27.1	-25.3	-24.7
3.9	-47.5	-46.7	-44.3	-40.9	37.1	-33.4	-30.4	-28.1	-26.8	-26.3
4.0	-43.8	-43.0	-40.9	-38.0	-34.8	-31.9	-29.5	-27.7	-26.7	-26.4
	θ=5°	15°	25°	35°	45°	55°	65°	75°	85°	
3.5	-42.7	-41.0	-37.3	-31.5	-24.1	-16.3	-9.3	-4.0	-1.2	
3.6	-49.6	-47.7	-43.8	-38.4	-32.0	-25.5	-20.0	-15.8	-13.7	
3.7	-51.5	-49.5	-45.8	-40.9	-35.4	-30.2	-25.8	-22.6	-21.0	
3.8	-50.2	-48.4	-45.0	-40.7	-36.2	-31.9	-28.5	-26.1	-24.9	
3.9	-47.3	-45.7	-42.7	-39.0	-35.2	-31.8	-29.0	-27.3	-26.4	
4.0	-43.6	-42.1	-37.5	-36.4	-33.3	-30.6	-28.5	-27.1	-26.4	

R /Å	θ=0°									
	ϕ=0°	10°	20°	30°	40°	50°	60°	70°	80°	90°
3.65	149.4	198.1	312.6	407.1	397.1	280.0	132.0	21.6	-35.1	-51.3
3.7	105.1	145.1	239.0	316.9	309.7	215.3	95.5	6.5	-38.9	-51.7
3.75	69.9	102.6	179.6	243.8	238.8	162.7	66.1	-5.3	-41.3	-51.4
3.8	42.2	68.9	136.8	184.7	181.3	120.3	42.8	-14.2	-42.6	-50.5
3.85	20.6	42.4	93.8	137.0	135.0	86.2	24.3	-22.8	-43.1	-49.2
3.9	3.9	21.6	63.4	98.9	97.8	59.0	9.8	-25.8	-42.9	-47.5
4	-18.3	-6.8	20.8	44.4	44.5	-20.5	-10.1	-31.5		
4.1	-30.3	-22.8	-4.9	10.8	11.5	-3.0	-21.2	-33.5		
4.2	-35.8	-31.0	-19.4	-9.2	-8.3	-16.6	-26.7	-33.2		
4.3	-33.2	-34.2	-27.0	-20.4	-19.3	-23.7	-29.0	-31.6		
4.4		-34.6	-30.1	-25.9	-24.8	-26.8	-29.0	-29.4		
4.5			-30.5	-27.9	-27.0	-27.5	27.7			
4.6			-29.4	-27.8	-27.0	-26.6	-25.8			
4.7				-26.6	-25.8	-25.0				
4.8				-23.6	-24.1					
4.9					-22.0					

Table 4-9: *Ab initio* interaction energies of Ne-ethylene with basis set 2 (in cm^{-1}).

R /Å	ϕ=90°									
	θ=0°	10°	20°	30°	40°	50°	60°	70°	80°	90°
3.5	-79.8	-78.8	-75.6	-70.4	-63.3	-55.5	-48.1	-41.8	-37.7	-36.3
3.6	-80.4	-79.3	-76.2	-71.3	-65.2	-58.8	-52.8	-48.0	-44.9	-43.8
3.7	-77.1	-76.1	-73.2	-68.8	-63.6	-58.4	-53.7	-50.0	-47.6	-46.8
3.8	-71.7	-70.8	-68.2	-64.4	-60.0	-55.8	-52.1	-49.3	-47.5	-46.9
3.9	-65.3	-64.5	-62.2	-59.0	-55.4	-52.0	-49.1	-46.9	-45.6	-45.1
4.0	-58.7	-58.0	-56.0	-53.3	-50.3	-47.6	-45.4	-43.8	-42.7	-42.4
4.1	-52.3	-51.7	-50.0	-47.7	-45.3	-43.1	-41.4	-40.1	-39.4	-39.1
4.2	-46.3	-45.8	-44.4	-42.4	-40.4	-38.7	-37.3	-36.4	-35.8	-35.6
4.3	-40.8	-40.4	-39.2	-37.6	-35.9	-34.5	-33.4	-32.7	-32.3	-32.2
4.4	-35.8	-35.5	-34.5	-33.2	-31.8	-30.7	-29.8	-29.2	-28.9	-28.9
4.5	-31.5	-31.2	-30.4	-29.3	-28.1	-27.2	-26.5	-26.1	-25.8	-25.8

R /Å	θ=0°									
	ϕ=0°	10°	20°	30°	40°	50°	60°	70°	80°	90°
3.5	265.7	348.3	543.4	706.5	690.3	488.0	233.0	44.5	-52.3	-79.8
3.6	128.9	185.1	317.3	428.5	420.4	288.8	122.1	-0.6	-62.9	-80.4
3.7	43.6	81.5	170.7	246.4	243.3	158.6	50.0	-27.2	-66.3	-77.1
3.8	-7.8	17.7	77.6	128.9	128.8	75.2	7.3	-41.6	-65.3	-71.7
3.9	-36.9	-19.9	20.2	54.8	56.1	23.2	-18.8	-48.2	-61.8	-65.3
4.0	-51.9	-40.5	-13.9	9.3	11.4	-8.2	-33.1	-50.0	-57.1	-58.7
4.1	-57.9	-50.4	-32.9	-17.3	-15.0	-26.0	-40.1	-48.8	-51.8	-52.3
4.2	-58.5	-53.6	-42.1	-31.7	-29.5	-35.1	-42.3	-46.0	-46.5	-46.3
4.3	-56.0	-52.9	-45.5	-38.6	-36.5	-38.7	-41.7	-42.3	-41.4	-40.8
4.4	-51.9	-50.0	-45.2	-40.7	-38.8	-39.1	-39.5	-38.4	-36.3	-35.8
4.5	-47.0	-45.9	-43.0	-40.0	-38.3	-37.6	-36.5	-34.5	-32.4	-31.5

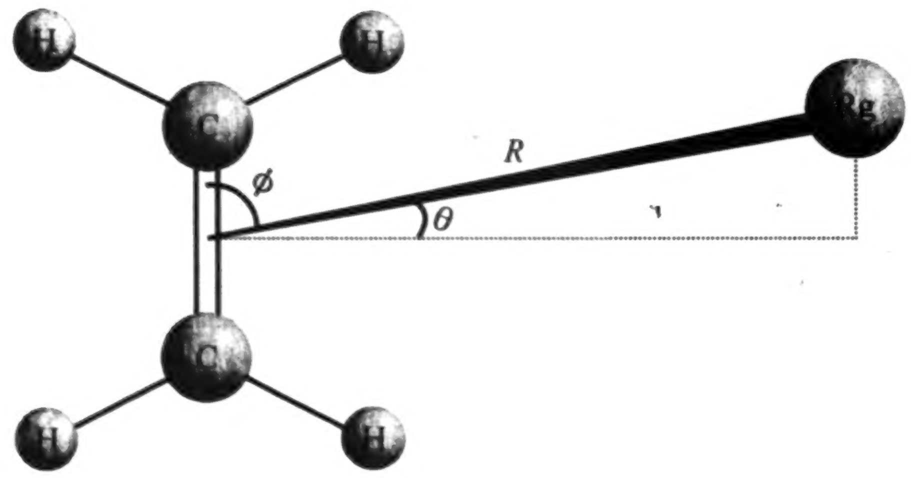

Figure 4-1: $(R\ \theta\ \phi)$ coordinates used to describe the geometry of Rg-C_2H_4. R is the distance between the Rg atom and the center-of-mass of the ethylene subunit. θ is the out-of-plane angle between the R vector and the ethylene molecular plane. ϕ is the angle between the R vector and the C=C bond. The global minimum was determined to be at R=3.89 Å, θ=10°, and ϕ=90° for Ar-C_2H_4 (*155*).

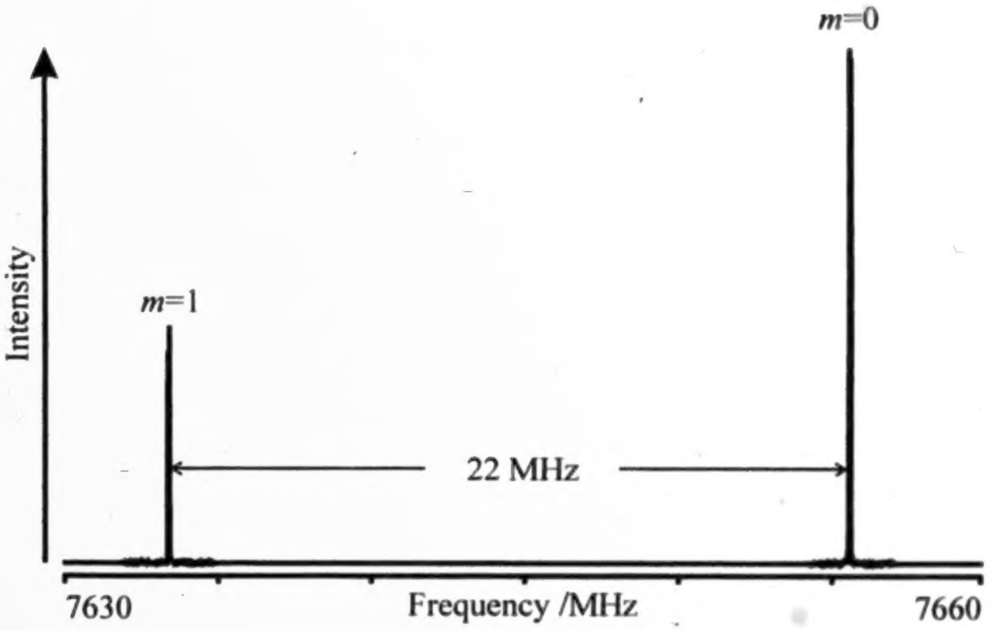

Figure 4-2: Observed transition doubling of the $J_{K_aK_c}=2_{02}-1_{01}$ transition of the Ar-C_2H_4 isotopomer. The spectrum is a composite spectrum obtained from two individual measurements, each taken with 20 nsec sampling interval and 20 averaging cycles. *m* is the internal rotation quantum number. Only the two lowest tunneling states, namely the *m*=0 and *m*=1 states, are populated in the molecular beam. A tunneling splitting of 22 MHz was observed. The *m*=0 transition is approximately twice as intense as the *m*=1 transition, in agreement with the spin statistical weight ratio of 7/3.

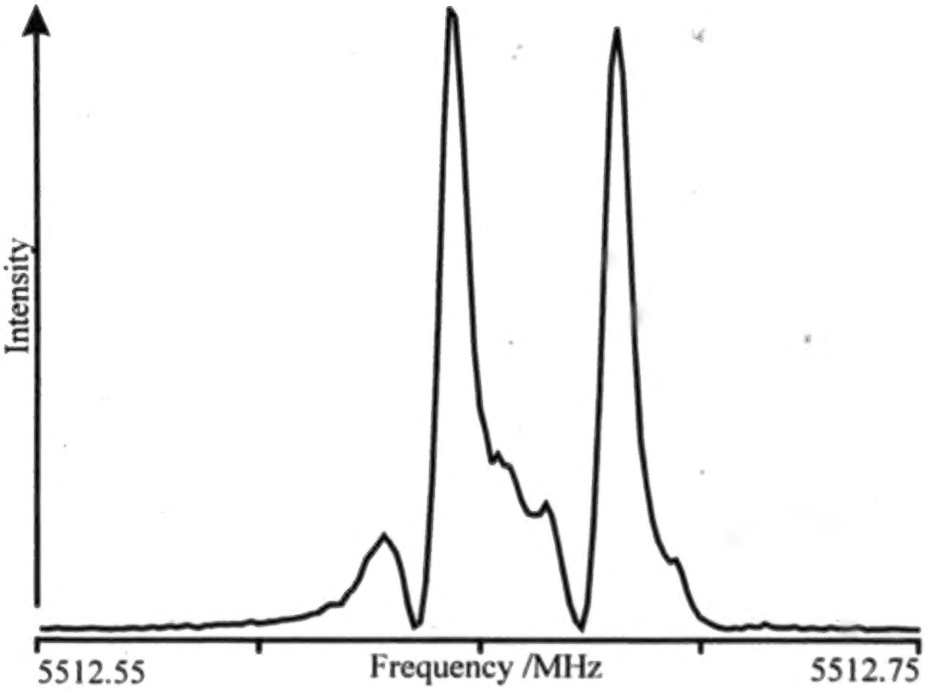

Figure 4-3: A representative spectrum of the $J_{K_aK_c}=1_{01}$-0_{00}, m=1 transition of ^{20}Ne-C_2H_4, recorded with 120 nsec sampling interval and 4000 averaging cycles. Hyperfine structure caused by the nuclear spin-spin and spin-rotation interactions was observed. Individual hyperfine components were tentatively assigned, but the fitting result was unsatisfactory. The frequency of the strongest component was recorded as the transition frequency.

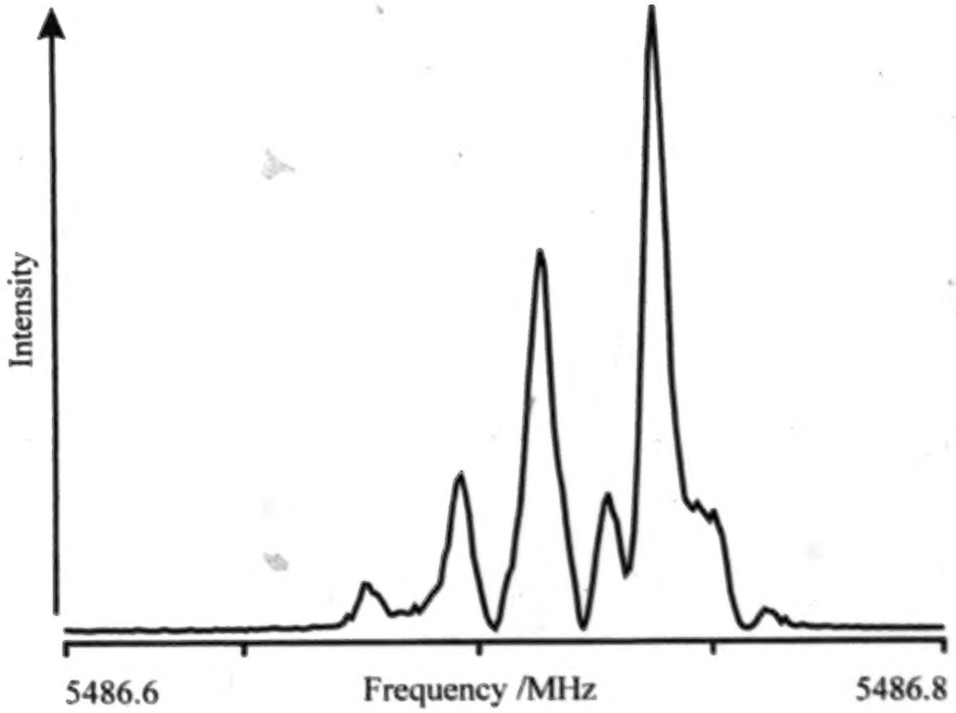

Figure 4-4: A spectrum of the $J_{K_aK_c}=1_{01}$-0_{00}, $m=0$ transition of ^{20}Ne-trans-D_2-ethylene. The spectrum was recorded with 120 nsec sampling interval and 4000 averaging cycles. The observed hyperfine structure was caused by the nuclear quadrupole interaction of the two spin $I=1$ deuterons with the overall rotation of the complex. Individual hyperfine components could not be assigned and the frequency of the strongest component was recorded as the centre frequency.

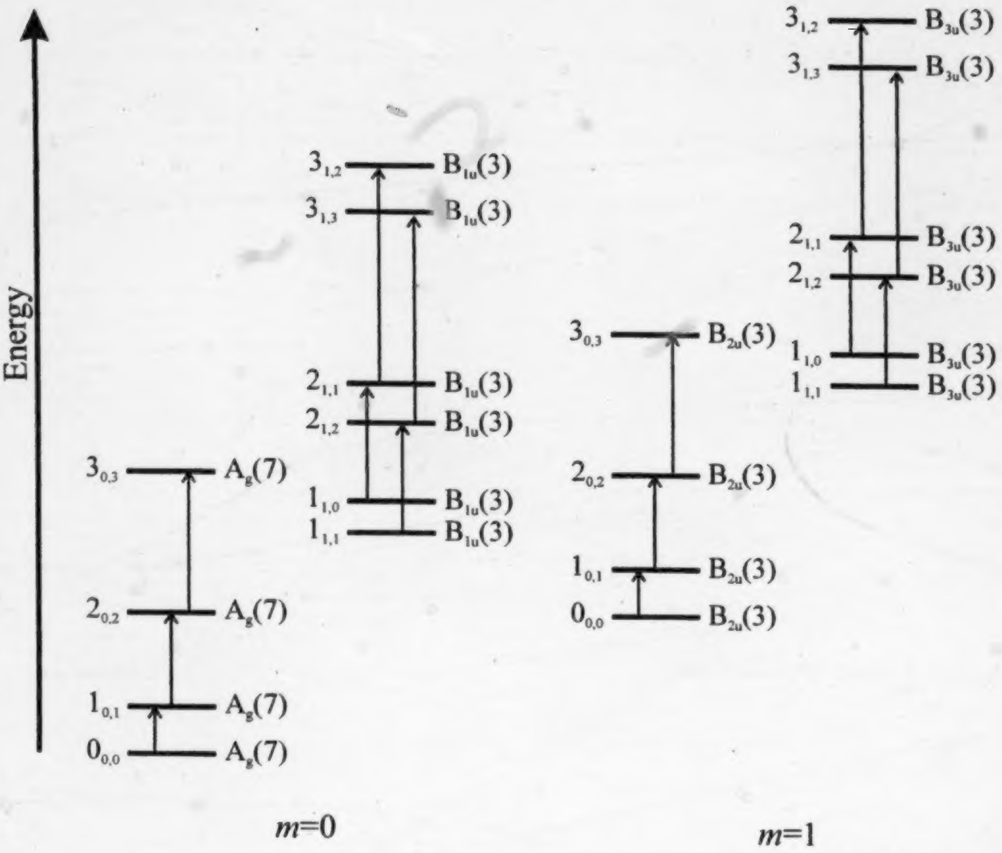
Energy
$3_{0,3}$ $A_g(7)$
$2_{0,2}$ $A_g(7)$
$1_{0,1}$ $A_g(7)$
$0_{0,0}$ $A_g(7)$
$3_{1,2}$ $B_{1u}(3)$
$3_{1,3}$ $B_{1u}(3)$
$2_{1,1}$ $B_{1u}(3)$
$2_{1,2}$ $B_{1u}(3)$
$1_{1,0}$ $B_{1u}(3)$
$1_{1,1}$ $B_{1u}(3)$
m=0
$3_{0,3}$ $B_{2u}(3)$
$2_{0,2}$ $B_{2u}(3)$
$1_{0,1}$ $B_{2u}(3)$
$0_{0,0}$ $B_{2u}(3)$
$3_{1,2}$ $B_{3u}(3)$
$3_{1,3}$ $B_{3u}(3)$
$2_{1,1}$ $B_{3u}(3)$
$2_{1,2}$ $B_{3u}(3)$
$1_{1,0}$ $B_{3u}(3)$
$1_{1,1}$ $B_{3u}(3)$
m=1

Figure 4-5: Schematic energy level diagram for Rg-C_2H_4. Each energy level is symmetry labeled with the symmetry of the respective nuclear spin wavefunctions. Each of the four observed states is associated with a nuclear spin wavefunction of a unique symmetry. As a result, all four states are metastable. Spin statistical weights obtained from molecular symmetry group analyses are given in parentheses. The analyses for the out-of-plane motion and the in-plane motion gave the same results. Arrows denote some of the measured rotational transitions.

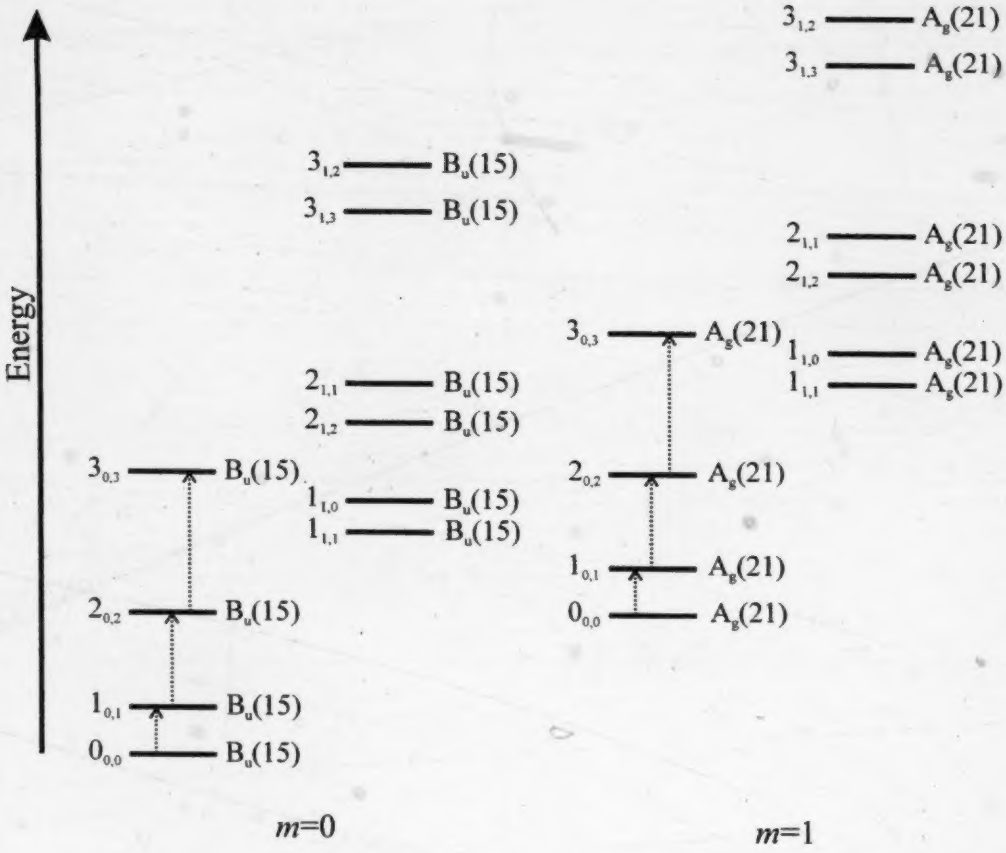
Energy
$3_{1,2}$ B$_u$(15)
$3_{1,3}$ B$_u$(15)
$2_{1,1}$ B$_u$(15)
$2_{1,2}$ B$_u$(15)
$3_{0,3}$ B$_u$(15)
$1_{1,0}$ B$_u$(15)
$1_{1,1}$ B$_u$(15)
$2_{0,2}$ B$_u$(15)
$1_{0,1}$ B$_u$(15)
$0_{0,0}$ B$_u$(15)
m=0
$3_{1,2}$ A$_g$(21)
$3_{1,3}$ A$_g$(21)
$2_{1,1}$ A$_g$(21)
$2_{1,2}$ A$_g$(21)
$3_{0,3}$ A$_g$(21)
$1_{1,0}$ A$_g$(21)
$1_{1,1}$ A$_g$(21)
$2_{0,2}$ A$_g$(21)
$1_{0,1}$ A$_g$(21)
$0_{0,0}$ A$_g$(21)
m=1

Figure 4-6: Schematic energy level diagram for Rg-trans-D_2-ethylene for the case of the in-plane motion. Spin statistical weights are given in parentheses. Only the K_a=0, m=0 and K_a=0, m=1 states are metastable, so that only transitions within these two K_a=0 states are expected, represented by dashed arrows. No transition within the K_a=1 states is expected to be observable due to low populations of these levels in the molecular beam.

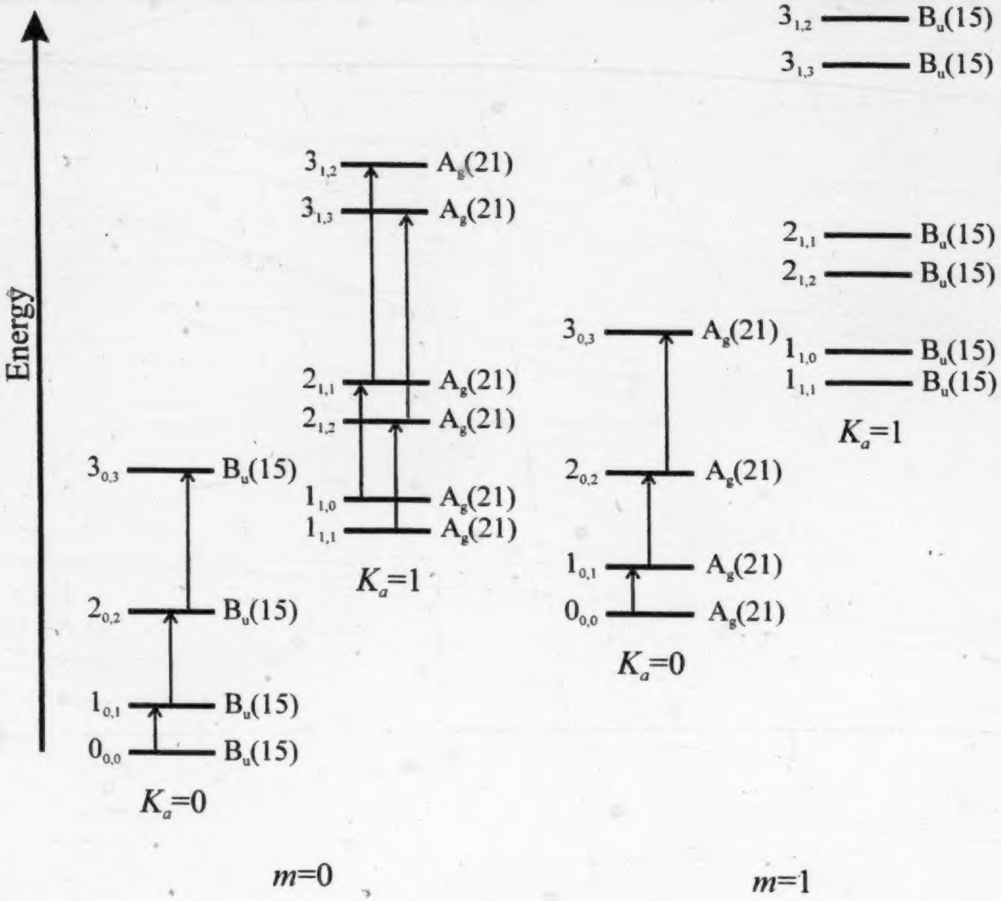

Energy
$3_{0,3}$ B$_u$(15)
$2_{0,2}$ B$_u$(15)
$1_{0,1}$ B$_u$(15)
$0_{0,0}$ B$_u$(15)
K_a=0
$3_{1,2}$ A$_g$(21)
$3_{1,3}$ A$_g$(21)
$2_{1,1}$ A$_g$(21)
$2_{1,2}$ A$_g$(21)
$1_{1,0}$ A$_g$(21)
$1_{1,1}$ A$_g$(21)
K_a=1
m=0
$3_{0,3}$ A$_g$(21)
$2_{0,2}$ A$_g$(21)
$1_{0,1}$ A$_g$(21)
$0_{0,0}$ A$_g$(21)
K_a=0
$3_{1,2}$ B$_u$(15)
$3_{1,3}$ B$_u$(15)
$2_{1,1}$ B$_u$(15)
$2_{1,2}$ B$_u$(15)
$1_{1,0}$ B$_u$(15)
$1_{1,1}$ B$_u$(15)
K_a=1
m=1

Figure 4-7: Schematic energy level diagram of Rg-trans-D_2-ethylene for the case of the out-of-plane motion. Depicted is the situation where the K_a=1, *m*=0 and K_a=0, *m*=1 states have similar energies, such that transitions within both states are expected. This is what was observed for Ne-trans-D_2-ethylene. The observed lowest *J* rotational transitions for this isotopomer are represented by arrows. The observation of the K_a=1 transitions excludes the possibility of the in-plane motion being the tunneling motion responsible for the observed transition doubling.

Figure 4-8: One dimensional *ab initio* potential energy curves for Ne-ethylene, calculated at the MP4 level, using basis set 1. R is fixed at the equilibrium value of 3.7 Å. The top trace was constructed by fixing ϕ at 90° and varying θ, which gives a barrier to the out-of-plane motion of 31 cm^{-1}. The bottom trace was constructed by fixing θ at 0° and varying ϕ, and gives a barrier to the in-plane motion of 369 cm^{-1}. The repulsive energies of such a constructed in-plane motion potential energy curve suggest that the in-plane internal rotation motion requires a significant amount of radial movement.

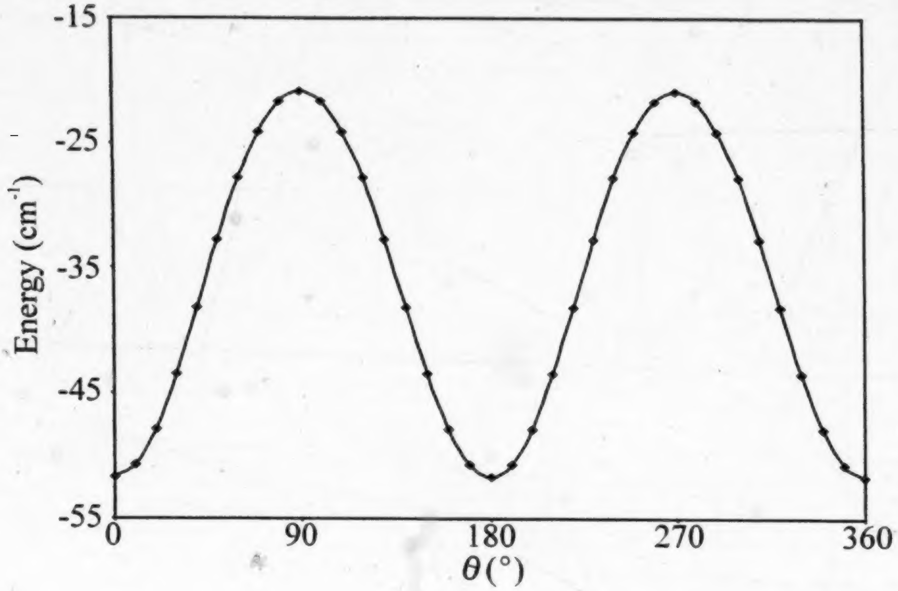
Energy (cm^{-1})
-15
-25
-35
-45
-55
0
90
180
270
360
θ(°)

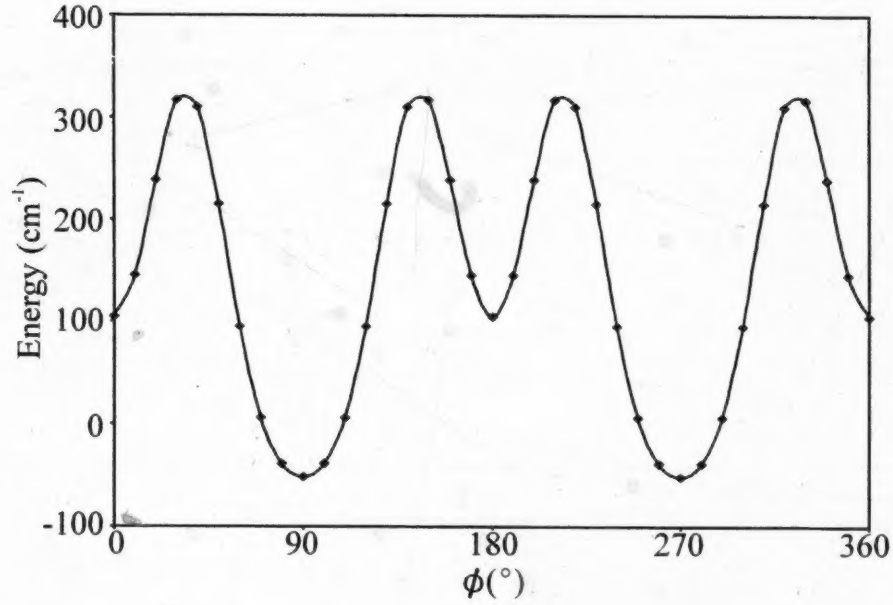
Energy (cm^{-1})
400
300
200
100
0
-100
0
90
180
270
360
ϕ(°)

Figure 4-9: Minimum energy paths for Ne-ethylene, calculated at the MP4 level and using basis set 1. *R* is allowed to vary to obtained the lowest energy at each θ, ϕ combination. The top trace is the path for the out-of-plane motion, where ϕ is fixed at 90°. The bottom trace is the path for the in-plane motion, where θ is fixed at 0°. The resulting barrier height and *R* variation are 25 cm^{-1} and 3.7-4.0 Å for the out-of-plane motion, and 25 cm^{-1} and 3.7-4.5 Å for the in-plane motion, respectively.

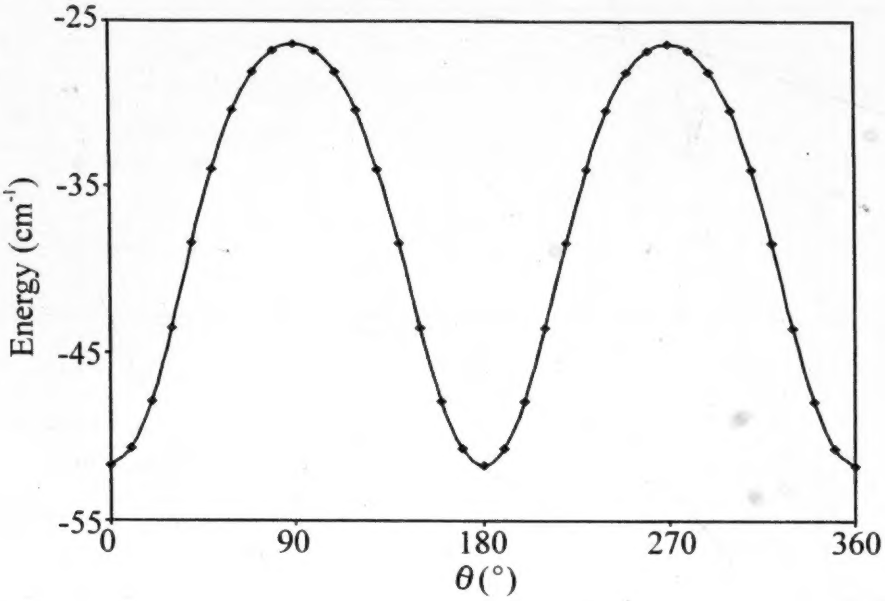

-25
-35
-45
-55
Energy (cm^{-1})
0
90
180
270
360
θ(°)

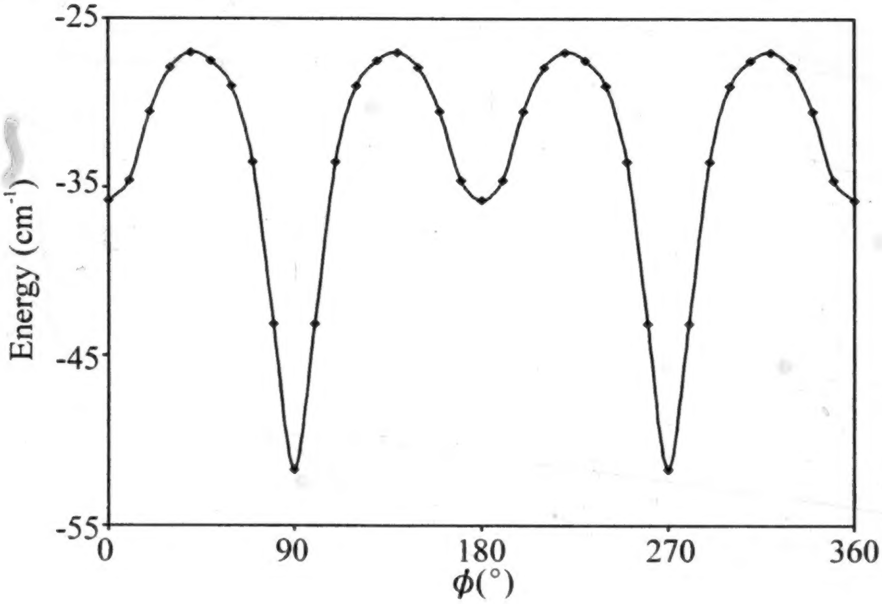

-25
-35
-45
-55
Energy (cm^{-1})
0
90
180
270
360
ϕ(°)

5

MICROWAVE AND *AB INITIO* STUDIES OF Ar-, Ne-ACETYLENE

The earliest studies of acetylene-containing van der Waals complexes seemed to suggest that acetylene does not form H-bonds, contrary to its isoelectronic cousin, HCN. The van der Waals bonds in a number dimers were found to form between the π electron cloud of acetylene and the other moiety, for example, in the HCN-acetylene (*199*) and CO_2-acetylene (*200*) dimers. Later, it was found that acetylene does form H-bonds. In the case of the NH_3-acetylene (*201*) and N_2-acetylene (*202*) dimers, NH_3 and N_2 were determined to bind to one of the hydrogen atoms of acetylene. Interestingly, in the case of HCl-acetylene, both the π-bonded and the H-bonded isomers were observed (*203*,*204*). One aspect of this study is to examine the binding properties of acetylene in complexes where the electrostatic term of the attractive force is missing and the dispersion term dominates.

The earliest studies on weakly bound systems focused on rare gas-diatomic molecule systems such as Ar-HCl (*205*,*206*). The nature of the corresponding interaction potential energy surfaces is relatively well understood. Compared to HCl, acetylene is spatially extended. Investigations of acetylene-containing systems therefore provide information about the distribution of intermolecular interactions over different parts of spatially extended species. Understanding the rules for such distribution is of relevance to extending the methods for determining the intermolecular potential energy surfaces of small molecules to larger systems.

Intermolecular interactions between acetylene and rare gas atoms have been extensively investigated using high resolution spectroscopy (*71,72,73,74,75,76,196*), scattering techniques (*207,208,209,210*), and *ab initio* methods (*196,211,212,213,214,215,216,217*). In this chapter, spectroscopic and theoretical results of the Ar-C_2H_2 and Ne-C_2H_2 van der Waals dimers are presented separately in two subsections, with more focus on the Ne-C_2H_2 system.

5.1 ISOTOPIC STUDY OF THE INTERNAL DYNAMICS OF Ar-C_2H_2[1]

5.1.1 Previous Work

The Ar-acetylene van der Waals dimer has been the subject of extensive high resolution spectroscopic and theoretical studies since the early 1980s. It was first studied by DeLeon and Muenter, using the molecular beam electric resonance technique (*71*). The $J_{K_aK_c}=1_{11}-1_{10}$ transition was measured for both Ar-HCCH and Ar-DCCD. A T-shaped structure was established based on the observed hyperfine structure and Stark effect measurements. An R value of 3.25 Å was determined. R is the distance from the Ar atom to the center-of-mass of the acetylene monomer (see figure 5-1). Based on the deuterium nuclear quadrupole coupling constant of Ar-DCCD, a θ value of 72° was determined. θ is the average angle between R and the molecular axis of the acetylene subunit (see figure 5-1). The determined θ value indicates the presence of a large amplitude zero-point angular motion. Later, this complex was studied by Endo and co-workers, using a pulsed nozzle Fourier transform microwave spectrometer (*72*). Eight *a*-type, i.e., $\Delta K_a=0$, pure rotational transitions were measured for the normal isotopomer, Ar-HCCH. The T-shaped structure was confirmed, but R was determined to be 4.04 Å, 0.8 Å larger than the previously reported value (*71*). From an analysis of the centrifugal distortion constants, an extremely low van der Waals bending frequency of ~9 cm^{-1} was estimated. Two different groups carried out infrared studies in the region of the ν_3 C-H asymmetric stretching mode (*73*) and in the region of the ν_5 bending mode (*74*), respectively. In the analyses of these infrared studies, the van der Waals bending motion was treated as a hindered internal rotation of the C_2H_2 monomer within the complex. Further high resolution infrared spectra included a combination band associated with the low frequency bending mode of both Ar-HCCH and Ar-DCCH (*75*,*76*).

---

[1] A version of this section has been published. Y. Liu and W. Jäger, J. Mol. Spectrosc. **205**, 177 (2001). Copyright © 2001 by Academic Press.

On the theoretical side, the first empirical potential energy surface for the Ar-acetylene complex was constructed by Thornley and Hutson in 1992 (*218*). Three potential energy surfaces were proposed, utilizing the microwave (*72*) and the infrared (*73*) data. It was confirmed that the hindered internal rotor model could describe the system more adequately than a rigid rotor model. Two years later, a semi-empirical potential energy surface was reported by Bemish *et al.* (*75*). *Ab initio* calculations were used together with the infrared data from the combination band (*75*) and the microwave data (*72*). However, it was later shown that all these potential energy surfaces could not reproduce the reported scattering data (*210*). An improved potential energy surface was then constructed by simultaneously fitting the scattering and the spectroscopic data (*210*).

Besides the abovementioned empirical and semi-empirical potentials, a number of *ab initio* studies also appeared in literature (*213*,*215*,*216*,*217*). An *ab initio* potential was constructed at the MP4 level with a large basis set containing bond functions by Tao *et al.* (*215*). Another potential was constructed by Yang *et al.* at the CCSD(T) level with the aug-cc-pVTZ basis set (*216*). Both potentials gave very small energy differences between the T-shaped and collinear geometries. More recently, Hasse *et al.* examined the interaction energies using symmetry adapted perturbation theory (SAPT) (*217*). The resulting potential energy surface was found to be very weakly anisotropic, in agreement with the previous *ab initio* studies (*215*,*216*). The global minimum was located at a skew T-shaped configuration with R=4.0 Å, θ=60°, and an energy of -118.2 cm^{-1}. A second minimum occurs at the linear configuration with R=4.68 Å, θ=0°, and an energy of -115.1 cm^{-1}, only 3.1 cm^{-1} above the global minimum.

In recording the rotational spectra of various isotopomers of Ar-ethylene, it is hoped that further spectroscopic evidence of the large amplitude angular motion and further information about the internal dynamics of this weakly bound system can be obtained.

5.1.2 Spectral Assignments and Analyses

The complex was generated using a gas mixture containing 0.5% HCCH and 1%

Ar. Enough Ne was used as backing gas to maintain a pressure of ~ 4-5 atm. $H^{13}C^{13}CH$ and DCCD-containing isotopomers were measured using enriched samples (99% ^{13}C and 99% D, respectively, Cambridge Isotope Laboratories). DCCH was synthesized using calcium carbide and a 1:1 H_2O/D_2O mixture. CaC_2 was added to the H_2O/D_2O mixture at liquid-nitrogen temperature. After pumping off the residual air in the reaction container, the mixture was allowed to warm up to produce a mixture of HCCH, DCCD, and DCCH. The mixture of acetylene isotopomers was kept at liquid-nitrogen temperature and was introduced into the sample system of the spectrometer without further purification by slowly warming the container from liquid-nitrogen temperature. The isotopomer containing $H^{13}C^{12}CH$ was measured in its natural abundance (~2%).

For the normal isotopomer, Ar-HCCH, the spectrum was predicted using the rotational and centrifugal distortion constants from ref. *72*. Altogether, eight additional transitions were recorded within 25 MHz of the predictions. In order to keep measurement uncertainties the same for all transitions, the eight transitions previously reported in ref. *72* were remeasured. The new measurements all agree with the previous data within their experimental uncertainties. The K_a=1 transitions were more intense than the K_a=0 transitions. This is in agreement with the spin statistical weights of 1 and 3 for the K_a=even and K_a=odd levels, respectively. The relative intensity comparison of the K_a=0 and K_a=1 transitions is shown in figure 5-2. No extra splittings due to the two spin I=½ hydrogen nuclei were observed.

Using a pseudodiatomic approach with scaled reduced masses, frequencies of the $J_{K_aK_c}=3_{03}-2_{02}$ transitions of the Ar-DCCD and Ar-$H^{13}C^{13}CH$ isotopomers were predicted to be at around 11.28 GHz. A transition was soon found for Ar-H^{13}C^{13}CH at 11294 MHz. The slightly higher than predicted frequency is consistent with the usual isotopic effect that substitution with heavier isotopes tends to shorten the van der Waals bond distance in such dimers. Using the same argument, one expects the corresponding transition frequency for Ar-DCCD to be even higher. However, this transition was located at 11261 MHz after some search. The lower than expected transition frequency indicates a larger than expected R value for this heavier isotopomer.

Fourteen and fifteen transitions were measured for Ar-DCCD and Ar-H^{13}C^{13}CH, respectively. Lines of Ar-DCCD were broadened due to the quadrupole interaction of the two spin I=1 deuterium nuclei with the overall rotation of the complex. From a nuclear spin statistical analysis of Ar-DCCD, the K_a=0 levels are associated with nuclear spin wavefunctions having total spins 0 and 2, while the K_a=1 levels are associated with total nuclear spin of 1. The $J_{K_aK_c}$=1_{01}-0_{00} transition was expected to show four hyperfine components. However, the narrow splittings were on the edge of the resolving power of the spectrometer, and the low signal-to-noise ratio achieved at 3.7 GHz further hampered the efforts to resolve the hyperfine structure. The highest point of the broadened peak was recorded as the transition frequency with an estimated accuracy of 10 kHz. For both isotopomers the observed intensity ratio between the K_a=0 and K_a=1 transitions agreed well with the spin statistical weights, 6 and 3 for Ar-DCCD, and 10 and 6 for Ar-H^{13}C^{13}CH, respectively.

For the Ar-DCCH and Ar-H^{13}C^{12}CH isotopomers, the substitution of one H with D or one ^{12}C with ^{13}C breaks the C_{2v} symmetry, so that the K_a=1 states are no longer metastable. As a result, levels in the K_a=1 state are much less populated than those in the K_a=0 state. The former is more than 1 cm^{-1} higher in energy than the latter, as estimated from the rotational constants of Ar-HCCH. Furthermore, transitions of Ar-DCCH were measured using a sample that contained a mixture of HCCH, DCCD, and DCCH, while Ar-H^{13}C^{12}CH was studied in its natural abundance of 2%. These factors further reduced the intensities of the observed transitions. Only the K_a=0 transitions could be measured. Five and four K_a=0 transitions were measured for Ar-DCCH and Ar-H^{13}C^{12}CH, respectively. Lines of Ar-DCCH were broadened by nuclear quadrupole interaction of the D nucleus, but the hyperfine components could not be resolved. A spectrum of the $J_{K_aK_c}=1_{01}-0_{00}$ transition of Ar-DCCH is shown in figure 5-3.

All observed transition frequencies of the five isotopomers are listed in table 5-1. Watson's *S*-reduction Hamiltonian in its I^r representation (*190*) was used to fit spectroscopic constants to the transition frequencies. Since only *a*-type transitions were measured, the *A* rotational constant could not be obtained. It was fixed at the value determined in ref. *73* (47550 MHz) for the normal isotopomer, and at values scaled with the *b* rotational constants of the corresponding substituted monomers for the remaining minor isotopomers. Two rotational constants, *B* and *C*, three quartic centrifugal distortion constants D_J, D_{JK}, and d_J, and three sextic centrifugal distortion constants, H_J, H_{JK}, and h_J, were determined for the symmetric isotopomers. For the asymmetric isotopomers, Ar-H^{13}C^{12}CH and Ar-DCCH, only $(B+C)/2$, D_J, and H_J were obtained from the fitting procedure. All resulting spectroscopic constants are listed in table 5-2, along with the standard deviations of the fits.

5.1.3 Results and Discussion

It is noted that the standard deviations of the fits are considerably larger than the corresponding experimental uncertainties. For example, for the three isotopomers of C_{2v} symmetry, the standard deviations are on the order of 40-60 kHz, even though several sextic centrifugal distortion constants were included in the fits. A fit without the sextic centrifugal distortion constants gave a standard deviation larger than 3 MHz for Ar-HCCH, although only transitions with J quantum numbers up to 6 were measured. This is an indication that the system is very flexible, and that the semi-rigid rotor model can not adequately describe the complex.

From the obtained rotational constants, one can in principle derive structural information about the dimer. For a planar molecule such as Ar-HCCH, only two structural parameters are needed, namely R and θ as described in figure 5-1, under the assumption that the acetylene monomer structure is unaffected by complex formation. It was pointed out by Fraser *et al.* that the C rotational constant is least affected by the large amplitude intermolecular motions such as van der Waals in-plane bending vibration (*219*). The effective separation R was thus derived from the C rotational constant using the expression $R = [\ (k/\mu)\ (1/C - 1/b)\ ]^{1/2}$. Here μ is the reduced mass of the complex in atomic mass units, b is the rotational constant of the acetylene monomer in MHz, and k is a conversion factor, 505379 MHz amu Å^2. The obtained R value is 4.046 Å (table 5-2), in agreement with the values of 4.04 Å and 4.045 Å reported in refs. *72* and *73*, respectively. R is considerably larger than the sum of the van der Waals radii for C and Ar, as noted before in ref. *72*. Assuming that the van der Waals radii for C and Ar are 1.5 Å and 1.88 Å

(*220*), respectively, this distance *R* is more than 0.6 Å larger than the sum. The difference is much smaller in other similar systems such as Ar-CO_2 (*219*), where the difference is only about 0.1 Å. This can be explained in terms of the fairly large amplitude in-plane vibrational motion of acetylene and a strong coupling between the radial and angular intermolecular coordinates. When the acetylene subunit moves away from the T-shaped structure toward the linear configuration, the distance between Ar and the center-of-mass of acetylene has to increase to reduce the developing steric hindrance. Since the ground state wavefunction samples not only the T-shaped configuration but also the linear configuration substantially, an anomalously large separation results. Evidence for the low angular anisotropy of the Ar-acetylene interaction was found in refs. *71* and *73*, where expectation values for the angle θ of 72° and 60° were derived from a D nuclear quadrupole hyperfine analysis and from the *A* rotational constant, respectively. The corresponding values for Ar-CO_2 (*221*), a relatively rigid system, are 84° and 82°. The value from a ^{14}N nuclear quadrupole hyperfine analysis for the isoelectronic Ar-HCN (*64*), a highly nonrigid system with linear equilibrium geometry, is 59°.

The obtained *R* values are 4.046 Å for Ar-DCCD and 4.041 Å for Ar-$H^{13}C^{13}CH$ (table 5-2) using $R = [\ (k/\mu)\ (1/C - 1/b)\ ]^{1/2}$. It is interesting to note that the value for Ar-DCCD is basically the same as that for Ar-HCCH. From a consideration of the isotope effect, one would expect a smaller *R* value for Ar-DCCD. A result of the D substitution is a lowering of the zero-point energy level, which in turn reduces the amplitude of the van der Waals bending motion because of the narrower potential. The complex geometry is therefore expected to stay closer to the T-shaped configuration, corresponding to a lower

R value. For the two asymmetric isotopomers, Ar-DCCH and Ar-H^{13}C^{12}CH, only the rotational constant $(B+C)/2$ is available, and *R* values were calculated using the pseudodiatomic expression $R = [\,(k/\mu)\,(2/(B+C))\,]^{1/2}$. The symmetric isotopomers were also reanalyzed with the same equation for comparison. The values thus obtained are also given in table 5-2. Also in this model, Ar-DCCD has a larger than expected *R* value.

It is instructive to treat the different *K*-stacks of Ar-HCCH as individual states to gain more insight into the causes for the anomalies observed in the spectra. For this purpose, it is more appropriate to use a free-rotor labeling of the energy levels with *J*, *j*, *K*, and *p* quantum numbers. Here, *J* is the total angular momentum quantum number, *j* is the internal rotation quantum number of the acetylene monomer, *K* is the projection of *j* onto the van der Waals bond, and *p* is the parity (*65*). In the free rotor limit, each *j* level is $(2j+1)$-fold degenerate. In the hindered rotor case, this degeneracy is lifted due to the barrier to the internal rotation of the acetylene subunit. Each *j* level is split according to the projection *K* onto the van der Waals bond. These levels can be labeled as Σ, Π, Δ, ..., corresponding to *K* values of 0, 1, 2, ... For Ar-acetylene, the K_a=0, lower K_a=1, and upper K_a=1 states in the semi-rigid rotor labeling scheme are labeled Σ_0, Π_1^e, and Π_1^f, respectively. The subscript is the *j* quantum number, and the superscript is the parity of the state, with *e* denoting $p= +(-1)^J$ and *f* denoting $p= -(-1)^J$ (*65*). The two Π_1 states are nearly degenerate. This approximate degeneracy can be lifted by a Coriolis interaction with a nearby Σ_1 state. The interaction can only occur between states with the same parity, such as the Π_1^e and Σ_1 states. The correlation between the free rotor and rigid rotor energy levels is schematically plotted in figure 5-4. The Σ_1 state, i.e., the first excited van der

Waals bending state, was not observed in this study. It was experimentally determined to be 6.22 cm^{-1} above the Σ_0 ground state for the normal isotopomer (*75*). Each of the three observed states was fitted separately to the linear rotor expression $E_{rot}=BJ(J+1)+DJ^2(J+1)^2+HJ^3(J+1)^3$ (*222*). The fitting results are listed in table 5-3.

From table 5-3, one can see that the standard deviations for the fits are now in the same order as the corresponding experimental uncertainties, and significantly lower than in the previous semi-rigid rotor fits. With closer examination, it is noted that the standard deviations for the Π_1^e state are larger than those for the Σ_0 and Π_1^f states in Ar-HCCH and Ar-H^{13}C^{13}CH. A possible reason is that the Π_1^e state is being Coriolis perturbed by the higher energy Σ_1 state. In addition, the slightly larger standard deviation from the fit of the Π_1^e state of Ar-H^{13}C^{13}CH, 3.8 kHz, as compared to that of Ar-HCCH, 1.1 kHz, may be an indication for a somewhat larger perturbation in the Ar-H^{13}C^{13}CH isotopomer. Prompted by this, the energy gap between the Π_1^e state and the Σ_1 state was examined. The bending frequency, i.e., the energy difference between the Σ_0 and the Σ_1 state, was calculated to drop by 0.23 cm^{-1} upon the substitution of ^{12}C with ^{13}C, using a harmonic force field calculation. At the same time, the Π_1^e state also moves downward relative to the Σ_0 state. This scales approximately with the *b* constant of the acetylene monomer and results in a drop of 0.06 cm^{-1}. Overall, the energy gap between the Π_1^e state and the Σ_1 state is reduced in the Ar-H^{13}C^{13}CH isotopomer. Therefore, the Coriolis interaction is more pronounced. A drop in bending frequency upon substitution with heavier isotopomers was experimentally observed. The bending frequencies for the normal and the heavier Ar-DCCH isotopomer were determined to be 6.22 cm^{-1} (*75*) and 5.47 cm^{-1} (*76*). A similar

Coriolis perturbation, though more severe, was reported for the isoelectronic Ar-HCN van der Waals dimer (*65*). It was theoretically determined that the energy difference between the Σ_1 and the Π_1 state reduces to 0.22 cm^{-1} in Ar-DCN from 0.57 cm^{-1} in Ar-HCN (*70*).

For Ar-DCCD, the standard deviations are all on the order of 6 to 26 kHz, mainly because of the unresolved deuterium nuclear quadrupole hyperfine structure. It is therefore difficult to use the standard deviations as indicators for the presence of a perturbation, as was done above for the Ar-HCCH and Ar-H^{13}C^{13}CH isotopomers. However, such Coriolis perturbation does exist in Ar-DCCD as can be found by closer inspection of the B_{eff} values in table 5-3. There is a relatively consistent increase in the values of B_{eff} for all isotopomers when going from the Σ_0 state to the unperturbed Π_1^f state. The increases are 1.9% for Ar-DCCD, 1.7% for Ar-H^{13}C^{13}CH, and 1.7% for Ar-HCCH. However, there is a much larger drop in the B_{eff} constant of Ar-DCCD when going from the Σ_0 state to the perturbed Π_1^e state than for the other two isotopomers. The values are 5.0% for Ar-DCCD, 3.8% for Ar-H^{13}C^{13}CH, and 3.9% for Ar-HCCH. This is because the energy gap between the Π_1^e state and the Σ_1 state, estimated with the same procedure as for Ar-H^{13}C^{13}CH, is the smallest for Ar-DCCD, leading to the most severe Coriolis perturbation.

5.2 ROTATIONAL SPECTRUM AND POTENTIAL ENERGY SURFACE OF Ne-C_2H_2

5.2.1 Motivation

Before now, spectroscopic studies of Rg-acetylene complexes mainly focused on

Ar-acetylene (see **5.1.1**). From the extensive spectroscopic investigations, it appears that despite the weak interaction between Ar and acetylene, the spectra of the dimer could be reasonably well described by a semi-rigid rotor type Hamiltonian for a T-shaped configuration. The weak anisotropy of the potential energy surface associated with the complex is only revealed when the spectroscopic results are carefully analyzed.

Rg-acetylene complexes have also been the subjects of a number of *ab initio* investigations. Besides the studies on Ar-acetylene (see **5.1.1**), there are also a few *ab initio* intermolecular potentials reported for the He-acetylene system. Slee *et al.* constructed a potential energy surface at the MP2 level (*212*), which failed to explain the recorded infrared spectrum (*223*). More recently, a SAPT potential energy surface for He-HCCH was constructed by Moszynski *et al.* (*214*). It shows that acetylene behaves as an essentially free internal rotor. The computed infrared spectrum based on the SAPT potential was in qualitative agreement with the experimental spectrum (*223*). However, despite the information from the computed spectrum, a definite assignment of the experimental spectrum was not achieved.

Previous investigations of the Ne-acetylene system are not as extensive as those of its Ar and He analogs. To date, there is only one combined spectroscopic and *ab initio* study reported for this complex. Miller and co-workers recorded rotationally resolved near-infrared spectra of Ne-HCCH and Ne-DCCH, in the region of the ν_3 C-H asymmetric stretching mode (*196*). These spectra appeared to be quite irregular and could not be assigned in the same way as for Ar-acetylene. A SAPT interaction potential was constructed, which displayed two nonequivalent potential minima. The global minimum was located at a skew configuration, R=3.81 Å, θ=53.1°, and a well depth of -52.310 cm^{-1} (see figure 5-1 for the definitions for R and θ). The local minimum is located at the linear configuration, R=4.36 Å, θ=0°, and a slightly higher energy of -50.542 cm^{-1}. Dynamical calculations were carried out to compute the near-infrared spectra of Ne-HCCH and Ne-DCCH, utilizing the SAPT potential. The recorded spectrum of Ne-DCCH was better resolved and could be assigned by comparing with the computed spectrum. The recorded spectrum of Ne-HCCH, on the other hand, could still not be definitely assigned, due to the fact that the Ne-HCCH transitions were broadened by a Fermi resonance between the ν_3 vibration and a combination of the C-C stretching mode with some low frequency bending vibration. It was concluded from this study that the acetylene monomer behaves as an only slightly hindered internal rotor in the Ne-acetylene complex. Furthermore, the fact that the calculated spectrum agrees so well with the experimental spectrum of Ne-DCCH illustrates the high quality of the SAPT potential.

By measuring the rotational spectrum of the Ne-acetylene complex, it is hoped that the quality of the SAPT potential could be further tested by comparing the experimentally determined transition frequencies with those obtained from the calculated energies reported in ref. *196*. Furthermore, by comparing the recorded spectrum with that of Ar-acetylene, information about the effects of a lighter and less polarizable binding partner on the features of the potential energy surfaces and the internal dynamics of van der Waals dimers may be deduced.

5.2.2 Observed Spectra and Assignments

The sample mixture consisted of 1% acetylene in Ne at a backing pressure about 5 atm. Isotopomers containing the ^{22}Ne isotope were measured in their natural abundances (~10%). Isotopomers containing H^{13}C^{13}CH and DCCD were measured using isotopically enriched samples (99% ^{13}C and 99% D, respectively, Cambridge Isotope Laboratories). DCCH was synthesized using two methods. It was first produced in the same way as described in **5.1.2**. Later, trimethylsilyl-acetylene (TMF-acetylene, 98%, $(CH_3)_3SiC{\equiv}CH$, F. W. 98.22), tetrabutylammonium fluoride (TBAF, 1.0 M solution in tetrahydrofuran, F. W. 261.47), and D_2O were used, in order to increase the yield of DCCH (*224*). Tetrahydrofuran (THF) was used as a solvent. D_2O, THF, TMF-acetylene were mixed, frozen, and degassed at liquid-nitrogen temperature. TBAF was quickly added to the frozen mixture. After resealing the reaction container and pumping off the residual gas, the mixture was allowed to warm up to produce DCCH. The same procedure as described for the first method was used to introduce DCCH into the sample system of the spectrometer. Between the two syntheses, better signal-to-noise ratio was obtained with the latter, due to a greater yield of DCCH.

Assuming a T-shaped structure similar to that of Ar-HCCH, the $J_{K_aK_c}$=2_{02}-1_{01} transition of ^{20}Ne-HCCH was predicted to be at ~11.2 GHz. The approximate separation between Ne and the center-of-mass of acetylene was estimated from comparison of the corresponding distances in the Ar-cyclopropane and Ne-cyclopropane complexes (*58*). A scan between 11.0 and 11.4 GHz located two transitions, one at 11094 MHz, the other at 11115 MHz. The one at higher frequency was approximately two to three times stronger than the other. Symmetry considerations of a T-shaped structure give total nuclear spins of I_H=0 and I_H=1 for the K_a=0 and K_a=1 states, respectively, so that K_a=1 transitions are expected to be three times as intense as K_a=0 transitions. Therefore, the transition at 11115 MHz was assigned to be the $J_{K_aK_c}$=2_{11}-1_{10} transition and the other one was assigned to be the $J_{K_aK_c}$=2_{02}-1_{01} transition. Using a pseudodiatomic approach with scaled reduced masses, the corresponding transitions of ^{22}Ne-HCCH were predicted and easily located. For the K_a=0 transition, other J transitions, ranging from J=0 to 4, were also recorded, together with the corresponding transitions of ^{22}Ne-HCCH. A normal spectral pattern was observed from this set of transitions, with all transitions approximately equally spaced. However, this was not the case for the assigned K_a=1 transition. The next higher J transition, namely the $J_{K_aK_c}$=3_{12}-2_{11} transition, was predicted to be at ~16672 MHz, approximately 1.5 times of the $J_{K_aK_c}$=2_{11}-1_{10} transition frequency. It was found to be at 16468 MHz, more than 200 MHz below the prediction. This frequency drop seemed to be too large to arise from centrifugal distortion effects. It was therefore attributed to a Coriolis interaction with the nearby first excited van der Waals bending state, analogous to the Σ_1-Π_1 interaction observed in Ar-HCCH (see **5.1.3**). Another set of K_a=1 transitions was expected to occur within the unperturbed Π_1 state. However, the search for these transitions, for example, the $J_{K_aK_c}$=2_{12}-1_{11} transition, revealed no additional transition. At the same time, an additional transition was measured at 5707 MHz, approximately 150 MHz above the $J_{K_aK_c}$=1_{01}-0_{00} transition. It appeared that the three transitions at 5707 MHz, 11115 MHz, and 16468 MHz, form a set of transitions that is analogous to the assigned set of K_a=0 transitions, with the lowest J quantum number being 0. The lowest J quantum number for a K_a=1 state is 1. This suggests that the abovementioned three transitions occur within a K_a=0 state. Therefore, they were reassigned to occur within the first excited van der Waals bending state. The intensities of the observed transitions also agree with the expected spin statistical weights of 3 and 1 for the first excited bending state and the ground state, respectively. Following the labeling scheme used for Ar-HCCH discussed in **5.1.3**, it was designated as Σ_1 state. To be consistent, the ground state was designated as Σ_0 state. Using this labeling scheme, the K_a and K_c quantum numbers could be omitted and only the J quantum number was used to label the rotational energy levels.

Using the observed spectra of the Ne-HCCH isotopomers as a guide, analogous transitions of Ne-$H^{13}C^{13}CH$ were measured. Contrary to the case of Ne-HCCH, the Σ_1 transitions were weaker than the Σ_0 ground state transitions. This observation agrees with the spin statistical weights of 6 and 10 for the Σ_1 and Σ_0 states, respectively.

The corresponding ground state transitions of the Ne-DCCD isotopomers were also measured. However, for the perturbed set of transitions, only two transitions, with J=2-1 and 3-2, were observed. No J=1-0 transition could be assigned. The absence of the J=1-0 transition suggests that the observed two transitions occur within a Π_1 state instead of the Σ_1 state. Therefore, the observed transitions were assigned to be Π_1 transitions. These transitions were weaker than the Σ_0 transitions, again in accord with the spin statistical weights of 3 and 6 for the two states, respectively. Nuclear quadrupole hyperfine structures arising from the two deuterium nuclei were observed and partially resolved for the J=1-0, Σ_0 transitions. A representative spectrum of the J=1-0, Σ_0 transition of ^{20}Ne-DCCD is shown in figure 5-5 (top trace). Broadening was observed in higher J transitions, but the hyperfine components could not be assigned. The highest point of the broadened peaks were recorded as the transition frequencies with estimated accuracies of 10 kHz.

For the isotopomers containing DCCH, only transitions within the ground state were observed. Nuclear quadrupole hyperfine structures due to the D nucleus were also observed and resolved for the J=1-0 transitions, as shown in figure 5-5 for ^{20}Ne-DCCH (bottom trace). The partial deuterium substitution breaks the C_{2v} symmetry of the dimer so that the excited van der Waals bending state is no longer metastable. Nonetheless, a spectral search for the excited state transitions was performed. No further transition could be assigned.

All measured transition frequencies are listed in tables 5-4 and 5-5. The ground state spectroscopic constants were obtained by fitting the Σ_0 transitions to the linear rotor Hamiltonian (*222*):

$$H = BJ(J+1) - D\,[J(J+1)]^2 + H\,[J(J+1)]^3, \qquad (5\text{-}1)$$

where B is the rotational constant, D and H are quartic and sextic centrifugal distortion constants, respectively. In the analyses of the Ne-DCCH and Ne-DCCD isotopomers, one more term, H_Q(D), was added to represent the deuterium nuclear quadrupole interaction. The assigned hyperfine components were first fitted using a first order quadrupole fit. The obtained hypothetical center frequencies were then used to fit rotational and centrifugal distortion constants. All obtained spectroscopic constants are listed in table 5-6, including the nuclear quadrupole coupling constants χ_{aa} for Ne-DCCH and Ne-DCCD. For the Σ_1 transitions, since the perturbing state was not observed in this study, no Coriolis terms could be fitted to account for the perturbation. The fitting procedure was not performed.

5.2.3 Discussion of Spectroscopic Results

a. Σ_0 *state*

Even though three parameters were used to fit four observed transitions, the resulting standard deviations are still considerably larger than the corresponding experimental uncertainties, especially for the isotopomers containing deuterium. These large deviations indicate that the Ne-acetylene van der Waals dimer is rather floppy. The inclusion of the sextic distortion constant H is necessary. A fit without H produced a standard deviation of larger than 0.3 MHz for ^{20}Ne-HCCH. Larger standard deviations for species containing deuterium are due to the fact that nuclear quadrupole hyperfine structures in the higher J transitions were not resolved.

There is a significant increase, by almost a factor of 10, in the centrifugal distortion constant when the binding partner of acetylene changes from Ar to Ne. The determined D value was 0.5823 MHz for ^{20}Ne-HCCH and was only 0.063568 MHz (table 5-3) for Ar-HCCH. This large increase is a result of a reduced anisotropy in the radial coordinate of the corresponding intermolecular potential. The value was also compared with that of the isoelectronic Ne-HCN dimer, which is characterized as a highly nonrigid molecule. The value for ^{20}Ne-HCN is 1.280 MHz (*66*).

The quartic centrifugal distortion constant can be related to the van der Waals stretching frequency, ν_s, of the dimer and its corresponding stretching force constant, k_s, through the pseudodiatomic expressions (*174*):

$$\nu_s = (4\,B^3 / D)^{1/2}$$

$$k_s = 4\,\pi^2\;\nu_s\,\mu. \tag{5-2}$$

The obtained values for ^{20}Ne-HCCH are ν_s = 12.8 cm^{-1} and k_s = 0.11 Nm^{-1}. For comparison, the values are $\nu_s = 23.1$ cm^{-1} and $k_s = 0.50$ Nm^{-1} for Ar-HCCH (values calculated using the constants in table 5-3 for the Σ_0 state), and $\nu_s = 8.6$ cm^{-1} and $k_s = 0.05$ Nm^{-1} for ^{20}Ne-HCN (values calculated using the constants reported in ref. *66*). The smaller ν_s and k_s values for Ne-acetylene compared to those for Ar-acetylene are a consequence of the weaker interaction between Ne and acetylene.

The ground state spectroscopic constants were used to determine the intermolecular separation *R*, using the pseudodiatomic approximation:

$$R=[(k / \mu) / B]^{1/2}, \tag{5-3}$$

as done for the Ar-acetylene isotopomers. The obtained values are included in table 5-6. It was determined to be 4.012 Å for the main isotopomer. The values for the isotopomers containing ^{22}Ne and ^{13}C are in line with this value, with small isotopic variations. The magnitude of the isotopic variations is comparable to that of Ne-HCN. For example, ΔR=0.002 Å for the ^{20}Ne-H^{12}C^{15}N/^{20}Ne-H^{13}C^{15}N pair, ΔR=0.004 Å for ^{20}Ne-H^{12}C^{15}N/^{22}Ne-H^{12}C^{15}N (values calculated from the rotational constants reported in ref. *66*), which are similar to the values ΔR=0.002 Å for ^{20}Ne-H^{12}C^{12}CH/^{20}Ne-H^{13}C^{13}CH, ΔR=0.004 Å for ^{20}Ne-H^{12}C^{12}CH/^{22}Ne-H^{12}C^{12}CH. One would also expect to see smaller *R* values for the Ne-DCCD and Ne-DCCH isotopomers, compared to the normal isotopomer. These isotopic variations are, in fact, expected to be larger because of the larger percentage mass increase. However, longer bond lengths were determined for Ne-DCCD and Ne-DCCH. The values are 4.028 Å for ^{20}Ne-DCCD and 4.019 Å for ^{20}Ne-DCCH. This is similar to the observed trends in the Ar-DCCD and Ne-DCN systems. For Ar-DCCD, *R* increases by 0.003 Å compared to that of Ar-HCCH (table

7

5-2). For Ne-DCN, this effect is much larger. The D substitution expands the dimer by 0.04 Å (calculated from the rotational constants reported in ref. *66*). This unusual observation is a strong indication of a strong coupling between the large amplitude angular and radial motions. On substitution of H with D, the large amplitude internal motions are slightly attenuated, leading to a different vibrational averaging of the effective R. It is also noticed that larger distortion constants were determined for the heavier D-containing isotopomers, in contrast to what is normally observed. Similarly, these unusually large distortion constants can be attributed to effects of a different vibrational averaging.

The R value of 4.012 Å is very close to the R value of 4.039 Å for Ar-HCCH (table 5-2), with a difference of less than 0.03 Å. In similar systems, substitution of Ar with Ne causes a much larger bond distance shortening. For example, in the case of Rg-cyclopropane, a difference of 0.13 Å was determined (3.803 Å for Ar-cyclopropane, 3.672 Å for Ne-cyclopropane) (*58*). This relatively small bond length shortening arises from a large decrease in the anisotropy of the corresponding potential energy surface. In the Ne-HCCH dimer, the ground state wavefunction is very much delocalized, and contains a significant contribution from the linear configuration, where the separation between Ne and the center-of-mass of acetylene is the largest. In the case of Ar-acetylene, as a consequence of a stronger anisotropy, the ground state wavefunction is more localized to the skew T-shaped equilibrium configuration (*217*), where R is relatively shorter.

In the study of weakly bound van der Waals dimers, nuclear quadrupole hyperfine structures are often used to deduce angular information, or average dynamics, of the dimer. In this study, such information was extracted from the nuclear quadrupole hyperfine structures caused by the nuclear quadrupole interactions of deuterium nuclei with the overall rotation of the complex. It is assumed that the interaction is cylindrically symmetric about the D-C bond and that the nuclear quadrupole coupling tensor of free acetylene is not affected by the formation of the dimer. The determined nuclear quadrupole coupling constants of the dimer χ_{aa} can be related to the coupling constant χ_0 of free DCCD or DCCH by projecting the monomer coupling constant onto the *a*-principal inertial axis of the dimer, using (*64*)

$$\chi_{aa} = \chi_0 \langle P_2(\cos\theta)\rangle. \tag{5-4}$$

Here, θ is the angle between the acetylene axis and the *a*-axis of the dimer, and the brackets indicate averaging over large amplitude motions. χ_0 of free DCCD and DCCH were previously determined to be 204.4 (10) kHz (*71*) and 200 (10) kHz (*225*), respectively. $\langle P_2(\cos\theta)\rangle$ values thus obtained are 0.096 for ^{20}Ne-DCCH, 0.097 for ^{22}Ne-DCCH, 0.079 for ^{20}Ne-DCCD, and 0.110 for ^{22}Ne-DCCD. The value of $\langle P_2(\cos\theta)\rangle$ is determined by both the geometry of the complex and the large amplitude motions. It is difficult to separate the contributions of these two factors to $\langle P_2(\cos\theta)\rangle$. Taking ^{20}Ne-DCCH as an example, the experimentally determined value, 0.096, is close to the value of 0.041 determined for a rigid equilibrium structure with the theoretical value of θ=53.1° (*196*). However, the value is close to zero, the value for the free rotor limit, especially when compared with extreme values of -0.5 at θ=90° (minimum) and 1 at θ=0° (maximum). This suggests that the large amplitude internal motion is the determining factor, and that the agreement with the rigid theoretically predicted equilibrium structure is just a coincidence. For comparison, the $\langle P_2(\cos\theta)\rangle$ value for Ar-DCCD was determined to be 0.355 (*71*). The free rotor character, as reflected from $\langle P_2(\cos\theta)\rangle$, is more pronounced in Ne-acetylene, as a consequence of the weaker binding. Also for comparison, the $\langle P_2(\cos\theta)\rangle$ value for the isoelectronic Ne-HCN is 0.203, approximately twice as large (*66*).

b. Coriolis perturbed state

For the Ne-HCCH and Ne-$H^{13}C^{13}CH$ isotopomers, the lowest *J* transition of the perturbed sets of transitions was located within 250 MHz of the ground state J=1-0 transition. It was therefore assigned to be the J=1-0 transition within the Σ_1 state. The transition pattern of the Σ_1 transitions can be compared to that of the Σ_0 transitions. The transitions of ^{20}Ne-HCCH will be used as examples. The J=1-0, Σ_1 transition is 150 MHz above the corresponding Σ_0 transition. The difference decreases in the J=2-1 transitions. The J=2-1, Σ_1 transition is only 21 MHz above the one within the Σ_0 state. For the J=3-2 transition, the one within the Σ_0 state becomes higher in frequency, i.e., 136 MHz above the Σ_1 transition. This compressed energy level pattern of the Σ_1 transitions is attributed to a Coriolis interaction with a nearby, higher energy Π_1 state that has the same parity. This is analogous to the Coriolis interactions observed in the Ar-HCN dimer (*65*). The energy level correlation diagram for Ar-HCCH in figure 5-4 can also be used for Ne-HCCH, except that the energy ordering of the Σ_1 and Π_1 states has to be reversed.

In the case of Ne-DCCD, no J=1-0 transition could be assigned. Therefore the observed transitions were assigned to occur within a Π_1 state. A compressed energy level pattern is also evident from the two observed transition frequencies, suggesting that this state is Coriolis perturbed by a higher energy Σ_1 state. Figure 5-4 can thus be used for the Ne-DCCD isotopomers, with the same energy ordering of the Σ_1 and Π_1 states as depicted. This indicates that a reversal in energy level ordering occurs upon deuterium substitution.

Upon close examination of the measured transition frequencies, it is noticed that the Σ_1 levels are more severely Coriolis perturbed in the Ne-H^{13}C^{13}CH isotopomers, compared to those of Ne-HCCH. For example, the J=2-1 transition of ^{20}Ne-H^{13}C^{13}CH is 350 MHz below twice the frequency of the J=1-0 transition. The difference is 300 MHz in ^{20}Ne-HCCH. This more pronounced perturbation suggests that the energy difference between the two perturbed states decreases upon substitution. A similar comparison of the frequency change between the J=2-1 and J=3-2 transitions shows that this perturbation is even more pronounced in Ne-DCCD, implying the energy gap further reduces in Ne-DCCD. This trend is similar to those in the Ar-acetylene and Ar-HCN dimers. In the case of the Ar-HCN complex, the substitution of H with D reduces the energy gap between the Σ_1 and Π_1 states from 0.57 cm^{-1} to 0.22 cm^{-1} (*70*).

A further example of a reversal of the energy level ordering upon substitution can, in fact, be found in the Ar-HCCH/^{20}Ne-HCCH systems. It is evident from the recorded rotational spectra of the two dimers that the energy ordering of the Σ_1 and Π_1 states is reversed. For Ar-HCCH, the K_a=1 transitions were recorded, suggesting that the Π_1 state is below the Σ_1 state. In the case of ^{20}Ne-HCCH, transitions within the Σ_1 state were recorded instead, implying this state is below the Π_1 state. A similar phenomenon was also found in the Ar-HCN/Ne-HCN systems. Recent high level theoretical calculations discovered that the Σ_1 state is above the Π_1 state in Ne-HCN (*197,226*), opposite to the ordering in the Ar-HCN dimer (*70*).

c. *Comparison with the calculated spectrum*

The recorded rotational spectra of ^{20}Ne-HCCH and ^{20}Ne-DCCH can be compared with those calculated from the reported energy values in ref. *196*. The (J j l) notation was employed to label the energy levels in the theoretical study (*196*), where J j l correspond to the quantum numbers for the total angular momentum, the internal rotation angular momentum of the acetylene monomer, and the end-over-end rotation angular momentum of the complex, respectively. It was pointed out by Klemperer that in the free rotor limit, j and l are "good" quantum numbers, such that the j quantum number establishes the pattern of "bending vibrational" levels, and the l quantum number establishes the pattern of rotational levels. When the system moves away from the free rotor limit, j and l serve as approximate labels (*68*). Based on this, the measured Σ_0 rotational transition frequencies were compared to those calculated from the computed (l 0 l) energy levels. The measured Σ_1 rotational transitions were compared to those calculated from the computed (l+1 1 l) energy levels, since the lowest allowed l quantum number is zero in the (l+1 1 l) state. The computed l=1-0 transition in this state corresponds to the observed J=1-0, Σ_1 transition. The comparison is tabulated in table 5-7.

The computed frequencies are in exceptionally good agreement with the experimentally determined ones, all within 1%. This is a further verification of the high quality of the *ab initio* potential energy surface used for the dynamical calculations, in addition to the good agreement between the measured and computed infrared spectra (*196*).

However, careful examination of the computed j=1 energy levels raises a number of questions. First of all, it was noted that the transition frequencies obtained from the calculated (l-1 1 l) energy levels form a rather unusual pattern. The l=2-1, 3-2, and 4-3 transition frequencies of ^{20}Ne-HCCH are 15210 MHz, 16050 MHz, and 21480 MHz, respectively (calculated from the values listed in TABLE III in ref. *196*). Note that l is the quantum number for the end-over-end rotation of the dimer. One would expect these rotational transitions to be approximately equally spaced. It is very unlikely that the difference between consecutive l transitions suddenly jumps from less than 1 GHz to more than 5 GHz. The l=2-1 transition frequency appears to be abnormally high. It is expected to be in the neighborhood of 11 GHz, close to the l=2-1 transition frequencies from all other states. The values are 10.92 GHz within the (l 0 l) state, 11.01 GHz within the (l+1 1 l) state, and 11.40 GHz within the (l 1 l) state. A similar unusual pattern was also found in the computed ^{20}Ne-DCCH spectrum. Fortunately, for the ^{20}Ne-DCCH isotopomer, the infrared spectrum was assigned and the transition frequencies were available (*196*). The energy spacings between the j=1 levels in the excited vibrational state could be calculated from combination differences, utilizing the reported infrared transition frequencies (*196*) and the determined ground state pure rotational transition frequencies from this study. The energy spacing between the (J j l)=(011) and (112) levels thus obtained was 10.99 GHz from the P(1), P(2) infrared frequencies, 3337.5136 cm^{-1} and 3337.51739 cm^{-1}, respectively (values obtained from TABLE IV in ref. *196*), and the

J=2-1, Σ_0 rotational transition frequency, 10874 MHz. This value appears to be much more reasonable. It is then assumed that these energy spacings do not change significantly upon intramolecular vibrational excitation. This assumption can be justified by the fact that except for the ($J\ j\ l$)=(112)-(011) transition mentioned above, all the other transition frequencies obtained using the computed ground vibrational state energies were within 3% of those calculated from the infrared and microwave combination differences. In particular, the frequencies obtained for other l transitions within the (l-1 1 l) state were in very good agreement. For example, the computed ($J\ j\ l$)=(213)-(112) and (314)-(213) transition frequencies, 15720 MHz and 21090 MHz (calculated from the values listed in TABLE III in ref. *196*), were very close to the values, 15662 MHz and 21070 MHz, determined from the infrared and microwave combination differences. An energy level diagram of ^{20}Ne-DCCH is schematically depicted in figure 5-6. The listed frequencies within the (l 0 l) state were those obtained from this microwave study. Those within the j=1 state were obtained from the infrared and microwave combination differences. The same procedure can be applied to ^{20}Ne-HCCH.

With the abnormality in the (l-1 1 l) state removed, a further discrepancy between the calculated and the measured rotational spectrum exists. It concerns the relative energies of the three j=1 states. The energy of the lowest rotational energy level within a state is considered the energy of the certain state. Therefore, the energies of the (l+1 1 l), (l 1 l), and (l-1 1 l) states are the energies of the ($J\ j\ l$)=(110), (111), and (011) levels, respectively. According to the computed spectrum, the (l+1 1 l) state has the lowest energy. The other two states are only slightly above this state. For example, according to the values reported in TABLE III in ref. *196, the* $(l\ 1\ l)$ *state lies only* 10200 MHz above the $(l+1\ 1\ l)$ state for the Ne-HCCH isotopomer. This suggests that the two higher energy states, namely the $(l-1\ 1\ l)$ and $(l\ 1\ l)$ states, should also be significantly populated. Assuming a beam temperature of 0.5 K, the lowest energy level in the $(l\ 1\ l)$ state, the $(J\ j\ l)=(1\ 1\ 1)$ level, should have a population of 40% of that of the lowest level in the $(l+1\ 1\ l)$ state. Experimentally, even though the $J=2$ level in the Σ_1 state is approximately 17 GHz (obtained from the determined rotational constant) above the $J=0$ level, the $J=3-2$ transition was still observed with a reasonable intensity. The $l=2-1$ transitions in the $(l-1\ 1\ l)$ and $(l\ 1\ l)$ states are then expected to have intensities comparable to, if not stronger than, that of the $J=3-2$, Σ_1 transition. The entire spectral region from 9 GHz to 12 GHz was carefully scanned and rescanned with a fair amount of averaging cycles. The corresponding regions were also searched for the Ne-DCCD and Ne-H^{13}C^{13}CH isotopomers. Despite the intensive searches, no further transition could be assigned.

For the Ne-DCCH isotopomer, the relative energies of the three states could again be obtained from infrared and microwave combination differences. It was found that the computed energy gap between the $(l+1\ 1\ l)$ and $(l\ 1\ l)$ states, 11190 MHz, was almost twice as large as the value, 5984 MHz, determined from the infrared and microwave combination differences. On the one hand, the computed energy level spacings within a state are within 3% of those determined experimentally. On the other hand, the energy differences between states are off by 50%. This suggests that the dynamical calculations, especially those for the energies of the $j=1$ levels, need to be carefully checked.

Still, the energy differences determined from the infrared and microwave combination differences, 2830 MHz between the (*l*+1 1 *l*)/(*l*-1 1 *l*) states and 5984 MHz between the (*l*+1 1 *l*)/(*l* 1 *l*) states, strongly suggest that all three j=1 states should be appreciably populated and that there should be no problem to detect transitions within all the states. This is clearly different from what was observed. Further spectroscopic measurements involving energy levels in these excited van der Waals bending states, such as direct millimeterwave absorption, may help to solve this puzzle.

5.2.4 Potential Energy Surfaces of Ne-C_2H_2

Recent investigations of the convergence of higher order Møller-Plesset perturbation theory made it clear that its convergence behavior depends significantly on the specific chemical system and on the choice of basis sets (*143*,*227*,*228*). A recent MP4 study of the Ne-HCN system (*229*) gave consistent results with the previously reported SAPT (*226*) and CCSD(T) (*197*) potentials, implying that the cheaper MP4 approach is suitable for the Ne-HCN complex. It would be interesting to see if this also applies to the isoelectronic Ne-acetylene system. Two potential energy surfaces were constructed for Ne-C_2H_2, one at the MP4 level and the other at the CCSD(T) level. Features of the two potentials were compared. They were also compared to the SAPT potential (*196*), which is believed to be highly accurate.

Computational details are given in **3.1.3**(*b*). The intermolecular energies were calculated at various distances ranging from 3.5 to 5.0 Å and angles from 0 to 90°. A total of 163 *ab initio* points were determined. Calculated MP4 interaction energies are listed in table 5-8. Those calculated with the CCSD(T) level of theory are listed in table 5-9.

The two potentials have very similar overall topologies. The MP4 potential is characterized by two minima. The global minimum is located at a skew T-shaped configuration with R=3.8 Å, θ=54.5°, and a well depth of -49.76 cm^{-1}. The local minimum occurs at the linear configuration with R=4.4 Å, θ=0°, and well depth= -47.45 cm^{-1}. Similarly, two minima are also located in the CCSD(T) potential. The global minimum is at R=3.9 Å, θ=50.0°, and well depth= -47.68 cm^{-1}, and the local minimum is at R=4.4 Å, θ=0°, and well depth= -46.59 cm^{-1}. Both potentials are in good agreement with the SAPT potential, which has a global minimum at R=3.8 Å, θ=53.1°, and well depth= -52.31 cm^{-1}, and a local minimum at R=4.4 Å, θ=0°, and well depth= -50.54 cm^{-1} (*196*). Small differences do exist. Using the CCSD(T) energies as standard, the MP4 and SAPT methods overestimated the interaction energy by 4.4% and 9.7% at the global minimum, respectively. The energy difference between the global minimum and the local minimum is also overestimated by 112% (MP4) and 62.4% (SAPT).

The angular dependence of the minimum interaction energy is plotted in figure 5-7. Shown is the minimum energy path, meaning that the radial coordinate was allowed to relax to obtain the minimum energy at each angle. It shows that the Ne-HCCH potential is rather isotropic along the angular coordinate, with a barrier of less than 5 cm^{-1} to sample the entire range of the angular coordinate. This further supports that the acetylene subunit undergoes large amplitude angular motion, in agreement with the observations from the rotational spectrum. Both potentials show strong radial-angular coupling, similar to the case of Ne-HCN (*66*). For the CCSD(T) potential, the bond distance has its maximum, 4.4 Å, at the linear configuration. It decreases to 3.9 Å in going to the global minimum, and further decreases to 3.7 Å at the T-shaped configuration with

θ=90°. This is also similar to Ar-HCCH, where a strong coupling between the van der Waals radial and angular coordinates leads to an unusually large intermolecular separation (see **5.1.3**).

5.3 SUMMARY

The rotational spectra of four minor isotopomers of Ar-acetylene, namely Ar-DCCD, Ar-H^{13}H^{13}H, Ar-DCCH, and Ar-H^{13}C^{12}CH, as well as eight additional transitions of the normal isotopomer, Ar-HCCH, were recorded. The measured transition frequencies were first analyzed using a semi-rigid rotor model. Unusually long bond distances were obtained, arising from the large amplitude angular motion of the acetylene monomer and a strong radial-angular coupling. Separate fits of transitions within the individual K-stacks were carried out. A possible Coriolis perturbation between the Π_1^e and Σ_1 states is inferred.

Rotational spectra of various Ne-acetylene isotopomers were measured. Transitions within both the Σ_0 ground state and the Σ_1 state, i.e., the first excited van der Waals bending state, were measured for the isotopomers containing HCCH and H^{13}C^{13}CH. For the Ne-DCCD isotopomers, besides the ground state transitions, those within the Π_1 state were recorded. In the case of the Ne-DCCH isotopomers only the ground state transitions were measured, since the excited state is no longer metastable. A reversal in the energy level ordering of the Σ_1 and the Π_1 state is proposed to account for the absence of the J=1-0 transition of the DCCD-containing isotopomers. Good agreement was found when comparing the computed transition frequencies based on the *ab initio* SAPT potential (*196*) with those obtained from this spectroscopic study, demonstrating the high quality of the *ab initio* potential. However, the computed (*l*-1 1 *l*) transition frequencies showed an abnormal pattern. In addition, the computed relative energies of the three j=1 states are in disagreement with the experimental observations. It is believed that the dynamical calculations of the energy levels need further checking. MP4 and CCSD(T) intermolecular potentials were constructed for the Ne-HCCH complex. The resulting MP4 potential is consistent with the CCSD(T) and the SAPT potential (*196*), indicating that this method is suitable for the Ne-HCCH complex, similar to the case of its isoelectronic species Ne-HCN (*229*). The potentials are very weakly anisotropic along the angular coordinate, further supporting that acetylene undergoes large amplitude angular motion within the dimer. In addition, a large variation in the radial coordinate accompanying the angular motion was revealed. This indicates that the radial and angular motions are strongly coupled in this dimer.

From this comparative spectroscopic study of the Ar-, Ne-acetylene systems, it is evident that the anisotropy of the potential energy surface greatly affects the appearance of the spectrum. The observed rotational spectra of the two dimers are drastically different. The Ar-HCCH spectrum contains K_a=0 and K_a=1 transitions within the ground van der Waals bending vibrational state. Despite the large amplitude internal motions, it could still be qualitatively described with a semi-rigid rotor Hamiltonian for a T-shaped structure. In the case of Ne-HCCH, only K_a=0 transitions within the ground state were observed. In addition, K_a=0 transitions within the first excited van der Waals bending state were observed.

Table 5-1: Rotational transition frequencies (in MHz) of Ar-acetylene isotopomers.

$J'_{K'_aK'_c}$-$J''_{K''_aK''_c}$	ν_{obs}	$\Delta\nu^a$	ν_{obs}	$\Delta\nu$	ν_{obs}	$\Delta\nu$
	Ar-HCCH		Ar-DCCD		Ar-$H^{13}C^{13}CH$	
1_{01}-0_{00}	3931.8894	42.8	3755.8541	-3.2	3766.4355	17.1
2_{02}-1_{01}	7862.2518	56.8	7510.1432	57.4	7531.466	23.7
2_{11}-1_{10}	7995.5668	-37.0	7656.8656	-59.1	7657.9048	-49.7
2_{12}-1_{11}	7559.0727	-36.0	7131.7726	-63.1	7244.5874	-10.5
3_{03}-2_{02}	11789.5515	24.7	11261.049	-2.4	11293.6798	11.8
3_{12}-2_{11}	11990.1002	-18.0	11482.254	8.4	11483.878	1.0
3_{13}-2_{12}	11334.3499	-19.0	10695.3853	6.6	10863.0879	-6.7
4_{04}-3_{03}	15712.2436	-38.0	15007.0844	-20.6	15051.656	-15.1
4_{13}-3_{12}	15980.7153	19.6	15303.9234	56.0	15306.2583	55.8
4_{14}-3_{13}	15104.452	20.0	14256.1821	66.7	14476.9703	3.4
5_{05}-4_{04}	19628.7591	-74.0	18746.5338	-31.2	18803.9554	-33.9
5_{14}-4_{13}	19966.0749	39.6	19120.6434	-26.2	19123.8192	-25.3
5_{15}-4_{14}	18867.5348	41.6	17813.1472	-32.2	18084.6305	27.7
6_{06}-5_{05}	23537.5041	48.9	22477.709	22.4	22549.1199	21.7
6_{15}-5_{14}	23944.8174	-25.0				
6_{16}-5_{15}	22621.6542	-27.0			21684.252	-13.9
	Ar-DCCH		Ar-$H^{13}C^{12}CH$			
1_{01}-0_{00}	3844.558	-5.2	3846.4783	-0.8		
2_{02}-1_{01}	7687.5795	3.2	7691.4966	0.8		
3_{03}-2_{02}	11527.4839	0.8	11533.5799	-0.3		
4_{04}-3_{03}	15362.7142	-1.3	15371.2472	0.1		
5_{05}-4_{04}	19191.6881	0.3				

$^a\Delta\nu = \nu_{\text{obs}} - \nu_{\text{calc}}$ in kHz.

Table 5-2: Spectroscopic constants of Ar-acetylene isotopomers.[a]

	Ar-HCCH	Ar-DCCD	Ar-H^{13}C^{13}CH	Ar-DCCH[d]	Ar-H^{13}C^{12}CH[d]
Rotational constants (in MHz):					
A	47550(fixed)[b]	34160(fixed)[c]	45140(fixed)[c]		
B	2074.98(2)	2009.31(4)	1986.51(2)		
C	1856.99(2)	1746.55(4)	1780.02(2)		
$(B+C)/2$	1965.98(2)	1877.93(4)	1883.26(2)	1922.411(1)	1923.3613(5)
Quartic centrifugal distortion constants (in kHz):					
D_J	29.7(4)	1.1(7)	27.2(4)	64.5(1)	60.85(6)
D_{JK}	21204(9)	29100(1)	20049(7)		
d_l	-8.1(5)	6.6(9)	-5.7(5)		
Sextic centrifugal distortion constants (in kHz):					
H_J	-0.002(6)	0.04(1)	0.009(6)	-0.008(2)	-0.011(2)
H_{JK}	-25.2(2)	-28.9(3)	-22.3(2)		
h_l	0.014(7)	0.01(2)	0.032(8)		
Standard deviation of the fit (in kHz):					
σ	54.5	60.7	38.2	4.5	1.2
Effective separation (in Å):					
R[e]	4.046	4.046	4.041		
R[f]	4.039	4.042	4.036	4.038	4.037

[a] Watson's *S*-reduction Hamiltonian in its I^r representation was used (*190*).

[b] Rotational constant *A* fixed at the value from ref. *73*.

[c] Fixed *A* value at the rotational constant of the acetylene monomer, scaled using θ=60° from ref. *73*.

[d] Only K_a=0 transitions observed; a fit in the symmetric top limit was used.

[e] Calculated using $R = [\,(k/\mu)\,(1/C - 1/b)\,]^{1/2}$, where b is the rotational constant of the acetylene monomer.

[f] Calculated using $R = [\,(k/\mu)\,(2/(B+C))\,]^{1/2}$.

Table 5-3: Spectroscopic constants of Ar-acetylene isotopomers from fits of individual *K*-stacks.

	Ar-HCCH		
	Σ_0	Π_1^e	Π_1^f
B_{eff} (MHz)	1966.07190(8)	1890.3317(3)	1999.32410(5)
D (kHz)	63.568(4)	70.25(2)	53.988(2)
H (Hz)	-9.25(6)	-34.6(2)	-9.06(3)
δ (kHz)	0.3	1.1	0.2
	Ar-H^{13}C^{13}CH		
	Σ_0	Π_1^e	Π_1^f
B_{eff} (MHz)	1883.33480(8)	1811.651(2)	1914.87250(3)
D (kHz)	58.495(5)	62.8(1)	49.481(2)
H (Hz)	-7.6(1)	-25(2)	-8.70(4)
δ (kHz)	0.2	3.8	0.1
	Ar-DCCD		
	Σ_0	Π_1^e	Π_1^f
B_{eff} (MHz)	1878.08(1)	1783.245(2)	1914.624(4)
D (kHz)	69.0(7)	37.4(2)	50.7(3)
H (Hz)	10(14)	-31(3)	-12(5)
δ (kHz)	25.6	5.8	9.9

Table 5-4: Measured transition frequencies (in MHz) of Ne-acetylene isotopomers.

J' - J''	Σ_0 state							
	ν_{obs}	$\Delta\nu^a$	ν_{obs}	$\Delta\nu$	ν_{obs}	$\Delta\nu$	ν_{obs}	$\Delta\nu$
	^{20}Ne-HCCH		^{22}Ne-HCCH		^{20}Ne-H^{13}C^{13}CH		^{22}Ne-H^{13}C^{13}CH	
1 - 0	5554.0305	2.8	5277.9042	2.5	5385.1240	2.8	5108.5464	2.1
2 - 1	11093.9134	-2.8	10542.9582	-2.5	10756.4696	-2.8	10204.6163	-2.1
3 - 2	16604.913	1.2	15781.8184	1.1	16099.6528	1.2	15275.2250	0.9
4 - 3	22071.0421	-0.2	20980.0901	-0.2	21398.9913	-0.2		
	^{20}Ne-DCCH		^{22}Ne-DCCH		^{20}Ne-DCCD		^{22}Ne-DCCD	
1 - 0	5444.9197	6.0	5169.3425	4.1	5337.3698	12.1	5062.1	9.1
2 - 1	10873.5415	-6.0	10323.9676	-4.1	10656.3906	-12.1	10107.5	-9.1
3 - 2	16268.5642	2.6	15448.3391	1.8	15937.2516	5.2	15118.7	3.9
4 - 3	21610.4965	-0.4	20525.1563	-0.3	21156.8489	-0.9	20074.9	0.7
	Σ_1 state							
	^{20}Ne-HCCH		^{22}Ne-HCCH		^{20}Ne-H^{13}C^{13}CH		^{22}Ne-H^{13}C^{13}CH	
1 - 0	5706.8491		5467.8554		5571.1998		5337.9305	
2 - 1	11114.6902		10583.1322		10789.4935		10259.8574	
3 - 2	16467.8034		15662.7397		15973.9506		15168.9051	
	^{20}Ne-DCCH		^{22}Ne-DCCH		^{20}Ne-DCCD		^{22}Ne-DCCD	
2 - 1					10999.2		10501.7	
3 - 2					16015.8		15233.2	

$^a\Delta\nu = \nu_{obs} - \nu_{calc}$ in kHz.

Table 5-5: Frequencies (in MHz) of the deuterium nuclear quadrupole hyperfine components of the J=1-0, Σ_0 transitions.

$F'I'$- $F''I''$	ν_{obs}	$\Delta\nu^a$	ν_{obs}	$\Delta\nu$	$F'I'$- $F''I''$	ν_{obs}	$\Delta\nu$	ν_{obs}	$\Delta\nu$
	^{20}Ne-DCCH		^{22}Ne-DCCH			^{20}Ne-DCCD		^{22}Ne-DCCD	
1 1 - 1 1	5444.9246	0.1	5169.3476	0.3	2 2 - 2 2	5337.3752	-0.2	5062.0626	-0.4
2 1 - 1 1	5444.9186	-0.2	5169.3410	-0.6	1 0 - 0 0	5337.3752	0.5	5062.0626	0.7
0 1 - 1 1	5444.9102	0.1	5169.3332	0.2	3 2 - 2 2	5337.3675	-0.6	5062.0518	-0.5
					1 2 - 2 2	5337.3595	0.3	5062.0394	0.2

$^a\Delta\nu = \nu_{obs} - \nu_{calc}$ in kHz.

Table 5-6: Spectroscopic constants of Ne-acetylene isotopomers (Σ_0 state).

	^{20}Ne-HCCH	^{22}Ne-HCCH	^{20}Ne-H^{13}C^{13}CH	^{22}Ne-H^{13}C^{13}CH
B (MHz)	2778.1822(16)	2640.0013(14)	2693.6975(19)	2555.3026(14)
D (MHz)	0.5823(2)	0.5295(2)	0.5667(2)	0.5137(2)
H (kHz)	-0.849(6)	-0.713(5)	-0.878(7)	-0.733(5)
σ (kHz)	3.6	3.1	4.2	3.0
R (Å)	4.012	4.008	4.010	4.007
	^{20}Ne-DCCD	^{22}Ne-DCCD	^{20}Ne-DCCH	^{22}Ne-DCCH
B (MHz)	2670.179(8)	2532.380(6)	2723.796(4)	2585.880(3)
D (MHz)	0.7455(9)	0.6749(4)	0.6666(5)	0.6032(3)
H (kHz)	-2.19(3)	-1.81(2)	-1.47(1)	-1.19(1)
σ (kHz)	18.0	13.5	8.9	6.1
χ_{aa} (MHz)	0.0161(8)	0.0236(8)	0.0192(4)	0.0194(8)
R (Å)	4.028	4.025	4.019	4.015

Table 5-7: Comparison of the experimental and calculated transition frequencies of Ne-acetylene.

J' - J''	Σ_0 state (l 0 l)		Σ_1 state (l+1 1 l)	
	Cal.[a]	Exp.[b]	Cal.	Exp.
		^{20}Ne-HCCH		
1 - 0	5580	5554.0305	5700	5706.8491
2 - 1	11110	11093.9134	11160	11114.6902
3 - 2	16620	16604.9130	16530	16467.8034
4 - 3	22080	22071.0421		
		^{20}Ne-DCCH		
1 - 0	5460	5444.9197	5730	
2 - 1	10920	10873.5415	11010	
3 - 2	16350	16268.5642	16290	
4 - 3	21720	21610.4965		

[a] Transition frequencies obtained using the computed energies in ref. *196*.

[b] Measured rotational transition frequencies.

Table 5-8: *Ab initio* MP4 interaction energies of Ne-HCCH (in cm^{-1}).

R /Å	θ=0°	10°	20°	30°	40°	50°	60°	70°	80°	90°
	MP4									
3.5			454.0	200.4	53.5	-10.6	33.2	39.8	-41.1	41.3
3.6			255.0	95.2	4.8	-32.6	-44.1	-46.2	-45.8	-45.5
3.7		241.9	128.0	29.7	-23.9	-44.1	-48.6	-48.1	-46.8	-46.2
3.8	152.6	118.4	49.0	-9.5	-39.5	-48.9	-49.3	-47.2	-45.5	-44.8
3.9	61.0	42.5	1.6	-31.6	-46.8	-49.6	-47.5	-44.7	-42.9	-42.1
4.0	7.5	-2.7	-25.6	-42.8	-48.9	-47.9	-44.6	-41.5	-38.5	-38.9
4.1	-23.0	-27.9	-39.7	-47.1	-47.8	-44.7	-40.9	-37.8	-35.9	-35.3
4.2	-38.9	-40.8	-45.7	-47.4	-45.0	-41.0	-37.0	-34.1	-32.3	-31.8
4.3	-45.9	-46.0	-46.8	-45.4	-41.4	-37.1	-33.2	-30.4	-28.9	-28.4
4.4	-47.5	-46.7	-45.2	-42.1	-37.5	-33.2	-29.6	-27.1	-25.7	-25.2
4.5	-15.9	-44.8	-42.3	-38.2	-33.7	-29.5	-26.2	-24.0	-22.7	-22.3
4.6	-42.6	-41.5	-38.5	-34.3	-29.9	-26.1	-23.2	-21.2		
4.7	-38.7	-37.6	-34.6	-30.6	-26.5	-23.0	-20.4	-18.7		
4.8	-35.7	-33.6	-30.8	-27.0	-23.3	-20.3	-18.0	-16.5		
4.9	-30.8	-29.8	-27.2	-23.8	-20.5	-17.8	-15.8	-14.5		
5.0	-27.3	-26.3	-23.9	-21.0	-18.0	-16.7	-13.9	-12.8		
	θ=52.5°	53°	53.5°	54°	54.5°	55°				
3.8	-49.5	-49.6	-49.7	-49.7	-49.8	-49.7				
3.9	-49.3	-49.2	-49.1	-49.0	-48.9	-48.8				
	θ=2.5°	5°	7.5°	82.5°	85°	87.5°				
4.4	-46.5	-46.2	-46.0							
3.7				-43.7	-43.5	-43.4				

Table 5-9: *Ab initio* CCSD(T) interaction energies of Ne-HCCH (in cm^{-1}).

R /Å	*θ*=0°	10°	20°	30°	40°	50°	60°	70°	80°	90°
					MP4					
3.5			457.6	203.3	56.7	-6.8	-29.1	-35.5	-36.9	-37.1
3.6			257.8	97.9	7.6	-29.3	-40.5	-42.6	-42.3	-42.1
3.7		244.7	130.3	31.9	-21.5	-41.2	-45.6	-45.1	-43.9	-43.4
3.8	152.6	120.6	50.9	-7.6	-37.4	-46.5	-46.7	-44.7	-43.0	-42.4
3.9	62.8	44.2	3.1	-29.9	-44.9	-47.5	-45.4	-42.6	-40.8	-40.1
4.0	9.0	-1.2	-24.2	-41.3	-47.2	-46.0	-42.7	-39.6	-37.8	-37.2
4.1	-21.7	-26.7	-38.4	-45.8	-46.3	-43.1	-39.3	-36.2	-34.4	-33.9
4.2	-37.9	-39.7	-44.6	-46.2	-43.7	-39.6	-35.6	-32.7	-31.1	-30.5
4.3	-45.0	-45.1	-45.9	-44.3	-40.3	-35.8	-32.0	-29.3	-27.8	-27.3
4.4	-46.6	-45.8	-44.4	-41.1	-36.5	-32.1	-28.5	-26.1	-24.7	-24.3
4.5	-45.1	-44.0	-41.4	-37.3	-32.7	-28.5	-25.3	-23.1	-21.9	-21.5
4.6	-41.8	-40.8	-37.7	-33.5	-29.0	-25.2	-22.3	-20.4		
4.7	-38.0	-36.9	-33.9	-29.8	-25.7	-22.3	-19.7	-18.0		
4.8	-34.0	-33.0	-30.1	-26.4	-22.6	-19.6	-17.4	-15.9		
4.9	-30.2	-29.2	-26.6	-23.2	-19.9	-17.2	-15.3	-14.0		
5.0	-26.7	-25.7	-23.4	-20.4	-17.5	-15.2	-13.5	-12.3		
	θ=52.5°	53°	53.5°	54°	54.5°	55°				
3.8	-47.0	-47.0	-47.1	-47.1	-47.2	-47.1				
3.9	-47.2	-47.1	-47.0	-46.9	-46.8	-46.7				
	θ=2.5°	5°	7.5°	82.5°	85°	87.5°				
4.4	-46.5	-46.2	-46.0							
3.7				-43.7	-43.5	-43.4				

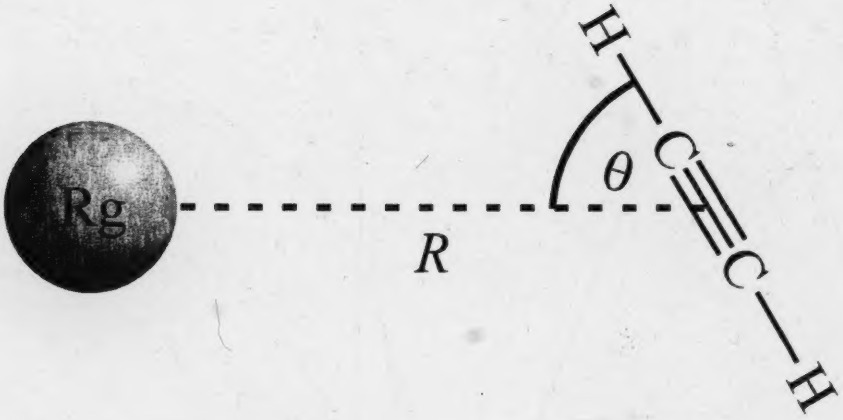

Figure 5-1: Structural parameters used to describe the Rg-acetylene van der Waals dimers. *R* is the distance from Ar atom to the center-of-mass of the acetylene monomer, and θ is the angle between the acetylene axis and the *R* vector.

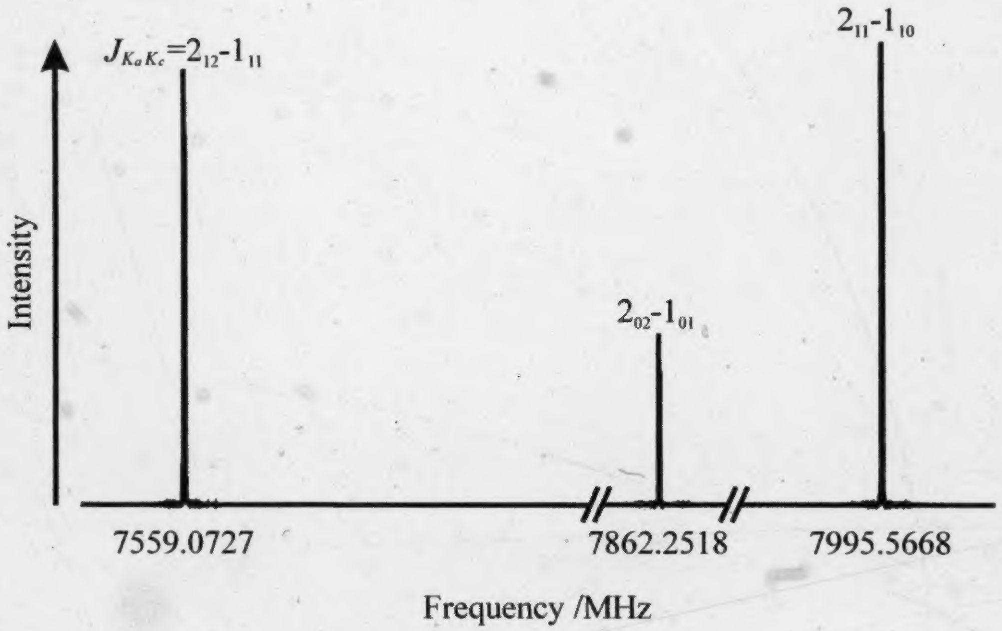

Figure 5-2: Observed transition intensities of the K_a=0 and K_a=1 transitions of Ar-C_2H_2. Shown are the $J_{K_aK_c}$=2_{12}-1_{11}, 2_{02}-1_{01}, and 2_{11}-1_{10} transitions. The two K_a=1 transitions are stronger than the K_a=0 transition. This is in agreement with the spin statistical weights of 3 and 1 for the K_a=1 and K_a=0 levels.

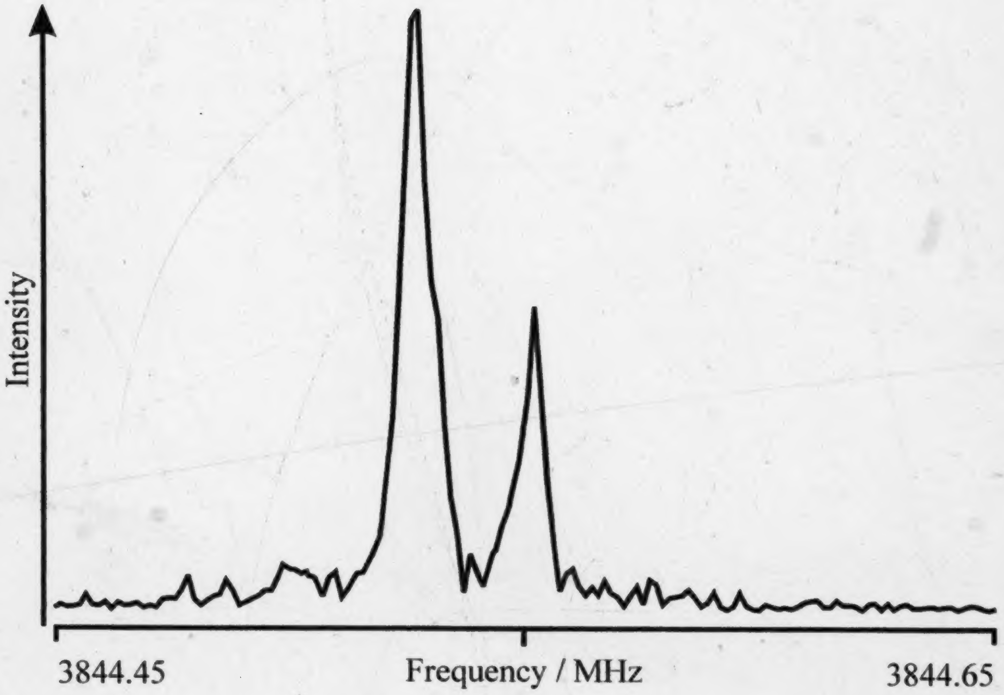

Figure 5-3: A spectrum of the $J_{K_aK_c}$=1_{01}-0_{00} transition of Ar-DCCH. Excitation frequency: 3844.570 MHz; sampling interval: 120 ns; number of averaging cycles: 5000. The rather low signal-to-noise ratio achieved is due to a combination of a very low transition frequency that is outside the normal operating range of the spectrometer, and the relatively small fraction of DCCH in the mixture of acetylene isotopomers.

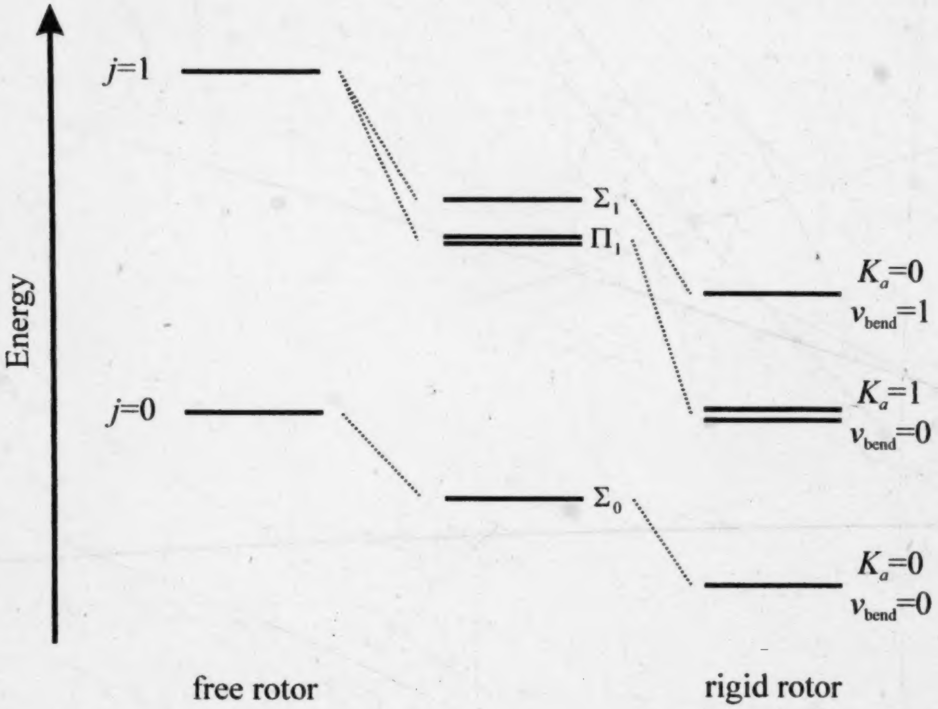

Energy
j=1
j=0
Σ1
Π1
Σ0
Ka=0
vbend=1
Ka=1
vbend=0
Ka=0
vbend=0
free rotor
rigid rotor

Figure 5-4: The correlation between the free rotor and rigid rotor energy levels for the Ar-HCCH van der Waals dimer. In the free rotor limit, the acetylene internal rotation quantum number *j* is a good quantum number, and each *j* level is (2*j*+1)-fold degenerate. As the anisotropy increases, the degeneracy is lifted. In the case of the *j*=1 state, it splits into a Σ_1 and two Π_1 states. The Greek letters Σ and Π denote the projection *K* of *j* onto the van der Waals bond, with *K*=0 and 1, respectively. The Σ_1 and Π_1 states correlate with the K_a=0 state in the first excited van der Waals bending state and the K_a=1 states in the ground state in the rigid rotor limit, respectively.

Figure 5-5: Representative spectra of the J=1-0, Σ_0 transitions of ^{20}Ne-DCCD (top trace) and ^{20}Ne-DCCH (bottom trace). Sampling interval: 120 nsec; number of averaging cycles: 2000. The Σ_0 state of ^{20}Ne-DCCD corresponds to total deuterium spins of I_D=0 and 2. The nuclear quadrupole hyperfine structure caused by the two equivalent deuterons was partially resolved and assigned. The assignments are also shown in the figure. For ^{20}Ne-DCCH, the nuclear quadrupole hyperfine structure due to the deuterium nucleus was also assigned. A sample containing a mixture of the HCCH, DCCD, and DCCH isotopomers was used, resulting in a relatively low signal-to-noise ratio.

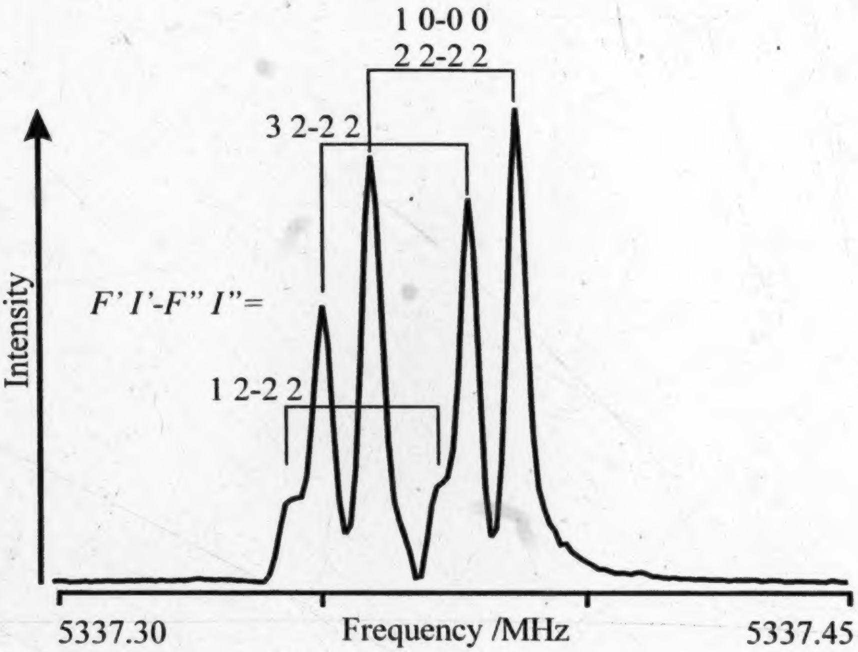
1 0-0 0
2 2-2 2
3 2-2 2
F' I'-F" I"=
1 2-2 2
Intensity
5337.30
Frequency /MHz
5337.45

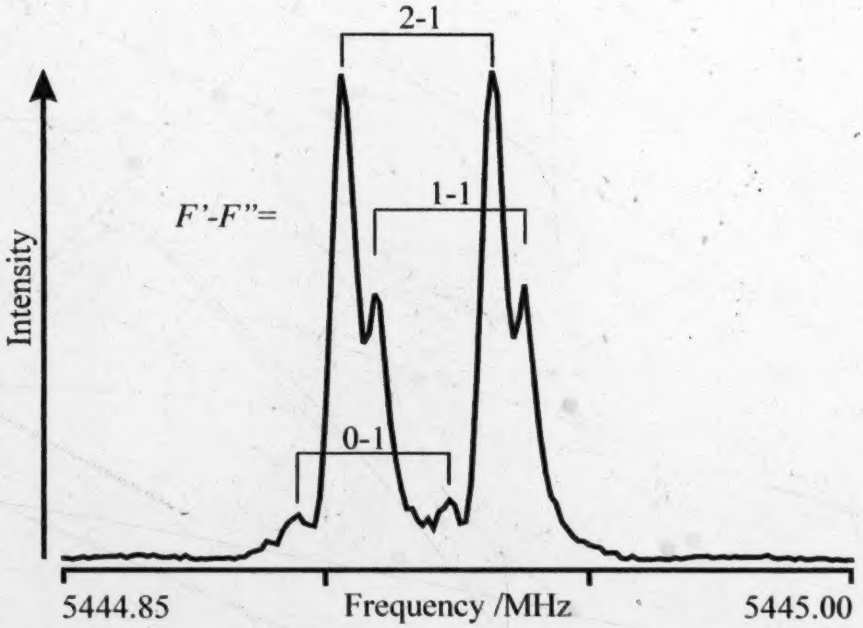
2-1
F'-F"=
1-1
0-1
Intensity
5444.85
Frequency /MHz
5445.00

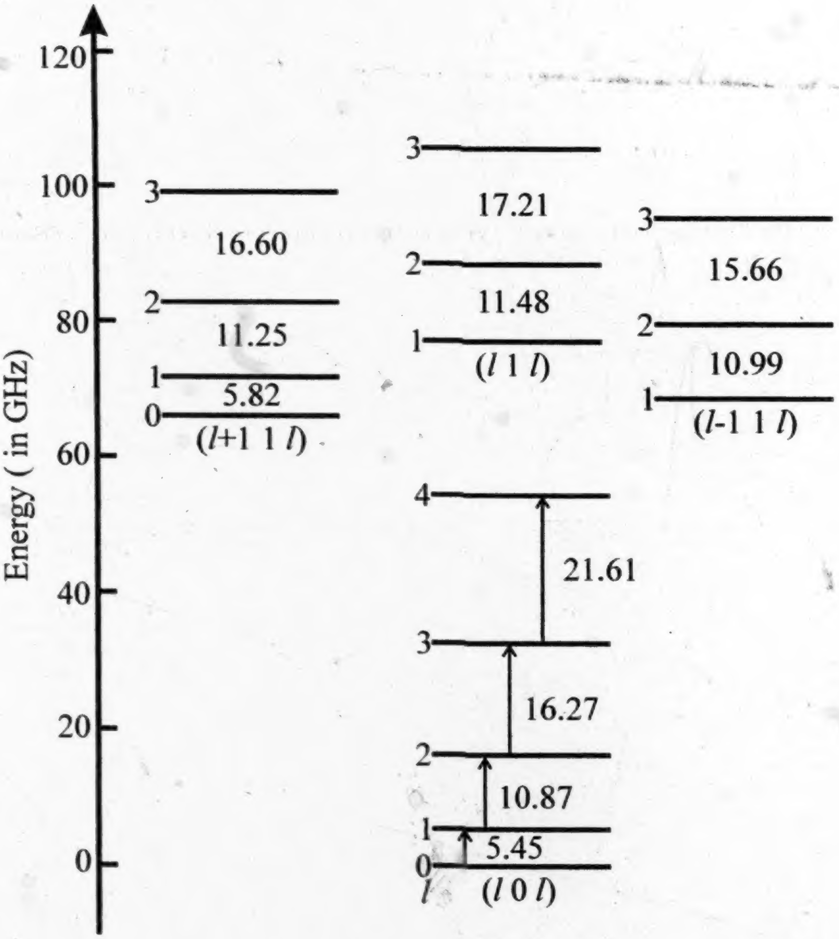
Energy (in GHz)
120
100
80
60
40
20
0
3
16.60
2
11.25
1
5.82
0
(l+1 1 l)
3
17.21
2
11.48
1
(l 1 l)
3
15.66
2
10.99
1
(l-1 1 l)
4
21.61
3
16.27
2
10.87
1
5.45
0
l
(l 0 l)

Figure 5-6: Schematic energy level diagram for ^{20}Ne-DCCH. The measured rotational transitions are represented by arrows. The energy spacings in the (*l* 0 *l*) state are determined from this study. Those in the (*l*+1 1 *l*), (*l* 1 *l*), and (*l*-1 1 *l*) states are obtained using the infrared data (*196*) and the microwave data. These values are, in fact, the energy spacings in the vibrationally excited state. They are used for the ground vibrational state assuming that they do not change significantly upon intramolecular vibrational excitation.

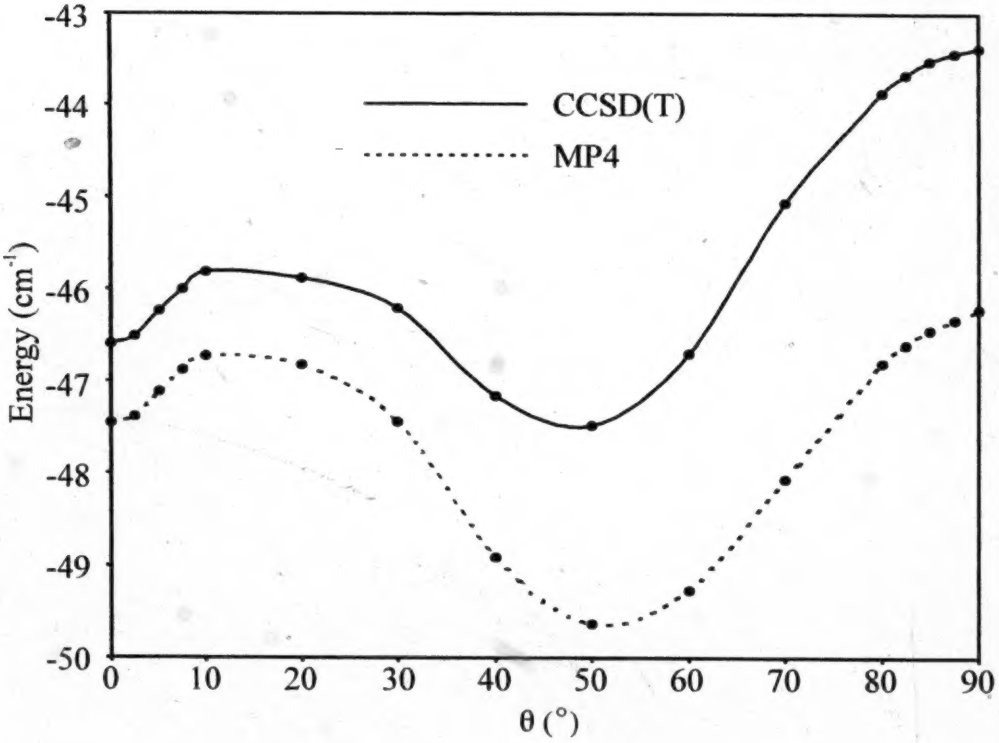

Figure 5-7: The angular dependence of the minimum interaction energy of Ne-HCCH.

6

SPECTROSCOPIC AND THEORETICAL STUDIES OF METHANE-CONTAINING VAN DER WAALS SYSTEMS

6.1 PREVIOUS STUDIES ON CH_4-CONTAINING VAN DER WAALS DIMERS

Methane occurs naturally in enormous quantities on earth (*230*). It not only exists in natural gas, it is also an active constituent of the earth atmosphere. Therefore, the interaction of methane with other simple molecules in the gas phase is relevant to how impurities in natural gas affect its properties and is also of interest in atmospheric chemistry.

In the microwave region, a series of investigations of the rotational spectra of the CH_4-HX (X=CN, Cl, Br, and HF) systems was carried out by Legon and co-workers, using the method of Fourier transform microwave spectroscopy (*231*,*232*,*233*,*234*). The observed spectra were complicated by the internal motions of the methane monomer. Different spectral patterns were observed for different dimers, providing information about the anisotropy of the associated potential energy surfaces. In the case of CH_4-HCN, each $(J+1)$-J transition consisted of four components, two of the K=0 type and two of the K=1 type. They were assigned to occur within the A, K=0; F, K=0; F, K=1; and E, K=1 states, respectively (*231*,*232*). As shown in table 3-5, *A*, *F*, and *E* are the symmetries of the associated nuclear spin wavefunctions of the *j*=0, 1, and 2 internal rotor states, respectively. The subscripts in table 3-5 are omitted here (*235*). *K* is the projection of the monomer angular momentum *j* onto the van der Waals bond. These states can be correlated with the *j*=0, 1, and 2 rotational states of free methane. An energy level correlation diagram for CH_4-HCN is schematically depicted in figure 6-1 (*45*). Since nuclear-spin-conversion is a forbidden process in the beam, the lowest energy state of each of the three symmetry species is metastable, leading to the observation of all *A*, *F*, and *E* transitions. In addition, due to a low anisotropy, the energy gap between the *K*=0 and *K*=1 states of *F* symmetry is small, leading to the observation of additional weak transitions within the *F*, *K*=1 state. In the case of the CH_4-HCl and CH_4-HBr systems, two *K*=0 and one *K*=1 components were observed, corresponding to the three lowest energy states of different symmetry (*233*,*234*,*235*). Due to an increased anisotropy and thus an increased energy gap between the *F*, *K*=0 and *F*, *K*=1 states, no *F*, *K*=1 transitions were measured. The observed spectrum of CH_4-HF is rather different. Only a single *K*=0 progression was observed (*233*). It was concluded that the internal rotation of CH_4 in the CH_4-HF dimer is quenched because of a stronger anisotropy. As a result, the spectrum follows more closely that of a conventional semi-rigid rotor. There are a number of other spectroscopic studies on methane-containing complexes, including the microwave spectrum of CH_4-O_3 (*236*), far-infrared and microwave spectra of CH_4-H_2O (*237*,*238*), infrared spectra of CH_4-*para*H_2 (*239*), and infrared spectra of CH_4-CO (*240*). The rotational spectra of CH_4-O_3 and CH_4-H_2O are further complicated by the internal motions of the O_3 and H_2O subunits, respectively.

It is desirable to use Rg-methane dimers to study the nature of the internal motions of methane within a complex, because of the reduced number of intermolecular degrees of freedom. Despite the fast progress in the spectroscopic studies of weakly bound van der Waals complexes, there are relatively few studies on rare gas-methane species. The first spectra of Kr-CH_4, Ar-CH_4, and Ne-CH_4 were recorded by McKellar, using a Fourier transform infrared spectrometer with a long path, low temperature sample cell (*32*). Strong transitions correlating to the R(0) transition of the ν_3 triply degenerate stretching mode of the CH_4 monomer were measured for Kr-CH_4 and Ar-CH_4. Only weak features were detected for Ne-CH_4. Although the spectra displayed partially resolved rotational structures, they were not well understood and no assignments were obtained. Spectra of Ar-CH_4 in the same spectral region were also recorded by Lovejoy and Nesbitt, using a diode laser absorption spectrometer in combination with a supersonic slit expansion (*241*). Predissociation broadening was observed, possibly due to a complex-induced intramolecular coupling between the ν_1 and ν_3 modes of CH_4. Further low temperature spectra of Ar-CH_4 under molecular beam conditions were reported by Block and Miller (*242*). The spectra were initially unassigned. However it was deduced from the large spacings between the sub-bands that methane is nearly freely rotating within the complex. The assignment of the spectrum (*242*) was not achieved until a few years later, after dynamical calculations were performed using an *ab initio* potential energy surface (*177,178,243*). The calculated spectrum agreed qualitatively with the recorded infrared spectrum (*242*) and assisted in assigning most of the transitions. Further spectroscopic studies included spectra of Ar-CH_4 and Kr-CH_4 recorded in the methane v_4 mode region by Pak *et al.*, with a tunable diode laser spectrometer (*175,244,245*). After an initial misassignment (*244)*, the spectra were later reassigned to the P, Q, and R branches corresponding to the Q(0) transition of the methane monomer, utilizing the theory developed by Brooks *et al.* for Ne-SiH_4 (*175,246*). A Coriolis term was explicitly incorporated into the Hamiltonian expression to be able to fit the spectrum. In addition, a number of nearly forbidden transitions were measured, from which ground state rotational constants were obtained using combination differences.

Surprisingly, *ab initio* results for Rg-CH_4 complexes are very limited. Szczęśniak *et al.* reported a few cuts through the interaction potential of Ar-CH_4, calculated at the MP2 level with a small basis set (*176*). The calculation predicted an equilibrium structure of a face configuration, where the Rg is on one of the C_3 axes of CH_4 and approaches the face of the CH_4 tetrahedron (see figure 6-2). The equilibrium intermolecular separation R_e between the Ar atom and the center-of-mass of methane was determined to be 7.5 bohr. A well depth of -113 cm^{-1} was obtained. However, it was proposed that the position of the minimum may have been overestimated by 0.5 bohr, while the well depth may have been underestimated by 25%, because of the low level of theory and the small basis set employed. More recently, Heijmen *et al.* applied SAPT to compute the Ar-CH_4 intermolecular potential energy surface. The minima were determined to be at face configurations, in agreement with the previous theoretical study (*176*), but R_e was determined to be 7.00 bohr, with a well depth of -144.30 cm^{-1} (*177*). The SAPT potential was fitted to an analytical form and was used to generate rotationally inelastic scattering cross sections for Ar-CH_4. It reproduced most of the experimentally observed features (*247*). It was also used to calculate the infrared spectrum, which assisted in assigning the observed spectra (*178,243*). However, it was evident from the comparison with the experimental infrared spectra that the potential energy surface needed further improvement. Nonetheless, the reported ground state energy levels are expected to guide further spectroscopic studies.

In the following sections, the rotational spectra of various isotopomers of the Kr-CH_4 and CO-CH_4 dimers are presented. The results are expected to facilitate further infrared spectral assignments. For Kr-CH_4, no infrared transition originating from the *E* or the *F* state has been reported so far. The same situation applies to CO-CH_4. There are many unassigned features in the infrared spectrum of CO-CH_4, which most likely correspond to the *E* and *F* states of CH_4 (*240*). This microwave investigation provides accurate information about the *E* and *F* levels in the ground vibrational state, which may be used in assigning infrared transitions originating from these levels. Potential energy surfaces were constructed for the Kr-CH_4 and Ar-CH_4 systems. In addition, dipole moments of these two dimers were also computed and compared.

6.2 OBSERVED SPECTRA AND ANALYSES

6.2.1 Kr-CH_4

The sample mixture contained 0.3% CH_4 and 1% Kr with enough Ne added to maintain a total pressure of 6 atm. Transition intensities dropped quickly when the sample mixture pressure fell below 3 atm. Five Kr isotopes were studied, all in their natural abundances (^{84}Kr: 56.90%,^{86}Kr: 17.37%, ^{82}Kr: 11.56%,^{83}Kr: 11.55%, and ^{80}Kr: 2.27%,). Isotopomers containing $^{13}CH_4$, CD_4, CH_3D, and CHD_3 were measured using isotopically enriched samples ($^{13}CH_4$, CH_3D, and CHD_3: 99% ^{13}C and 98% D, respectively, Cambridge Isotope Laboratories, CD_4: 98% D, Merck Sharp & Dohme of Canada).

Due to the extremely small cross section for nuclear-spin-relaxation, complex energy states correlating with all three spin modifications of CH_4, namely *A*, *E*, and *F*, are expected to present in the molecular beam. Due to the large rotational constant of CH_4 (5.24 cm^{-1}) (*179*) and the low temperature of the molecular beam (< 1 K), only the few lowest energy dimer states of each spin modification are populated. They are the j=0, K=0 state of *A* symmetry, the j=1, K=0 and 1 states of *F* symmetry, and the j=2, K=1 state of *E* symmetry. State density ratios for free methane are approximately 1:1:3 for *A*:*E*:*F* (*181*, *235*). Nuclear spin statistical weights for the three spin modifications are 5, 2, and 3, respectively (see table 3-5). Therefore, the relative populations of the *A*, *E*, and *F* Kr-CH_4 symmetry species are 5, 2, and 9, respectively. Here, the ($J\,j\,K$) labeling scheme is employed to label the rotational levels, where J denotes the total angular momentum of the dimer, j denotes the angular momentum of the methane monomer, and K denotes the projection of j onto the intermolecular axis. The energy gap between the j=1, K=0 and the j=1, K=1 state depends on the angular anisotropy of the corresponding potential energy surface (*45*,*235*). In the free rotor limit, these two states are degenerate. In the rigid rotor limit, the separation between the two states is the largest. The j=1, K=1 state is doubly degenerate. The degeneracy can be lifted by a Coriolis interaction with the j=1, K=0 state, which couples the j=1, K=0 state to only one of components of the j=1, K=1 state (*175*). The effect of the Coriolis interaction is schematically shown in figure 6-3.

The *j*=0, *K*=0 ground state transition frequencies of the main isotopomer, ^{84}Kr-CH$_4$, were predicted using the previously determined ground state rotational constant from the infrared spectrum (*175*). The *J*=2-1 transition was predicted to be at 8964 MHz, and was located at 8960 MHz. Other *J* transitions and transitions containing other Kr isotopes were located straightforwardly. The *K*=0 assignment was confirmed by finding the *J*=1-0 transition at approximately half the frequency of the *J*=2-1 transition. The frequency spacings among different isotopomers follow the pattern of a pseudodiatomic molecule where methane is considered as one moiety with a total mass of 16 amu. Nuclear hyperfine structure arising from the spin *I*=9/2 ^{83}Kr nucleus was observed, further confirming the assignment to a Kr-containing species. Four transitions, ranging from *J*=0 to *J*=4 were measured for the ^{86}Kr-CH$_4$, ^{84}Kr-CH$_4$, and ^{82}Kr-CH$_4$ isotopomers, respectively. The *J*=4-3 transition could not be measured for the ^{80}Kr-CH$_4$ isotopomer, due to the low natural abundance of the ^{80}Kr isotope (2.27%). Only the two lowest *J* transitions were recorded for ^{83}Kr-CH$_4$, due to the hyperfine splittings.

The searches for the *j*=1 transitions were not as straightforward. No rotational constant was available for the *j*=1 state in the ground vibrational state. Furthermore, it was observed in the infrared spectrum that the *j*=1 rotational levels are severely perturbed in the excited vibrational state as a result of a Coriolis interaction between the *j*=1, *K*=0 and *j*=1, *K*=1 states (*175*). A similar situation is expected for the ground vibrational state, which may give rise to irregular rotational transition patterns. The *j*=1 transition frequencies were predicted using the determined *j*=1 rotational constant and the Coriolis term for the excited vibrational state (*175*), assuming that the rotational structure does not vary much upon intramolecular vibrational excitation. The J=2-1, K=0 transition was thus predicted to be at 6457 MHz. The entire range from 6 GHz to 7 GHz was scanned, but no additional Kr-CH_4 transition was observed. From the observed rotational spectrum of the closely related Ar-SiH_4 dimer, it was noticed that the j=1, K=0 transitions were located at higher frequencies compared to the ground state transitions (*45*). The higher frequency range, from 9 GHz to 10 GHz, was then scanned. Still, no new Kr-CH_4 transition could be located. The lower frequency range from 7 GHz upwards, were then searched. After an extensive search, a strong transition was located at 7956 MHz, accompanied by two weaker transitions, one below and one above. The two weaker transitions showed the appropriate isotopic spacings for Kr binding to a unit with mass 16 amu. This set of transitions was therefore assigned to the J=2-1, K=0 transition of different isotopomers of Kr-CH_4. The assignment was confirmed by finding a ^{83}Kr-CH_4 transition with nuclear quadrupole hyperfine structure. The search for the other J transitions was complicated by the Coriolis interaction with a nearby K=1 state and involved wide frequency range scanning. A microwave-microwave double resonance technique was applied to confirm the relateness of these perturbed j=1, K=0 transitions. The pump microwave radiation was introduced into the microwave cavity through a horn antenna. It travels perpendicularly to the molecular beam (*107*). The molecular ensemble passes through the pump radiation when it travels from the nozzle to the other end the microwave cavity. During this passing-through period, the pump radiation can affect the population distribution of the involved rotational levels if it is in resonance with a rotational transition. This population change can then be detected by monitoring the intensity of a second rotational transition that involves one of the pump transition energy levels. For example, in one experiment, the pump radiation was adjusted to be at the frequency of the *J*=3-2 transition. The intensity of the probe transition, the *J*=2-1 transition, increased when the pump radiation was on compared to the case when the pump radiation was off. This is because the pump radiation effectively decreased the population of the *J*=2 rotational level and therefore increased the population difference between the *J*=1 and 2 levels. Compared to the corresponding *j*=0 transitions, the newly assigned *j*=1 transitions are only slightly more intense, in disagreement with the expected ratio of the spin statistical weights of 9:5 for the two states. This can be partially accounted for by the observation of narrow splittings in the *j*=1, *K*=0 transitions. One possible reason for the splittings is spin-spin and spin-rotation interactions associated with the four spin *I*=1/2 hydrogen nuclei. The *j*=1 internal rotor state is associated with nuclear spin wavefunctions of *F* symmetry, with a total spin of *I*=1. Therefore, spin-spin and spin-rotation interactions are possible in the *j*=1 internal rotor state. The frequency of the most intense component was recorded as the transition frequency. An example spectrum of the *J*=1-0 transition is shown in figure 6-4. Representative spectra of the *J*=1-0 and 2-1 transitions of ^{83}Kr-CH_4 showing the ^{83}Kr nuclear quadrupole hyperfine structure are given in figure 6-5.

With no information about the *j*=2, *K*=1 state available, the search for the transitions within this state started in the frequency range above the corresponding ground state transitions, based on the observation of higher frequency *j*=2, *K*=1 transitions for

Ar-SiH_4 (*45*). The search turned out be unsuccessful. At the same time, two transitions, namely J=2-1 and 3-2, were measured by the NIST group for the ^{84}Kr-CH_4 and ^{86}Kr-CH_4 isotopomers (*248*). These transitions were located below the corresponding j=0, K=0 transitions, and were relatively more intense. With the frequencies provided by the NIST group, the J=4-3 transition was measured, as well as transitions for three other minor isotopomers, namely ^{83}Kr-CH_4, ^{82}Kr-CH_4, and ^{80}Kr-CH_4. These transitions follow a regular a-type transition pattern. No J=1-0 transition was recorded, indicating that these transitions occur within a K=1 state. Even though the relative intensities disagree with the spin statistical weight of 2 for a j=2 state, this set of transitions was tentatively assigned to be the j=2, K=1 transitions.

All measured transition frequencies are listed in tables 6-1 and 6-2. A pseudodiatomic model was used to fit the transition frequencies to the rotational constant B and the centrifugal distortion constant D (see table 6-1). Despite the Coriolis perturbation, the j=1, K=0 transitions could be fitted to the same set of parameters. The Coriolis interaction is clearly revealed by the negative centrifugal distortion constants and the large standard deviations obtained from the fitting procedures. For the ^{83}Kr-CH_4 isotopomer, a first order quadrupole fit was used to obtain the nuclear quadrupole coupling constant χ_{aa} (see table 6-2).

A pseudodiatomic approach with scaled reduced mass was used to predicate the locations of the transitions of the Kr-$^{13}CH_4$ and Kr-CD_4 isotopomers. The measured transition frequencies are listed in tables 6-2 to 6-5. Among the three sets of transitions, the j=0, K=0 transitions are the weakest. The j=1, K=0 transitions are more intense, in agreement with the spin statistical weights of 5/5 and 9/18 (Kr-$^{13}CH_4$/Kr-CD_4) for the two states. However, the tentatively assigned j=2, K=1 transitions again appeared to be more intense than expected with a spin statistical weight of 2/4 (Kr-$^{13}CH_4$/Kr-CD_4). No nuclear quadrupole hyperfine structure due to the spin I=1 deuterium nuclei were resolved for the j=0, K=0 transitions of Kr-CD_4. Narrow splittings were also observed in the j=1, K=0 transitions, similar to the case of Kr-CH_4. They are possibly due to nuclear quadrupole interaction of the deuterium nuclei with the overall rotation of the complex, or spin-spin and spin-rotation interactions. A similar fitting procedure as described for Kr-CH_4 was applied and the resulting spectroscopic constants can be found in tables 6-2 to 6-5.

For the Kr-CH_3D and Kr-CHD_3 isotopomers, the partial substitution breaks the T_d(M) symmetry. The two isotopomers have C_{3v}(M) symmetries instead (see table 3-5). Spin statistical weights of the j=0 and j=1 internal rotor states are 4 and 4 for Kr-CH_3D and 11 and 16 for Kr-CHD_3. The j=2 internal rotor state is no longer metastable (see **3.2.3** (*b*)). Consequently, only transitions within the j=0, K=0 and j=1, K=0 states were recorded. The observed relative intensities are in qualitative agreement with the spin statistical weights. The measured transition frequencies for the Kr-CH_3D and Kr-CHD_3 isotopomers are listed in tables 6-5 and 6-6, along with fitted spectroscopic constants. A spectrum of the J=1-0, j=0, K=0 transition of ^{83}Kr-CH_3D is given in figure 6-6 as an example.

6.2.2 CO-CH_4

Compared to Kr-CH_4, the rotational spectrum of the CO-CH_4 complex is expected to be further complicated by the internal rotation of the CO moiety. However, it was determined from the infrared spectrum that the separation between the two lowest CO internal rotor states, namely the j_{CO}=0, K=0 and j_{CO}=1, K=1 states, is 2.181 cm^{-1} (*240*). Energy levels in the j_{CO}=1, K=1 internal rotor state are therefore not expected to be well populated. Spectral searches were focused on the transitions within the j_{CO}=0, K=0 internal rotor state.

The sample mixture consisted of 0.5% CH_4 and 0.5% CO in Ne with pressures up to 6 atm. Isotopomers containing $^{13}CH_4$, CD_4, CH_3D, and CHD_3 were measured using isotopically enriched samples ($^{13}CH_4$, CH_3D, and CHD_3: 99% ^{13}C and 98% D, respectively, Cambridge Isotope Laboratories, CD_4: 98% D, Merck Sharp & Dohme of Canada). Isotopomers containing ^{13}CO were investigated with a sample containing 99% ^{13}C (Cambridge Isotopes Laboratories). It is specified to contain ~10% $^{13}C^{18}O$, and was found to contain a trace amount of $^{13}C^{17}O$.

The spectral search followed closely that of Kr-CH_4. For the main isotopomer CO-CH_4, the j=0, K=0 transitions were easily located following the predications by McKellar and co-workers (*240*). They were all within 1 MHz of the predictions. The j=1, K=0 and j=2, K=1 transitions were straightforwardly located by comparing to the trend of the observed transitions of Kr-CH_4. The relative intensity pattern was also similar to that of Kr-CH_4. Once the rotational spectrum of the main isotopomer was recorded, the spectra of the seven minor isotopomers, namely CO-$^{13}CH_4$, CO-CD_4, CO-CH_3D, CO-CHD_3, ^{13}CO-CH_4, $^{13}C^{18}O$-CH_4, and $^{13}C^{17}O$-CH_4, were predicted and recorded. Nuclear hyperfine structure due to the spin I=5/2 ^{17}O nucleus was observed. The individual hyperfine components were assigned for the J=1-0 transitions of the

$^{13}C^{17}O$-CH_4 isotopomer. The spectrum of the *J*=1-0, *j*=0, *K*=0 transition is shown in figure 6-7. The measured transition frequencies are given in tables 6-7 and 6-8.

An extensive search for the transitions within the j_{CO}=1, *K*=1 internal rotor state was performed. Samples much richer in CO (5-10%) and CH_4 (5-10%) were used in attempts to raise the rotational temperature of the beam (*249*). However, no additional transition could be assigned.

6.3 DISCUSSION OF SPECTROSCOPIC RESULTS OF Kr-CH_4

6.3.1 Spectroscopic Constants and Structure

The ground state *B* rotational constant of ^{84}Kr-CH_4, 2240.27 MHz, is in very good agreement with the previously obtained value from the infrared spectrum by Pak *et al.*, 2241.39 MHz (*175*). The small difference is partly due to the fact that the quadratic centrifugal distortion constant *D* was assumed to be the same for the ground and the excited vibrational state in ref. *175*. A value of 39.35 kHz was determined for *D* in the infrared work (*175*), 18% smaller than the value of 47.88 kHz determined here.

The obtained spectroscopic constants were used to determine the van der Waals bond length *R*, the van der Waals stretching frequency ν_s, and the corresponding force constant k_s, using the pseudodiatomic expressions (*45*):

$$\begin{aligned} B &= \hbar^2 / 2\mu R^2 \\ \nu_s &= \left(4B^3/D\right)^{1/2} \\ k_s &= 4\pi^2 \nu_s^2 \mu, \end{aligned} \qquad (6\text{-}1)$$

where μ is the pseudodiatomic reduced mass. This calculation was performed only for the

j=0, K=0 and j=2, K=1 states, but not for the j=1, K=0 state because of the Coriolis interaction involved. The results are listed in table 6-9. The R value is determined to be 4.097 Å for the ground state of ^{84}Kr-CH$_4$, slightly longer than the previously determined value of 4.094 Å (*175*), reflecting the slightly larger B rotational constant from the infrared study. Ground state R values for the other isotopomers are in line with this value, with small isotopic variations. The normal trend of a decrease in R upon substitution with a heavier isotope is observed, with the magnitude of isotopic variation smallest for Kr substitution and largest for deuterium substitution. The stretching force constant k_s is determined to be 0.828 Nm^{-1} for ^{84}Kr-CH$_4$, comparable to, but smaller than, the corresponding values for ^{84}Kr-H$_2$O (1.06 Nm^{-1}) (*82*) and ^{84}Kr-NH$_3$ (1.02 Nm^{-1}) (*84*). The van der Waals bond is more rigid in the Kr-CD$_4$ isotopomers. The k_s value for ^{84}Kr-CD$_4$ is 0.928 Nm^{-1}, more than 10% greater than that of ^{84}Kr-CH$_4$. It is noticed, however, that the k_s values for the Kr-CH$_3$D and Kr-CHD$_3$ isotopomers are surprisingly small. For example, the k_s values are 0.686 and 0.757 Nm^{-1} for ^{84}Kr-CH$_3$D and ^{84}Kr-CHD$_3$, 17% and 9% smaller than that of ^{84}Kr-CH$_4$, respectively. Similar trends were also observed in the Ar-NH$_3$ (*85*) and Kr-NH$_3$ (*84*) complexes. It was found that the partially deuterated species, Ar/Kr-NH$_2$D and Ar/Kr-NHD$_2$, have smaller force constants than that of Ar/Kr-NH$_3$. This may be a result of an increased anisotropy in the internal rotation coordinate for the partially deuterated species, since orientations where deuterons are closer to Kr are expected to be more stable in these systems. This unusual trend is an indication of the inadequacy of the pseudodiatomic approximation applied, which neglects the coupling between the van der Waals radial coordinate and the internal rotation coordinate. Compared to the ground state, the j=2, K=1 state has a slightly longer van der Waals bond and a reduced stretching force constant.

Angular information may be obtained from the observed nuclear quadrupole hyperfine structures that are due to the spin I=9/2 ^{83}Kr nucleus. For an isolated Kr atom, the nuclear quadrupole coupling constant is zero because of the spherically symmetric electric charge distribution. The determined non-zero quadrupole coupling constant values can to a first approximation be considered measures of the distortion of the spherical charge distribution caused by the electric field created by the methane molecule at the site of the Kr nucleus. The Kr nuclear quadrupole coupling constant χ_{aa} can be expressed as the product of the quadrupole moment Q of the ^{83}Kr nucleus and the electric field gradient q at the nuclear site (*250*):

$$\chi_{aa} = -\frac{eqQ}{h}, \tag{6-2}$$

where e is the electron charge and h is the Plank's constant. The field gradient q can be written as $q = q_0\,(1\text{-}\gamma)$, where γ is the Sternheimer shielding constant, determined to be -77.5 for ^{83}Kr (*250*). The contributions to the field gradient at the Kr site due to the methane moiety arise from the first few non-zero electric moments of methane and can be evaluated using (*250*):

$$q_0 = -20\Omega\left\langle\frac{P_3(\cos(\theta - 54.74))}{R^6}\right\rangle - 30\Phi\left\langle\frac{P_4(\cos\theta)}{R^7}\right\rangle - .... \tag{6-3}$$

θ is the angle between the R vector and the z-axis as defined in figure 6-2. The brackets indicate averaging over large amplitude motions of methane. Only Ω and Φ, the electric octopole and hexadecapole moments of methane, will be considered here. Because of the tetrahedral symmetry of methane, it is possible to characterize the components of the multipole moments by single scalar quantities (*251*). The values determined are Ω=2.22 DÅ^2 and Φ=4.8 DÅ^3 (*251*,*252*). Here, Ω and Φ correspond to the magnitude of the components along the $(x\ y\ z)=(\sqrt{2}\ \ 0\ 1)$ direction, i.e., θ=54.74° and ϕ=0° and the z-axis, i.e., θ=0° and ϕ=0°, respectively, using the xyz axes frame defined in figure 6-2 (*251*,*252*). The nuclear quadrupole moment of ^{83}Kr Q(Kr) was determined to be 0.27 b (*253*). Using R=4.097 Å and χ_{aa} = -1.147 MHz as determined for the j=0, K=0 state of ^{83}Kr-CH$_4$, an unphysical value was obtained for $\langle\cos\theta\rangle$. On the other hand, using R=4.118 Å and χ_{aa} = -0.842 MHz as determined for the j=2, K=1 state of ^{83}Kr-CH$_4$, values of average $\langle\theta\rangle$ were obtained as 116.6° and 133.6°. Assuming there would be very little changes when going from Kr to Ar, this result agrees rather well with the available theoretical results for Ar-CH$_4$. The contour plot of the lowest energy E symmetry wavefunction of Ar-CH$_4$ shows that the j=2, K=1 state is rather localized near the global minimum, i.e., at the face configuration with θ=125.26° (*178*). The determined values for ^{83}Kr-CH$_4$ bracket the equilibrium θ value with angular excursions of 9° in both directions.

As pointed out in **5.2.3(*a*)**, it is often difficult to separate the two contributions to the determined nuclear quadrupole coupling constant, namely the contribution from the geometry of the dimer and from the large amplitude internal motions. In this case, extreme χ_{aa} values for rigid structures were calculated using equation (6-3). The maximum and minimum values were determined to be 1.7 MHz and -1.0 MHz for θ=176.5° and 125.3°, respectively. The ground state χ_{aa} value of -1.147 MHz is beyond the lower limit. This explains the unphysical value obtained for $\cos\theta$. For the j=2, K=1 state, the χ_{aa} value, -0.842 MHz, is relatively closer to the minimum value at the face configuration, θ=125.3°. This is in agreement with the localized nature of this state. For the case of freely rotating CH_4, values of zero for q_0 and χ_{aa} result. It is somewhat surprising that the obtained ground state χ_{aa} value is not close to this free rotation value.

One possible reason for the failure of using the above equation to deduce meaningful angular information about the ground state might be the significant contribution of other effects to the distortion of the ^{83}Kr electron clouds, such as dispersion interaction. Previous studies on the Kr-HX (X=CN, F, and Cl) (*24,250,254*) and Kr-Ne (*255*) systems have shown that these effects may not be negligible. The determined ^{83}Kr nuclear quadrupole coupling constants of Kr-HX series were plotted as a function of the electric field gradients q_0 at the Kr nucleus, calculated from the multipole moments of the individual binding partner. A straight line resulted, having a χ_{aa} intercept of -0.44 MHz (*24*). For a electric field gradient q_0=0, a nonzero value for χ_{aa} results, which can be regarded as a contribution from other effects. This is in agreement with the non-zero χ_{aa} value of -0.5205 MHz determined for Kr-Ne, where q_0 is zero using the above equation (*255*). In the case of Kr-methane, where the octopole moment term is the leading term contributing to q_0 in equation (6-3), one may need to take into account other effects that contribute to q_0. When the value of -0.5205 MHz (*255*) was taken as the contribution of other effects and was subtracted from the experimentally determined values for ^{83}Kr-CH_4, θ angles of 111.1°/138.7° and 105.9°/143.1° were obtained for the j=0, K=0 and the j=2, K=1 state, respectively.

6.3.2 Coriolis Interaction in the *j*=1 State

The observed irregular transition patterns of the *j*=1, *K*=0 transitions suggest that the involved levels are Coriolis perturbed by nearby *j*=1, *K*=1 levels. Since the perturbing *K*=1 levels were not observed in this microwave study, a fitting procedure that includes a Coriolis interaction term, as described in ref. *175*, could not be applied. However, qualitative information about the energy difference between the two perturbing states can be obtained by comparing the severity of the perturbation in different vibrational states and different isotopomers.

The consequence of the Coriolis interaction is to compress the energy levels in the lower energy state, which in this case is the *j*=1, *K*=0 state, leading to a reduced effective *B* rotational constant. How severe this perturbation effect is depends on how large the energy gap between the two interacting states is. Generally, the closer the two states are, the more severe the perturbation is. For the Kr-CH_4 van der Waals complex, the energy gap between the *j*=1, *K*=0 and the *j*=1, *K*=1 state is determined by the angular anisotropy of the associated potential energy surface (*175*). In the free-rotor limit, the two states are degenerate. As the anisotropy increases, the energy gap also increases. In the rigid rotor limit, where the anisotropy is the greatest, the energy gap also reaches its maximum. It becomes the energy difference between the *K*=0 and the *K*=1 state for a semi-rigid symmetric top (*235*). Using the fitted parameters for the excited ν_4 vibrational state (*175*), the *J*=2-1, *j*=1, *K*=0 transition can be predicted to be at 6457 MHz. The corresponding transition within the ground vibrational state was located at 7956 MHz, 1.5 GHz higher than the value within the excited vibrational state. This comparison suggests that the perturbation effect is more pronounced in the excited vibrational state. Therefore, one may say that the energy difference between the j=1, K=0 and the j=1, K=1 state is larger in the ground vibrational state than that in the excited state. It in turn suggests that the angular anisotropy decreases upon vibrational excitation.

The severity of the perturbation in different isotopomers was also examined. The difference between the J=3-2 transition frequency and 1.5 times of the J=2-1 transition frequency was compared. The values obtained were 94.4, 75.0, 1.6, 154.4, and 2.9 MHz for ^{84}Kr-CH_4, ^{84}Kr-$^{13}CH_4$, ^{84}Kr-CD_4, ^{84}Kr-CH_3D, and ^{84}Kr-CHD_3, respectively. The J=1-0 transition of ^{84}Kr-CD_4 was not measured, since it lies out of the normal operating range of the spectrometer. Nonetheless, the comparison of the difference between the J=2-1 transition frequency and twice of the J=1-0 transition frequency for the other isotopomers gave the same trend. This comparison implies that the Coriolis perturbation is more pronounced in the lighter isotopomers. The smaller standard deviations of the fits for the heavier isotopomers can also be considered indicators of less severe Coriolis perturbations (see tables 6-1, 6-3, 6-4, and 6-6). This conclusion can be interpreted in the following way. A heavier isotopomer experiences a slightly stronger anisotropy as a consequence of a lower zero-point energy. This leads in turn to a slightly larger separation between the two perturbing states and to a less pronounced perturbation. A similar effect was very recently reported for the CN-H_2/D_2 (j=1) van der Waals complexes by Heaven and co-workers (*256*). It was observed that the impact of isotopic substitution on the rotational constant is unusually small from their rotationally resolved electronic spectra of CN-H_2 and CN-D_2. It was proposed that this unusual isotope effect is caused by a more pronounced Coriolis interaction in the lighter CN-H_2 dimer based on theoretical calculations.

6.3.3 Tentative Assignment of the j=2, K=1 State

The third, unperturbed set of transitions was tentatively assigned to be occurring within the j=2, K=1 state, despite the fact that the relative intensity of this set of transitions does not agree with the predicted spin statistical weights from the molecular symmetry group analysis (see **3.2.3** (*b*)). Symmetry considerations suggest that these j=2 transitions of E symmetry should be the weakest among all. However, these tentatively assigned j=2, K=1 transitions are more intense than the j=0, K=0 transitions. At first sight, it may appear that this set of transitions is more likely to be the unperturbed j=1, K=1 transitions of F symmetry. In the absence of a Coriolis interaction, the j=1, K=1 state is doubly degenerate. The degeneracy is removed by the Coriolis interaction with the nearby j=1, K=0 state. The interaction can only occur between the j=1, K=0 and j=1, K=1^+ states as shown in figure 6-3. This leaves the j=1, K=1^- component unperturbed. Here the superscripts + and - are used to denote the even and odd parities of the states. It is believed that this third set of transitions does not occur within the j=1, K=1, F symmetry state, based on the following reasoning.

First of all, from the molecular symmetry group analyses for the isotopomers with C_{3v} symmetry , it is determined that the j=0 and the j=1 internal rotor states correlate with different spin modifications of the methane monomer. However, the j=2 states are no longer metastable (see **3.2.3** (*b*) and table 3-5). Consequently, they are not expected to be appreciably populated in the cold molecular beam. If the additional set of transitions measured for the Kr-CH_4, Kr-$^{13}CH_4$, and Kr-CD_4 isotopomers are the j=1, K=1 transitions, the same set of transitions should also be observable for the two isotopomers with C_{3v} symmetry. On the other hand, if this set of transition is occurring within a j=2 state, it would not be surprising that the same set of transitions is not observable for the Kr-CH_3D and Kr-CHD_3 isotopomers. No corresponding transitions were measured for the Kr-CH_3D and Kr-CHD_3 isotopomers. This strongly supports the assignment to the j=2, K=1 state.

Secondly, this set of transitions is also too intense for the j=1, K=1 transitions. Using 2α (α=0.338232 cm^{-1}, see ref. *175*) as the energy separation between the j=1, K=1 and j=1, K=0 states in the excited vibrational state, assuming a temperature of 0.5 K and Boltzmann distribution, the relative population of the j=1, K=1 state compared to that of the j=1, K=0 state is 0.14. Since the energy separation is even larger in the vibrational ground state (see previous section), the relative population is expected to be even lower than this value. It is further reduced by the lowering of the j=1, K=0 state as a result of the Coriolis interaction. Consequently, it is expected that the j=1, K=1 transitions have approximately 1/10 of the intensities of the j=1, K=0 transitions. An accurate intensity comparison is complicated by the observed splittings in the j=1, K=0 transitions. However, by comparing higher J transitions, where the splitting is not as pronounced, it is concluded that this third set of transitions is too intense to be the j=1, K=1 transitions.

On the other hand, the assignment to the j=2, K=1 state is qualitatively supported by comparison with the calculated Ar-CH_4 energy levels (*178*), assuming that Kr-CH_4 and Ar-CH_4 behave similarly. From the calculated energy levels (see TABLE IV in ref. *178*), the J=2-1 transition frequencies of Ar-CH_4 were determined to be at 11010 MHz, 8940 MHz, and 10710 MHz for the j=0, K=0; j=1, K=0; and j=2, K=1 states, respectively. This trend is very similar to that of the measured frequencies for Kr-CH_4. The observed J=2-1 transitions for the ^{84}Kr-CH_4 isotopomer are at 8960 MHz, 7956 MHz, and 8869 MHz for the same three states. Also from the calculated energy levels, the unperturbed J=2-1, j=1, K=1 transition is predicted to be at 11070 MHz, above the 11010 MHz determined for the same transition within the j=0, K=0 state. This may be used to further support that the observed transition at 8869 MHz is not a j=1, K=1 transition, since its frequency is below that of the corresponding j=0, K=0 transition.

The obvious enhancement of the transition intensity remains a puzzle. One possible reason might be a relatively large effective dipole moment in this state as a result of a different vibrational averaging. The transition intensity is directly proportional to the vibrationally averaged dipole moment of the system (see equation 2-18 in chapter 2). For systems such as Kr-CH_4, the dipole moments are expected to be very small, so that a small increase in dipole moment may have a large impact on transition intensity. The notion of an increased effective dipole moment is supported by a shorter experimentally determined optimal excitation microwave pulse length for the j=2, K=1 transitions. The contour plots of the lowest A symmetry, i.e., j=0, K=0, and F symmetry, i.e., j=1, K=0, wavefunctions for Ar-CH_4 (see FIG. 1 in ref. *178*) were shown to be similar and very much delocalized. On the other hand, the wavefunction of the E symmetry, j=2, K=1 state appears to be quite localized. So, it is expected that the vibrational averaging is quite different for the j=2, K=1 state. A similar situation is anticipated to occur in the Kr-CH_4

dimer. It was established before that there is little change in the angular motion dynamics in Rg-molecule systems when going from Kr to Ar (*82*). Similar nuclear quadrupole coupling constants were determined for the Kr/Ar-NH_3 (*84,85*), Kr/Ar-H_2O (*82,257*), Kr/Ar-N_2 (*258,259*), and Kr/Ar-HCN (*24,64*) pairs. The close resemblance of the Kr-CH_4 and Ar-CH_4 infrared spectra is also supportive of this view (*175*). A different vibrational averaging of the *E* symmetry *j*=2, *K*=1 state is evident from the determined nuclear quadrupole coupling constants. χ_{aa} values of -1.139 MHz, -1.237 MHz, and -0.842 MHz were determined for the *j*=0; *K*=0, *j*=1; *K*=0, and *j*=2, *K*=1 states, respectively. The value for the *j*=2, *K*=1 state is rather different from the ones for the other two states.

The dipole moment of Kr-CH_4 was computed at various configurations (see **3.1.3** (*c*)). The obtained values are given in table 6-10. The angular dependence of the dipole moment is depicted in figure 6-8. At each angle, the dipole moment was obtained with *R* fixed at the value that gives the minimum interaction energy. A negative dipole moment points from the C atom to the Kr atom. The calculated results are supportive of the above consideration on the abnormally high intensity of the *j*=2, *K*=1 transitions. From figure 6-8, it is seen that the maximum magnitude of the dipole moment occurs at the global minimum, i.e., θ=125.26° and ϕ=0° (see the following section). In a certain internal rotor state, any averaging over the large amplitude internal motion reduces the effective dipole moment from its maximum value at the global minimum. The more delocalized the wavefunction, the smaller the effective dipole moment. Thus, the effective dipole moment is expected to be the largest in the *j*=2, *K*=1 state among the three states involved in this study, since this state is the most localized around the global minimum.

6.4 POTENTIAL ENERGY SURFACE OF Kr-CH_4

In the above discussion, it was often assumed that Kr-CH_4 and Ar-CH_4 behave similarly in order to make use of the previously reported theoretical results for Ar-CH_4 (*177*). *Ab initio* potential energy surfaces for the two dimers were constructed at the CCSD(T) level of theory, in order to check the validity of the assumption.

Computational details are given in **3.1.3** (*c*). Interaction energies were calculated with R ranging from 3.5 to 4.5 Å, θ ranging from 0 to 180°, and ϕ ranging from 0 to 90° (see figure 6-2). Additional points at the face (Rg atom approaching the face center of the CH_4 tetrahedron, θ=125.26° and ϕ=0°), edge (Rg atom approaching the edge of the CH_4 tetrahedron, θ=0° and ϕ=0°), and vertex (Rg atom approaching an H atom, θ=54.74° and ϕ=0°) configurations were calculated. All obtained energies are given in tables 6-11 and 6-12.

It is clear that the two interaction potentials have very similar features. Both have the global minimum at the face configuration, a local minimum at the edge configuration, and a saddle point between the minima at the vertex configuration. This is shown in figure 6-9, where the angular dependence of the minimum interaction energy is plotted. At each θ angle, R is allowed to vary in order to obtain the minimum energy. For Kr-CH_4, the global minimum has a well depth of -157.85 cm^{-1} at R=3.85 Å, the local minimum has an energy of -129.90 cm^{-1} at R=4.05 Å, and the saddle point is determined to have an energy of -101.90 cm^{-1} at R=4.40 Å. For Ar-CH_4, the corresponding values are determined to be -135.45 cm^{-1} at R=3.70 Å (face), -110.77 cm^{-1} at R=3.90 Å (edge), and -84.88 cm^{-1} at R=4.25 Å (vertex). The values for Ar-CH_4 are in very good agreement with the values previously reported for the SAPT potential: -135.20 cm^{-1} at *R*=3.72 Å (face), -110.76 cm^{-1} at *R*=3.91 Å (edge), and -85.00 cm^{-1} at *R*=4.18 Å (vertex) (*177*).

From this comparison, it is believed that there is little change in the angular internal dynamics when the binding partner of CH_4 changes from Ar to Kr.

6.5 DISCUSSION OF CO-CH_4

The measured rotational spectrum of CO-CH_4 resembles closely that of Kr-CH_4. The number of states observed is the same and the relative intensity patterns are similar. Even the perturbed spectral pattern in the j=1, K=0 state is very similar. This indicates that CO is nearly free rotating within the complex. In that case, CO in its j_{CO}=0 state behaves like a rare gas atom. A similar situation is thought to occur in the CO-CH_4 (j_{CO}=0, $j_{methane}$=1) and Ar-CH_4 ($j_{methane}$=1) pair by McKellar and co-workers (*240*).

On the other hand, from the $j_{methane}$=0 infrared spectrum, McKellar and co-workers concluded that CO-CH_4 is very similar to the CO-rare gas complexes. This implies that CH_4 moiety is also nearly free rotating in the complex and behaves like a rare gas atom in its j=0 state. R, ν_s, and k_s values for various isotopomers of CO-CH_4 are listed in table 6-13, calculated using equation (6-1). A comparison of these values with those of the CO-rare gas dimers is given in table 6-14. The values for the CO-rare gas dimers were calculated using the previously reported rotational and centrifugal distortion constants for the main isotopomers in refs. *249* and *260*. Even though the mass of CH_4 is closest to Ne, it appears that the properties of the CO-CH_4 dimer fall more in line with the heavier CO-rare gas complexes. The force constant of the CO-CH_4 dimer is closer to those of the CO-Ar, CO-Kr, and CO-Xe complexes than to that of CO-Ne. The van der Waals stretching frequency decreases from CO-CH_4 to CO-Ar, and continues to decrease in CO-Kr and CO-Xe, as a result of an increase in reduced mass. This is an indication of a similar level of flexibility along the radial coordinate for these four systems.

Angular information about the CO part can be obtained from the nuclear quadrupole coupling constant of the $^{13}C^{17}O$-CH_4 isotopomer. The expression

$$\chi_{aa} = \chi_{CO}\left\langle \frac{3\cos^2\beta - 1}{2} \right\rangle \qquad (6\text{-}4)$$

was used. β is the angle between the CO bond and the *a*-principal inertial axis of the dimer and χ_{CO} is the ^{17}O nuclear quadrupole coupling constant of free $^{13}C^{17}O$. Assuming that the χ_{CO} value for $^{13}C^{17}O$ is the same as that of $^{12}C^{17}O$ (4.43 (10) MHz (*261,262*)), β values of 72.4 ° for the j=0 state and 72.9 ° for the j=1 state were obtained. The j=0 state β value is also given in table 6-14, together with the corresponding values for the CO-rare gas complexes. The β value for CO-CH_4 is close to those of CO-Ar and CO-Kr.

6.6 DISCUSSION OF Ar-CH_4

Tremendous efforts have been put into the spectral searches for rotational transitions of Ar-CH_4. However, no transition could be assigned to the Ar-CH_4 dimer. The J=1-0, j=0, K=0 transition was calculated to be at 5527 MHz using the spectroscopic constants determined from the infrared spectrum (*175*), in good agreement with the value of 5520 MHz predicted from the SAPT potential (*178*). The good agreement between the Kr-CH_4 rotational constant determined from the rotational spectrum and the one from the infrared spectrum in ref. *175* is an additional indication that the values from the infrared spectra are reliable. It is frustrating that even with the very good prediction, no rotational spectrum was recorded for the Ar-CH_4 system, despite all the efforts.

One possible explanation for this unsuccessful search is that Ar-CH_4 may have an effective dipole moment that is accidentally close to zero. In an attempt to qualitatively justify this notion, the dipole moment of Ar-CH_4 was computed at various configurations. The obtained values are listed in table 6-15. The angular dependence of the dipole moment is also plotted in figure 6-8. It is noted that the dipole moment has a negative value at the θ=0° edge configuration. When the Ar moves away from the edge of the CH_4 tetrahedron, the dipole moment increases and reaches its positive maximum at the θ=54.7° vertex configuration. On going to the θ=125.26° face configuration, the dipole moment decreases and arrives at its negative minimum at the global minium. This θ change can be viewed as the internal rotations of the methane subunit. Considering that methane is nearly free rotating within the complex, the effective dipole moment is expected to average over a wide range of the angular coordinate. It is possible that the positive and negative dipole moment values almost cancel out and a close to zero effective value results.

One may argue that the j=2, K=1 state may still have a considerable effective dipole moment, since this state is very much localized around the global minimum. Dipole moments of -0.022 D and -0.013 D were obtained for Kr-CH_4 and Ar-CH_4 at the face configuration, respectively. The value for Kr-CH_4 is almost twice as large as that for Ar-CH_4. As a result of the small dipole moment, rotational transitions of Ar-CH_4 are expected to require an extremely high microwave power to achieve the π/2 condition (see chapter 2), which may be beyond the current spectrometer setup.

6.7 SUMMARY

The first pure rotational spectrum of a Rg-methane system, namely the Kr-CH_4 van der Waals complex, is presented in this chapter. Methane is nearly free rotating within the complex, which leads to the measurements of transitions within various internal rotor states. The relative intensities of the $j=0$, $K=0$ and $j=1$, $K=0$ transitions agree with the respective nuclear spin statistical weights obtained from molecular symmetry group analyses. The irregular spectral patterns of the $j=1$, $K=0$ transitions indicate that a Coriolis interaction occur between the $j=1$, $K=0$ state and a nearby $j=1$, $K=1$ state. It is determined that the perturbation is less pronounced in the ground vibrational state than in the excited vibrational state, suggesting a reduced angular anisotropy upon intramolecular vibrational excitation. The tentatively assigned $j=2$, $K=1$ transitions are more intense than expected. The enhanced intensities are attributed to a relatively larger vibrationally averaged dipole moment than in the $j=0$, $K=0$ and $j=1$, $K=0$ states. This is supported by the *ab initio* dipole moment calculations. *Ab initio* potential energy surfaces were constructed for Kr-CH_4 and Ar-CH_4 at the CCSD(T) level. It is shown that the angular internal dynamics does not change much when the binding partner changes from Kr to Ar. The calculated CCSD(T) potential of Ar-CH_4 is consistent with the previously reported SAPT potential (*177*).

The rotational spectrum of the CO-CH_4 van der Waals complex was also recorded. It is very similar to that of the Kr-CH_4 dimer, indicating that the CO subunit in its j_{CO}=0 internal rotor state behaves similarly to a rare gas atom. The properties of the CO-CH_4 system were compared with those of the CO-rare gas complexes. It is shown that CO-CH_4 resembles more closely the behavior of the heavier CO-rare gas dimers.

Ab initio dipole moment calculations suggest that an accidentally close to zero effective dipole moment may be responsible for the unsuccessful spectral searches for rotational transitions of Ar-CH_4.

Table 6-1: Measured transition frequencies (in MHz) of Kr-CH_4 isotopomers.

$J' - J''$	^{86}Kr-CH_4		^{84}Kr-CH_4		^{82}Kr-CH_4		^{80}Kr-CH_4	
	ν_{obs}	$\Delta\nu^a$	ν_{obs}	$\Delta\nu$	ν_{obs}	$\Delta\nu$	ν_{obs}	$\Delta\nu$
				j=0, K=0				
1 - 0	4463.9550	0.3	4480.3482	-0.8	4497.5310	-0.8	4515.5632	-0.5
2 - 1	8926.7675	-1.0	8959.5482	-0.6	8993.9052	-0.3	9029.9610	0.4
3 - 2	13387.3016	0.9	13436.4516	1.2	13487.9654	1.3	13542.0240	-0.1
4 - 3	17844.4102	-0.3	17909.9042	-0.4	17978.5485	-0.4		
B /MHz	2232.0724(3)		2240.2703(3)		2248.8624(3)		2257.8791(2)	
D /kHz	47.534(9)		47.88(1)		48.24(1)		48.61(1)	
δ /kHz	1.0		1.2		1.2		0.6	
				j=1, K=0				
1 - 0	3944.0348	6.9	3955.6488	7.1	3967.7913	7.3		
2 - 1	7931.9252	2.5	7955.9612	2.5	7981.1114	2.6	8007.4553	5.5
3 - 2	11990.6780	-7.8	12028.3018	-8.0	12067.6937	-8.1	12108.5943	-6.2
4 - 3	16126.1332	2.9	16178.4122	2.9	16233.1704	3.0	16290.5943	2.0
B /MHz	1973(2)		1979(2)		1985(2)		1992(2)	
D /kHz	-1.36(7)		-1.38(8)		-1.40(8)		-1.40(9)	
δ /MHz	7.8		8.0		8.2		8.5	
				j=2, K=1				
2 - 1	8837.9770	-0.3	8868.6752	-0.5	8900.8354	-0.2	8934.5647	0.0
3 - 2	13254.0276	0.3	13300.0568	0.6	13348.2776	0.3	13398.8524	0.0
4 - 3	17666.5509	-0.1	17727.8876	-0.2	17792.1476	-0.1		
B /MHz	2209.8861(1)		2217.5633(2)		2225.606(1)		2234.0404(1)	
D /kHz	48.977(4)		49.290(8)		49.602(4)		49.91 (fixed)	
δ /kHz	0.4		0.8		0.4		0.0	

[a] $\Delta\nu = \nu_{obs} - \nu_{calc}$, the unit of $\Delta\nu$ is the same as of δ.

Table 6-2: Measured transition frequencies (in MHz) of ^{83}Kr-CH$_4$ and ^{83}Kr-^{13}CH$_4$.

J' - J''	F' - F''	j=0, K=0		j=1, K=0		j=2, K=1	
		ν_{obs}	$\Delta\nu$[a]	ν_{obs}	$\Delta\nu$	ν_{obs}	$\Delta\nu$
				^{83}Kr-CH$_4$			
1 - 0	3.5 - 4.5	4488.9266	0.1	3961.7625	2.0		
	5.5 - 4.5	4488.8794	0.3	3961.7078	-1.7		
	4.5 - 4.5	4488.6699	-0.4	3961.4818	-0.3		
2 - 1	3.5 - 4.5	8976.6495	-0.6	7968.5460	1.3	8884.7048	1.7
	5.5 - 4.5	8976.5487	0.2	7968.4337	-0.6	8884.6264	-1.5
	4.5 - 4.5	8976.5487	0.2	7968.4337	-0.6	8884.6264	-1.5
	2.5 - 3.5	8976.5363	0.1	7968.4216	0.6	8884.6187	0.2
	6.5 - 5.5	8976.5167	0.8	7968.3982	-0.7	8884.6061	2.3
	3.5 - 3.5	8976.3924	-1.4	7968.2634	-3.0	8884.5106	-3.1
	5.5 - 5.5	8976.3392	-0.4	7968.2075	0.0	8884.4738	0.2
	4.5 - 5.5	8976.3392	-0.4	7968.2075	0.0	8884.4738	0.2
	4.5 - 3.5	8976.2937	1.5	7968.1588	2.9	8884.4404	1.9
χ_{aa} /MHz		-1.139(2)		-1.237(5)		-0.842(6)	
				^{83}Kr-^{13}CH$_4$			
1 - 0	3.5 - 4.5	4271.4989	-0.3	3805.9531	0.0		
	5.5 - 4.5	4271.4522	0.7	3805.8984	2.4		
	4.5 - 4.5	4271.2412	-0.5	3805.6728	-2.4		
2 - 1	3.5 - 4.5	8541.9082	-0.3	7647.0550	-0.4	8476.6908	2.8
	5.5 - 4.5	8541.8062	-0.2	7646.9437	0.4	8476.6116	-0.4
	4.5 - 4.5	8541.8062	-0.2	7646.9437	0.4	8476.6116	-0.4
	2.5 - 3.5	8541.7938	-0.3	7646.9316	1.9	8476.6016	-1.2
	6.5 - 5.5	8541.7737	0.1	7646.9077	0.4	8473.5856	-2.0
	3.5 - 3.5	8541.6526	1.6	7646.7719	-0.8	8476.4961	-0.2
	5.5 - 5.5	8541.5967	0.1	7646.7128	-0.1	8476.4554	-0.2
	4.5 - 5.5	8541.5967	0.1	7646.7128	-0.1	8476.4554	-0.4
	4.5 - 3.5	8541.5479	-1.0	7646.6590	-1.6	8476.4224	2.1
χ_{aa} /MHz		-1.146(2)		-1.257(4)		-0.852(5)	

[a] $\Delta\nu = \nu_{obs} - \nu_{calc}$ in kHz.

Table 6-3: Measured transition frequencies (in MHz) of Kr-$^{13}CH_4$ isotopomers.

J' - J''	^{86}Kr-$^{13}CH_4$		^{84}Kr-$^{13}CH_4$		^{82}Kr-$^{13}CH_4$		^{80}Kr-$^{13}CH_4$	
	ν_{obs}	$\Delta\nu$[a]	ν_{obs}	$\Delta\nu$	ν_{obs}	$\Delta\nu$	ν_{obs}	$\Delta\nu$
				j=0, K=0				
1 - 0	4246.4892	-0.8	4262.9088	0.1	4280.1178	0.6	4298.1783	0.2
2 - 1	8491.9460	0.1	8524.7792	-0.1	8559.1907	-0.7	8595.3012	-0.2
3 - 2	12735.3420	0.5	12784.5716	0.1	12836.1678	0.3	12890.3116	0.0
4 - 3	16975.6472	-0.2	17041.2481	0.0	17110.0060	-0.1		
B /MHz	2123.3301(2)		2131.5410(4)		2140.1464(2)		2149.1770(1)	
D /kHz	42.944(7)		43.281(1)		43.615(6)		43.999(6)	
δ /kHz	0.7		0.1		0.7		0.3	
				j=1, K=0				
1 - 0	3787.6845	4.9	3799.6516	5.1	3812.1701	5.2		
2 - 1	7609.5690	1.8	7634.1757	1.9	7659.9228	1.9	7686.8942	4.0
3 - 2	11488.0116	-5.6	11526.2517	-5.8	11566.2843	-5.9	11608.2467	-4.6
4 - 3	15429.7150	2.1	15482.5512	2.1	15537.8878	2.2	15595.9110	1.4
B /MHz	1894(1)		1900(1)		1906(1)		1914(2)	
D /kHz	-1.09(5)		-1.11(5)		-1.13(6)		-1.12(6)	
δ /MHz	5.6		5.8		5.9		6.2	
				j=2, K=1				
2 - 1	8429.6150	0.2	8460.5420	0.7	8492.9418	0.0	8506.9253	-0.4
3 - 2	12641.7261	-0.2	12688.0984	-0.8	12736.6768	0.0	12787.6319	0.3
4 - 3	16850.5938	0.1	16912.3928	0.2	16977.1290	0.0		
B /MHz	2107.7636(2)		2115.4978(3)		2123.6002(1)		2132.0986(1)	
D /kHz	44.961(8)		45.27(1)		45.597(1)		45.92(fixed)	
δ /kHz	0.7		1.0		0.1		0.5	

[a] $\Delta\nu = \nu_{obs} - \nu_{calc}$, the unit of $\Delta\nu$ is the same as of δ.

Table 6-4: Measured transition frequencies (in MHz) of Kr-CD_4 isotopomers.

J' - J''	^{86}Kr-CD_4		^{84}Kr-CD_4		^{82}Kr-CD_4		^{80}Kr-CD_4	
	ν_{obs}	$\Delta\nu^a$	ν_{obs}	$\Delta\nu$	ν_{obs}	$\Delta\nu$	ν_{obs}	$\Delta\nu$
	j=0, K=0							
1 - 0	3807.6973	-1.2	3824.417	-0.6	3841.9379	-1.2		
2 - 1	7614.6376	-0.1	7648.0684	-0.7	7683.1044	-0.7	7719.8663	-0.3
3 - 2	11420.0592	1	11470.1896	1.2	11522.7268	1.7	11577.8495	0.2
4 - 3	15223.2005	-0.4	15290.0091	-0.4	15360.0255	-0.6		
B /MHz	1903.9125(3)		1912.2726(3)		1921.0340(4)		1930.2267(1)	
D /kHz	31.64(1)		31.92(1)		32.21(1)		32.51(fixed)	
δ /kHz	1.1		1.1		1.6		0.4	
	j=1, K=0							
2 - 1	7377.4985	42.5	7408.0382	44.2	7440.0243	45.8	7473.5638	47.2
3 - 2	11067.818	-48.6	11113.7005	-51	11161.7571	-52	11212.1490	-53.9
4 - 3	14759.7319	15.2	14821.0334	15.8	14885.2424	16.4	14952.5766	16.9
B /MHz	1844.19(2)		1851.82(2)		1859.80(2)		1868.18(2)	
D /kHz	-24.3(7)		-25.4(7)		-26.7(7)		28.0(8)	
δ /kHz	66.4		69.0		71.5		73.6	
	j=2, K=1							
2 - 1	7503.1382	-0.6	7534.7668	-0.9	7567.9007	-0.8	7602.6524	-0.7
3 - 2	11252.7479	0.7	11300.1765	1.1	11349.8609	0.9	11401.9723	0.8
4 - 3	15000.0021	-0.2	15063.2113	-0.3	15129.4278	-0.3	15198.8801	-0.2
B /MHz	1876.0462(3)		1883.9554(4)		1892.2410(3)		1900.9310(3)	
D /kHz	32.68(1)		32.94(2)		33.20(1)		33.47(1)	
δ /kHz	1.0		1.5		1.2		1.0	

[a] $\Delta\nu = \nu_{obs} - \nu_{calc}$, the unit of $\Delta\nu$ is the same as of δ.

Table 6-5: Measured transition frequencies (in MHz) of deuterated ^{83}Kr-CH$_4$.

$J' - J''$	$F' - F''$	ν_{obs}	$\Delta\nu^a$	ν_{obs}	$\Delta\nu$	ν_{obs}	$\Delta\nu$
				^{83}Kr-CD$_4$			
		j=0, K=0		j=1, K=0		j=2, K=1	
1 - 0	3.5 - 4.5	3833.1864	-0.2				
	5.5 - 4.5	3833.1297	2.2				
	4.5 - 4.5	3833.8651	-0.2				
2 - 1	3.5 - 4.5	7665.5426	-2.1	7424.0448	1.6	7551.2908	0.4
	5.5 - 4.5	7665.4172	-0.8	7423.8962	-0.3	7551.2081	-1.4
	4.5 - 4.5	7665.4172	-0.8	7423.8962	-0.3	7551.2081	-1.4
	2.5 - 3.5	7665.4027	0.0	7423.8760	-2.8	7551.1978	-1.9
	6.5 - 5.5	7665.3801	2.8	7423.8525	3.0	7551.1888	5.2
	3.5 - 3.5	7665.2264	1.2	7423.6714	-2.1	7551.0838	-2.7
	5.5 - 5.5	7665.1578	0.2	7423.5935	-1.8	7551.0446	1.2
	4.5 - 5.5	7665.1578	0.2	7423.5935	-1.8	7551.0446	1.2
	4.5 - 3.5	7665.0978	-0.6	7423.5313	4.5	7551.0048	-0.8
χ_{aa} /MHz		-1.420(5)		-1.644(9)		-0.906(8)	

$J' - J''$	$F' - F''$	ν_{obs}	$\Delta\nu$	ν_{obs}	$\Delta\nu$	ν_{obs}	$\Delta\nu$	ν_{obs}	$\Delta\nu$
		^{83}Kr-CH$_3$D				^{83}Kr-CHD$_3$			
		j=0, K=0		j=1, K=0		j=0, K=0		j=1, K=0	
1 - 0	3.5 - 4.5	4298.7324	0.5			3973.4830	-1.7		
	5.5 - 4.5	4298.6824	0.9			3973.4280	0.3		
	4.5 - 4.5	4298.4585	-1.4			3973.1782	1.4		
2 - 1	3.5 - 4.5	8596.1295	1.0	7531.0496	2.9	7945.9008	1.1	7641.0080	-2.3
	5.5 - 4.5	8596.0188	-1.7	7560.9292	-0.1	7945.7767	-0.8	7640.8758	-0.1
	4.5 - 4.5	8596.0188	-1.7	7530.9292	-0.1	7945.7767	-0.8	7640.8758	-0.1
	2.5 - 3.5	8596.0092	1.7	7530.9136	-1.6	7945.7649	2.1	7640.8592	-0.4
	6.5 - 5.5	8595.9862	0.3	7530.5900	-1.7	7945.7382	-0.2	7640.8361	3.3
	3.5 - 3.5	8595.8541	-2.3	7530.7485	-2.3	7945.5918	0.0	7640.6739	2.5
	5.5 - 5.5	8595.7987	-0.2	7530.6888	0.6	7945.5259	-0.8	7640.5994	-0.4
	4.5 - 5.5	8595.7987	-0.2	7530.6888	0.6	7945.5259	-0.8	7640.5994	-0.4
	4.5 - 3.5	8595.7517	3.2	7530.6354	1.9	7945.4700	0.3	7640.5348	-2.2
χ_{aa} /MHz		-1.209(5)		-1.315(6)		-1.368(3)		-1.506(6)	

[a] $\Delta\nu = \nu_{obs} - \nu_{calc}$ in kHz.

Table 6-6: Measured transition frequencies (in MHz) of Kr-CH_3D and Kr-CHD_3.

J' - J''	ν_{obs}	$\Delta\nu$[a]	ν_{obs}	$\Delta\nu$	ν_{obs}	$\Delta\nu$	ν_{obs}	$\Delta\nu$
j=0, K=0								
	^{86}Kr-CH_3D		^{84}Kr-CH_3D		^{82}Kr-CH_3D		^{80}Kr-CH_3D	
1 - 0	4273.5953	-1.4	4290.0946	-0.8	4307.3852	-2.5	4325.5301	-3.1
2 - 1	8545.9210	-0.6	8578.9082	-1.1	8613.4835	0.0	8649.7639	0.0
3 - 2	12815.7047	1.8	12865.1623	1.8	12916.9972	1.8	12971.3915	2.2
4 - 3	17081.6682	-0.6	17147.5668	-0.6	17216.6310	-0.7	17289.1060	-0.9
B /MHz	2136.9043(4)		2145.1545(4)		2153.8015(5)		2162.8752(7)	
D /kHz	52.99(2)		53.39(2)		53.82(2)		54.27(3)	
δ /kHz	1.7		1.7		2.2		2.8	
	^{86}Kr-CHD_3		^{84}Kr-CHD_3		^{82}Kr-CHD_3		^{80}Kr-CHD_3	
1 - 0	3948.0881	-0.1	3964.7482	-0.1	3982.2076	-0.2	4000.5298	0.0
2 - 1	7895.1812	0.4	7928.4924	0.2	7963.4038	1.0	8000.0370	-0.1
3 - 2	11840.2828	-0.1	11890.2283	-0.1	11942.5739	-0.4	11997.4996	0.1
4 - 3	15782.3862	-0.4	15848.9507	-0.2	15918.7018	-1.0	15991.8957	0.2
B /MHz	1974.1272(9)		1982.4579(6)		1991.1887(2)		2000.3500(4)	
D /kHz	41.490(4)		41.844(2)		42.22(1)		42.595(2)	
δ /kHz	0.4		1.0		0.2		0.2	
j=1, K=0								
	^{86}Kr-CH_3D		^{84}Kr-CH_3D		^{82}Kr-CH_3D		^{80}Kr-CH_3D	
1 - 0	3709.7500	16.0	3720.6656	16.4	3732.0750	16.8		
2 - 1	7495.5545	5.1	7518.8443	5.2	7543.2077	5.3	7568.7236	11.9
3 - 2	11390.7409	-17.2	11428.1502	-17.6	11467.3197	-18.1	11508.3799	-13.6
4 - 3	15387.0890	6.4	15439.8671	6.5	15495.1570	6.7	15553.1466	4.3
B /MHz	1859(4)		1864(4)		1870(4)		1879(5)	
D /kHz	-2.0(2)		-2.1(2)		-2.1(2)		-2.1(2)	
δ /MHz	17.6		18.1		18.5		18.6	
	^{86}Kr-CHD_3		^{84}Kr-CHD_3		^{82}Kr-CHD_3		^{80}Kr-CHD_3	
1 - 0	3796.9715	77.7	3812.0072	84.0	3827.7469	96.9		
2 - 1	7595.1130	39.9	7625.2322	39.1	7656.7778	35.9	7689.8554	74.6
3 - 2	11395.4671	-101.1	11440.7340	-104.7	11488.1462	-110.3	11537.8655	-85.3
4 - 3	15198.7064	36.5	15259.2160	38.0	15322.5960	40.5	15389.0659	26.7
B /MHz	1898.44(2)		1905.95(2)		1913.83(3)		1922.10(3)	
D /kHz	-43.9(9)		-45(1)		-47(1)		-48(1)	
δ /kHz	97.9		102.5		110.6		116.4	

[a] $\Delta\nu = \nu_{obs} - \nu_{calc}$, the unit of $\Delta\nu$ is the same as of δ.

Table 6-7: Measured transition frequencies (in MHz) of $^{12}C^{16}O-CH_4$ isotopomers.

$J' - J''$	ν_{obs}	$\Delta\nu^a$	ν_{obs}	$\Delta\nu$	ν_{obs}
	j=0, K=0		j=1, K=0		j=2, K=1^b
			CO-$^{12}CH_4$		
1 - 0	6216.0218	1.7	5760.1048	0.7	
2 - 1	12428.3284	-1.4	11540.5304	-0.5	12255.2698
3 - 2	18633.1900	0.3	17355.8302	0.1	18375.2154
B /MHz	3108.3218(8)		2878.9(3)		3064.8427
D /MHz	0.15500(5)		-0.77(2)		0.12816
δ	2.3 kHz		0.9 MHz		
			CO-$^{13}CH_4$		
1 - 0	5994.2462	1.4	5580.9546	0.5	
2 - 1	11985.0714	-1.1	11178.3304	-0.4	11842.9057
3 - 2	17969.0426	0.3	16804.2064	0.1	17757.1462
B /MHz	2997.4092(7)		2789.5(2)		2961.6881
D /MHz	0.14271(4)		-0.62(2)		0.12021
δ	1.9 kHz		0.7 MHz		
			CO-$^{12}CD_4$		
1 - 0	5587.0901	1.1	5439.3448	-5.4	
2 - 1	11171.6486	-0.9	10877.8090	4.7	10931.1952
3 - 2	16751.1348	0.2	16314.8090	-1.2	16391.5339
B /MHz	2793.7568(5)		2719.736(3)		2733.4999
D /MHz	0.10561(3)		0.0334(2)		0.08764
δ	1.4 kHz		7.6 kHz		
			CO-CH_3D		
1 - 0	6040.4148	1.7	5637.8714	0.9	
2 - 1	12076.8787	-1.4	11297.5776	-0.7	
3 - 2	18105.4262	0.3	16993.7506	0.2	
B (MHz)	3020.5379(8)		2817.7(4)		
D (MHz)	0.16482 (5)		-0.81(3)		
δ	2.3 kHz		1.1 MHz		
			CO-CHD_3		
1 - 0	5726.9039	0.3	5530.9869	20.4	
2 - 1	11450.5987	-0.2	11061.8680	-16.4	
3 - 2	17167.8728	0.1	16592.3682	4.1	
B (MHz)	2863.7196(1)		2765.517(9)		
D (MHz)	0.133747(9)		0.0068(6)		
δ	0.4 kHz		26.1 kHz		

[a] $\Delta\nu = \nu_{obs} - \nu_{calc}$, the unit of $\Delta\nu$ is the same as of δ.

[b] Two measured transitions were used to calculate B and D.

Table 6-8: Measured transition frequencies (in MHz) of ^{13}CO-CH$_4$ isotopomers.

J' - J''	j=0, K=0		j=1, K=0		j=2, K=1[b]
	ν_{obs}	$\Delta\nu$ (kHz)[a]	ν_{obs}	$\Delta\nu$ (MHz)	ν_{obs}
			$^{13}C^{16}O$-$^{12}CH_4$		
1 - 0	6141.9033	1.6	5706.8423	0.6	
2 - 1	12280.1945	-1.3	11431.8927	-0.5	12119.5274
3 - 2	18411.2481	0.3	17188.3131	0.1	18171.7977
B (MHz)	3071.2538(7)		2852.3(3)		3030.881
D (MHz)	0.15069(5)		-0.69(2)		0.12489
δ	2.1 kHz		0.8 MHz		
			$^{13}C^{18}O$-$^{12}CH_4$		
1 - 0	6001.2046	2.3	5593.9594	0.5	
2 - 1	11998.8410	-1.8	11203.4736	-0.4	11851.5268
3 - 2	17989.3216	0.5	16839.9930	0.1	17769.9076
B (MHz)	3000.901(1)		2796.0(2)		2963.866
D (MHz)	0.14894(7)		-0.59(2)		0.12304
δ	3.0 kHz		0.6 MHz		
F'-F''			$^{13}C^{17}O$-$^{12}CH_4$ (J=1-0)		
2.5 - 2.5	6068.8892	0.7	5648.4330	0.5	
3.5 - 2.5	6069.2245	-2.2	5648.7757	-1.8	
1.5 - 2.5	6069.3732	1.6	5648.9267	1.3	
χ_{aa} /MHz	-1.61(1)		-1.64(1)		

[a] $\Delta\nu = \nu_{obs} - \nu_{calc}$, the unit of $\Delta\nu$ is the same as of δ.

[b] Two measured transitions were used to calculate B and D.

Table 6-9: Bond length, stretching frequency, and force constant of Kr-methane isotopomers.

	j=0, K=0 state			
	^{86}Kr-CH$_4$	^{84}Kr-CH$_4$	^{82}Kr-CH$_4$	^{80}Kr-CH$_4$
R (Å)	4.097	4.097	4.097	4.097
ν_s (cm^{-1})	32.25	32.31	32.37	32.44
k_s (Nm^{-1})	0.828	0.828	0.828	0.828
	^{86}Kr-^{13}CH$_4$	^{84}Kr-^{13}CH$_4$	^{82}Kr-^{13}CH$_4$	^{80}Kr-^{13}CH$_4$
R (Å)	4.095	4.095	4.095	4.095
ν_s (cm^{-1})	31.48	31.54	31.61	31.67
k_s (Nm^{-1})	0.830	0.830	0.830	0.830
	^{86}Kr-CD$_4$	^{84}Kr-CD$_4$	^{82}Kr-CD$_4$	^{80}Kr-CD$_4$
R (Å)	4.045	4.045	4.045	4.045
ν_s (cm^{-1})	31.14	31.2	31.28	31.36
k_s (Nm^{-1})	0.929	0.928	0.928	0.929
	^{86}Kr-CH$_3$D	^{84}Kr-CH$_3$D	^{82}Kr-CH$_3$D	^{80}Kr-CH$_3$D
R (Å)	4.082	4.082	4.082	4.082
ν_s (cm^{-1})	28.61	28.67	28.73	28.78
k_s (Nm^{-1})	0.686	0.686	0.686	0.685
	^{86}Kr-CHD$_3$	^{84}Kr-CHD$_3$	^{82}Kr-CHD$_3$	^{80}Kr-CHD$_3$
R (Å)	4.056	4.056	4.056	4.057
ν_s (cm^{-1})	28.71	28.77	28.83	28.9
k_s (Nm^{-1})	0.757	0.757	0.757	0.757
	j=2, K=1 state			
	^{86}Kr-CH$_4$	^{84}Kr-CH$_4$	^{82}Kr-CH$_4$	^{80}Kr-CH$_4$
R (Å)	4.117	4.118	4.118	4.119
ν_s (cm^{-1})	31.29	31.36	31.43	31.53
k_s (Nm^{-1})	0.780	0.780	0.781	0.781
	^{86}Kr-^{13}CH$_4$	^{84}Kr-^{13}CH$_4$	^{82}Kr-^{13}CH$_4$	^{80}Kr-^{13}CH$_4$
R (Å)	4.110	4.111	4.111	4.112
ν_s (cm^{-1})	30.43	30.49	30.55	30.63
k_s (Nm^{-1})	0.776	0.776	0.776	0.776
	^{86}Kr-CD$_4$	^{84}Kr-CD$_4$	^{82}Kr-CD$_4$	^{80}Kr-CD$_4$
R (Å)	4.075	4.075	4.076	4.076
ν_s (cm^{-1})	29.97	30.04	30.12	30.2
k_s (Nm^{-1})	0.860	0.860	0.861	0.861

Table 6-10: Computed dipole moment values (in D) for Kr-CH_4 (ϕ=0°).

R /Å	θ=0°	30°	60°	90°	120°	150°
3.5	-0.0317	0.0447	0.1115	0.0062	-0.0393	-0.0971
3.6	-0.0259	0.0361	0.0900	0.0048	-0.0327	-0.0294
3.7	-0.0211	0.0294	0.0730	0.0037	-0.0274	-0.0244
3.8	-0.0173	0.0240	0.0595	0.0030	-0.0230	-0.0203
3.9	-0.0142	0.0198	0.0488	0.0024	-0.0195	-0.0169
4.0	-0.0117	0.0165	0.0402	0.0020	-0.0166	-0.0142
4.1	-0.0096	0.0138	0.0334	0.0017	-0.0142	-0.0120
4.2	-0.0080	0.0117	0.0280	0.0014	-0.0123	-0.0103
4.3	-0.0067	0.0100	0.0236	0.0012	-0.0107	-0.0088
4.4	-0.0056	0.0086	0.0201	0.0011	-0.0094	-0.0076
4.5	-0.0047	0.0075	0.0172	0.0010	-0.0082	-0.0066

Edge: θ=0°		Vertex: θ=54.7°		Face: θ=125.26°	
R=4.05	-0.0106	R=4.2	0.0290	R=3.7	0.0277
4.15	-0.0086	4.25	0.0266	3.75	-0.0254
		4.3	0.0244	3.8	-0.0233
		4.35	0.0225	3.85	-0.0214
		4.4	0.0208	3.9	-0.0197
		4.45	0.0192	3.95	-0.0182
		4.5	0.0178	4.0	-0.0168
		4.55	0.0165	4.05	-0.0156
		4.6	0.0154	4.1	-0.0144

Table 6-11: Interaction energies (in cm^{-1}) of Kr-CH_4.

R /Å	*θ*=0°	30°	60°	90°	120°	150°
				ϕ=0°		
3.5	121.8	510.0	830.0	270.6	-66.1	15.4
3.6	10.8	280.0	501.9	114.5	-117.6	-61.9
3.7	-58.6	125.5	277.3	12.8	-144.5	-107.3
3.8	-99.3	-24.3	126.6	-51.0	-155.2	-131.0
3.9	-120.6	-39.6	27.9	-88.6	-155.6	-140.5
4.0	-129.0	-77.7	-34.3	-108.4	-149.7	-140.8
4.1	-129.2	-98.2	-71.5	-116.5	-140.1	-135.5
4.2	-124.3	-107.1	-91.7	-116.9	-128.8	-127.0
4.3	-116.6	-108.4	-100.5	-112.7	-116.9	-116.9
4.4	-107.3	-105.0	-102.1	-105.8	-105.2	-106.9
4.5	-97.6	-98.9	-99.1	-97.5	-94.0	-95.6
	Edge: *θ*=0°		Vertex: *θ*=54.7°		Face: *θ*=125.26°	
	R=4.05	-129.9	*R*=4.2	-90.7	*R*=3.7	-147.3
	4.15	-127.2	4.25	-96.6	3.75	-153.7
			4.3	-100.0	3.8	-157.0
			4.35	-101.7	3.85	-157.8
			4.4	-101.9	3.9	-156.7
			4.45	-100.9	3.95	-154.1
			4.5	-99.1	4.0	-150.3
			4.55	-96.6	4.05	-145.7
			4.6	-93.6	4.1	-140.5
				ϕ=30°		
3.5		363.0	484.8	158.3	54.2	117.3
3.6		178.3	262.6	36.2	-35.1	8.4
3.7		56.0	113.6	-41.1	-89.0	-59.6
3.8		-22.2	16.4	-87.4	-118.8	-99.4
3.9		-70.0	-44.7	-112.7	-132.6	-120.1
4.0		-96.9	-80.8	-123.9	-135.9	-128.2
4.1		-109.8	-100.0	-126.1	-132.6	-128.3
4.2		-113.4	-108.0	-122.5	-125.4	-123.3
4.3		-111.4	-108.8	-115.6	-116.2	-115.5
4.4		-105.8	-105.0	-107.0	-106.1	-106.3
4.5		-98.3	-98.7	-97.6	-95.9	-96.6

Table 6-11: (continued)

R /Å	*θ*=0°	30°	60°	90°	120°	150°
				ϕ=60°		
3.5		117.3	54.2	-158.3	484.8	363.0
3.6		8.4	-35.1	-36.2	262.2	178.3
3.7		-59.6	-89.0	-41.1	113.6	56.0
3.8		-99.4	-118.8	-87.4	16.4	-22.2
3.9		-120.2	-132.6	-112.7	-44.7	-70.0
4.0		-128.2	-135.9	-123.9	-80.8	-96.9
4.1		-128.3	-132.6	-126.1	-100.1	-109.8
4.2		-123.3	-125.5	-122.5	-108.0	-113.4
4.3		-115.5	-116.2	-115.6	-108.8	-111.4
4.4		-106.3	-106.1	-107.0	-106.1	-105.8
4.5		-96.6	-95.9	-97.6	-98.8	-98.3
				ϕ=90°		
3.5		15.4	-66.1	270.6	830.0	510.0
3.6		-61.9	-117.6	114.5	501.9	280.0
3.7		-107.3	-144.5	12.8	277.3	125.5
3.8		-131.0	-155.2	-51.0	126.6	24.2
3.9		-140.5	-155.6	-88.6	27.9	-39.6
4.0		-140.8	-149.7	-108.4	-34.3	-77.7
4.1		-135.5	-140.1	-116.5	-71.5	-98.2
4.2		-127.0	-128.8	-116.9	-91.7	-107.0
4.3		-116.8	-116.9	-112.7	-100.5	-108.4
4.4		-106.2	-105.2	-105.8	-102.0	-105.0
4.5		-95.6	-94.0	-97.5	-99.1	-98.9

Table 6-12: Interaction energies (in cm^{-1}) of Ar-CH_4 (ϕ=0°).

R /Å	θ=0°	30°	60°	90°	120°	150°
3.5	-10.3	222.0	417.8	80.6	-111.3	-67.7
3.6	-63.2	92.7	224.3	-1.8	-128.9	-100.6
3.7	-92.7	9.8	96.9	-51.9	-134.1	-116.3
3.8	-106.7	-41.0	15.2	-80.3	-131.5	-120.9
3.9	-110.8	-70.3	-35.0	-94.2	-124.4	-118.6
4.0	-108.7	-85.1	-64.0	-98.7	-115.0	-112.3
4.1	-103.0	-90.5	-78.8	-97.4	-104.6	-103.9
4.2	-95.3	-90.1	-84.6	-92.6	-94.0	-94.6
4.3	-86.8	-86.1	-84.5	-86.0	-83.9	-85.2
4.4	-78.3	-80.3	-81.0	-78.5	-74.4	-76.1
4.5	-70.0	-73.5	-75.7	-70.9	-64.8	-67.7

Edge: θ=0°		Vertex: θ=54.7°		Face: θ=125.26°	
R=3.85	-109.7	R=3.9	-32.9	R=3.5	-114.6
3.95	-110.3	3.95	-50.0	3.55	-124.7
		4.0	-62.7	3.6	-131.1
		4.05	-71.8	3.65	-134.4
		4.1	-78.1	3.7	-135.4
		4.15	-82.1	3.75	-134.6
		4.2	-84.2	3.8	-132.3
		4.25	-84.9	3.85	-129.0
		4.3	-84.4	3.9	-124.9

Table 6-13: Bond length, stretching frequency, and force constant of CO-methane isotopomers.

	CO-CH_4	CO-$^{13}CH_4$	CO-CD_4	^{13}CO-CH_4	$^{13}C^{18}$O-CH_4	CO--CH_3D	CO-CHD_3
				j=0, K=0 state			
R (Å)	3.996	3.992	3.938	3.995	3.995	3.977	3.949
ν_s (cm^{-1})	29.35	28.96	30.29	29.23	28.4	27.26	27.94
k_s (Nm^{-1})	0.518	0.524	0.632	0.520	0.502	0.464	0.522
				j=2, K=1 state			
R (Å)	4.024	4.016	3.981	4.021	4.020		
ν_s (cm^{-1})	31.6	30.99	32.19	31.48	30.67		
k_s (Nm^{-1})	0.600	0.560	0.713	0.603	0.586		

Table 6-14: Comparison of CO-CH_4 with CO-rare gas complexes.[a]

	CO-CH_4 (j=0)	CO-Ne	CO-Ar	CO-Kr	CO-Xe
R (Å)	3.996	3.645	3.849	3.976	4.194
ν_s (cm^{-1})	29.4	20.0	25.5	23.4	21.6
k_s (Nm^{-1})	0.52	0.27	0.63	0.68	0.63
β (°)	72.4	58.5	68.9	71.5	

[a] Values for the CO-rare gas complexes calculated with constants reported in refs. *249* and *260*.

Table 6-15: Computed dipole moment values (in D) of Ar-CH_4 (ϕ=0°).

R /Å	θ=0°	30°	60°	90°	120°	150°
3.5	-0.0055	0.0513	0.1016	0.0213	-0.0149	-0.0011
3.6	-0.0056	0.0399	0.0799	0.0159	-0.0135	-0.0099
3.7	-0.0055	0.0310	0.0629	0.0117	-0.0122	-0.0092
3.8	-0.0053	0.0242	0.0497	0.0086	-0.0111	-0.0085
3.9	-0.0051	0.0189	0.0395	0.0062	-0.0101	-0.0078
4.0	-0.0048	0.0149	0.0315	0.0044	-0.0092	-0.0071
4.1	-0.0044	0.0117	0.0253	0.0031	-0.0083	-0.0065
4.2	-0.0041	0.0093	0.0205	0.0022	-0.0076	-0.0060
4.3	-0.0038	0.0075	0.0167	0.0015	-0.0069	-0.0054
4.4	-0.0034	0.0061	0.0138	0.0009	-0.0062	-0.0049
4.5	-0.0031	0.0050	0.0115	0.0006	-0.0057	-0.0045

Edge: θ=0°		Vertex: θ=54.7°		Face: θ=125.26°	
R=3.85	-0.0052	R=3.9	0.0407	R=3.5	-0.0015
3.95	-0.0049	3.95	0.0303	3.55	-0.0146
		4.0	0.0325	3.6	-0.0139
		4.05	0.0291	3.65	-0.0132
		4.1	0.0261	3.7	-0.0126
		4.15	0.0235	3.75	-0.0120
		4.2	0.0211	3.8	-0.0114
		4.25	0.0191	3.85	-0.0108
		4.3	0.0173	3.9	-0.0103

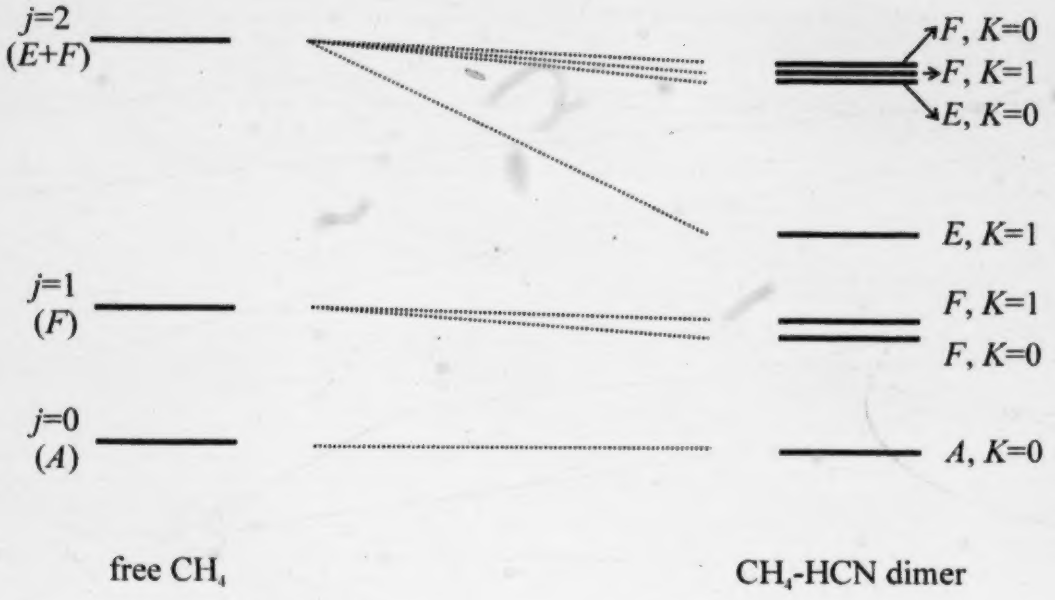

Figure 6-1: Energy level correlation diagram for CH_4-HCN. To the left are the rotational levels of free CH_4. To the right are the internal rotor states of the complex. Only the few lowest energy states of each spin modification are shown. j is the internal rotor quantum number. K is the projection of j onto the van der Waals bond. In the molecular beam, the A, K=0; F, K=0; and E, K=1 states are all metastable and well populated. Intensities of transitions within these states are proportional to the corresponding spin statistical weights, 5, 9, and 2 for j=0, 1, and 2 states, respectively (see table 3-5).

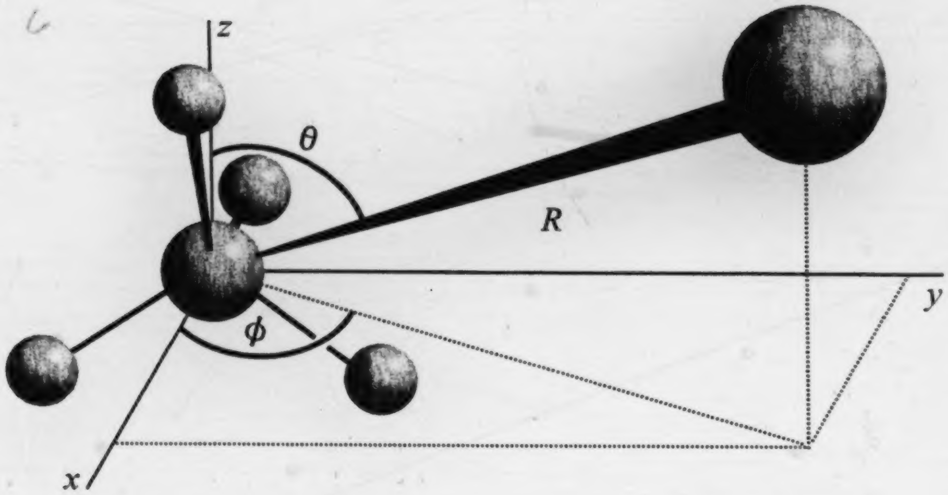

Figure 6-2: Structural parameters used to describe the Rg-methane van der Waals complexes. The molecule-fixed axes frame of methane is defined such that the two hydrogens with positive *z* values are in the *xz*-plane, and those with negative *z* values are in the *yz*-plane. The position of the Rg atom in the complex can then be described by spherical coordinates (R, θ, ϕ). R is the distance from the Rg atom to the C atom, i.e., the center-of-mass of the methane monomer, θ is the angle between the R vector and the *z*-axis, and ϕ is the azimuthal angle. When the azimuthal angle ϕ is 0°, θ=0° corresponds to Rg binding to a H-H midpoint configuration (edge), θ=54.7° corresponds to a linear C-H···Kr configuration (vertex), and θ=125.7° corresponds to Rg binding to a three H face center configuration (face).

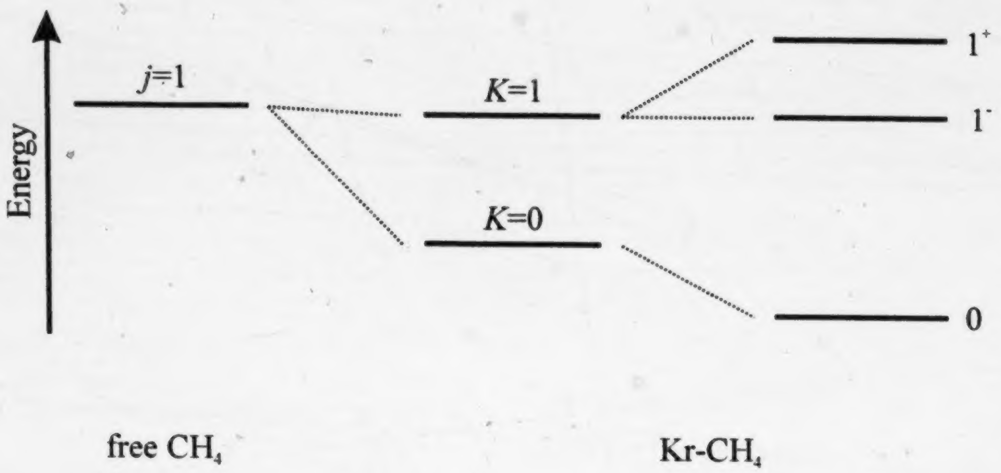

Figure 6-3: The Coriolis interaction between the j=1, K=0 and j=1, K=1 states. To the left is the j=1 rotational state of free CH_4. To the right are the j=1, K=0 and j=1, K=1 states of the Kr-CH_4 dimer. The j=1, K=1 state is doubly degenerated. The degeneracy can be resolved by a Coriolis interaction between the j=1, K=0 and j=1, K=1 states, since it occurs between the j=1, K=0 state and only one of components of the j=1, K=1 state. The superscripts + and - are used to denote the even and odd parities of the states (*175*). The perturbation pushes down the j=1, K=0 state and raises the j=1, K=1^+ state.

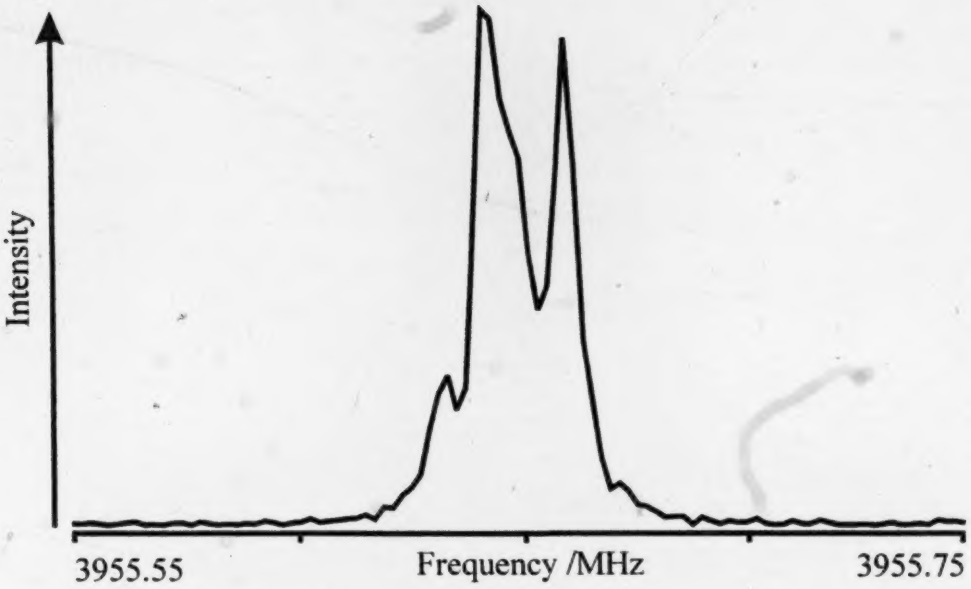

Figure 6-4: Rotational spectrum of the J=1-0 transition of ^{84}Kr-CH$_4$ (j=1, K=0). The spectrum was taken with 60 nsec sampling interval and 500 averaging cycles. Narrow splittings, possibly due to spin-spin and spin-rotation interactions, were observed. The j=1 internal rotor state is associated with nuclear spin wavefunctions of F symmetry, corresponding to a total spin of I=1.

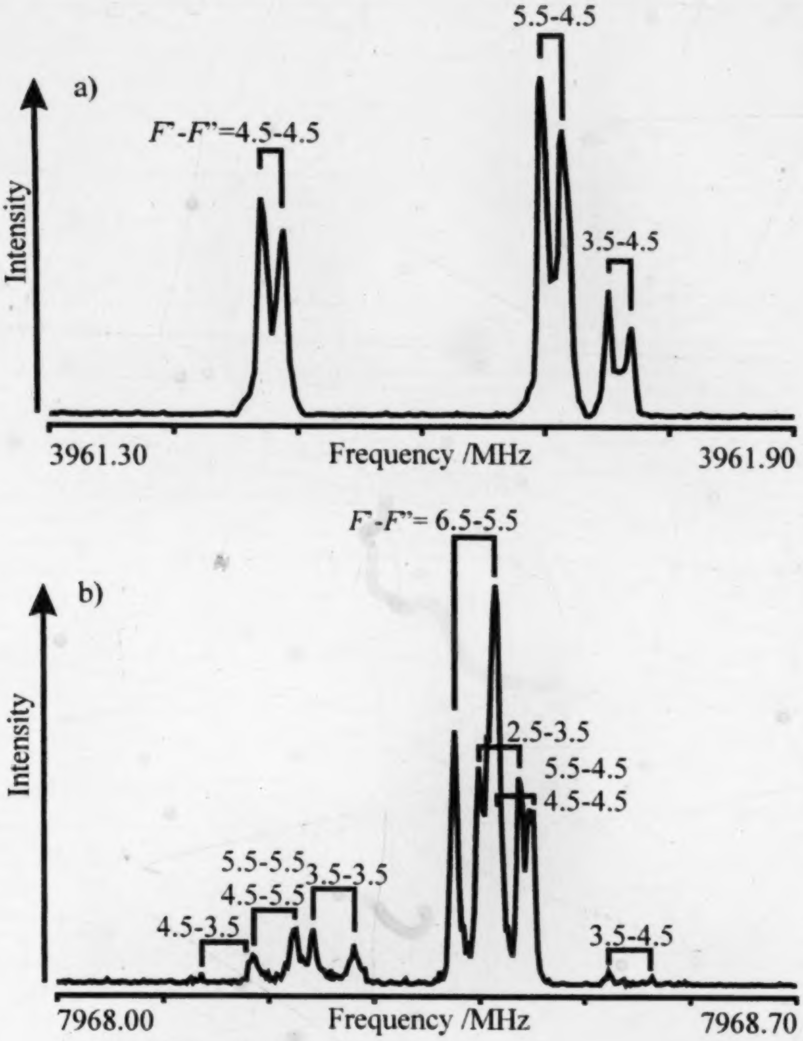

Figure 6-5: Representative spectra of the J=1-0 (a) and 2-1 (b) transitions of ^{83}Kr-CH$_4$ (j=1, K=0), recorded with 60 nsec sampling interval. Both spectra are composite spectra obtained from two individual measurements. The spectrum (a) and (b) were obtained using 3000 and 2000 averaging cycles, respectively. The hyperfine structure arising from the spin I=9/2 ^{83}Kr nucleus is assigned.

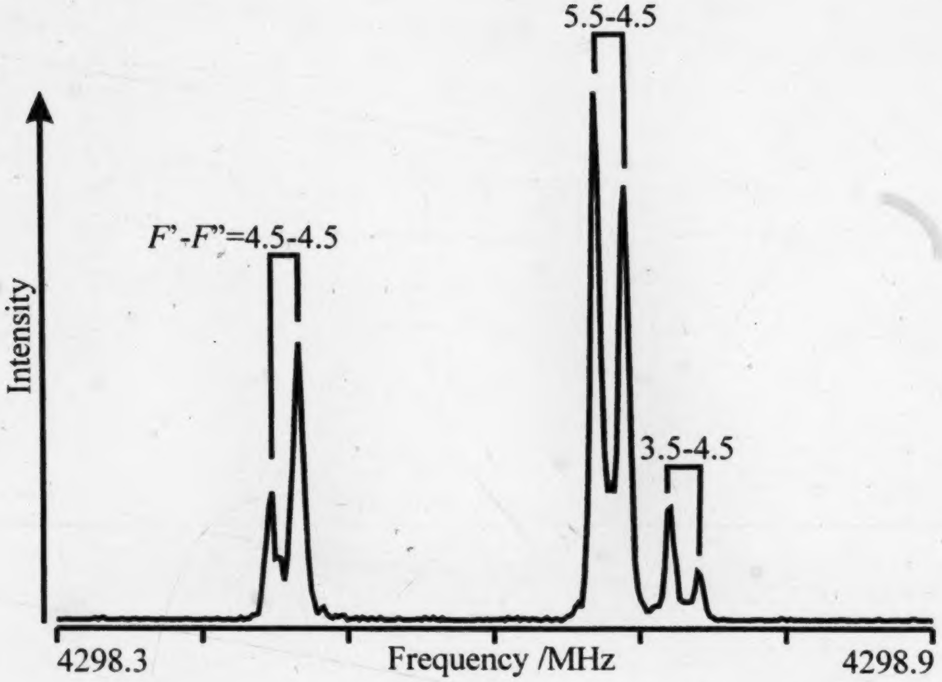

Figure 6-6: Spectrum of the J=1-0 rotational transition of ^{83}Kr-CH$_3$D (j=0, K=0 state). The observed hyperfine structure is due to the ^{83}Kr nucleus (I=9/2) and was fitted to give a χ_{aa} value of -1.209 MHz. No additional hyperfine splitting arising from the deuterium nucleus was resolved. Shown is a composite spectrum obtained from two individual measurements. Each individual spectrum was obtained with 2000 averaging cycles and 60 nsec sampling interval.

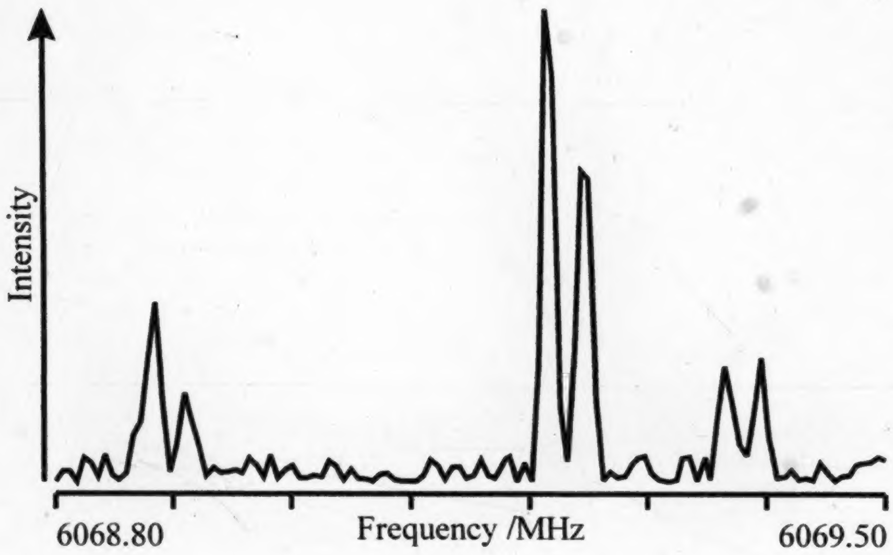

Figure 6-7: Representative spectrum of the J=1-0 transition of $^{13}C^{17}O$-CH_4 (j=0, K=0). The hyperfine structure is due to the spin I=5/2 ^{17}O nucleus. Shown is a composite spectrum obtained from three individual measurements. Each individual spectrum was obtained with 2000 averaging cycles and 20 nsec sampling interval. The low signal-to-noise ratio is a result of the trace concentration of $^{13}C^{17}O$ in the sample.

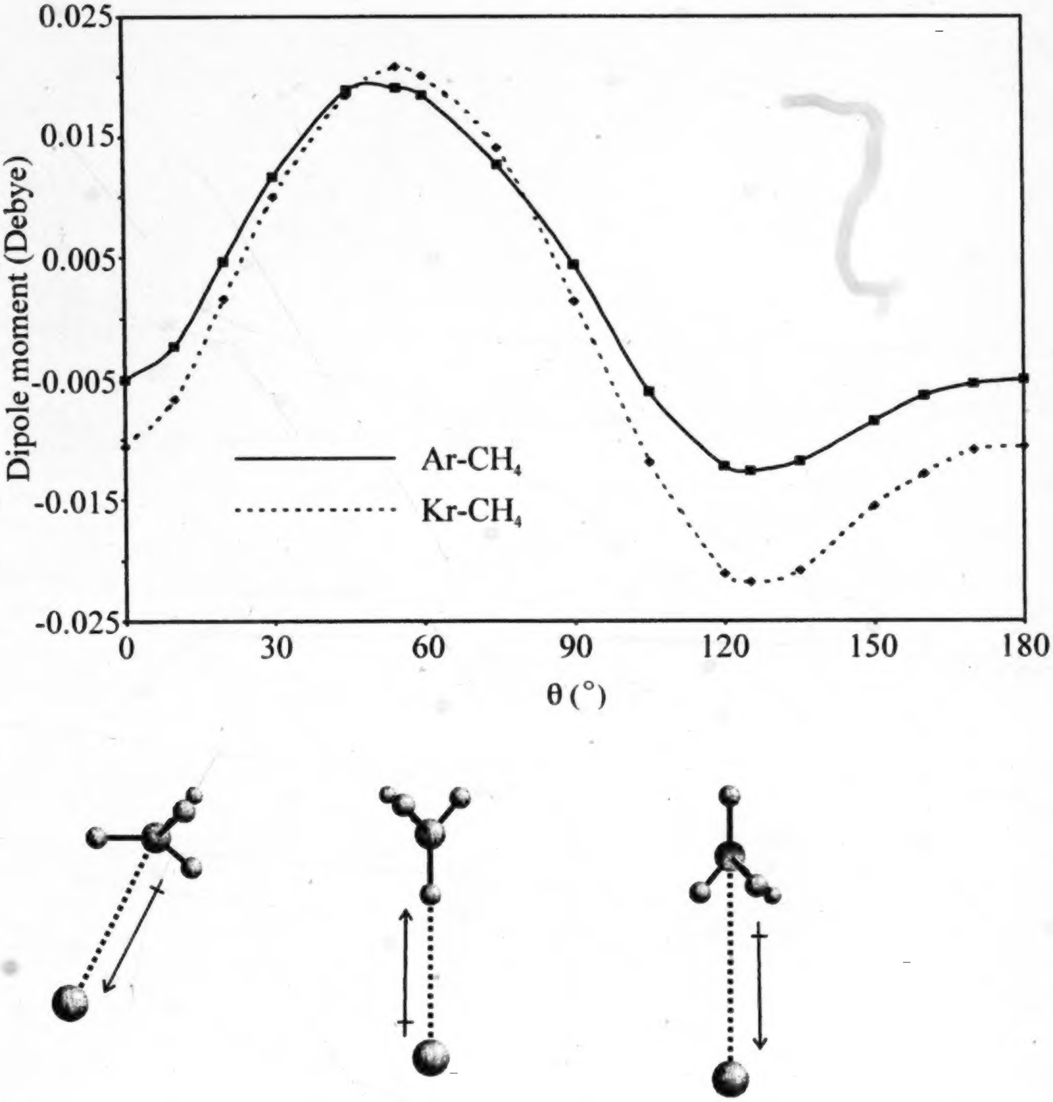

Figure 6-8: The angular dependence of the dipole moments of Kr-CH$_4$ and Ar-CH$_4$ (ϕ fixed at 0°).

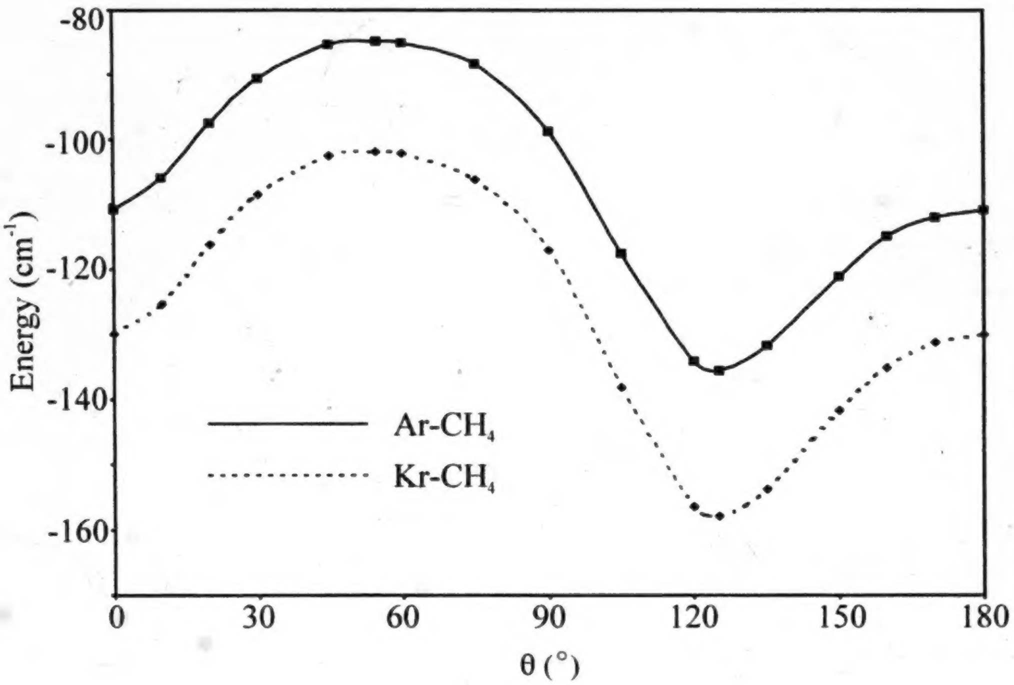

Figure 6-9: The angular dependence of the interaction energies of Kr-CH$_4$ and Ar-CH$_4$ (ϕ fixed at 0°).

7

CONCLUSIONS

Many conclusions can be drawn based on the results presented in chapters 4 to 6. A number of them have been summarized in the corresponding chapters. Here, a few general comments are made.

First of all, the work presented further shows that the method of Fourier transform microwave spectroscopy is indeed an advanced technique to study weakly bound systems in general. Utilizing the high sensitivity and high resolution of this method, detailed information about several weakly bound molecular systems, namely Rg-ethylene, Rg-acetylene, Rg-methane, and CO-methane, was obtained. From the recorded rotational and rovibrational spectra, not only structural information was deduced utilizing the obtained spectroscopic constants such as rotational, centrifugal distortion, and nuclear quadrupole coupling constants, but also detailed information about the features of the corresponding potential energy surfaces and the internal dynamics of these systems was inferred. In the case of the Rg-ethylene systems, a T-shaped, planar structure, where the Rg atom is located on the *b*-principal inertial axis of ethylene, was determined from the spectra. Transition doubling was observed, which is attributed to an internal rotation motion of the ethylene monomer. The tunneling motion responsible for the observed transition doubling was unambiguously determined to be the internal rotation of ethylene about the C=C bond from the spectra of the isotopomers containing trans-D_2-ethylene. In addition, information about the energy level ordering of the $K_a=1$, $m=0$ and $K_a=0$, $m=1$ states and the barrier to the internal rotation motion was obtained. In the case of the Rg-acetylene dimers, the presence of strongly coupled, large amplitude angular and radial internal motions was evident from an analysis of the obtained spectroscopic constants. Information about the energy gap between the Σ_1 and Π_1 states was obtained from the perturbed spectral pattern of the transitions within these states. The rotational spectra of the Kr-CH_4 and CO-CH_4 dimers provided evidence for nearly free internal rotation of the methane subunit from the observation of transitions within various internal rotor states. The close resemblance of the CO-methane and Kr-methane spectra indicates that CO is also nearly freely rotating within the complex. By the comparative studies of a molecular subunit binding to different Rg atoms, namely Ar and Ne, the effect of the size and polarizability of the Rg atom on the features of the potential energy surface and the internal dynamics were observed. Examples include the spectra of the Ar/Ne-trans-D_2-ethylene dimers and the spectra of the Ar/Ne-acetylene systems. In the case of the Ar/Ne-trans-D_2-ethylene pair, a reduced angular anisotropy for Ne-trans-D_2-ethylene compared to that of the Ar analog led to the observation of the additional $K_a=1$, $m=0$ transitions and the Coriolis interaction between the lower $K_a=1$, $m=0$ and $K_a=0$, $m=1$ states. In the case of the Ar/Ne-HCCH pair, transitions within the Σ_0 and Π_1 states were observed for Ar-HCCH, whereas transitions within the Σ_0 and Σ_1 states were observed for Ne-HCCH instead. This is an indication of a Σ_1/Π_1 energy level reordering upon the substitution of Ar with Ne.

Secondly, it can be also concluded from this work that *ab initio* methods are indeed powerful tools to provide complementary information about the nature of potential energy surfaces and internal dynamics of weakly bound complexes. In addition to the information obtained from the spectroscopic measurements, i.e., the rotational and rovibrational spectra using the Fourier transform microwave method, the theoretical results contribute to an in-depth understanding of the systems of interests. For the Ne-ethylene system, *ab initio* minimum energy paths for the two possible tunneling motions predict that the in-plane motion is less likely to be responsible for the observed tunneling splitting, mainly because it involves a large variation in the radial coordinate. For the Ne-acetylene van der Waals dimer, the strong radial-angular coupling is evident from the constructed MP4 and CCSD(T) potential energy surfaces. For the Rg-methane systems, the *ab initio* potential energy surfaces of Kr-CH_4 and Ar-CH_4 indicate that the angular dynamics does not change significantly when the binding partner of methane changes from Kr to Ar. The *ab initio* dipole moment calculations provide qualitative explanations for the intensity enhancement of the j=2, K=1 transitions of Kr-CH_4 and for the unsuccessful spectral searches for rotational transitions of Ar-CH_4.

Through the intimate interplay between the spectroscopic and *ab initio* methods shown in this thesis, qualitative information was obtained from the computed *ab initio* potential energy surfaces and helped to understand the weakly bound systems studied. A further step would be to extract quantitative information and to compare it with the accurate spectroscopic measurements. To this end, analytical representations of these *ab initio* potential energy surfaces and subsequent quantum treatments of nuclear dynamics are needed to obtain energies of bound rovibrational levels. The spectroscopic and *ab initio* results presented in this thesis are expected to contribute to accurate representations of the associated potential energy surfaces. Accurate intermolecular dimer potentials can be used to, for example, study the non-additive effects in larger clusters, such as the three-body effects in ternary systems.

The present work can be regarded as a starting point of a systematic work into larger clusters containing organic species, and eventually, a better understanding of the solvation processes involving these species. By gradually increasing the number of Rg atoms, fundamental aspects of solvation processes, such as the size dependence of the structural and dynamical properties of clusters, may be studied as they change from the behavior of small molecular associations to that of bulk phases (*263*).

BIBLIOGRAPHY

1. P. R. Bunker and P. Jensen, *Molecular Symmetry and Spectroscopy*, second edition (NRC research Press, Ottawa, 1998).

2. A. D. Buckingham, P. W. Fowler, and J. M. Hutson, Chem. Rev. **88**, 963 (1988).

3. W. Klemperer, J. Mol. Struc. **59**, 161 (1980).

4. C. M. Western, Chem. Soc. Rev. **24**, 299 (1995).

5. M. Rigby, E. B. Smith, W. A. Wakeham, and G. C. Maitland, *The Forces Between Molecules*, (Oxford University Press, New York, 1986).

6. J. O. Hirschfelder, C. F. Curtiss, and R. B. Bird, *Molecular Theory of Gases and Liquids*, (Wiley, New York, 1954).

7. R. E. Miller, Science **24**, 447 (1988).

8. S. Sugano, *Microcluster Physics*, (Springer, Berlin, 1991).

9. P. Kebarle, Annu. Rev. Phys. Chem. **28**, 445 (1997).

10. A. Stace, Science **294**, 1292 (2001).

11. J. D. Lambert, *Vibrational and Rotational Relaxation in Gases*, (Clarendon, Oxford, 1977).

12. J. T. Yaedley, *Introduction to Molecular Energy Transfer*, (Academic, New York, 1980).

13. S. R. Leone, *A Compilation of Rate Coefficients for Vibrational Energy Transfer Involving the Hydrogen Halides*, J. Phys. Chem. Ref. Data **11**, 953 (1981).

14. S. R. Leone, Adv. Chem. Phys. **50**, 255 (1982).

15. *Structural Chemistry and Molecular Biology*, edited by A. Rich and N. Davidson, (Freeman, San Francisco, 1968).

16. A. Kornychev and S. Leikin, Proc. Natl. Acad. Sci. USA **95**, 13579 (1988).

17. W. Ferdinand, *The Enzyme Molecule*, (Wiley, London, 1976).

18. A. Watanable and H. L. Welsh, Phys. Rev. Lett. **13**, 810 (1964).

19. T. Dyke, B. Howard, and W. Klemperer, J. Chem. Phys. **56**, 2442 (1972).

20. S. Novick, P. Davies, S. Harris, and W. Klemperer, J. Chem. Phys. **59**, 2273 (1973).

21. S. J. Harris, S. E. Novick, W. Klemperer, J. Chem. Phys. **60**, 3208 (1974).

22. M. R. Keenan, L. W. Buxton, E. J. Campbell, A. C. Legon, and W. H. Flygare, J. Chem. Phys. **74**, 2133 (1981).

23. M. R. Keenan, E. J. Campbell, T. J. Balle, L. W. Buxton, T. K. Minton, P. D. Soper, and W. H. Flygare, J. Chem. Phys. **72**, 3070 (1980).

24. E. J. Campbell, L. W. Buxton, and A. C. Legon, J. Chem. Phys. **78**, 3483 (1983).

25. G. Winnewisser, B. S. Dumesh, I. Pak, L. A. Surin, F. Lewen, D. A. Roth, and F. S. Rusin, J. Mol. Spectrosc. **192**, 243 (1998).

26. L. A. Surin, D. A. Roth, I. Pak, B. S. Dumesh, F. Lewen, and G. Winnewisser, J. Chem. Phys. **112**, 4064 (2000).

27. D. G. Melnik, S. Gopalakrishnan, T. A. Miller, F. C. De Lucia, and S. Belov, J. Chem. Phys. **114**, 6100 (2001).

28. A. R. W. McKellar, J. K. G. Watson, and B. J. Howard, Mol. Phys. **86**, 273 (1995).

29. J. K. G. Watson and A. R. W. McKellar, Can. J. Phys. **75**, 181 (1997).

30. A. L. L. East, A. R. W. McKellar, and J. K. Watson, J. Chem. Phys. **109**, 4378 (1998).

31. D. J. Nesbitt, Faraday Discuss. Chem. Soc. **97**, 1 (1994).

32. A. R. W. McKellar, Faraday Discuss. Chem. Soc. **97**, 69 (1994).

33. A. Amirav, U. Even, and J. Jortner, J. Phys. Chem. **85**, 309 (1981).

34. A. Amirav, U. Even, and J. Jortner, J. Phys. Chem. **86**, 3345 (1982).

35. U. Even, A. Amirav, S. Leutwyler, M. O. Onderchen, Z. Berkovitch-Yellin, and J. Jortner, Faraday Discuss. Chem. Soc. **86**, 439 (1982).

36. D. H. Levy, Adv. Chem. Phys. **47**, 323 (1981).

37. J. S. Muenter, *Structure and Dynamics of Weakly Bound Molecular Complexes*, edited by A. Weber, (NATO Advanced Scientific Institute Series C 212, 1987).

38. A. C. Legon, *Structure and Dynamics of Weakly Bound Molecular Complexes*, edited by A. Weber, (NATO Advanced Scientific Institute Series C 212, 1987).

39. A. C. Legon, Ann. Rev. Phys. Chem. **34**, 275 (1983).

40. K. I. Peterson, G. T. Fraser, D. D. Nelson, Jr., and W. Klemperer, *Comparison of Ab Initio Quantum Chemistry with Experiment for Small Molecules. The State of the Art*, edited by R. J. Bartlett (Reidel Holland. Kluwer Academic, 1985).

41. D. J. Nesbitt, Chem. Rev., **88**, 843 (1988).

42. R. C. Cohn and R. J. Saykally, J. Phys. Chem. **96**, 1024 (1992).

43. K. R. Leopold, G. T. Fraser, S. E. Novick, and W. Klemperer, Chem. Rev. **94**, 1807 (1994).

44. S. E. Novick, Bibliography of Rotational Spectra of Weakly Bound Complexes, (2001). Electronic updates are available on the web at http://www.wesleyan.edu/chem/faculty/novick/vdw.html.

45. Y. Kawashima, R. D. Suenram, G. T. Fraser, F. J. Lovas, and E. Hirota, J. Mol. Spectrosc. **197**, 232 (1999).

46. G. Chałasiński and M. Gutowski, Chem. Rev. **88**, 943 (1988).

47. G. Chałasiński and M. M. Szczęśniak, Chem. Rev. **94**, 1723 (1994).

48. B. Jeziorski, R. Moszynski, and K. Szalewicz, Chem. Rev. **94**, 1887 (1994).

49. G. Chałasiński and M. M. Szczęśniak, Chem. Rev. **100**, 4277 (2000).

50. R. Moszynski, T. Korona, P. E. S. Wormer, and A. van der Avoird, J. Phys. Chem. A **101**, 4690 (1997).

51. G. C. Mcbane and S. M. Cybulski, J. Chem. Phys. **110**, 11734 (1999).

52. S. Leutwyler and J. Bösiger, Chem. Rev. **90**, 489 (1990).

53. L. E. Fried and S. Mukamel, J. Chem. Phys. **96**, 116 (1991).

54. T. Troxler and S. Leutwyler, J. Chem. Phys. **99**, 4363 (1992).

55. A. Heidenreich, D. Bahatt, N. Ben-Horin, U. Even, and J. Jortner, J. Chem. Phys. **100**, 6300 (1994).

56. T. Droz, T. Bürgi, and S. Leutwyler, J. Chem. Phys. **103**, 4035 (1995).

57. F. Y. Naumkin and F. R. W. McCourt, J. Chem. Phys. **107**, 1185 (1997).

58. Y. Xu and W. Jäger, J. Chem. Phys. **106**, 7968 (1997).

59. T. B. Pedersen, B. Fernández, H. Koch, and J. Makarewicz, J. Chem. Phys. **115**, 8431 (2001).

60. A. M. Andrews, A. Taleb-Bendiab, M. S. LaBarge, K. W. Hillig II, and R. L. Kuczkowski, J. Chem. Phys. **93**, 7030 (1990).

61. G. T. Fraser, F. J. Lovas, R. D. Suenram, J. Z. Gillies, and C. W. Gillies, Chem. Phys. **163**, 91 (1992).

62. R. J. Bemish, P. A. Block, L. G. Pedersen, and R. E. Miller, J. Chem. Phys. **102**, 7788 (1995).

63. R. J. Bemish, W. H. Rhee, L. G. Pedersen, and R. E. Miller, J. Chem. Phys. **104**, 4411 (1996).

64. K. R. Leopold, G. T. Fraser, F. J. Lin, D. D. Nelson, Jr., and W. Klemperer, J. Chem. Phys. **81**, 4922 (1984).

65. S. Drucker, A. C. Cooksy, and W. Klemperer, J. Chem. Phys. **98**, 5158 (1993).

66. H. S. Gutowsky, J. D. Keen, T. C. Germann, T. Emilsson, J. D. Augspurger, and C. E. Dykstra, J. Chem. Phys. **98**, 6801 (1993).

67. E. Arunan, T. Emilsson, and H. S. Gutowski, J. Chem. Phys. **103**, 493 (1995).

68. S. Drucker, F. Tao, and W. Klemperer, J. Phys. Chem. **99**, 2646 (1995).

69. K. Uemura, A. Hara, and K. Tanaka, J. Chem. Phys. **104**, 9747 (1996).

70. K. Tanaka, S. Bailleux, A. Mizoguchi, and K. Harada, J. Chem. Phys. **113**, 1524 (2000).

71. R. L. DeLeon and J. S. Muenter, J. Chem. Phys. **72**, 6020 (1980).

72. Y. Ohshima, M. Iida, and Y. Endo, Chem. Phys. Lett. **161**, 202 (1989).

73. T. A. Hu, D. G. Prichard, L. Sun, J. S. Muenter, and B. J. Howard, J. Mol. Spectrosc. **153**, 486 (1992).

74. Y. Ohshima, Y. Matsumoto, M. Takami, and K. Kuchitsu, J. Chem. Phys. **99**, 8385 (1993).

75. R. J. Bemish, P. A. Block, L. G. Pedersen, W. Yang, and R. E. Miller, J. Chem. Phys. **99**, 8585 (1993).

76. R. J. Bemish and R. E. Miller, Chem. Phys. Lett. **281**, 272 (1997).

77. G. T. Fraser, F. J. Lovas, R. D. Suenram, and K. Matsumura, J. Mol. Spectrosc. **144,** 97 (1990).

78. R. C. Cohen, K. L. Busarow, K. B. Laughlin, G. A. Blake, M. Havenith, Y. T. Lee, and R. J. Saykally, J. Chem. Phys. **89,** 4494 (1988).

79. J. M. Hutson, J. Chem. Phys. **89,** 157 (1990).

80. R. C. Cohen, L. L. Busarow, Y. T. Lee, and R. J. Saykally, J. Chem. Phys. **92,** 169 (1990).

81. T. C. Germann and H. S. Gutowsky, J. Chem. Phys. **98,** 5235 (1993).

82. J. van Wijingaarden and W. Jäger, Mol. Phys. **98,** 1575 (2000).

83. C. A. Schmuttenmaer, J. G. Loeser, and R. J. Saykally, J. Chem. Phys. **101**, 139 (1994).

84. J. van Wijingaarden and W. Jäger, Mol. Phys. **99,** 1215 (2001).

85. J. van Wijingaarden and W. Jäger, J. Chem. Phys. **114,** 3968 (2001).

86. J. van Wijingaarden and W. Jäger, J. Chem. Phys. **115,** 6504 (2001).

87. G. Chałasiński, C. M. Cybulski, M. M. Szczęśniak, and S. Scheiner, J. Chem. Phys. **91**, 7809 (1989).

88. M. Bulski, P. E. S. Wormer, and A. van der Avoird, J. Chem. Phys. **94**, 491 (1991).

89. F. Tao and W. Klemperer, J. Chem. Phys. **101**, 1129 (1994).

90. G. Chałasiński, M. M. Szczęśniak, and S. Scheiner, J. Chem. Phys. **97**, 8181 (1992).

91. C. M. Lovejoy, J. M. Hutson, and D. J. Nesbitt, J. Chem. Phys. **97**, 8009 (1992).

92. P. A. Block and R. E. Miller, Chem. Phys. Lett. **226**, 317 (1994).

93. H. C. Chang, F. Tao, W. Klemperer, C. Healy, and J. M. Hutson, J. Chem. Phys. **99**, 9337 (1993).

94. M. Jeziorska, P. Jankowski, K. Szalewicz, and B. Jeziorski, J. Chem. Phys. **113**, 2957 (2000).

95. J. Ekkers and W. H. Flygare, Rev. Sci. Instrum. **47**, 448 (1976).

96. J. C. McGurk, T. G. Schmalz, and W. H. Flygare, Adv. Chem. Phys. **25**, 1 (1974).

97. T. J. Balle and W. H. Flygare, Rev. Sci. Instrum. **52**, 33 (1980).

98. T. J. Balle, E. J. Campbell, M. R. Keenan, and W. H. Flygare, J. Chem. Phys. **71**, 2723 (1979).

99. E. J. Campbell and W. G. Read, J. Chem. Phys. **78**, 6490 (1983).

100. E. J. Campbell, W. G. Read, and J. A. Shea, Chem. Phys. Lett. **94**, 69 (1983).

101. J. -U. Grabow and W. Stahl, Z. Naturforsch. **45a**, 1043 (1990).

102. U. Andresen, H. Dreizler, J. -U. Grabow, and W. Stahl, Rev. Sci. Instrum. **61**, 3694 (1990).

103. C. Chuang, C. J. Hawley, T. Emilsson, and H. S. Gutowsky, Rev. Sci. Instrum. **61**, 1629 (1990).

104. Y. Xu, W. Jäger, and M. C. L. Gerry, J. Mol. Spectrosc. **151**, 206 (1992).

105. H. O. Leung, D. Gangwani, and J. -U. Grabow, J. Mol. Spectrosc. **184**, 106 (1997).

106. L. Martinache, S. Jans-Bürli, B. Vogelsanger, W. Kresa, and A. Bauder, Chem. Phys. Lett. **149**, 424 (1988).

107. V. N. Markov, Y. Xu, and W. Jäger, Rev. Sci. Instrum. **106**, 4061 (1998).

108. R. D. Suenram, F. J. Lovas, and K. Matsumura, Astrophys. J. **342**, L103 (1989).

109. K. A. Walker and M. C. L. Gerry, J. Mol. Spectrosc. **182**, 178 (1997).

110. J. -U. Grabow, N. Heineking, and W. Stahl, Z. Naturforsch. **46a**, 914 (1991).

111. Y. Hirahara, Y. Ohshima, and Y. Endo, J. Chem. Phys. **101**, 7342 (1994).

112. L. H. Coudert, F. J. Lovas, R. D. Suenram, and J. T. Hougen, J. Chem. Phys. **87**, 6290 (1987).

113. E. J. Campbell, L.W. Buxton, T. J. Balle, and W. H. Flygare, J. Chem. Phys. **74**, 813 (1981).

114. E. J. Campbell, L. W. Buxton, T. J. Balle, M. R. Keenan, and W. H. Flygare, J. Chem. Phys. **74**, 829 (1981).

115. H. Dreizler, Mol. Phys. **59**, 1 (1986).

116. R. L. Shoemaker, *Laser and Coherence Spectrscopy* (Plenum Press, New York, 1978), pp. 198.

117. H. Dreizler, Ber. Bunsenges. Phys. Chem. **99**, 1451 (1995).

118. R. C. Tolman, *The Principle of Statistical Mechanics* (Oxford University Press, Lodon, 1962), pp. 78.

119. J. Vanier, *Basic Theory of Lasers and Masers*, (Gorden & Breach Science Publishes, 1971), pp. 22*f*.

120. K. Blum, *Density Matrix Theory and Application* (Plenium Press, 1981).

121. F. Bloch, Phys. Rev. **70**, 460 (1946).

122. F. Bloch, Phys. Rev. **102**, 104 (1956).

123. R. K. Harris, *Nuclear Magnatic Resonance Spectroscopy, A Physicochemical View* (Pitman, London, 1983) pp. 66.

124. D. H. Levy, Ann. Rev. Phys. Chem. **31**, 197 (1980).

125. R. E. Smalley, L. Wharton, and D. H. Levy, Acct. Chem. Res. **10**, 139 (1977).

126. *Atomic and Molecular Beam Methods*, edited by G. Scoles (Oxford University Press, Lodon, 1988) Vol. 1, Chapter 2.

127. R. Campargue, A. Lebehot, J. C. Lemonnier, D. Marette, and J. Pebay, Comptes Rendus 5e Symposium International sur les Jets Molecularies, April 7-11, 1975, Nice, France.

128. R. E. Smally, L. Wharton, and D. H. Levy, J.Chem. Phys. **64**, 3266 (1976).

129. O. F. Hagena and W. O. Gert, J.Chem. Phys. **56**, 1793 (1972).

130. O. F. Hagena, *Molecular Beam and Low Density Gas Dynamics*, edited by P. P. Weginer (Marcel Dekker, New York, 1974) Vol 4, Chapter 2.

131. T. R. Dyke, G. R. Tomasevich, W. Klemperer, and W. E. Falconer, J. Chem. Phys. **57**, 2277 (1972).

132. T. J. Balle, E. J. Campbell, M. R. Keenan, and W. H. Flygare, J. Chem. Phys. **72**, 922 (1980).

133. A. van der Avoird, P. E. S. Wormer, and R. Moszynski, Chem. Rev. **94**, 1931 (1994).

134. *Molecular Interactions from van der Waals to Strongly Bound Complexes*, edited by S. Scheiner (Wiley, 1997).

135. P. E. S. Wormer and A. van der Avoird, Chem. Rev. **100**, 4109 (2000).

136. J. A. Pople, Faraday Discuss. Chem. Soc. **73**, 7 (1982).

137. J. A, Pople, J. S. Binkley, and R. Seeger, Int. J. Quant. Chem. Symp. **10**, 1 (1976).

138. C. Møller and M. S. Plesset, Phys. Rev. **46**, 618 (1934).

139. M. Urban, I. Cernusak, V. Kellö, J. Noga, *Methods in Computational Chemistry*, edited by S. Wilson (Plenum Press, New York, 1987) Vol. 1, pp. 117.

140. P. Jensen, *Introduction to Computational Chemistry* (Wiley, 1999).

141. K. Raghavachari, G. W. Trucks, J. A. Pople, and M. Head-Gordon, Chem. Phys. Lett. **157**, 479 (1989).

142. J. Paldus and X. Li, Adv. Chem. Phys. **110**, 1 (1999).

143. M. L. Leininger, W. D. Allen, and H. F. Schaefer III, J. Chem. Phys. **112**, 9213 (2000).

144. T. H. Dunning, Jr., J. Chem. Phys. **90**, 1007 (1989).

145. R. A. Kendall, T. H. Dunning, Jr., R. J. Harrison, J. Chem. Phys. **96**, 6796 (1992).

146. D. E. Woon and T. H. Dunning, Jr. J. Chem. Phys. **98**, 1358 (1993).

147. A. K. Wilson, D. E. Woon, K. A. Peterson, and T. H. Dunnling, Jr., J. Chem. Phys. **110**, 7667 (1999).

148. F. Tao and Y. Pan, Chem. Phys. Lett. **194**, 162 (1992).

149. F. Tao and Y. Pan, J. Chem. Phys. **97**, 4989 (1992).

150. F. Tao, J. Chem. Phys. **98**, 2481 (1993).

151. F. Tao, J. Chem. Phys. **98**, 3049 (1993).

152. R. Burcl, G. Chałsiński, R. Bukowski, and M. M. Szczęśniak, J. Chem. Phys. **103**, 1498 (1995).

153. S. F. Boys and F. Bernardi, Mol. Phys. **19**, 553 (1970).

154. M. Gutowski and G. Chałsiński, J. Chem. Phys. **98**, 5540 (1993).

155. P. A. Block, L. G. Pedersen, and R. E. Miller, J. Chem. Phys. **98**, 3754 (1993).

156. P. F. Vohralik, R. E. Miller, and R. O. Watts, J. Chem. Phys. **90**, 2182 (1989).

157. S. Huzinaga, J. Chem. Phys. **42**, 1293 (1965).

158. A. J. Sadlej, Collect. Czech. Chem. Commun. **53**, 1995 (1988).

159. Basis sets were obtained from the Extensible Computational Chemistry Environment Basis Set Database, Version 9/12/01, as developed and distributed by the Molecular Science Computing Facility, Environmental and Molecular Sciences Laboratory which is part of the Pacific Northwest Laboratory, P.O. Box 999, Richland, Washington 99352, USA, and funded by the U.S. Department of Energy. The Pacific Northwest Laboratory is a multi-program laboratory operated by Battelle Memorial Institue for the U.S. Department of Energy under contract DE-AC06-76RLO 1830. Contact David Feller or Karen Schuchardt for further information.

160. M. J. Frish, Æ. Frish, and J. B. Foresman, *Gaussian 94 User's Reference*, (Gaussian, Pittsburgh, 1996).

161. GAUSSIAN 94, Revision E.3, M. J. Frisch, G. W. Trucks, H. B. Schlegel, P. M. W. Gill, B. G. Johnson, M. A. Robb, J. R. Cheeseman, T. Keith, G. A. Petersson, J. A. Montgomery, K. Raghavachari, M. A. Al-Laham, V. G. Zakrzewski, J. V. Ortiz, J. B. Foresman, J. Cioslowski, B. B. Stefanov, A. Nanayakkara, M. Challacombe, C. Y. Peng, P. Y. Ayala, W. Chen, M. W. Wong, J. L. Andres, E. S. Replogle, R. Gomperts, R. L. Martin, D. J. Fox, J. S. Binkley, D. J. Defrees, J. Baker, J. P. Stewart, M. Head-Gordon, C. Gonzalez, and J. A. Pople (Gaussian, Inc., Pittsburgh PA, 1995).

162. G. Herzberg, *Molecular Spectra and Molecular Structure II. Infrared and Raman Spectra of Polyatomic Molecules* (D. van Nostrand Company, Inc., New York, 1996).

163. MOLPRO is a package of *ab initio* programs written by H. -J. Werner and P. J. Knowles, with contributions rom R. D. Amos, A. Bernhardsson, A. Berning, P. Celani, D. L. Cooper, M. J. O. Deegan, A. J. Dobbyn, F. Eckert, C. Hampel, G. Heltzer, T. Korona, R. Lindth, A. W. Lloyd, S. J. McNicholas, F. R. Manby, W. Meyer, M. E. Mura, A. Nicklass, P. Palmieri, R. Pitzer, G. Rauhut, M. Schütz, H. Stoll, A. J. Stone, R. Tarroni, and Thorsteinsson.

164. G. Strey and I. M. Mills, J. Mol. Spectrosc. **59**, 103 (1976).

165. C. Hampel, K. Peterson, and H. -J. Werner, Chem. Phys. Lett. **190**, 1 (1992) and references therein. The program to compute the perturbative triples corrections has been developed by M. J. O. Deegan and P. J. Knowles (1992).

166. D. L. Gray and A. G. Robbitte, Mol. Phys. **37**, 1901 (1979).

167. G. Maroulis, J. Chem. Phys. **108**, 5432 (1998).

168. G. Maroulis, J. Phys. Chem. A **104**, 4772 (2000).

169. G. Maroulis and A. Haskopoulos, Chem. Phys. Lett. **349**, 335 (2001).

170. H. -J. Werner and P. J. Knowles, *MOLPRO User's Manual Version 2000.1* (University of Birmingham, 1999) pp. 162.

171. H. C. Longuet-Higgins, Mol. Phys. **6**, 445 (1963).

172. N. Wright and H. M. Randall, Phys. Rev. **48**, 63 (1935).

173. E. B. Wilson, Jr., J. Chem. Phys. **3**, 276 (1935).

174. W. Gordy and R. L. Cook, *Microwave Molecular Spectra*, third edition (Wiley, 1984).

175. I. Pak, D. A. Roth, M. Hepp, G. Winnewisser, D. Scouteris, B. J. Howard, and K. M. T. Yamada, Z. Naturforsch. **53a**, 725 (1998).

176. M. M. Szczęśniak, G. Chałasiński, and S. M. Cybulski, J. Chem. Phys. **96**, 463 (1992).

177. T. G. Heijmen, T. Korona, R. Moszynski, P. E. S. Wormer, and A. van der Avoird, J. Chem. Phys. **107**, 902 (1997).

178. T. G. A. Heijmen, P. E. S. Wormer, A. van der Avoird, R. E. Miller, and R. Moszynski, J. Chem. Phys. **110**, 5639 (1999).

179. G. Tarrago, M. Dang-Nhu, G. Poussigue, G. Guelachvili, and C. Amiot, J. Mol. Spectrosc. **57**, 246 (1975).

180. J. M. Hutson and A. E. Thornley, J. Chem. Phys. **100**, 2505 (1994).

181. J. T. Hougen, *International Review of Science, Physical Chemistry, Ser. 2, Vol. 3, Spectroscopy*, edited by D. A. Ramsay (Butterworths, London, 1976).

182. S. M. Resende and W. B. De Almeida, J. Chem. Phys. **102**, 4184 (1995).

183. W. L. Liu, K. Kolenbrander, and J. M. Lisy, Chem. Phys. Lett. **112**, 585 (1984).

184. M. P. Casassa, D. S. Bomse, and K. C. Janda, J. Chem. Phys. **74**, 5044 (1981).

185. C. M. Western, M. P. Casassa, and K. C. Janda, J. Chem. Phys. **80**, 4781 (1984).

186. J. M. Hutson, D. C. Clary, and J. A. Beswick, J. Chem. Phys. **81**, 4474 (1984).

187. A. C. Peet, D. C. Clary, and J. M. Hutson, J. Chem. Soc. Faraday Trans. **83**, 1719 (1987).

188. A. R. Tiller, A. C. Peet, and D. C. Clary, J. Chem. Phys. **91**, 1079 (1989).

189. A. R. Tiller and D. C. Clary, Chem. Phys. **139**, 67 (1989).

190. J. K. G. Watson, *Vibrational Spectra and Structure: A Series of Advances*; edited by J. R. Durig, (Elservier, New York, 1977), Vol. 6.

191. H. M. Pickett, J. Mol. Spectrosc. **148**, 371 (1991).

192. K. I. Peterson and W. Klemperer, J. Chem. Phys. **85**, 725 (1986).

193. A. M. Andrews and R. L. Kuczkowski, J. Chem. Phys. **98**, 791 (1993).

194. A. M. Andrews, K. W. Hillig. II, and R. L. Kuczkowski, J. Am. Chem. Soc. **114**, 6765 (1992).

195. R. Meyer, J. Mol. Spectrosc. **76**, 266 (1979).

196. R. J. Bemish, L. Oudejans, R. E. Miller, R. Moszynski, T. G. A. Heijmen, T. Korona, P. E. S. Wormer, and A. van der Avoird, J. Chem. Phys. **109**, 8968 (1998).

197. R. Toczyłowski, F. Doloresco, and S. M. Cybulski, J. Chem. Phys., **114**, 851 (2001).

198. W. Jäger, Y. Xu, G. Armstrong, M. C. L. Gerry, F. Y. Naumkin, F. Wang, and F. R. W. McCourt, J. Chem. Phys. **109**, 5420 (1998).

199. P. D. Aldrich, S. G. Kukolich, and E. J. Campell, J. Chem. Phys. **78**, 3521 (1983).

200. D. G. Prichard, R. N. Nandi, J. S. Muenter, and B. J. Howard, J. Chem. Phys. **89**, 1245 (1988).

201. G. T. Fraser, K. R. Leopold, and W. Klemperer, J. Chem. Phys. **80**, 1423 (1984).

202. A. C. Legon, A. L. Wallwork, and P. W. Fowler, Chem. Phys. Lett. **184**, 175 (1991).

203. A. C. Legon, P. D. Aldrich, and W. H. Flygare, J. Chem. Phys. **75**, 625 (1981).

204. A. I. Jaman, T. C. Germann, H. S. Gutowsky, J. D. Augspurger, and C. E. Dykstra, Chem. Phys. **154**, 281 (1991).

205. J. M. Hutson, J. Chem. Phys. **89**, 4550 (1988).

206. J. M. Hutson, J. Chem. Phys. **96**, 6752 (1992).

207. L. J. Danielson, M. Keil, and P. J. Dunlop, J. Chem. Phys. **88**, 4218 (1988).

208. L. J. Danielson, K. M. McLeod, and M. Keil, J. Chem. Phys. **87**, 239 (1987).

209. U. Buck, I. Ettischer, S. Schlemmer, M. Yang, P. Vohralik, and R. O. Watts, J. Chem. Phys. **99**, 3494 (1993).

210. M. Yang and R. O. Watts, J. Chem. Phys. **100**, 3582 (1994).

211. C. R. Le Sueur, A. J. Stone, and P. Fowler, J. Phys. Chem. **95**, 3519 (1991).

212. T. Slee, R. J. Le Roy, and C. E. Andchuaqui, Mol. Phys. **77**, 111 (1992).

213. R. G. A. Bone, J. Phys. Chem. **98**, 3126 (1994).

214. R. Moszynski, P. E. S. Wormer, and A. van der Avoird, J. Chem. Phys. **102,** 8385 (1995).

215. F. Tao, S. Drucker, and W. Klemperer, J. Chem. Phys. **102**, 7289 (1995).

216. M. Yang, M. H. Alexander, H. -J. Werner, and R. J. Bemish, J. Chem. Phys. **105**, 10462 (1996).

217. R. D. Hasse, M. W. Severon, M. M. Szczęśniak, G. Chałasiński, P. Cieplak, R. A. Kendall, and S. M. Cybulski, J. Mol. Structure **436**, 387 (1997).

218. A. E. Thornley and J. M. Hutson, Chem. Phys. Lett. **198**, 1 (1992).

219. G. T. Fraser, A. S. Pine, and R. D. Suenram, J. Chem. Phys. **88**, 6157 (1988).

220. Source: WebElements [http://www.webelements.com/].

221. H. Mäder, N. Heineking, W. Stahl, W. Jäger, and Y. Xu, J. Chem. Soc., Faraday Trans. **92**, 901 (1996).

222. C. H. Townes and A. L. Schawlow, *Microwave Spectroscopy*, (McGraw-Hill, New York, 1955).

223. R. J. Bemish and R. E. Miller, (unpublished results).

224. E. J. Corey and B. B. Snider, J. Am. Chem. Soc. **94**, 2549 (1972).

225. J. F. Harrison, J. Chem. Phys. **48**, 2379 (1968).

226. G. Murdachaew, A. J. Misquitta, R. Bukowski, and K. Szalewicz, J. Chem. Phys. **114**, 764 (2001).

227. J. Olsen, P. Jorgensen, T. Helgaker, and O. Christiansen, J. Chem. Phys. **112**, 9736 (2000).

228. F. H. Stillinger, J. Chem. Phys. **112**, 9711 (2000).

229. D. Xie, Y. Lu, and G. Yan, Chem. Phys. Lett. **339**, 14 (2001).

230. R. P. Wayne, *Chemistry of Atmosphere*, (Clarendon Press, Oxford, 1985).

231. A. C. Legon and A. L. Wallwork, J. Chem. Soc., Chem. Commun. 588 (1989).

232. A. C. Legon and A. L. Wallwork, J. Chem. Soc. Faraday Trans. **88**, 1 (1992).

233. A. C. Legon, B. P. Roberts, and A. L. Wallwork, Chem. Phys. Lett. **173**, 107 (1990).

234. M. J. Atkins, A. C. Legon, and A. L. Wallwork, Chem. Phys. Lett. **192**, 368 (1992).

235. Y. Ohshima and Y. Endo, J. Chem. Phys. **93** 6256 (1990).

236. A. R. Hight Walker, G. T. Fraser, R. D. Suenram, and F. J. Lovas, J. Chem. Phys. **113**, 2139 (2000).

237. L. Dore, R. C. Cohen, C. A. Schmuttenmaer, K. L. Busarow, M. J. Elrod, J. G. Loeser, and R. J. Saykally, J. Chem. Phys. **100**, 863 (1994).

238. R. D. Suenram, G. T. Fraser, F. J. Lovas, and Y. Kawashima, J. Chem. Phys. **101**, 7230 (1994).

239. A. R. W. McKellar, D. A. Roth, I. Pak, and G. Winnewisser, J. Chem. Phys. **110**, 9989 (1999).

240. C. Xia, K. A. Walker, and A. R. W. McKellar, J. Chem. Phys. **114**, 4824 (2001).

241. D. J. Nesbitt, Faraday Discuss. Chem. Soc. **97**, 175 (1994).

242. R. E. Miller, Faraday Discuss. Chem. Soc. **97**, 177 (1994).

243. R. E. Miller, T. G. A. Heijmen, P. E. S. Wormer, A. van der Avoird, and R. Moszynski, J. Chem. Phys. **110**, 5651 (1999).

244. I. Pak, M. Hepp, D. A. Roth, G. Winnewisser, and K. M. T. Yamada, Z. Naturforsch. **51 a**, 997 (1996).

245. I. Pak, M. Hepp, D. A. Roth, and G. Winnewisser, Rev. Sci. Instrum. **68**, 1668 (1997).

246. M. D. Brooks, D. J. Hughes, and B. J. Howard, J. Chem. Phys. **100**, 7051 (1994).

247. W. B. Chaoman, A. Schiffman, J. M. Hutson, and D. J. Nesbitt, J. Chem. Phys. **105**, 3497 (1996).

248. I. Pak and R. Suenram, private communication.

249. K. A. Walker, T. Ogata, W. Jäger, and M. C. L. Gerry, J. Chem. Phys. **106**, 7519 (1997).

250. E. J. Campbell, L. W. Buxton, M. R. Keenan, and W. H. Flygare, Phys. Rev. A **24**, 812 (1981).

251. C. G. Gray and K. E. Gubbins, *Theory of Molecular Fluids*, Volume 1: *Fundamentals* (Clarendon, Oxford, 1984).

252. G. Birnbaum, E. G. Cohen, J. Chem. Phys. **62**, 3807 (1975).

253. W. L. Faust and L. Y. Chow Chiu, Phys. Rev. **129**, 1214 (1963).

254. L. W. Buxton, E. J. Campbell, and W. H. Flygare, Chem. Phys. **54**, 173 (1981).

255. Y. Xu, W. Jäger, J. Djauhari, and M. C. L. Gerry, J. Chem. Phys. **103**, 2827 (1995).

256. A. L. Kaledin and M. C. Heaven, Chem. Phys. Lett. **347**, 199 (2001).

257. G. T. Fraser, F. J. Lovas, R. D. Suenram, and K. Matsumura, J. Mol. Spectrosc. **144**, 97 (1990).

258. W. Jäger, Y. Xu, N. Heineking, and M. C. L. Gerry, J. Chem. Phys. **99**, 7510 (1993).

259. W. Jäger and M. C. L. Gerry, Chem. Phys. Lett. **196**, 274 (1992).

260. T. Ogata, W. Jäger, I. Ozier, and M. C. L. Gerry, J. Chem. Phys. **98**, 9399 (1993).

261. W. H. Flygare and V. W. Weiss, J. Chem. Phys. **45**, 2785 (1966).

262. B. Rosenblum and A. H. Nethercot, Jr., J. Chem. Phys. **27**, 828 (1957).

7

263. F. A. Gianturco, L. Lewerenz, F. Paesani, and J. P. Toennies, J. Chem. Phys. **112**, 2239 (2000).